**Optical chemosensors for the inline detection
of long-term thermal degradation
in unsaturated poly(ester imides)**

Dissertation

zur Erlangung des Doktorgrades der Naturwissenschaften
(Dr. rer. nat.)

der

Naturwissenschaftlichen Fakultät II
Chemie, Physik und Mathematik

der Martin-Luther-Universität
Halle-Wittenberg

vorgelegt von

Herrn Alexander Funtan
geb. am 07.08.1989 in Kassel

Gutachter:

1. Prof. Dr. Wolfgang H. Binder

2. Prof. Dr. Stefan Mecking

Verteidigung: 14.11.2022

Abstract

During its application, a polymer material suffers from aging, leading to a reduced time of usage. Suitable sensor systems can detect occurring damage in a polymer and thus improve its safety by indicating necessary repairs in time.

Poly(ester imides) (PEIs) are high-performance polymers featuring an outstanding temperature stability and thus are used as coating material, e.g. on copper windings in electric motors. In operation, thermal stress leads to their thermal degradation and consequently restricts their usability.

The aim of this thesis was the development of a suitable sensor system, capable of detecting the aging condition of PEIs by means of inline measurements at any time.

Therefore, in a first step thermal degradation experiments of two PEIs and the corresponding PEI resins cross-linked with styrene were conducted at several temperatures. Degradation experiments were performed in self-built apparatuses which allowed to collect and analyze the formed gaseous degradation products. Thereby the alcohol neopentyl glycol (NPG) was identified as a main degradation product which was released over the entire period of 5000 h.

Subsequently, three potential optical, alcohol sensitive chemosensors were synthesized. These trifluoroacetyl functionalized stilbenes and an azobenzene can indicate the nucleophilic addition of an alcohol by a shift of their UV-Vis- and emission maximum due to their donor-acceptor properties. First, all sensor molecules were tested in solution experiments to prove their suitability to act as potential sensor molecules for NPG. Thereby, the influence of different nucleophilic analytes on the activation kinetics was tested and detection was done by UV-Vis- and fluorescence spectroscopy. All sensor molecules could be activated by different alcohols and amines with different kinetics depending on the analyte, whereas the azo dye was found to be unsuitable due to its non-fluorescent properties. Both stilbene dyes additionally showed a good thermal stability and thus were found to be suitable for further investigations in the solid state for which fluorescence spectroscopy was the analytic method of choice.

The activation within the solid state was first accomplished under model conditions by embedding the sensor molecules within a poly(styrene-*co*-divinylbenzene) resin which was exposed to a *n*-butylamine (*n*-BuA) solution and detected by fluorescence spectroscopy. Subsequently, the sensors were embedded within the two PEI-resins, which also were activated by *n*-BuA solution. Afterwards the within PEI-resins embedded sensors were successfully activated by gaseous NPG, the main analyte, as proven by fluorescence spectroscopy. Finally, sensor activation within the PEI-resins was done by in-situ analyte formation triggered by thermal aging of the specimens. Thereby the activation kinetics of the sensors were in good accordance with the degradation kinetics of both PEI-resins observed during the aging experiments. Furthermore, time-resolved fluorescence spectroscopy was performed and revealed a complex emission pattern of both stilbene molecules within the PEI resin. As a concentration dependency was observed, aggregation of the dye molecules within the resins was assumed.

Kurzzusammenfassung

In Folge ihrer Anwendungen treten in polymeren Werkstoffen Alterungserscheinungen auf, die zu deren Unbrauchbarkeit führen können. Geeignete Sensorsysteme können auftretende Schäden detektieren und die Sicherheit polymerer Werkstoffe verbessern, da notwendige Reparaturen rechtzeitig angezeigt werden.

Poly(esterimide) (PEI)s sind Hochleistungspolymere, die auf Grund ihrer außergewöhnlichen Temperaturbeständigkeit als Imprägniermaterialien, z.B. auf Kupferspulen in Elektromotoren, zum Einsatz kommen. Im laufenden Betrieb führt die auftretende thermische Belastung dennoch zu deren thermischem Abbau und schränkt ihre Verwendbarkeit ein.

Ziel dieser Arbeit war die Entwicklung eines geeigneten Sensorsystems, das es ermöglicht den Alterungszustand von PEIs mittels Inline-Messtechnik zu jedem Zeitpunkt zu überprüfen.

Dafür wurden in einem ersten Schritt thermische Zersetzungsexperimente durchgeführt, in denen zwei PEIs sowie deren mit Styrol vernetzten PEI-Harze bei verschiedenen Temperaturen gealtert wurden um den Zersetzungsprozess qualitativ und quantitativ zu erfassen. Die Abbauexperimente wurden in einer selbst konzipierten Apparatur durchgeführt, mit der die gebildeten gasförmigen Abbauprodukte aufgefangen und analysiert werden konnten. Dabei wurde der Alkohol Neopentylglykol (NPG) als Hauptabbauprodukt über das gesamte Intervall von 5000 h identifiziert.

Im Folgenden wurden drei potentielle optische, alkoholsensitive Chemosensoren synthetisiert. Dabei handelte es sich um trifluoroacetyl-funktionalisierte Stilbene und ein Azobenzol, die auf Grund ihrer Donor-Akzeptor-Eigenschaften nach nukleophiler Addition eines Alkohols, das Bindungsereignis durch eine Verschiebung von Absorptions- und Emissionsmaximum anzeigen. Alle Sensormoleküle wurden in Lösungsexperimenten auf ihre Tauglichkeit getestet. Dabei wurde der Einfluss verschiedener nukleophiler Analyten auf die Aktivierungskinetik untersucht. Die Detektion erfolgte mittels UV-Vis- und Fluoreszenzspektroskopie. Alle Sensormoleküle konnten in Abhängigkeit des Analyten mit verschiedenen Kinetiken aktiviert werden, wobei der Azo-Farbstoff auf Grund seiner fehlenden Fluoreszenz als nicht geeignet erkannt wurde. Die beiden Stilben-Farbstoffe verfügten zusätzlich über eine gute thermische Stabilität und wurden als geeignete Kandidaten für weitere Untersuchungen im Festkörper angesehen, in denen sich die Fluoreszenzspektroskopie als Methode der Wahl etabliert hat.

Die Aktivierung im Harz wurde zunächst unter Modelbedingungen durch Einbringung der Sensormoleküle in ein Styrol-Divinylbenzol-Copolymer in stark nukleophiler *n*-Butylaminlösung (*n*-BuA) mit Fluoreszenzspektroskopie demonstriert. Anschließend erfolgte die Sensoreinbettung in zwei PEI-Harze, welche ebenfalls durch *n*-BuA aktiviert werden konnten. Im Folgenden wurden die in die PEI-Harze eingebrachten Sensoren in gasförmigen NPG, dem späteren Hauptanalyten, erfolgreich aktiviert und mittels Fluoreszenzspektroskopie detektiert. Schließlich erfolgte die Aktivierung der Sensoren in den PEI-Harze durch in-situ Analytenbildung während der thermischen Alterung der Probekörper. Dabei spiegelten sich die beobachteten Abbaukinetiken beider PEI-Harze während der Alterungsexperimente in den Aktivierungskinetiken der Sensoren wieder.

Weiterführend wurde zeitaufgelöste Fluoreszenzspektroskopie durchgeführt, die ein komplexes Emissionsverhalten beider Stilben-Farbstoffe in der PEI-Matrix aufzeigte. Die dabei beobachtete Konzentrationsabhängigkeit ließ auf Aggregationsverhalten der Farbstoffmoleküle im Harz schließen.

Table of contents

VI

List of abbreviations

ABS	acrylonitrile butadiene styrene
ACN	acetonitrile
AIBN	2,2'-azobis(2-methylpropionitrile) / azobisisobutyronitrile
AIE	aggregation induced emission
Ar	aryl
ATR	attenuated total reflection
BDE	bond dissociation energy (kJ/mol)
BHT	3,5-di-*tert*-butyl-4-hydroxytoluene / butylated hydroxytoluene
CDCl$_3$	deuterated chloroform
CFRP	carbon-fiber-reinforced polymer
CHCl$_3$	chloroform
CNT	carbon nanotube
CPCM	conductor-like polarizable continuum model
DADPM	4,4'-methylenedianiline / 4,4'-diaminodiphenylmethane
DBU	diazabicyclo[5.4.0]undec-7-ene
DCM	dichlormethane
DFT	density functional theory
DPA	diphenylamine
DIPEA	*N*,*N*-diisopropylethylamine
DLTP	didodecyl 3,3'-thiodipropionate
DMF	*N*,*N*-dimethylformamide
EG	ethylene glycol
EtOAc	ethyl acetate
eq.	equivalent
F_T	tensile force
GC	gas chromatography
GPC	gel permeation chromatography
HCl	hydrochloric acid
HDPE	high density polyethylene
HOMO	highest occupied molecular orbital
HPLC	high-performance liquid chromatography
HR	high-resolution
ICT	intramolecular charge transfer
Imidol 6	1,2,3,6-tetrahydro-*N*-(2-hydroxyethyl)phthalimide
IR	infrared
s	strong
m	middle
w	weak
LDPE	low density polyethylene
LOD	limit of detection
LUMO	lowest unoccupied molecular orbital
MALDI	matrix-assisted laser desorption/ionization

MDI	4,4-methylendi(phenylisocyante)
MeOH	methanol
MIP	molecularly imprinted polymer
MMA	methyl-2-methylprop-2-enoate / methyl methacrylate
MS	mass-spectroscopy
n-BuA	n-butylamine
n-BuLi	n-butyllithium
NIP	non-imprinted polymer
NMR	nuclear magnetic resonance
s	singlet
d	doublet
dd	doublet of doublets
t	triplet
m	multiplet
NPG	neopentyl glycol
PA6	polycaprolactam / polyamide 6 / nylon 6
PAI	poly(amide imide)
PAN	polyacrylonitrile
PC	polycarbonate
PE	polyethylene
PEG	poly(ethylene glycol)
PEI	poly(ester imide)
PET	poly(ethylene terephthalate)
PLA	polylactide
PMA	poly(methyl acrylate)
PMMA	poly(methyl methacrylate)
PP	polypropylene
PS	polystyrene
PTHF	poly(tetrahydrofuran)
PU	polyurethane
PVC	poly(vinyl chloride)
SPS	solvent-purification-system
T_B	boiling point
t-BuOH	$tert$-butanol
T_c	ceiling temperature
TD-DFT	time dependent density functional theory
TEA	triethylamine
T_g	glass transition temperature
TGA	thermogravimetric analysis
THEIC	1,3,5-tris(2-hydroxyethyl)isocyanurate
THF	tetrahydrofuran
TLC	thin-layer chromatography
T_m	melting point

TMA	1,3-dihydro-1,3-dioxo-5-isobenzofurancarboxylic acid / trimellitic anhydride
TMDBIO	1,1,3,3-tetramethyldibenzo[e,g]isoindolin-2-yloxyl
TMP	2,4,6-trimethylphenol
TOF	time-of-flight
T_{onset}	onset temperature of decomposition
TPA	benzene-1,4-dicarboxylic acid / terephthalic acid
TPE	tetraphenylethene
T_{recry}	recrystallization temperature
TVA	thermal volatilization analysis
UV	ultraviolet
Vis	visible
VR	vibrational relaxation
1-BuOH	1-butanol
1,4-BuOH	1,4-butanediol

Parts of this thesis have been published in:

Funtan, A.; Michael, P.; Rost, S.; Omeis, J., Lienert, K.; Binder, W. H., Self-Diagnostic Polymers – Inline Detection of Thermal Degradation of Unsaturated Poly(ester imide)s, *Advanced Materials* **2021**, 2100068.

Funtan, A.; Binder, W. H., Thermischen Abbau erkennen, *Nachrichten aus der Chemie* **2022**, *70*, 40.

Funtan, A.; Binder, W. H., Towards in-line detection of thermal polymer degradation, *Research Outreach* **2021**, *125*, 190.

Parts of this thesis have been protected by the patent 10577PFA WO filed from ALTANA AG.

1. Introduction
1.1. Engineering materials
The processing and use of materials has always played a crucial role in the development of mankind. Wood and stone, the first natural materials, were used in Stone Age, offering a great benefit when they have been processed into tools. Since then, other materials, requiring advanced processing methods but providing a wider range of application possibilities, have been discovered. The most important are ceramics[1-3] and metals[4-6], particularly alloys, which are processed by sintering or melting, respectively.

Due to technical advances, possibilities and requirements for the materials changed and enabled the emergence of a new class of synthetic materials which considerably differed from the hitherto known inorganic materials and whose existence was first described in 1920 by Hermann Staudinger[7]: *Polymers*. Polymers are large molecules which compose of small, covalently linked organic molecules. Monomers and their orientation in the polymer chain affect the properties of the polymer, precisely tailoring their characteristics such as thermal stability, mechanical stiffness, electric conductivity or chemical resistivity to the intended application by having a wide variation and combination of monomers and polymerization techniques at choice[8-17]. Together with their low density, polymers are predestinated to be used wherever a low weight is advantageous, e.g. as packaging material, for weight reduction and the associated reduction in fuel consumption in automotive industry, as objects of daily use or in fiber-optic communication, thus engendering huge progress in the development of new and improvement of yet existing products[18-23].

Having the choice between numerous materials requires to consider which material is best suited for a specific application, especially with regard to its form stability and durability, which both are heavily influenced by the conditions the material is exposed to during its service lifetime. External influences can change the structure of a material, which in turn also changes the material properties. Because they impair the functionality by reducing the service lifetime or even may be life-threating, these changes are usually disadvantageous and thus this process is undesirable. For metals the common ways to undergo structural changes are corrosion[24-26] through chemical or electrochemical interaction with a surrounding substance and fatigue through mechanical and thermal load[27-29]. The most prominent example might be rusting of iron[30] in the presence of water or humidity leading to material embrittlement. Ceramics usually fail when they are exposed to high mechanical loads due to their low fracture toughness[31-33]. Due to the organic nature of polymers and their different chemical compositions, external influences, such as heat, oxygen, mechanical load, light or chemicals can trigger numerous different consequences depending on the polymer class[34-36]. Heat and mechanical load are the most significant aging parameters for polymers being used as components for industrial products. Therefore polymeric materials are divided in three different classes regarding their thermal and mechanical properties which should be briefly discussed in the following part.

1.1.1. Thermosets
Thermosets are rigid materials, consisting of a three-dimensional, covalently linked polymeric network[37-38] (**Figure 1a**). As the motion of the polymer chains is restricted by the cross-linking process, once they are formed, thermosets cannot be reshaped. Thus, upon heating and applying a mechanical force, thermosets will not become ductile. Thermosets are amorphous materials

and exposing them to high temperatures or mechanical force will result in a thermal decomposition respectively to a breakage of the specimen.
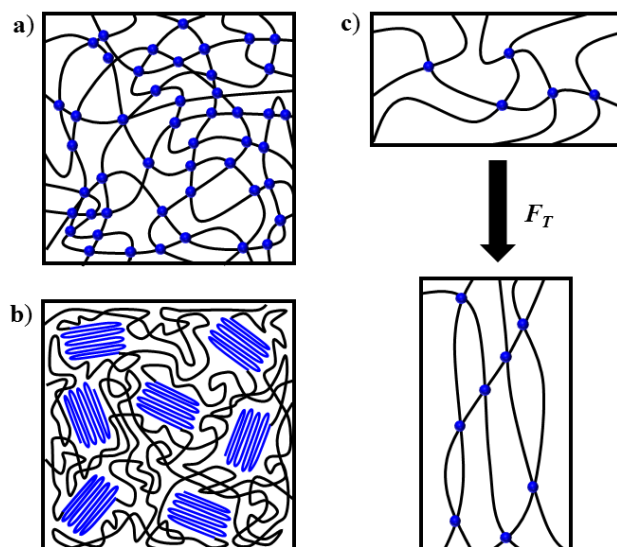
Figure 1 Classification of polymers according to their mechanical-thermal behavior: a) Thermosets are rigid due to their high network density, b) thermoplastics are semi-crystalline, non cross-linked polymers, showing shapeability when heated above T_m and c) elastomers are lightly cross-linked polymers featuring elastic behavior when applying a tensile force F_T.

Commonly, thermosets are formed by stepgrowth-reactions, including polycondensation or polyaddition, to form pre-condensates which later can be further polymerized by using a hardener leading to the formation of the three-dimensional network. Well-known examples of thermosets are polyurethanes, phenolic resins and epoxy resins[37, 39]. As their properties not only depend on choice of monomer and their molecular weight, but especially on the cross-link density, they feature a wide range of characteristics and thus can be used for many applications, e.g. for furniture, as insulation material and binders, or in building industry[37, 40].

1.1.2. Thermoplastics

Unlike the covalently cross-linked networks in thermosets, thermoplastic polymers consists of non-covalent linked long carbon chains which are subjected to intermolecular interactions such as van der Waals interactions or hydrogen bonds[41-42]. By aligning the polymer chains in a parallel pattern, efficiency of these intermolecular forces can be enhanced and crystalline domains might be formed (**Figure 1b**). Heating a thermoplastic polymer above its glass-transition temperature T_g and its melting point T_m will drastically reduce the strength of the intermolecular forces between the polymer chains, forming a mouldable melt, and allowing the original polymer to be reshaped by applying a mechanical force[43]. After cooling, the reshaped polymer is maintaining its new appearance and the process is repeatable as long as the temperature does not exceed the decomposition temperature of the polymer. However, repeated processing might lead to material deterioration even at temperatures below the decomposition temperature[43]. As for the thermosets, exceeding the decomposition temperature will lead to a breaking of the covalent bonds of the polymer backbone and thus to an irreversible damage.

The most common thermoplastics are polyethylene (PE), polypropylene (PP), poly(vinyl chloride) (PVC), poly(ethylene terephthalate) (PET) and acrylonitrile butadiene styrene

(ABS)[44], becoming an indispensable part of everyday life due to their excellent processability and favorable properties. Thermoplastic polymers are primarily used for packaging and manufacturing of engineering components[45].

1.1.3. Elastomers

Like thermosets, elastomers are amorphous polymers but have a significantly lower cross-linking density. Consequently, elastomers feature elastic behavior because the entangled polymer chains can partially untangle as long as a tensile force is applied (**Figure 1c**). Due to the cross-linkages, polymer chains will return to their coil structure after the mechanical force is removed[46], but repeated cyclic deformation typically leads to wear due to friction and abrasion[47]. Elasticity may only be present when the elastomer is used above its T_g and an increase of temperature might further increase elastic behavior because chain movement is facilitated, but at the same time this leads to material fatigue due to accelerated thermal oxidation[48]. As for thermosets and thermoplastics, exposing an elastomer to temperatures above its decomposition temperature will result in a rupture of the covalent bonds of the polymer backbone and thus to an irreversible damage.

Well-known elastomers are natural rubber, which predominantly consists of *cis*-1,4-polyisoprene, and styrene-butadiene rubber (SBR), a synthetic copolymer of styrene and 1,3-butadiene, the most important material in the production of car tires[49].

1.2. Stability of polymers

The most important issue concerning polymer degradation is its progress over time, resulting in chemical and physical changes of the polymer that are detrimental to its application and ultimately prevent ongoing application. The following part deals with different influential factors causing or accelerating polymer degradation with the emphasis placed on thermal polymer degradation, as it was the predominant aging parameter for the polymeric materials investigated in this thesis.

1.2.1. Thermal stability of polymers

The major drawback of polymers is their high thermal susceptibility compared with inorganic materials, restricting their use as engineering materials. While for ceramics and metals the thermal strain is limited by their melting point or thermal expansion, commonly notable at temperatures above 1000 °C because of strong ionic interactions and metallic bonds[50-52], thermal stability of polymers is significantly lower due to a weaker covalent character of the polymeric backbone. Although both are organic molecules, the consequences of thermal stress on polymers are not comparable to that of their corresponding monomers. Exposing a solid, low molecular weight organic molecule to a temperature above its melting point T_m causes the molecule to melt, followed by evaporation when the temperature is further increased and reaches the boiling point T_B.

Because of the covalent bonds within the polymer chain, as well as due their intermolecular interactions and the associated capabilities for chain arrangement providing a variety of different microstructures, in particular amorphous and crystalline domains, polymers show a different characteristic thermal behavior. Amorphous domains, in which the polymer strands are disordered, are not able to melt but their mobility is increased with increasing temperature and they are able to rearrange after reaching the glass transition temperature T_g showing a

second order phase transition[53]. Intermolecular interactions between polymers chains or attached substituents in the polymer backbone can cause a preferable alignment of polymer chains, leading to ordered crystalline domains, which are able to melt after being heated above the melting point T_m showing a first order phase transition[54]. Often polymers are semi-crystalline, thus exhibiting both a T_g and a T_m.

Contrary to their low molecular weight monomers, polymers do not have a vapor pressure, because the energy required to vaporize a polymer is much higher than the energy required to destroy the weakest covalent bond within a polymer, which usually are C–C bonds with a bond dissociation energy (BDE) of roughly 322 - 348 kJ/mol and C–O bonds with a BDE of roughly 322 - 331 kJ/mol, respectively[55-56]. Thus, significantly exceeding the temperature above T_g or T_m will not lead to evaporation but to a decomposition of the polymer. **Table 1** lists T_g, T_m and decomposition temperatures T_{onset} of some common polymers.

Table 1 Glass transition temperatures T_g, melting points T_m and decomposition temperatures T_{onset} under oxygen and nitrogen atmosphere for common polymers heated with a constant heating rate of a) 9.2 K/min· b) 9.0 K/min, c) 9.1 K/min, d) 8.2 K/min, e) 5.0 K/min and f) 10.0 K/min[57-60].

Polymer	T_g [°C]	T_m [°C]	T_{onset} [°C] in O_2	T_{onset} [°C] in N_2
PE	-125	138	220[a]	350[b]
PP	-10	176	180[c]	250[d]
PS	105	240	200[d]	250[b]
PVC	81	220	220[e]	220[e]
PET	69	270	350[f]	400[f]
PMMA	45 - 115	160 - 200	285[f]	325[f]
PC	123 - 149	170 - 267	420[f]	470[f]
PA6	50 - 75	215 - 226	350[f]	400[f]

Due to the complexity of thermal polymer decomposition, the involved kinetics are often determined by approximation using various models. The general equation for the kinetics of polymer degradation is given by equation (**1**), with α being the degree of conversion, T the temperature and $f(\alpha)$ the reaction model[61].

$$\frac{d\alpha}{dt} = k(T)f(\alpha) \tag{1}$$

The temperature dependent function $k(T)$ might be substituted by the Arrhenius equation, yielding equation (**2**), where A is the pre-exponential factor, E the activation energy and R the universal gas constant.

$$\frac{d\alpha}{dt} = A \exp\left(-\frac{E}{RT}\right) f(\alpha) \tag{2}$$

The most common approach to determine degradation kinetics are isoconversional methods, which assumes that a constant conversion function $f(\alpha)$ is independent from the heating rate for any value of α[61-62]. Among isoconversional methods, methods developed by Ozawa-Flynn-Wall[63-64], Friedman[65] and Kissinger-Akahira-Sunose[66-67] are the most popular. Isoconversional methods require the measurement of temperatures for fixed values of α at different heating rates[61] by means of thermogravimetric analysis, yielding values for the activation energy E_α of degradation processes in dependence from the conversion α[62]. Plotting E_α against α often shows that the activation energy varies for different conversion, thus demonstrating the complexity of

degradation processes, which might change at different extends of conversion, e.g. thermal degradation, cross-linking or crystallization[62]. However, when E_α is independent from α, a single-step progress can be assumed[62]. The results from isoconversional studies can be used to predict the thermal behavior of a material, for instance the time at which a certain conversion will be reached at a given temperature and thus are a very useful tool to make assumptions about the thermal long-term stability of a polymer[62].

It is worth mentioning that the microstructure of polymers has a decisive influence on their thermal properties[68]. Since e.g. molecular weight, molecular weight distribution and tacticity affect the thermal properties[69], two samples of the same homopolymer but different in those properties mentioned above might show different values for thermal parameters. For example, syndiotactic PMMA has both a significantly higher T_g and T_m compared to its isotactic form (**Table 1**)[60]. For PE frequently different decomposition temperatures are reported, depending on whether it is high density polyethylene (HDPE) with an activation energy of 238 - 247 kJ/mol or low density polyethylene (LDPE) with an activation energy of 215 - 221 kJ/mol. A higher degree of branching increases the susceptibility towards thermal degradation by facilitating chain scission due to enhanced radical stabilization, thus significantly lowering the polymer stability[70]. Branching lowers the activation energy (179 - 188 kJ/mol) to trigger the decomposition of PP, thus being less thermal stable compared to PE[70-71]. Furthermore extrinsic parameters play a crucial role, e.g. the thermal history of the polymer or additives added during the production process which can differ depending on the manufacturer[57]. Consequently, in literature often different ranges of T_g and T_m are reported.

Concerning the thermal stability of polymers, usually given by the decomposition temperature T_{onset}, literature also frequently provides different values. Apart from the aforementioned reasons, this is mainly due to the used method, thermogravimetric analysis (TGA), for determining T_{onset}. In TGA measurements the time-dependent mass loss of a polymer sample caused by degradation processes associated with a temperature increase is determined. T_{onset} is the temperature at which the first mass loss is detected. Typically, these measurements are carried out under dynamic conditions, i.e. the temperature is increased linearly until the maximum temperature is reached. In literature, the heating rate is chosen arbitrarily, usually between 5 and 20 K/min, but can have a crucial influence on the thermal decomposition pattern. At lower heating rate a polymer is longer exposed to elevated temperatures which can be particularly important at temperatures above T_g and T_m but below T_{onset} because here degradation processes preferentially induce structural changes instead of causing a bond breaking within the polymer backbone. These might be reactions whose activation energy is smaller compared to a bond cleavage, for instance reactions of substituents attached to the polymer chain[72] or physical processes, e.g. the transition between amorphous and crystalline segments[73]. Even if these processes, which are described in detail in chapter 1.2.1.2, do not necessarily lead to a mass loss, the thermal history of the polymer changes, thus influencing the subsequent degradation mechanism[74].

When measuring thermal polymer degradation, the results of a TGA measurement are even more influenced by the choice of the purge gas, usually nitrogen or oxygen. In many cases, nitrogen is preferred because it prevents sample oxidation and results are easier to analyze. This is contrary to the fact that commonly polymer degradation, e.g. in engineering materials used in industry, does not take place in an inert atmosphere, but under atmospheric oxygen. The

extent to which the thermal stability of a polymer depends on surrounding atmosphere becomes apparent by checking **Table 1**; the values for T_{onset} under oxygen atmosphere are significantly lower, partially by more than 100 °C, compared to T_{onset} determined in nitrogen atmosphere. This observation is reasonable because the generally accepted mechanism for the thermal degradation of polymers follows an autocatalytic thermal-oxidative pathway[57, 75-76] which is shown in **Figure 2**.
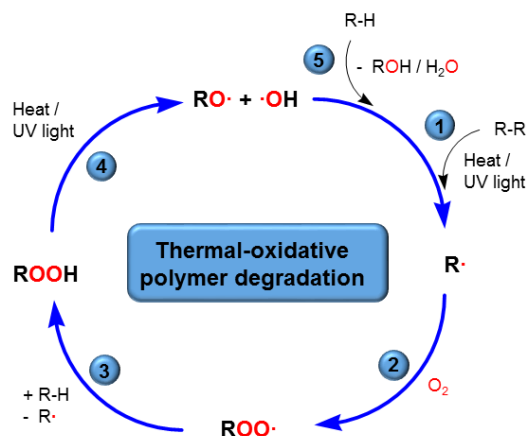
Figure 2 Autocatalytic cycle of thermal-oxidative polymer degradation.

The formation of the radicals in step (1) enabling the polymer decomposition, is attributed to the manufacturing process. In general, shaping requires high thermal and mechanical loads, for instance during melt extrusion, resulting in incorporation of different kinds of fragile defects, e.g. incorrectly inserted monomers which lead to tacticity defects[77-81], residual catalyst or metal ions[82-86] due to the production process or an introduction of functional groups such as ketone groups into the polymer due to partial oxidation especially promoting photochemical degradation[76, 87-89] and formation of peroxide bonds[58, 90-92] featuring significant lower BDE of roughly 167 - 188 kJ/mol, capable of triggering the autocatalytic degradation[93-94]. The presence of oxygen supports the formation of peroxide radicals by reducing the activation energy required for polymer degradation.

Wight *et al.* compared the thermal decomposition of PE and PP under oxygen and nitrogen atmosphere[58]. Under oxygen atmosphere the initial degradation processes of PE and PP require an activation energy of 80 - 90 kJ/mol. Under nitrogen, the activation energy for initial degradation of PE and PP is 150 kJ/mol but continues to increase as thermal decomposition progresses, reaching 240 and 250 kJ/mol, respectively. Thus, the supporting effect of oxygen on polymer degradation becomes obvious.

Additionally, the increasing values for activation energy under nitrogen also indicate the presence of the aforementioned weakest links, whose rupture requires less energy compared to later degradation processes occurring during the breakage of the main polymer chain. Following the autocatalytic thermal-oxidative degradation mechanism shown in **Figure 2** the initially formed radical may react with oxygen to form a peroxide radical (2) which can subtract a hydrogen atom from another polymer chain (3) to form an alkyl radical and a peroxide. Decomposition into two radicals (4) allows to trigger further degradation processes like fragmentation, chain scission or cross-linking accompanied by the release of oxidative by-products (5). However, this thermal-oxidative mechanism only gives a very rough overview of

the processes that actually take place during the thermal degradation of polymers, which have not yet been fully understood.

Commonly three approaches focusing on the chemical structure, i.e. the bonding properties in the main chain as well as attached substituents, are used, to provide a more precise insight in the decomposition mechanism, especially regarding the identification of degradation products. Nevertheless, it should always be considered that, in addition to the chemical polymer structure, other intrinsic polymer parameters, e.g. molecular weight and microstructure[69], as well as the measurement parameters used in the determination of thermal decomposition processes[57] have a decisive influence, which not only complicates a proper investigation itself but also limits the comparability of literature values. Especially with regard to the transferability for application-related quests in industry, the results of numerous existing thermal decomposition studies can only be used to a limited extend, since they are determined under scientific model conditions that do not reflect operating terms. The previously mentioned different structural-related approaches to describe thermal polymer degradation are explained in the following part.

1.2.1.1. Thermal degradation by chain scission
Usually, thermal polymer degradation is associated with a rupture of bonds located within the polymer backbone, thus with a decrease in molecular weight due to the release of low molecular weight degradation products. In fact, there are two degradation mechanisms matching the previously mentioned criteria: chain end scission and random main chain scission. The difference will be explained below and is depicted in **Figure 3**.
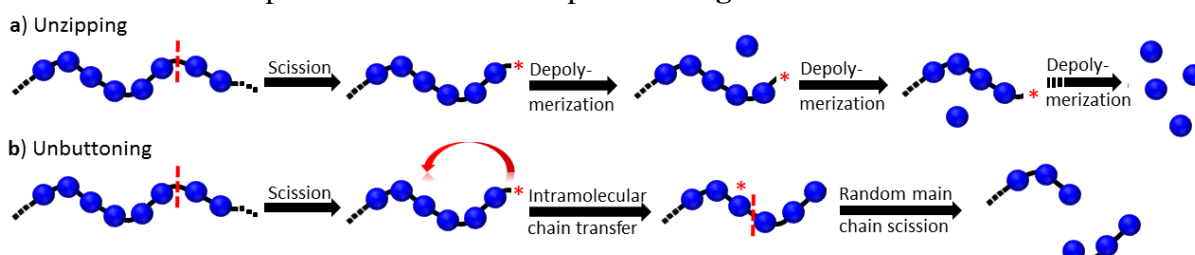
Figure 3 Schematic representation of the thermal polymer degradation processes accompanied by a loss of molecular weight. a) Initial homolytic chain scission followed by depolymerization at the chain end (unzipping) and b) defragmentation by random main chain scission due to intramolecular chain transfer after initial homolytic chain scission (unbuttoning).

During chain-growth polymerization the addition of further monomers to a growing polymer chain (polymerization reaction) is in equilibrium with the cleavage of the monomer from the active chain end (depolymerization reaction). The equilibrium position depends on the temperature, the monomer concentration and the aggregate state of the polymer and the monomer, finally determined by the ceiling temperature T_c as expressed in equation (**3**) where $\Delta H°$ and $\Delta S°$ are the standard free polymerization enthalpy and entropy, R the universal gas constant and *[M]* the monomer concentration[72, 95].

$$T_c = \frac{\Delta H°}{\Delta S° + R \, ln[M]} \tag{3}$$

When the reaction temperature exceeds the ceiling temperature, depolymerization proceeds faster than polymerization and effectively no chain growth takes place since the cleavage of

monomers is faster than monomer addition, resulting in a loss of molecular weight. Consequently, the expectable pathway of thermal degradation is a reversion of polymerization, a stepwise depropagation by monomer release after a homolytic chain scission of the weakest bond located within the polymer backbone. In literature this process is denoted as chain-end scission or unzipping.

Unzipping often involves the formation of radicals and thus is highly dependent on the chemical structure of the polymers and the decomposition temperature. Radicals are highly reactive, unpaired single electrons usually occur as unstable intermediates and are formed due to decomposition of weakest links within the polymer chain incorporated during the production[58, 77]. The stability of radicals primarily is determined by hyperconjugation hence by their substituents decreasing from tertiary to primary substitution. The best illustration for both, unzipping and the relevance of radical stability, is the thermal degradation mechanism of PMA compared to PMMA as depicted in **Figure 4**.
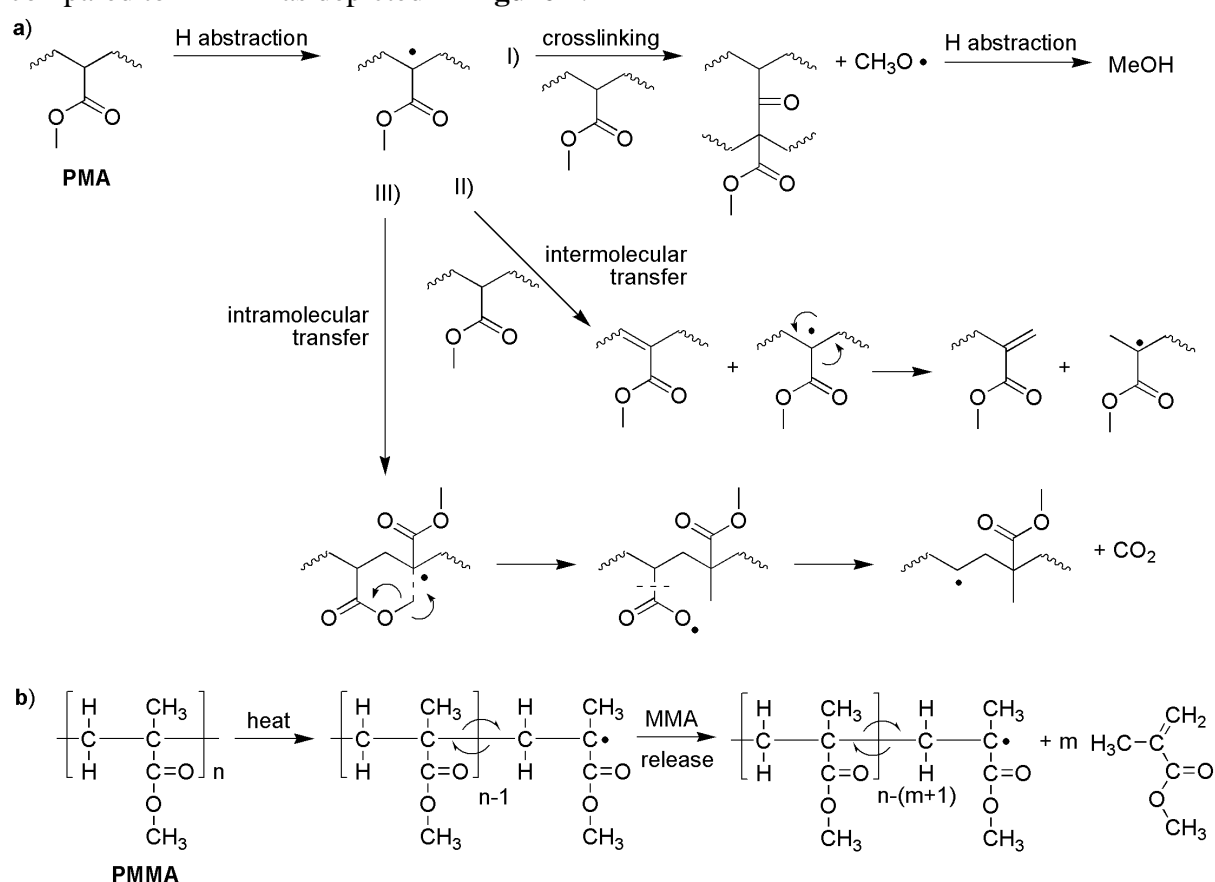
Figure 4 a) Possible thermal degradation steps of PMA to form I) alcoholic degradations products by cross-linking, II) olefins by intermolecular chain transfer and III) carbon dioxide through intramolecular chain transfer and b) unzipping mechanism of PMMA resulting in monomer recovery.

Pyrolyzing PMMA at 425 °C recovers 99.4 % of the monomer methyl methacrylate while for the decomposition of PMA no monomer recovery is observable[96-97]. Due to the additional methyl group of PMMA the formed tertiary radicals are stabilized thus enabling a stepwise depolymerization by cleaving off monomer from the active chain end. In contrast to this unzipping mechanism, for PMA the lack of stabilization enhances random main chain scission by intra- and intermolecular chain transfer and thus leads to the formation of more complex multicomponent degradation mixtures. Such degradation mixtures often contain short chain

fragments, i.e. dimers, trimers, etc., alcohols, olefins and carbon dioxide[96-98] but only a small amount of monomer, usually a maximum of 0.3 % referred to the original polymer weight[97]. As during these processes the radical is shifted from the chain end to positions located within the polymer chain, enabling the release of bigger chain fragments by a random main chain scission, this process is referred to as unbuttoning[58, 99].

Random main chain scission often competes with cross-linking processes, which can also be observed for the thermal degradation of PMA and accounts for the release of methanol[98]. However, monomer recovery of thermally degraded PMMA drastically decreases when the polymer is exposed to higher temperatures, promoting secondary reactions by intra- and intermolecular chain transfer to form monomer derivatives and facilitating the formation of gaseous degradation products, e.g. water, carbon dioxide and low molecular organic compounds such as methane and ethane. Thermally degrading PMMA at 825 °C will reduce the monomer yield to 37.4 %[96].

Another example for the relevance of radical stability becomes apparent by comparing the thermal decomposition mechanism of PE and PP[71, 97] as depicted in **Figure 5**. Degradation of both, PE and PP, is triggered by a homolytic chain scission within the polymer backbone, leading to the formation of highly reactive radicals. Subsequently the formed radicals can undergo either unzipping or unbuttoning to crack the polymer radicals into low molecular weight degradation products.

Due to the exclusive formation of highly unstable primary radicals, the thermal degradation of PE is dominated by intermolecular chain transfer, preferentially leading to the formation of numerous olefins by random main chain scission while only traces of ethene are formed, making depolymerization negligible[72, 100].

In PP the methyl substitution enables the formation of unstable primary radicals, predominantly triggering unbuttoning by intermolecular radical transfers[97]. Additionally, more stable secondary radicals promoting unzipping via intramolecular chain transfer[97]. However, the secondary radical is less stable then the tertiary radical formed during degradation of PMMA, thus the thermal degradation of PP is also dominated by random main chain scission.

In order to maintain the clarity **Figure 5** shows the thermal decomposition of pure PE and PP under vacuum, any defects within the chain and the presence of oxygen would extend the pattern by further degradation processes. Michal *et al.* investigated the composition of volatile degradation products of PE and PP formed during pyrolysis in helium and the thermo-oxidation in air[100]. Under thermo-oxidative conditions the majority of the decomposition products of PE are oxidized, with aldehydes (48.2 %), especially butyraldehyde and valeraldehyde, and ketones (2.8 %), presumably resulting from branching points, being the main oxidized species. The proportions of olefins, particularly 1,3-butadiene, and paraffins, especially *n*-pentane, are 25.1 % and 11.9 %, respectively.

During pyrolysis PE mainly decomposes into olefins (59.4 %), particularly 1-hexene and paraffins (35.0 %), especially *n*-heptane. The main degradation products of PP using thermo-oxidative conditions are methyl alkyl ketones (57.4 %), especially acetone, which are favorably formed due to methyl substitution. The major volatile degradation products during pyrolysis are the branched olefins 2,6-dimethyl-3-heptene (49.0 %) and 2-methyl-1-pentene (8.8 %) plus the linear paraffin *n*-pentane (18.7 %). Under both conditions only small amounts of propylene were formed, 1.1 % during pyrolysis and 0.03 % during thermal oxidation, confirming that thermal PP degradation follows random main chain scission because stabilization by the

secondary radical is not sufficient to promote unzipping as dominating degradation pathway. In total, more than 70 and 50 different degradation products have been found for the decomposition of PE and PP, respectively.
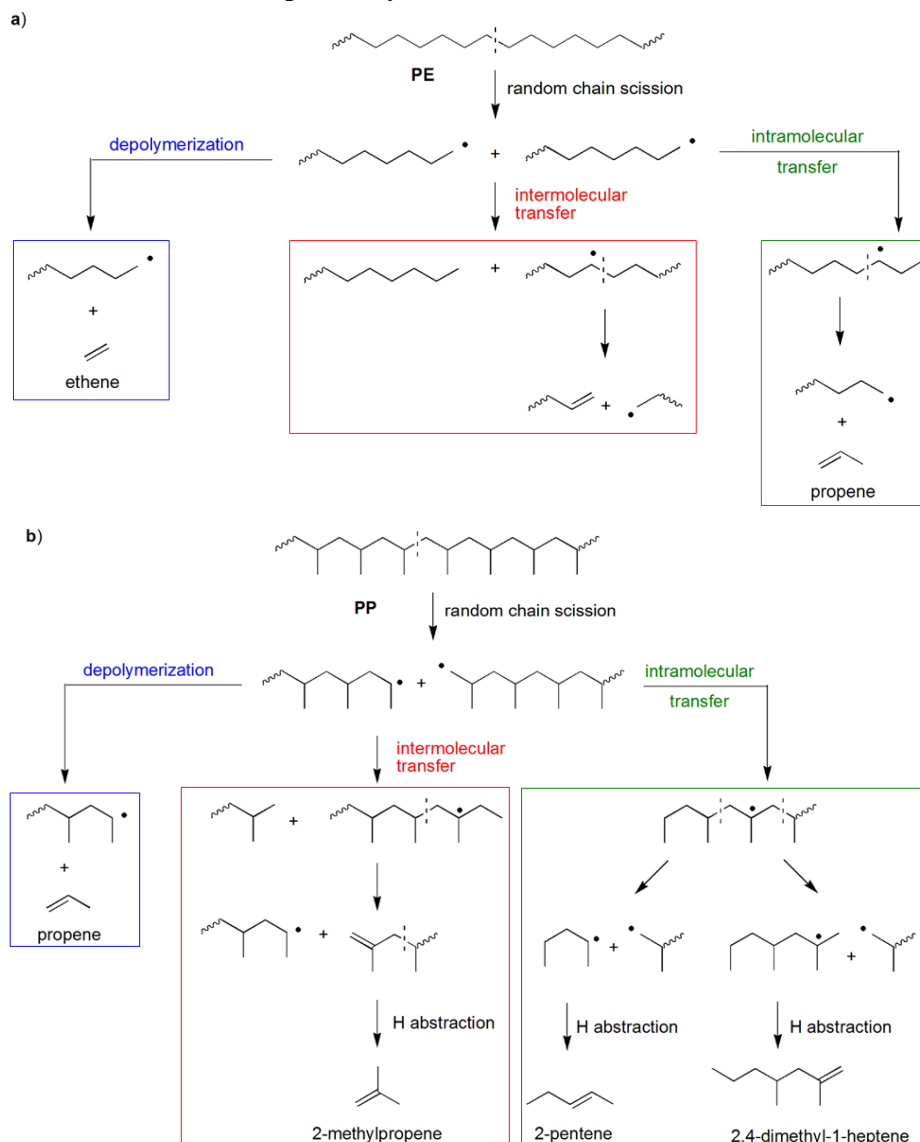
Figure 5 Pattern of the thermal degradation mechanism of a) PE and b) PP in vacuum.

Unzipping usually dominates the thermal degradation pattern of polymers with an aliphatic backbone, e.g. chain-growth polymers synthesized by radical polymerization. Nevertheless, as previously demonstrated, even for aliphatic chain-growth polymers unbuttoning is a common degradation mechanism, unless the formed radicals are not stabilized and chain transfer prevents a stepwise depolymerization at the active chain end.

In polymers such as step-growth polymers, e.g. polyesters and polyamides synthesized by polycondensation or polyurethanes polymerized by polyaddition, main chain scission preferentially occurs by non-homolytic scission at functional groups, constituting the weakest links[72, 97]. The mechanism schematically is shown in **Figure 6**. Random chain scission usually proceeds by intramolecular hydrogen transfer, thus without the formation of radicals, leading

to degradation products which often are more narrowly defined because chain transfer processes are less distinct[57, 72].
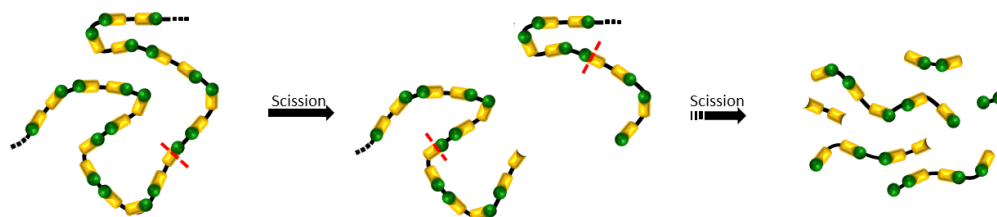
Figure 6 Schematic degradation mechanism of a step-growth polymer triggered by a random main chain scission at a functional group within the polymer backbone.

However, because typically non-volatile oligomeric functionalized degradation products are formed, secondary reactions, e.g. cross-linking and cyclization reactions, are likely to occur[72]. Similar to the thermal degradation of chain-growth polymers, the exact degradation pattern depends on the chemical structure and on external conditions, especially regarding the possibility of thermal-oxidative degradation.

Polycondensation of terephthalic acid and ethylene glycol yields PET, a well-known polyester. Common degradation mechanisms reported in literature are summarized in **Figure 7**[97, 101-104].
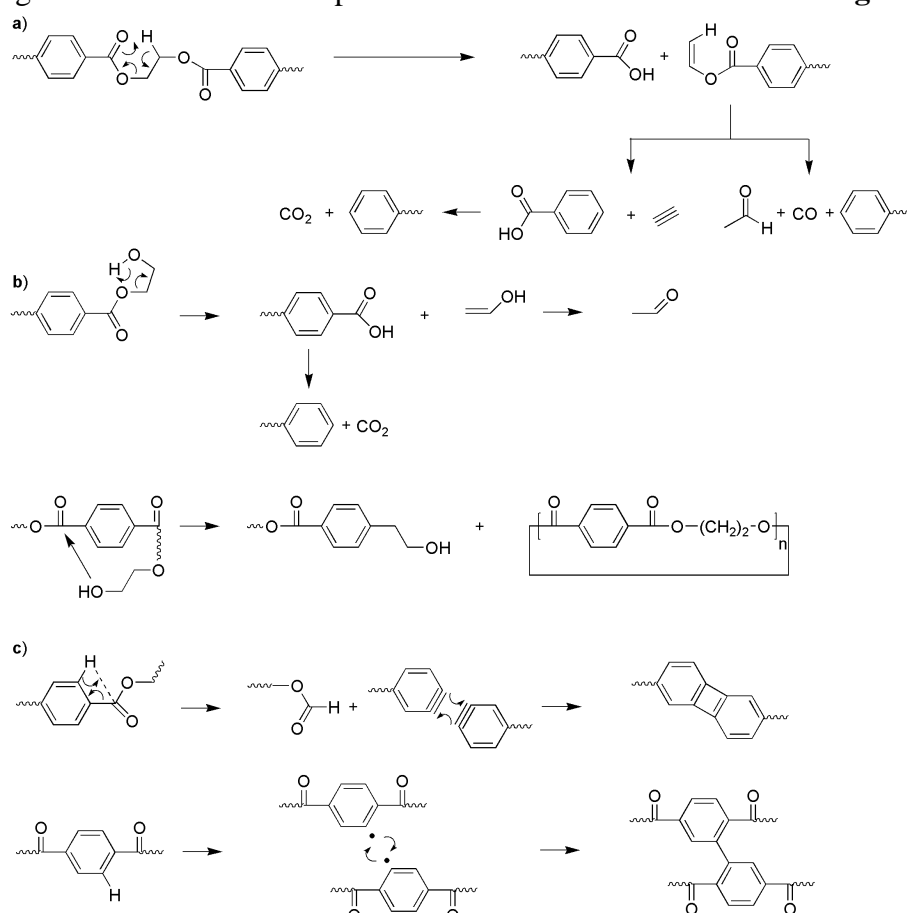
Figure 7 Possible thermal degradation steps of PET with a) non-homolytic chain scission via β-C-H transfer, b) rearrangements at the hydroxyl terminated polymer ends and c) cross-linking of the residual aromatic structures.

The main volatile degradation product above 350 °C is acetaldehyde, which is released by elimination from the vinyl ester intermediate formed by a β-C-H hydrogen transfer as shown in

Figure 7a[97]. At higher temperatures degradation products such as acetylene, methane and CO_2 indicate the occurrence of additional homolytic chain scission via a radical mechanism[97, 101]. In **Figure 7b** degradation processes which are likely to occur at the hydroxyl terminated polymer ends are depicted. Elimination yields a polymer with an acid-end group and monomeric vinyl alcohol which is subsequently transformed into the thermodynamically stable acetaldehyde[101]. Furthermore, in literature the formation of macrocylces by cyclization of the terminal hydroxyl group with a carbonyl group located in the polymer backbone is reported[102]. During the vaporization of the low molecular weight fragments, macrocylces and aromatic compounds accumulate and undergo cross-linking reactions to form residual char. Cross-linking reactions can follow a radical mechanism but literature also states Diels-Alder addition of two benzynes to form *bis*-phenylene as depicted in **Figure 7c**. Under inert atmosphere PET decomposes in a single step between 400 °C and 500 °C leaving about 20 % mass residue due to the cross-linking of aromatic structures resulting in char formation[103, 105]. Using thermo-oxidative conditions, a second decomposition step between 500 °C and 600 °C leads to the complete combustion of the char[103, 105]. The structural diversity of stepgrowth polymers complicates the comparison between different degradation studies accessible in literature.

Table 2 summarizes commonly reported degradation products for different polymer classes predominantly following a non-homolytic chain scission at functional groups in the polymer backbone. Especially the presence of sidechains significantly reduces their thermal stability[106]. While monomers and their oxidation products are rather formed at lower temperatures near the initial decomposition temperature by non-homolytic chain scission, at higher temperatures radical homolytic chain-scission, especially under thermo-oxidative conditions, will also effort aliphatic hydrocarbons and olefins[97, 107].

Table 2 Overview of the thermal stability and expected degradation products of various polymer classes predominantly degraded by a non-homolytic chain scission.

Polymer class	Structural element	T_{onset} [°C]	Degradation products	Literature
Polyester	$\left[R-\underset{O}{\overset{\parallel}{C}}-O \right]_n$	210 - 400	aldehydes, aromatic + aliphatic hydrocarbons, olefins, CO	104, 106, 108-109
Polycarbonate	$\left[R-O-\underset{O}{\overset{\parallel}{C}}-O \right]_n$	250 - 450	phenols, aldehydes, cyclic oligomers, CO_2, CO	107, 110-112
Polyamide	$\left[R-\underset{O}{\overset{\parallel}{C}}-\overset{H}{N} \right]_n$	280 - 475	nitriles, cyclic monomer (lactams) + oligomers, aliphatic + cyclic hydrocarbons, olefins, CO_2	113-115
Polyurethane	$\left[R-O-\underset{O}{\overset{\parallel}{C}}-\overset{H}{N} \right]_n$	250 - 450	alcohols, amines, isocyanates, nitriles, olefins, aromatic compounds, CO_2	116-118

1.2.1.2. Thermal degradation without chain scission

Thermal degradation via homolytic and non-homolytic chain scission is always accompanied by a decrease of the degree of polymerization due to bond breakage of the weakest link within the main chain. Since the activation barriers for thermal decomposition are sufficiently high, these processes often play a subordinated role considering polymer degradation under normal conditions. However, there are possibilities for thermally induced structural changes to occur within the polymer without being exposed to high temperatures.

The activation energies for thermal reactions of substituents attached to the polymer main chain are significantly lower and are predominantly based on elimination or cyclization reactions, which occur intramolecularily or intermolecularily depending on the structure of the polymer and the assembly of the substituents. Because thermally more stable vinyl or aromatic systems are formed, these molecular rearrangements are a protective mechanism to decelerate thermal degradation of the polymer backbone. Even though in these processes structural changes can be partially beneficial, often more serious negative consequences, e.g. color formation, embrittlement and loss of mechanical stability, resulting in impairments and thus preventing a further application, can be observed[119]. Several examples for this type of molecular rearrangements are shown in **Figure 8**.
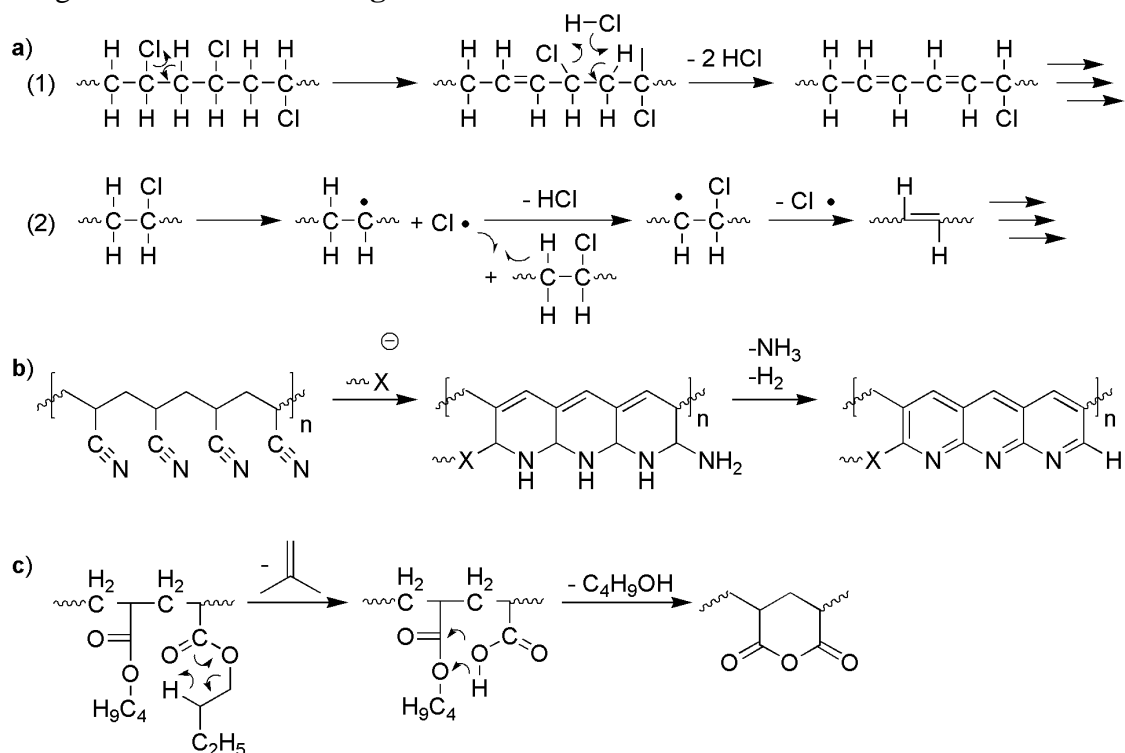
Figure 8 Possible thermal degradation steps without main chain scission by a) dehydrochlorination of PVC, b) aromatization of PAN and c) olefin elimination subsequently followed by anhydride formation in poly(*tert*-butyl methacrylate).

Dehydrochlorination of polyvinyl choride (PVC), the elimination of the chlorine substituents attached to the backbone, causes a release of HCl and the formation of polyene structures in the main chain[72, 120]. Dehydrochlorination can follow a HCl-catalyzed mechanism involving four- and six-membered transition states or a radical mechanism involving homolytic C-Cl-scission (**Figure 8a**)[97]. Although the mass loss during the dehydrochlorination at 200 to 300 °C amounts up to 56 %, the degree of polymerization remains almost unaffected[119]. Only in a second

degradation step between 350 and 525 °C, the remaining dehydrochlorinated PVC will crack down into organic low molecular weight compounds[120].

Heating a polyacrylonitrile (PAN) to 200 °C results in the elimination of low molecular weight fragments, predominantly H_2, NH_3 and HCN along with a variety of nitriles, causing cyclization reactions which are increasing the thermal stability of the remaining char (**Figure 8b**)[72, 121-122]. Hydroxide peroxides, which are used during the production process, are likely to introduce alkoxy groups into PAN which subsequently serve as the initiating nucleophiles to trigger its degradation[122].

Furthermore the functional groups for molecular rearrangements might not be present in the original polymer but are formed by a previous elimination step within a side chain, e.g. anhydride formation after generation of carboxyl group by γ-H-transfer leading to olefin-elimination in a poly(*tert*-butyl methacrylate) (**Figure 8c**)[72, 123].

Chemical changes are not always responsible for a polymer being impaired in its functionality. Moderate temperatures above the T_g are sufficient to soften a polymer and, if structural conditions are met, to induce a slow crystallization of the formerly amorphous domains. Consequently, the increasing crystallinity associated with the chain rearrangements alters the mechanical properties of the polymer without a bond breakage within the backbone or sidechain elimination (**Figure 9**).
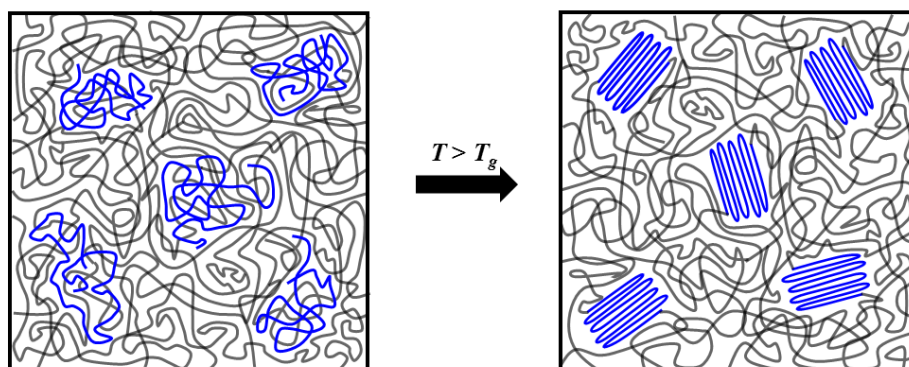
Figure 9 Increased chain mobility at temperatures above the glass transition temperature T_g allows amorphous chain segments in a polymer to rearrange, thus enabling the formation of crystalline domains that can affect the properties of the polymer.

A deterioration of physical properties might also be observed when a polymer is exposed to temperature fluctuation which can induce volume expansion and contraction, respectively[75]. This is comparable to swelling, a process in which solvent diffuses into a polymeric network and its incorporation leads to a volume expansion. Such continuous volume changes triggered by temperature can constitute a high load, damaging the material e.g. by crack formation. Another important factor is the migration and degradation of additives used for polymer stabilization, which will be briefly discussed in the following part.

1.2.2. Additives for polymer stabilization

The usage of additives is essential to provide a polymer with desired properties such as coloring by pigment addition, weight and cost reduction by filler supplements or modification of the mechanical stability and processability by means of plasticizers to meet certain material requirements for its application[124-127]. Like polymers, additives are prone to aging and their

degradation can result in both optical consequences by only changing the appearance of the polymer, as well as in material damage, limiting a further use of the polymer.

Stabilizers, whose concentration is usually 0.01 up to 1 wt%[128], are particularly noteworthy as their purpose is to slow down polymer degradation and thus ensure its usability during service lifetime[93, 129-132]. Nevertheless, decomposition or evaporation of stabilizers will cause a polymer to lose its protective mechanisms and thus lead to an acceleration of polymer degradation[128, 133-135]. The focus here will be on the thermal stabilization, since this was the decisive factor for this work. As the oxidative-thermal degradation follows a radical pathway (see **Figure 2**), thermal stabilizers are designed to deactivate formed radicals and thus interrupt the autocatalytic degradation cycle. Regarding thermal stabilization of polymers it should be noted that it is necessary to distinguish whether the stabilizer is intended to prevent thermal-oxidative degradation at high temperatures during processing or over a longer period during the service lifetime under moderate conditions[75, 136-137]. To optimize polymer protection, synergistic effects of various stabilizers are used to exploit their full potential and their interactions should always be considered[138-144].

1.2.2.1. Primary antioxidants

The common thermal protection is afforded by chain-breaking antioxidants, so called primary antioxidants, which scavenge radicals by donating a labile hydrogen atom and thereby prevent further degradation processes[145-148].
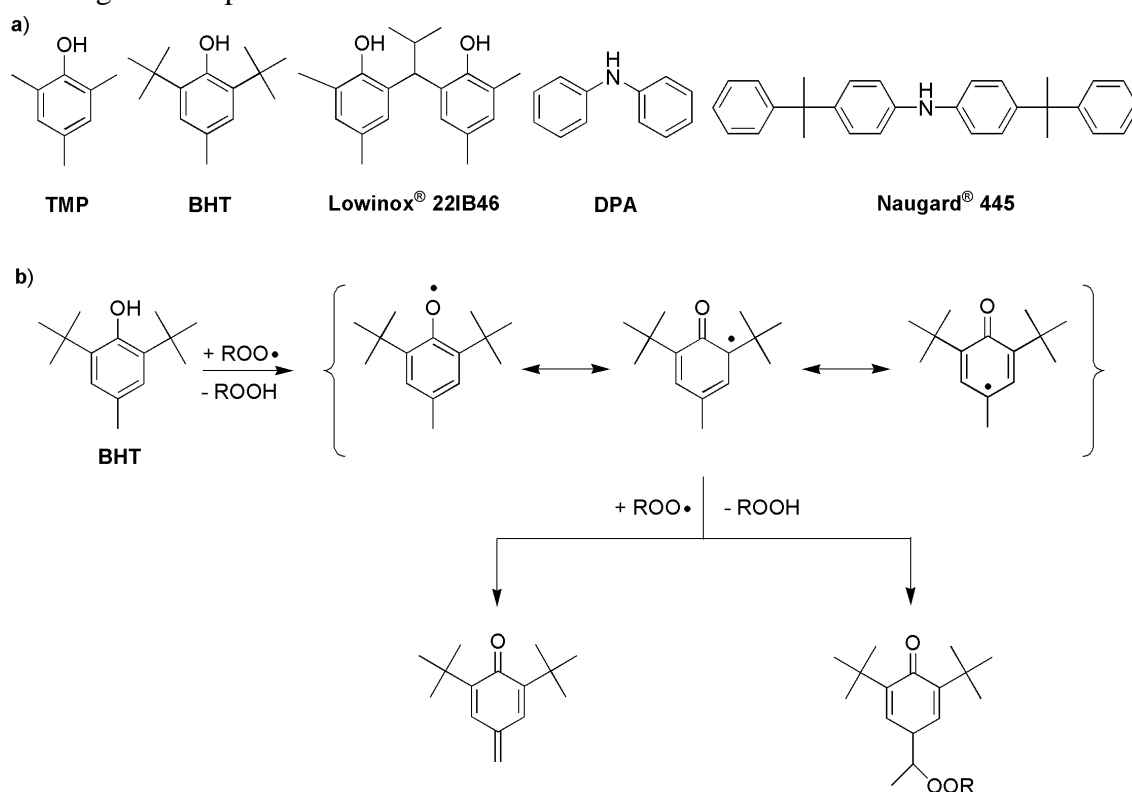

Figure 10 a) Examples of hindered phenols and aromatic amines used as chain-breaking antioxidants and b) stabilization mechanism of BHT to retard thermal polymer degradation.

The best-known chain-breaking antioxidants are hindered phenols and aromatic amines[75, 92, 131]. Examples for both substance classes are depicted in **Figure 10a**.

Figure 10b exemplarily shows the stabilization process using the hindered phenol 3,5-di-*tert*-butyl-4-hydroxytoluene (BHT)[75, 92, 131]. The phenol moiety is able to react with alkoxy- and peroxide radicals which are released during the degradation when the polymer is exposed to thermal stress (compare **Figure 2**). After the radical has been transferred to the phenol, the formed phenoxy radical is well stabilized due to its steric hindrance and resonance structure and therefore is incapable of abstracting hydrogen atoms from the polymer. However, the phenoxy radical can react with another peroxide radical, thus the antioxidant is formally capable to interrupt two oxidation processes. It should be noted that the formation of secondary peroxide is undesirable because it offers a new radical source, consequently decreasing the protection efficiency[75]. The use of bulky substituents, e.g. the *tert*-butyl groups in BHT, can reduce the extent of this reaction[75].

Consumed antioxidants lead to the formation of carbonyl groups, altering the optical properties of the polymer and make it more susceptible to UV light absorption and thus to photochemical degradation, whereas this process is even more distinct in the case of aromatic amine stabilizers. Typically, polymer stabilizers contain several stabilizer groups and a higher molecular weight to improve their efficiency and to lower the risk of antioxidant evaporation[149-151] which must be prevented, since the antioxidants do not have a catalytic effect but are consumed during the stabilization process.

1.2.2.2. Secondary antioxidants

Secondary antioxidants, often denoted as hydroperoxide decomposers, convert hydroperoxides, potential radical sources, into stable, non-radical products[92, 124, 137, 152]. Frequently organophosphorus compounds are used, which are illustrated in **Figure 11** together with their protective mechanism[124, 143].
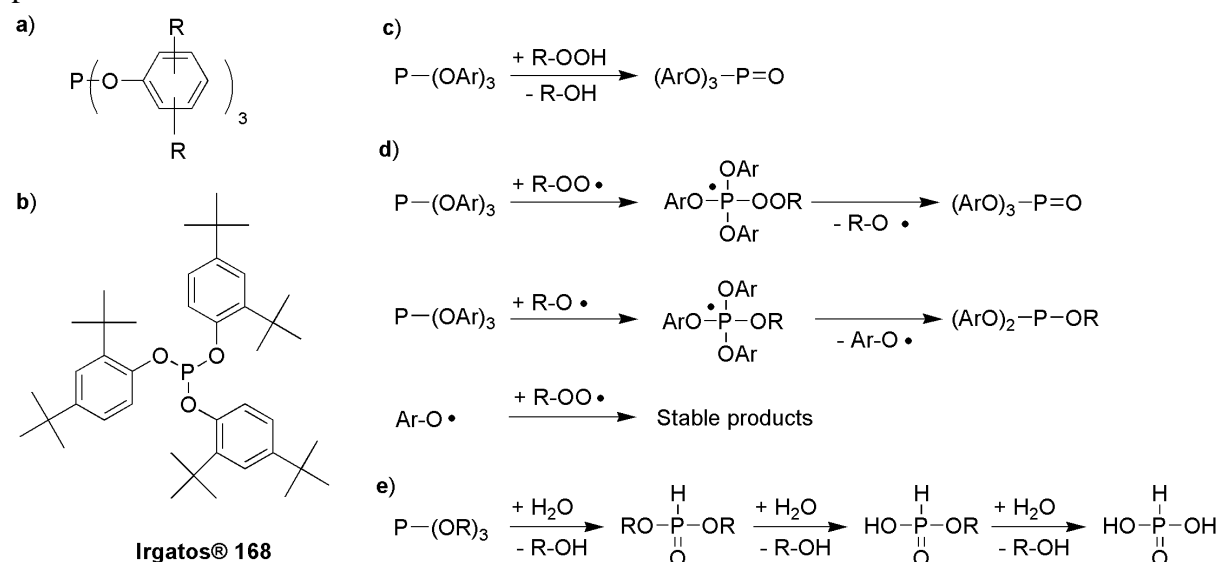
Figure 11 a) General structure of an organophosphorus compound and b) exemplary of Irgatos® 168 used as secondary antioxidants. They act as c) hydroperoxide decomposer and d) scavenger for peroxyl radicals to prevent polymer oxidation but e) undergo stepwise hydrolysis in the presence of water (R = alkyl, Ar = aryl).

Phosphites and phosphonites act as reducing agent by converting hydroperoxides into their corresponding alcohols and thereby getting oxidized into phosphates (**Figure 11c**).

Additionally, they trap peroxyl radicals and thereby are converted into phosphates and alkyl aryl phosphites (**Figure 11d**). Subsequently, stable aroxyl radicals are released which are too unreactive to maintain the oxidation chain reaction[153-154]. Due to their susceptibility towards hydrolysis (**Figure 11e**), the stability of organophosphorus compounds is tuned by using aromatic substituents and by adding small amounts of a base serving as acid scavenger[92, 153]. Especially during processing of polymers at high temperatures, organophosphorus compounds offer excellent protection. In synergy with primary antioxidants, particularly hindered amines, they provide long-term thermal protection[44, 124].

Likewise organophosphorus compounds, thioester-based antioxidants are capable of reducing hydroperoxides into their corresponding alcohols and thereby undergo oxidation into sulfoxides (**Figure 12**)[124]. Sulfoxides formed during these process can again act as hydroperoxide decomposers, thus offering additional protection[124]. To effectively protect a polymer against long-term thermal degradation, combination of organic sulfur compounds with primary antioxidants is also common, which then are denoted as thiosynergists[44, 124, 155].

For the sake of completeness, metal deactivators should be mentioned as a third class of secondary antioxidants. Their application is limited to polymers which are in contact with metals, e.g. insulation materials, and might be effected by metal ion migration. Traces of metal ions such as copper, iron or cobalt are known to support decomposition of hydroperoxide and thus to accelerate the thermal-oxidative degradation mechanism (**Figure 12d**).
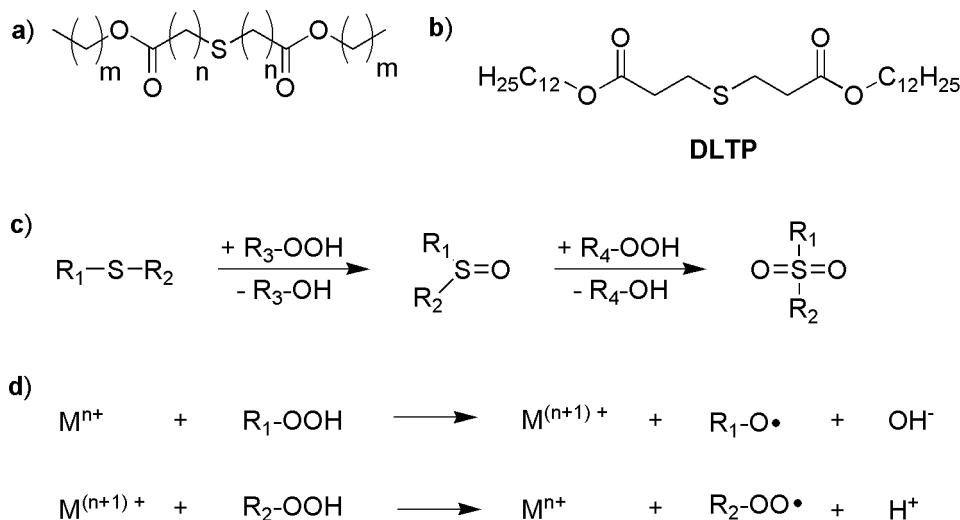
Figure 12 a) General structure of a thioester compound and b) exemplary of didodecyl 3,3'-thiodipropionate (DLTP) used as secondary antioxidants together with their protective mechanism for hydroperoxide decomposition and d) the hydroperoxide decomposition initiated by metal ions (R = alkyl).

Therefore, metal ions are deactivated by adding stabilizers capable of forming stable metal chelate complexes, e.g. nickel complexes[75, 92].

1.2.3. Non-thermal polymer degradation

Beside thermal degradation also non-thermal degradation pathways may cause damage to a polymer, however, they are not relevant in the context of this thesis and will only be discussed briefly. Mechanical friction might be associated with applying a force to an object which consequently will break when the tensile force exceeds a certain value. However, mechanical

degradation of a polymer is usually related to a shearing force applied to a polymer during its processing. While small molecules are not able to transfer tensile and shear force, for polymers efficient energy transfer is observed during melt processing, leading to its rupture in the center of the chain and consequently yielding radical fragments[156-159]. Mechanical stress can therefore support the degradation of polymers, especially as polymer shaping is performed at high temperatures. Additionally, surface damage through scratches or microcracks occurring during the use of a polymer can accelerate its degradation by facilitating the diffusion of gases and liquids into the specimen[160].

Oxidative degradation follows the similar mechanism as thermal degradation (see **Figure 2**). After their formation, radicals will react with atmospheric oxygen to form hydroperoxides. In contrast to the thermal degradation, decomposition rate of these peroxides is slow at ambient temperatures and thus leads to a hydroperoxide accumulation within the polymer[156, 161]. The increasing hydroperoxide concentration will accelerate the decomposition rate and will consequently greatly speed up the degradation process. Therefore, polymer condition remains relatively constant over a long period of time, but then deteriorates abruptly within a very short period of time[156].

Photochemical degradation requires a chromophoric group, capable of absorbing energy as electromagnetic radiation and subsequently triggering polymer decomposition[162]. Common chromophores in polymers are carbonyl functionalities and delocalized electron systems such as aromatic structural elements[162]. The mechanisms for photochemical degradation are manifold and depend on the polymer structure as depicted in **Figure 13**.

A Norrish type I reaction will effort radicals via α-bond scission and a Norrish type II reaction will induce a non-radical scission by H-abstraction[72, 162]. While both, Norrish type I and II, will trigger a molecular weight loss, aromatic ester might undergo a radical Photo-Fries rearrangement which will not change the length of the polymer backbone[162].
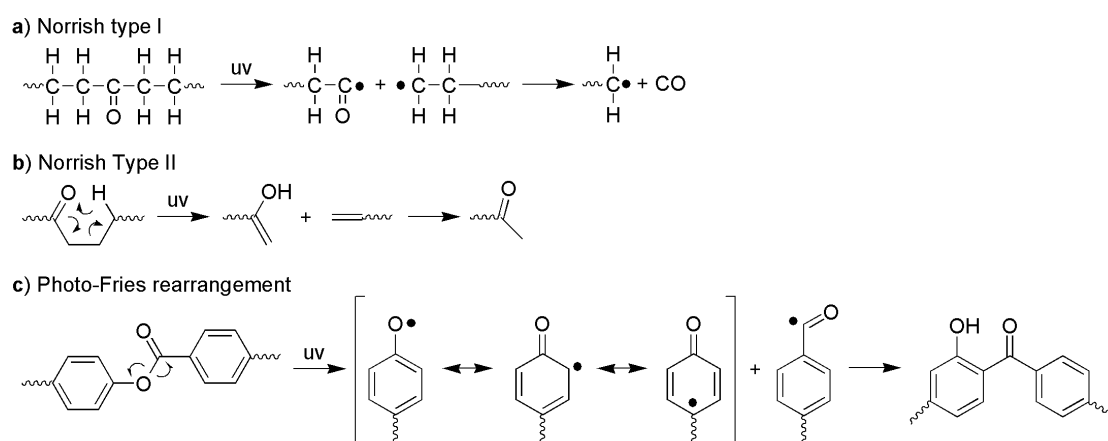
Figure 13 Photochemical polymer degradation via a) radical Norrish type I, b) non-radical Norrish type II and c) Photo-Fries rearrangement.

Under ambient conditions, photochemical initiation is followed by oxidative degradation[156]. The combination of both processes is denoted as photochemical oxidation. Chemical degradation includes all possibilities in which structural changes and loss of molecular weight are caused by contact with a corrosive media, e.g. acids, bases, organic solvents and water[163]. Dominating processes involved in chemical degradation are solvolysis, hydrolysis and

abstraction reactions[164]. Under ambient conditions usually non-thermal degradation processes, in particular photochemical oxidation, are responsible for structural and chemical changes triggering polymer deterioration. Use of polymers at high temperatures will accelerate thermal degradation and thus requires the application of high-performance polymers, whose thermal stability is increased by suitable design. An overview of these high-performance polymers and their applications is given in the following chapter.

1.3. High-performance polymers

In order to explain the design of thermally resistant high-performance polymers, it is first necessary to define the term "thermal stability". Thermal stability might refer to a long-term parameter, providing thermal protection over a long timescale at moderate temperatures, or to the decomposition temperature, i.e. very high thermal load for short times. In the first case temperatures of about 180 °C are assumed in periods of more than 10.000 hours, in the second case the polymer might be exposed to temperatures up to 450 °C, over a course of minutes[55, 165].

Both types of thermal stability can be reached by a polymer when using appropriate monomers, especially aromatic structures and incorporating functional groups such as imides. The choice of suitable monomers primarily results in an increase in primary bond strength, e.g. the BDE increased from 322 - 348 kJ/mol for a C–C bond[55] up to 600 kJ/mol for a C=C bond[55], and in additional stabilization through the introduction or enhancement of chain interactions, such as hydrogen bonding (25 - 42 kJ/mol[55]) and van der Waals interactions. Aromatic and heterocyclic structures have the greatest influence due to their resonance stabilization contributing with 167 – 292 kJ/mol[55] and therefore are the basic structural elements for temperature resistant high-performance polymers. Another advantage of aromatic structures is the possibility of radical stabilization due to delocalization, leading to reduced radical reactivity and thus to a slower degradation[165]. Primary bond strength can although be tuned by introducing fluorinated groups into a polymer as then the BDE is increased from 414 kJ/mol for a C-H bond to 514 kJ/mol[165] for a C-F bond.

Excellent thermal stability together with their outstanding mechanical, chemical, electrical and oxidative resistance highlight these polymers for use as high-performance materials[166]. An overview of high temperature polymers is presented in **Table 3**.

The first class of temperature-resistant polymers were polyimides developed by DuPont in the 1950s and 1960s[167]. Kapton® was prepared by polycondensation of an aromatic diamine and dianhydride subsequently followed by a cyclodehydration as depicted in **Figure 14a**[167]. Due to its simple and inexpensive synthesis together with the possibility to adapt the properties to desired application, polyimides rapidly became an important material in the automotive, aerospace and electronic industry[168-169]. However, due to their high aromatic content, polyimides have an extraordinary high T_g and T_m causing a high chain stiffness which drastically reduce their processability because of a poor solubility and low melt-processing properties[166, 170-171]. Therefore, significant efforts were put into the investigation of structural influences on high-performance polymers subsequently leading to the establishment of numerous specialty chemicals tailored for specific applications. The problem of poor processing abilities has been tackled by introducing bridging heteroatoms to increase chain flexibility, e.g. the basic structures of parylenes have been modified to poly(aryl ether ketones)

or polysulfones. Thereby a loss of thermal stability due to lower BDEs of heteroatoms compared to C–C bonds is accepted[55, 165].

Table 3 Different polymer classes used as high performances materials due to their excellent thermal stability (Ar = aryl).

Substance class	Decomposition temperature [°C]	Structural element
Polyimide	> 500 °C[172]	
Poly(aryl ether ketone)	> 420 °C[170]	
Polysulfone	> 500 °C[173]	
Parylene	> 450 °C[174]	

Selected structures of common high-performance polymers with optimized processing properties are shown in **Figure 14b**[175-177].
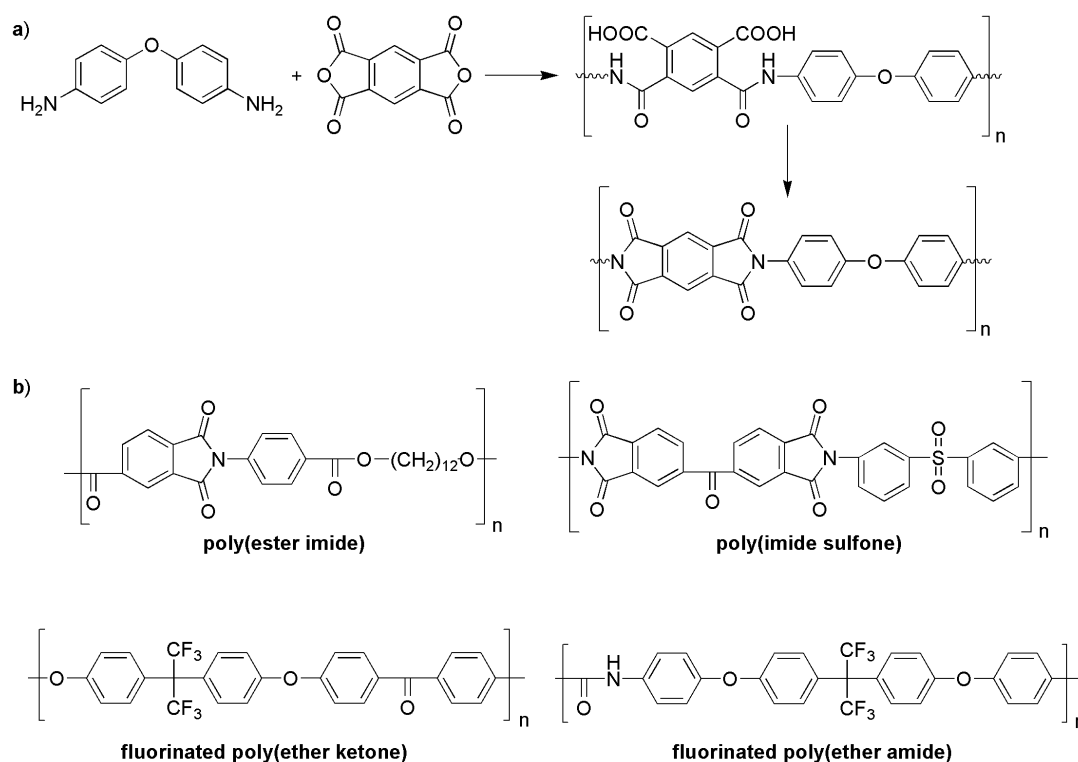

Figure 14 a) Synthetic pathway of the first high-performance polymer Kapton® and b) examples of common high-performance polymers with optimized processing properties.

In addition to the structural influences other aspects related to the synthesis of the polymer must be taken into account in order to maintain the thermal stability. A high molecular weight and a

narrow molecular weight distribution tend to increase the thermal stability of a polymer since low molecular weight fragments are causing plastization by lowering its T_g[165]. Cross-linking can have a beneficial effect on thermal stability since several bonds need to be broken in order to release lower molecular weight fragments. However, at the same time this is worsening the processability of the polymer by increasing its rigidity[165]. To ensure thermal stability of a polymer, endgroup control is very important, because as can be seen in **Figure 7b** specific degradation processes might preferentially be proceeded at functional groups located at the end of polymer chains[101].

Impurities, such as metals from catalysts, accelerate polymer degradation, thus polymers with high purity are advantageous[55]. Furthermore, additives, which differ depending on the manufacturer, have a significant influence on slowing down decomposition processes and thus increasing thermal stability of a polymer (chapter 1.2.2.)[165]. Finally, the main decomposition mechanism, i.e. unzipping and unbuttoning, determines how quickly decomposition steps trigger material changes which make the polymer unusable for further application (chapter 1.2.1.1.)[55]. Exemplarily, applications and thermal degradation of poly(ester imides) (PEI)s, will be highlighted in the following part, as this polymer class has been investigated in the course of this work.

1.3.1. Poly(ester imides)

As previously described, polyimides are characterized by outstanding thermal stability, but are difficult to process due to their rigid structure. Consequently, copolyimides, including PEIs, were developed, whose thermal stability was partially sacrificed in favor of better processability[178]. The first publication dealing with synthesis of a PEI was reported in 1966 by Loncrini, who reacted trimellitic anhydride (TMA) with aromatic diacetoxy compounds yielding a bisesteranhydride via transesterification which subsequently was reacted with an aromatic diamine[179]. After elimination of water, the precursor polymer was converted into the PEI. The reaction scheme is presented in **Figure 15**. Beside breaking up the rigid polyimide structure by introducing more flexible ester groups, not only a melt extrusion process is improved but also the solubility in common organic solvents and thus the possibility of solvent processing[178]. **Figure 16** shows a compilation of monomers used to tune the properties of common PEIs[180].
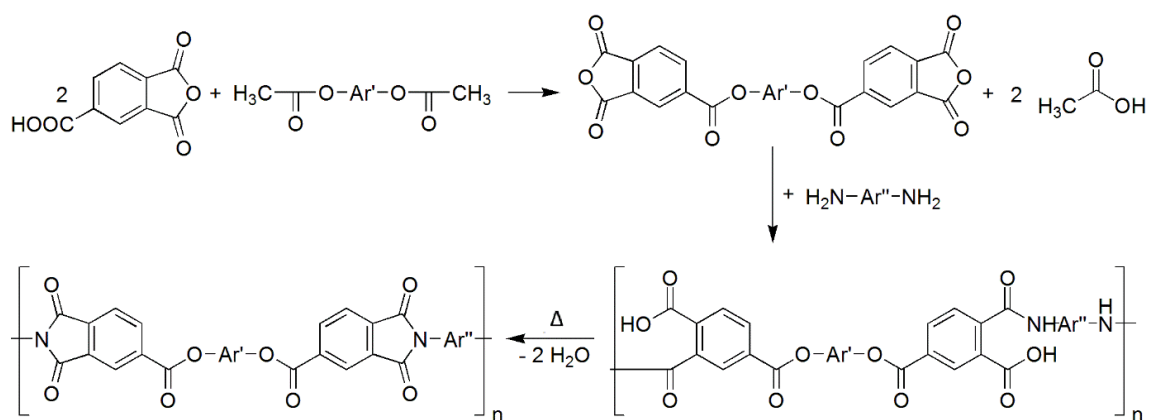

Figure 15 Schematic synthetic pathway of the PEI by transesterification with TMA followed by the formation of the polyamic acid and the subsequent conversion into the cyclic imide.

Typically, the imide structure is introduced by reacting diacids capable of forming five-membered rings, e.g. TMA, with an primary amine containing an additional functional group, e.g. 2-aminoethan-1-ol[180]. Another frequently used basic monomer for introducing the imide functionality is isocyanuric acid or its derivates such as 1,3,5-tris(2-hydroxyethyl)isocyanurat (THEIC)[180].
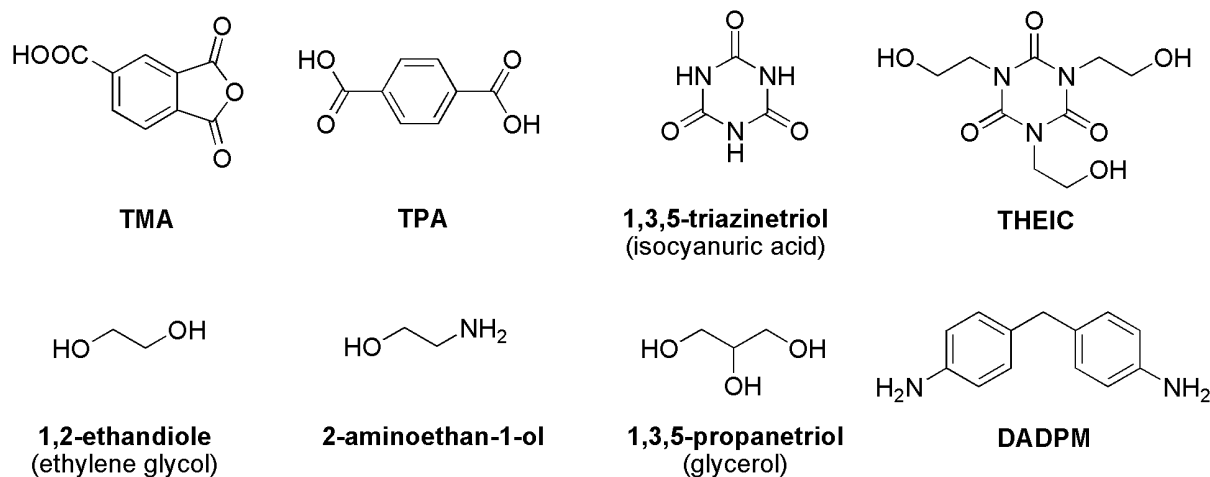

Figure 16 Compilation of monomers used for the synthesis of common PEIs.

1.3.1.1. Application of poly(ester imides)

The synthesis and characterization of PEIs is, compared to other polymer classes, still rather poorly described. This is mainly due to the predominant applications for industrial purposes, especially as specialty chemicals in the electrical industry. Therefore, many research results are processed in patents rather than in scientific publications, which makes them considerably more difficult to access[178].

The main application of PEIs is their usage as coating material for wires, especially in windings such as copper and aluminum coils[181]. They serve as primary insulating materials in many electric devices such as generators, electric motors and household appliance[180-182], providing electrical components with mechanical protection and electrical insulation to prevent short-circuiting[183].

Conventionally, coatings are casted by means of a continuous enameling process[180]. Therefore, often unsaturated PEIs are used, as the internal double bond serves as network site for an unsaturated comonomer, e.g. styrene, to cure the PEI by a radical polymerization[180, 184-185]. The wires are dipped into the dissolved PEI, specifically oligomeric precursor polymers, and after removal of the excess coating solution, the remaining PEI is cured in an oven forming the first coating layer on the wire. Because the casted enamel layer is very thin, this process is repeated several times after the wire has cooled down. Additives accelerate the curing process and support a blister-free film formation which is necessary to ensure the mechanical, thermal and electric properties of the casted coating[180]. Due to the heat generated during rapid engine rotation, the coating materials are exposed to high temperatures, which therefore require sufficient thermal stability[183].

Since the temperatures differ during engine operation, thermal classes have been established to indicate the maximum temperature to which the impregnating polymer may be exposed over the cause of 20.000 hours. The most important thermal classes of polymeric insulating materials are summarized in **Table 4**[186-187].

Table 4 Overview of the different thermal classes, their maximum operating temperature and the corresponding polymer classes used as insulation material.

Thermal class	Maximum temperature [°C]	Insulation material
A	105	Polyurethane
B	130	Polyurethane, epoxy
F	155	Polyurethane, polyester
H	180	Poly(ester imide)
N	200	Poly(ester imide), poly(amide imide)
S	240	Polyimide

In addition to their high thermal resistance, PEIs are also characterized by good electric properties which are equally decisive for their application as coating materials in electric devices[187-188]. An important criterion for PEIs is their dielectric strength indicating the highest electric field strength to which the polymeric coating can be exposed without losing its insulating properties due to a voltage breakdown[189]. Applying an electric field to the insulating PEI results in the generation of heat due to charge displacement, which is referred to as dielectric loss[190]. Especially at high voltages dielectric loss has to be taken into account as it can generate overheating in the winding[191].

The application of impregnated components in engines also requires chemical stability as the protective function should be maintained even after contact with chemical substances such as cleaning agents, refrigerants or transformer oils[191].

Finally, during both production, e.g. during the winding process, and operation, e.g. during rapid rotation, mechanical forces can damage the wire enamels which is why abrasion resistance and adhesion are required[191]. Among the high-performance polymers used as coating materials in electronic devices, PEIs are the most important and frequently used polymer class[181, 191]. Dual coatings of 60 – 80 % PEIs with a top layer of 20 – 40 % poly(amide imides) (PAIs) might further increase the abrasion resistance due to the outstanding mechanical properties of PAIs[181].

1.3.1.2. Thermal degradation of poly(ester imides)

During operation, components which have been impregnated with PEIs, are exposed to high thermal stress caused by the rapid engine rotation. Despite their high thermal stability an application at high temperatures is limited because thermal load will trigger mass loss, microcracking, a decrease of dielectric properties and delamination processes consequently leading to material failure over time[192]. When the electrical insulation is damaged, not only the concerning component might fail, but short circuits and overheating can damage the entire device[192].

Even though in recent years the scientific community has frequently put effort into the optimization of PEI-synthesis, PEI-processing and tailoring their thermal properties[193-197], their application as a specialty chemical in the electronic industry limits the available literature concerning stability studies, as these are veiled in patents[180]. As thermal polymer degradation is, under ambient and operating conditions, a very slow process, studies often rely on combined methods of experimental results and model-based Arrhenius calculations in order to predict long-term thermal behavior[192] or use extremely high temperatures to accelerate polymer degradation, even if this does not match degradation under operating conditions[186]. The

experimental results of the latter studies, which are usually obtained by complete PEI decomposition in a TGA, indicate their thermal stability, but give little information on their long-term stability[193, 198-202].

Additionally, measurement conditions for investigations of thermal degradation are not standardized, impeding the comparability of results (see chapter 1.2.1.1.). The thermal decomposition of PEIs is mainly carried out in bulk with specimen having a regular geometric shape, thus deviating from their thin film appearance coated on copper wires when installed in machines[192]. It has already been demonstrated that copper significantly accelerates the degradation of PEIs by promoting a simultaneously decomposition of both imide- and ester-bonds, whereas normally in the initial stage, a predominantly breakage of the ester linkages can be observed whereas the imide bond only breaks as decomposition progresses[203]. Therefore, in the case of a PEI-coated copper wire, after 4500 hours of thermal aging at 230 °C, the mass loss of 33.8 % is about 16 times higher compared to an aluminum wire specimen coated with the same PEI, showing a mass loss of only 2.1 %. The formation of a copper oxide layer between the copper wire and the enamel plus migration of copper ions into the PEI have been reported to be responsible for the accelerated decomposition kinetics[203-204].

In terms of commercial application, the biggest drawback is the requirement to determine the thermal endurance of impregnating resins according to ISO 2578[205]. For PEI-enamels, testing of mass loss over 5000 hours is mandatory[205]. Baumgarten and Hegemann used isothermal thermogravimetric analysis under oxidative and inert conditions to establish a testing method for unsaturated PEIs with different styrene and vinyltoluene as comonomers on a shorter time scale of a maximum of 80 hours[205]. They used thin film specimen with a thickness of 100 µm coated on glass cloth. The results can indicate the short-term thermal endurance, but cannot be correlated with the long-term investigations by the means of ISO 2578 due to incomplete mapping of changes in the degradation mechanism that occur over a long period of time and during possible temperature fluctuations. As PEIs are predominantly used for industrial applications, stability studies are aiming for an evaluation of the consequences concerning endurance and performance after thermal load, potentially restricting the service lifetime. However, the decomposition processes causing the thermal aging of the PEIs are not investigated. Publications that have studied the decomposition processes of PEIs in more detail state benzene, cyano-benzenes, alcohols, in particular phenols, amines, in particular aniline and carbon dioxide as the main degradation products[203, 206].

Guo *et al.* have shown the strong temperature influence on the composition kinetics of the gaseous degradation products by performing pyrolysis-GC/MS of an PEI, which is illustrated in **Figure 17**[206]. The investigated PEI was partially hydrolyzed by the absorbed moisture. At decomposition temperatures between 350 °C and 450 °C, cleavage of the ester linkages caused the release of various alcohols, which were determined as main degradation products, in particular 2,7-naphalenediol. Starting at 520 °C, cleavage of the imide ring led to the formation of cyano compounds, in particular variously substituted benzenes and phtalimides. As the temperature increased up to 700 °C, the formation of carbon dioxide was strongly supported. However, the detailed mechanistic studies have been carried out under conditions that are not comparable with realistic requirements during application. This is due to the slowness of degradation processes at low temperatures as well as the difficulty of detecting gaseous analytes over a long decomposition period.
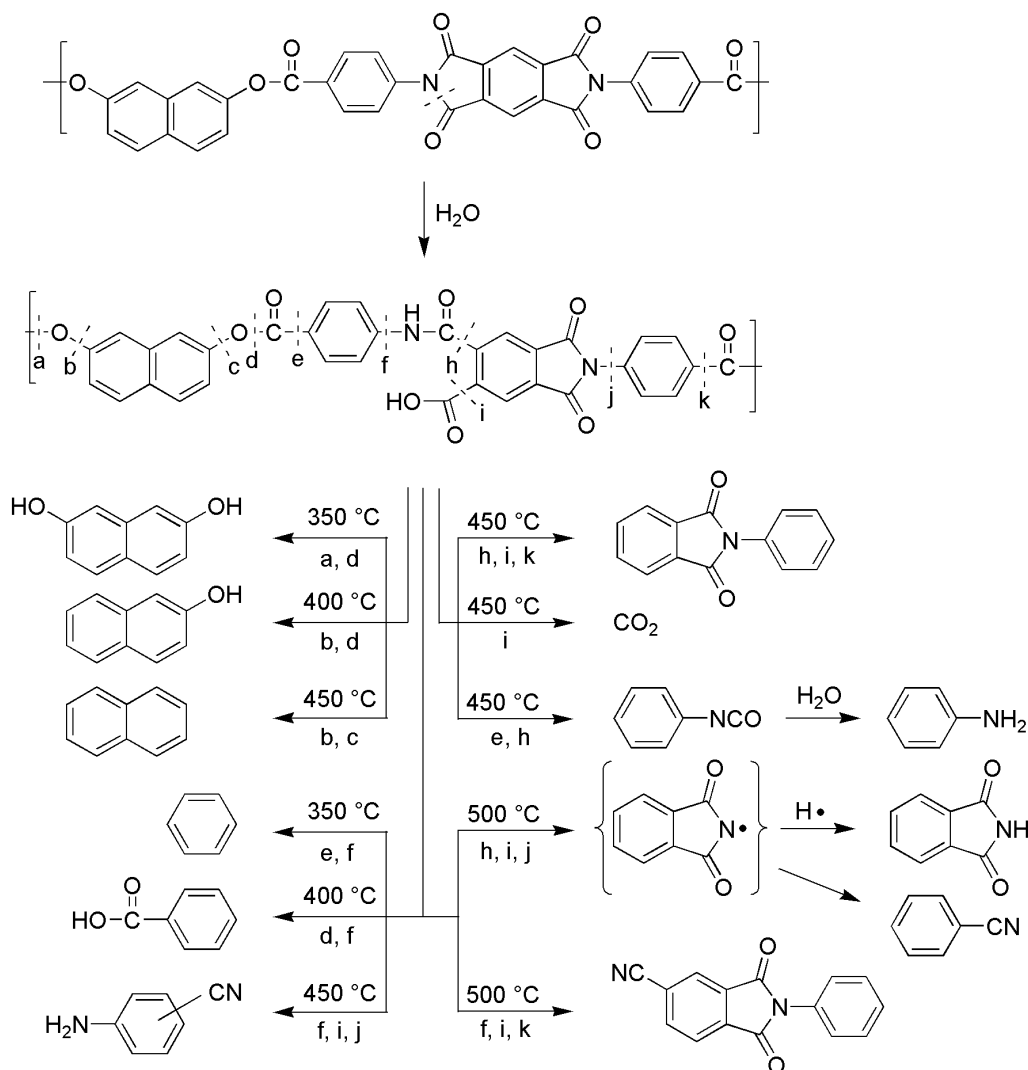
Figure 17 Thermal degradation pattern of the pyrolysis of a PEI at 350 °C to 500 °C. Figure was adapted by permission from Springer Nature Customer Service Centre GmbH: Springer Nature, *J. Polym. Res.*[206], Copyright 2007.

1.4. Detection of polymer degradation

There are a variety of methods that are suitable for detecting polymer degradation thus the objective of the investigation must be defined. An overview of the different methods and their possible applications is given in the following chapter.

1.4.1. Analytical methods

As polymer degradation is always accompanied by material changes, observing the material properties allow statements about the polymer condition. Ideally, characteristic parameters, e.g. molecular weight and molecular weight distribution of the virgin polymer are known. Chain scission and cross-linking process will cause changes of the molecular weight and the molecular weight distribution, which can be detected by conventional methods used for polymer analysis, for instance gel permeation chromatography (GPC) and matrix-assisted laser desorption/ionization time-of-flight mass spectroscopy (MALDI-TOF-MS)[72, 207]. Tensile testing frequently is used to determine a deterioration of mechanical properties due to polymer

aging[208]. The carbonyl index indicates how far oxidative polymer degradation has progressed[209].

Regarding thermal degradation, the most commonly used method is TGA (also see chapter 1.2.1.)[72]. The observation of a temperature dependent mass loss profile visualizes in which temperature range polymer thermal degradation takes places. By flexibly adjusting the heating rate, in particular by reducing the heating rate while mass losses occur, the resolution can be increased to discriminate between different decomposition processes in a similar temperature range[210].

However, the aforementioned methods have two major drawbacks: Sample and measurement requirements limit their use as control instrument during operation and the results indicate progressing degradation, but information on ongoing degradation pathways are restricted. In the case of thermal decomposition the latter point can be remedied by coupling the TGA to an additional detection device. The gaseous degradation products formed during decomposition are flushed into an infrared (IR)-spectrometer or a MS[72]. Prior detection, the multicomponent degradation mixtures are usually separated by the means of gas chromatography (GC) to facilitate analyte evaluation[72]. Knowing the exact degradation products helps to determine structural elements and bonds within the polymer that are most likely to be broken down first. During TGA measurements, a sample is pyrolyzed within a few minutes, thus much faster compared to actual operating conditions. Especially when the TGA is coupled to a detection instruments, e.g. GC-MS, long-term investigations are inefficient due to the obstruction of several analytic devices.

A much more feasible method is the thermal volatilization analysis (TVA)[211]. A sample is decomposed in a vacuum chamber and due to pressure changes conclusions about the decomposition rate and the volatiles can be made. The use of cold traps allows a fractionation of the degradation products, thus providing further information about the actual decomposition mechanism. The volatiles collected and fractionated in the cold traps can subsequently be analyzed using conventional analytical methods such as NMR- and IR-spectroscopy without the need for on-line coupling[72]. Due to the lack of commercially available TVA equipment, usually self-built equipment is used. Long-term thermal investigations in the context of this thesis required the setup of a self-built apparatus, whose construction and functionality is extensively explained in the Experimental part 4.2.

1.4.2. Advanced detection methods

Whenever it comes to in-situ monitoring of polymers that may be incorporated in devices and are difficult to access, the analytic methods mentioned so far fail due to their impracticability. For application-related issues several established methods are available, enabling a non-destructive material testing in bulk. Depending on the application and the material being tested, different measurement principles are used for direct or indirect testing[212]. Direct non-destructive testing techniques can detect material damage on a microstructural level, e.g. cracking or breakage, while indirect non-destructive techniques monitor global material abrasion, e.g. loss of mechanical properties or electrical resistivity[213]. An overview of different non-destructive testing techniques and their range of application is shown in **Figure 18**.

One area of non-destructive testing includes acoustic methods, e.g. ultrasonic waves, which are used in the evaluation of the structural integrity in aviation or wind turbines[213]. Due to their unhindered propagation within a material and a deviating scattering pattern in case of material

defects, the elastic waves can localize damage in bulk material. Imaging techniques can be used to visually depict the internal structures of an object[213].
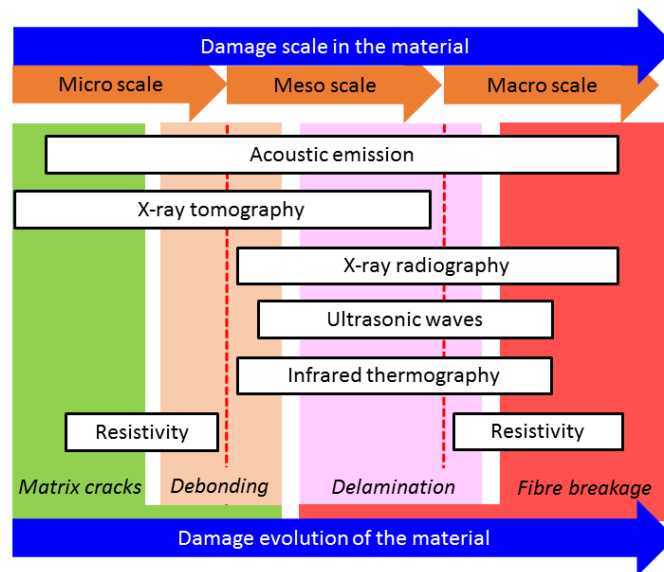

Figure 18 Compilation of non-destructive testing methods together with their scope of application as well as occurring damage processes. Figure was adapted by permission from Springer Nature Customer Service Centre GmbH: Springer Nature, *J. Mater. Sci.*[213], Copyright 2018.

For example, X-ray radiography might be used to detect and localize material damage and a thermogram recorded by infrared thermography allows to anticipate possible damage due to local temperature stress. In polymer composites carbon-fiber-reinforced polymers (CFRP)s are used to localize mechanical damage[214]. Non-conductive matrices, for instance epoxy resins, are reinforced with conductive carbon nanotubes (CNT)s. These CNTs not only improve the mechanical properties of the material, additionally they visualize damage by the means of electrical resistance measurements due to a reduction in their electric conductivity after breakage. A chemical approach for the investigation of degradation processes is offered by sensor technology, which will be discussed in the next section.

1.4.3. Sensor technology

A sensor responds to the detection of a specific event by emitting a signal. The type of event a sensor can perceive as well as the form of an emerging signal depends on its intended application and design. Sensors are primarily known as electronic components in process technology, allowing the automatization of working steps[215]. Their potential was quickly recognized and the development of novel sensor technologies and application possibilities is advancing. The following chapter is a brief overview of sensor technologies used to monitor material conditions.

1.4.3.1. Molecularly imprinted polymers

Recently a lot of effort has been put into the development of sensors capable of detecting and displaying degradation by a usable signal. One detection principle relies on molecularly imprinted polymers (MIPs), first mentioned in 1984 and 1985 by Mosbach *et al.*[216] and Wulff *et al.*[217], respectively. MIPs contain templated binding cavities which follow a "lock and key" mechanism to selectively bind specific molecules and therefore can be described as synthetic

receptors[218]. Synthesizing MIPs requires functional monomers which are polymerized in the presence of the subsequent target molecule[219]. During polymerization, the presence of the analyte introduces cavities in the polymer that remain even after analyte extraction and thus serve as recognition sites. **Figure 19** depicts the synthetic pathway and the working principle of a MIP.
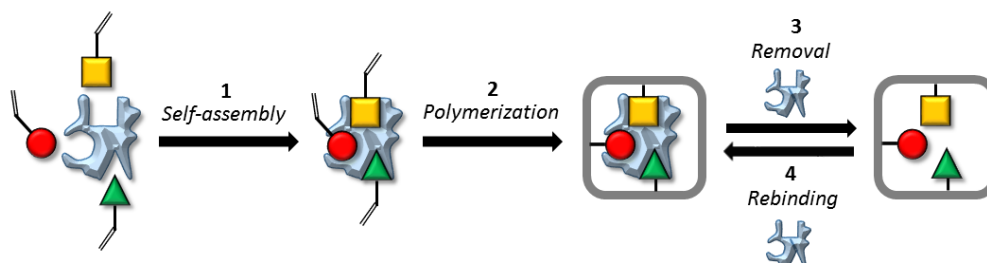

Figure 19 Synthetic pathway for a MIP: In the presence of a template, self-assembly of functional monomers occurs (1) which are subsequently fixed in their position by polymerization (2) and leave a polymer with a recognition site after template removal (3). The recognition site is able to bind the target molecule again (4).

The efficiency of MIPs is verified by synthesizing non-imprinted polymers (NIPs), for which the polymerization is carried out under same conditions but in the absence of the target molecule[220]. NIPs should therefore show a significant lower binding affinity to the analyte compared to MIPs due to the absence of templated recognition sides. Additionally, MIPs should have a high selectivity, i.e. their cross-reactivity with molecules structurally related to the analyte should be low[220]. This requires a specific shape and defined intermolecular interactions of the recognition sites[221]. Selectivity might be increased by using a covalent approach for analyte binding, which in turn suffers from higher synthetic effort together with slower adsorption and desorption kinetics[217, 222]. Since MIPs are working similar to enzymes, they were often used for the detection of molecules relevant to biological processes[216-217]. Today, the fields of application for MIPs have considerably expanded. They find usage in the detection of gaseous and dissolved analytes for environmental issues, i.e. sensing of pesticides[223-224], and in food industry, i.e. for detecting alcohols such as bisphenol A, migrating from plastic packaging[220], and ethanol[225]. Furthermore literature cites MIPs application for pharmaceutical issues, e.g. drug detection[226], and sensing of explosives[227].

Together with the expansion of the applications, detection methods have been further developed, offering numerous sophisticated characterization techniques. On-line methods, for instance coupling MIPs column to the detection system, e.g. HPLC or ESI-MS, or performing MS analysis directly on the MIPs surface, e.g. via MALDI-TOF-MS[219] enable a fast analyte identification and quantification. Optical, especially fluorescence[228-229], electrochemical and mass sensing, in particular quartz crystal microbalance[218, 230], approaches are enabling a simple and portable on-line analysis with small limits of detection (LOD). It should be noted that MIPs not only find application as sensor molecules, but also for chromatographic separation and targeted drug delivery[218].

1.4.3.2. Thermo-responsive sensors

In recent years, the development of functional materials has gained in importance. The polymers ability to indicate received damage by itself has become of great value in the age of safety and sustainability.

A frequently used substance class in the development of such smart functional materials are sterically hindered α-cyanostilbenes (**Figure 20a**), which has been intensively studied due to their excellent fluorescent properties[231-233], especially in solid state, and their potential application as optical sensors[234-235]. Due to a low rotational energy barrier in α-cyanostilbene, non-radiative deactivation processes triggered by torsional movement lead to very low quantum yields, thus to low fluorescence intensities[236]. However, in solid state the aggregation and the restricted rotation prevents non-radiative deactivation and enables aggregation induced emission (AIE)[235]. In the case of α-cyanostilbene, AIE is mainly based on molecular stacking, in particular through π-π-interactions which enable excimer fluorescence. Excimers, excited dimers, are associations of two molecules that only exists as long as one of the participated molecules is in an excited state. Excimer fluorescence, compared with monomer fluorescence, is characterized by a broader and red-shifted emission with shorter fluorescence-lifetimes[237-239]. The molecular stacking, e.g. excimer formation, of α-cyanostilbenes can be disrupted by thermal stimuli, triggering changes in their fluorescence behavior[237, 240]. Incorporated into polymer matrices, they are suitable as temperature sensor by locally indicating thermal stress through shifting their emission wavelength accompanied by a color change[234, 236, 241].

The thermo-responsive AIE behavior of fluorescent tetraphenylethene (TPE) is exploited when it is covalently incorporated into nylon 6 (**Figure 20b**)[242]. A temperature increase from 30 °C to 120 °C leads to the destruction of the hydrogen bonds between the nylon 6 chains and thus induces a volume expansion. Consequently, the motion of the phenyl rings is enhanced which triggers a decrease of fluorescence intensity together with a blue shift of the emission maximum.
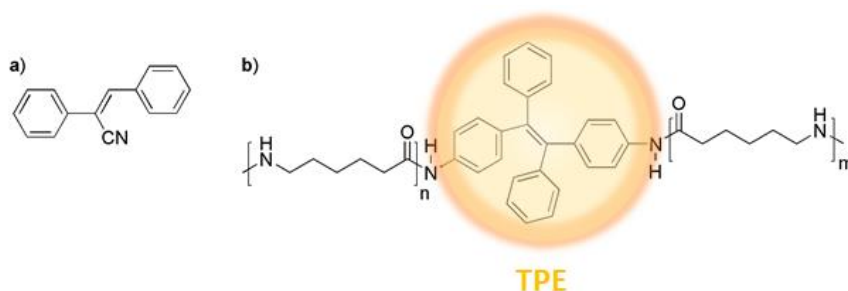

Figure 20 Chemical structure of a α-cyanostilbene and b) tetraphenylethene covalently cross-linked in a nylon 6 matrix acting as thermo-responsive sensors by showing an intense fluorescence upon heating.

The same behavior is exploited when TPE is covalently linked with PS. Exceeding the T_g, an important criterion for the stability of polymeric materials, leads to a strong decrease of the fluorescence emission and allows the monitoring of potential material failure caused by thermal stress[243].

TPE, which is incorporated in polystyrene/polylactide (PS/PLA) blends, is also possible to determine thermal induced chain motion within the polymer[244]. While in a polystyrene-*b*-polylactide (PS-*b*-PLA) block copolymer the fluorescence of TPE is affected by segment movements of PS and PLA, due to missing connections in PS and PLA, in the polymer blend a

fluorescence decrease is only observed for the segments in which TPE is incorporated. Thus, the method allows to monitor thermally induced structural changes on a microstructural level. The ability to locally detect and simultaneously optically indicate increased thermal stress in polymeric materials makes it possible to respond to potential damage in time and thereby prevent serious consequences.

1.4.3.3. Chemosensors

Chemosensors bear a receptor group which is capable of recognizing various analytes and indicate the reaction by a detectable signal[245]. Frequently, chemosensors rely on changes in their chromogenic behavior displaying their activation by color change and thus are constituted as optical chemosensors[246-248]. There are a variety of polymer-based optical chemosensors in which receptor groups, capable of binding specific analytes, are attached to the polymer chain and indicate the binding event by an optical signal. Polymers are predestinated to be used in sensor technology because of their conjugated structure they allow a strong signal amplification and thus achieve sensitivities down to a picomolar range[249]. The majority of these polymeric optical chemosensors are used for the detection of metal ions[245, 249] and for bioimaging[250-253]. However, the application of chemosensors is nowadays predominantly limited to sense analytes in solution and yet there are only few examples when they are used for solid-state monitoring. Profluorescent nitroxides, such as 1,1,3,3-tetramethyldibenzo[e,g]isoindolin-2-yloxly (TMDBIO), are used to monitor radically induced polymer degradation[254-256]. In their radical state, the fluorescence of these nitroxides is quenched due to the free radical located at the nitroxide group. After formation of the corresponding alkoxyamine by reaction with an alkyl radical formed during thermal polymer degradation, a strong fluorescence can be observed as shown in **Figure 21**.
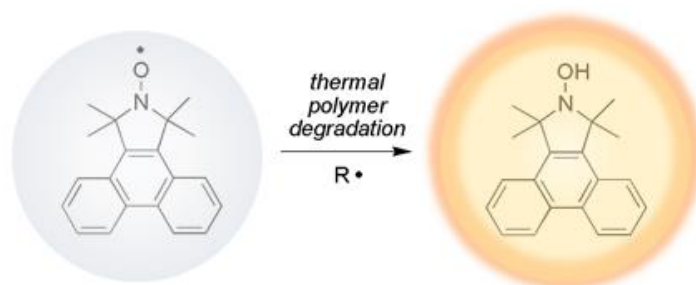

Figure 21 After the reaction of the non-fluorescent TMDBIO with an alkyl radical generated during the thermal degradation of the polymer matrix, the highly fluorescent alkoxyamine is formed and thus serves as optical chemosensor for thermal polymer degradation (R = alkyl).

The suitability of nitroxide sensors was demonstrated by embedding the sensor molecule in PP and in cross-linked polyester coatings and subsequently monitoring the increasing fluorescence intensity during thermal aging[254-256]. Nitroxide sensors were able to detect thermal degradation within 200 min and thus more quickly than conventional methods such as the carbonyl index using IR spectroscopy or the determination of the mass loss which both took 300 hours of accelerated aging[255]. Furthermore, due to their ability to scavenge radicals, nitroxide sensors simultaneously act as stabilizers and retard the thermal degradation process in the polymer. These examples demonstrate the great potential for an easy and fast monitoring of thermal polymer degradation by optical chemosensors.

2. Aim and Concept

2.1. Aim

The aim of this thesis is the development of a suitable optical sensor system that can be embedded within a poly(ester imide) (PEI) and is able to detect the aging state of the resin by easy feasible inline measurements (**Figure 22**), thereby improving the safety and sustainability of PEI coatings.
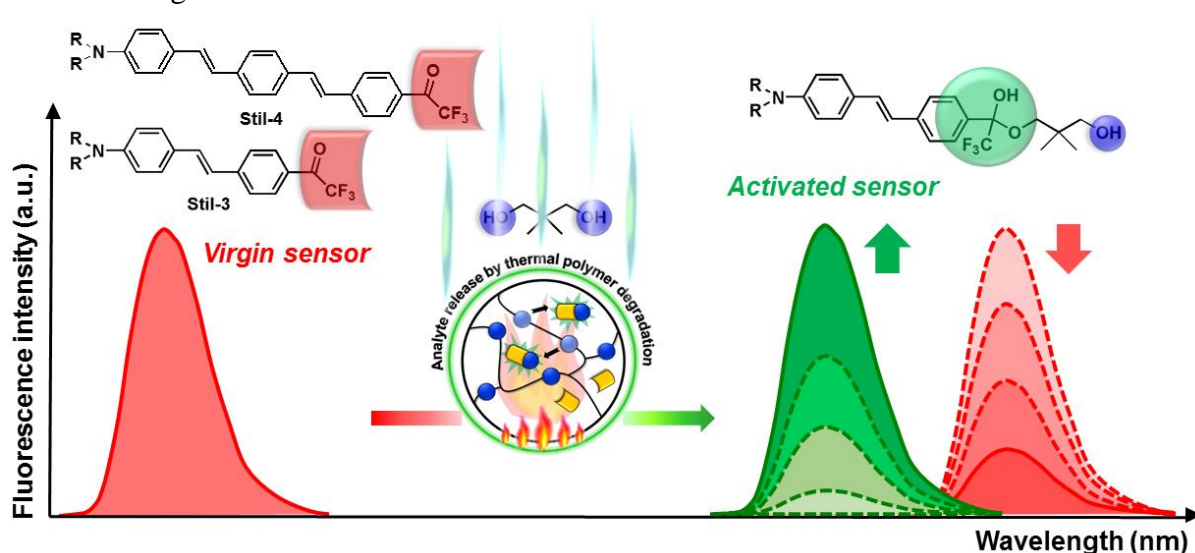

Figure 22 When embedded within a PEI resin, trifluoroacetyl functionalized sensor molecules are able to sense alcoholic degradation products released during thermal PEI degradation and thereby indicating sensor activation by a shift of the emission maxima.

PEIs are high-performance polymers, used as coating and casting materials, e.g. on copper coils in electric motors. During operation, electric motors develop heat which, despite their outstanding temperature stability, leads to aging of the PEI coatings. Polymer aging is an undesirable process that causes deterioration of material properties and, if too advanced, can impair the overall equipment functionality and may have life-threating consequences. Therefore it is desirable to monitor the condition of the PEI coating at any time, even during operation, in order to be able to replace defective components in time.

Furthermore, the sensor molecules should be compliant with the processing conditions of the PEI resin, so to allow a direct embedding into the regular processing lines used in industry.

2.2. Concept

Initially, investigation of the thermal degradation of the PEI resins **PEI-1** and **PEI-2** and their corresponding uncured pre-condensates **PEI-1PC** and **PEI-2PC** is required to identify possible analytes released during thermal degradation and usable for triggering a sensor activation (**Scheme 1a**). Thermal polymer degradation should be investigated at realistic application temperatures of 180 °C to 220 °C and therefore is expected to proceed slowly over times of month, if not years. This requires analyte detection over a period of 5000 h, which is why common detection methods such as TGA-GC/MS coupling are not feasible. Thus long-term thermal degradation experiments should be realized by a self-built apparatus which allows thermal polymer aging and trapping of thereby released gaseous degradation products over a period of 7 months. Subsequently, the trapped degradation products are analyzable by common analytic methods, such as NMR spectroscopy and ESI-TOF-MS.
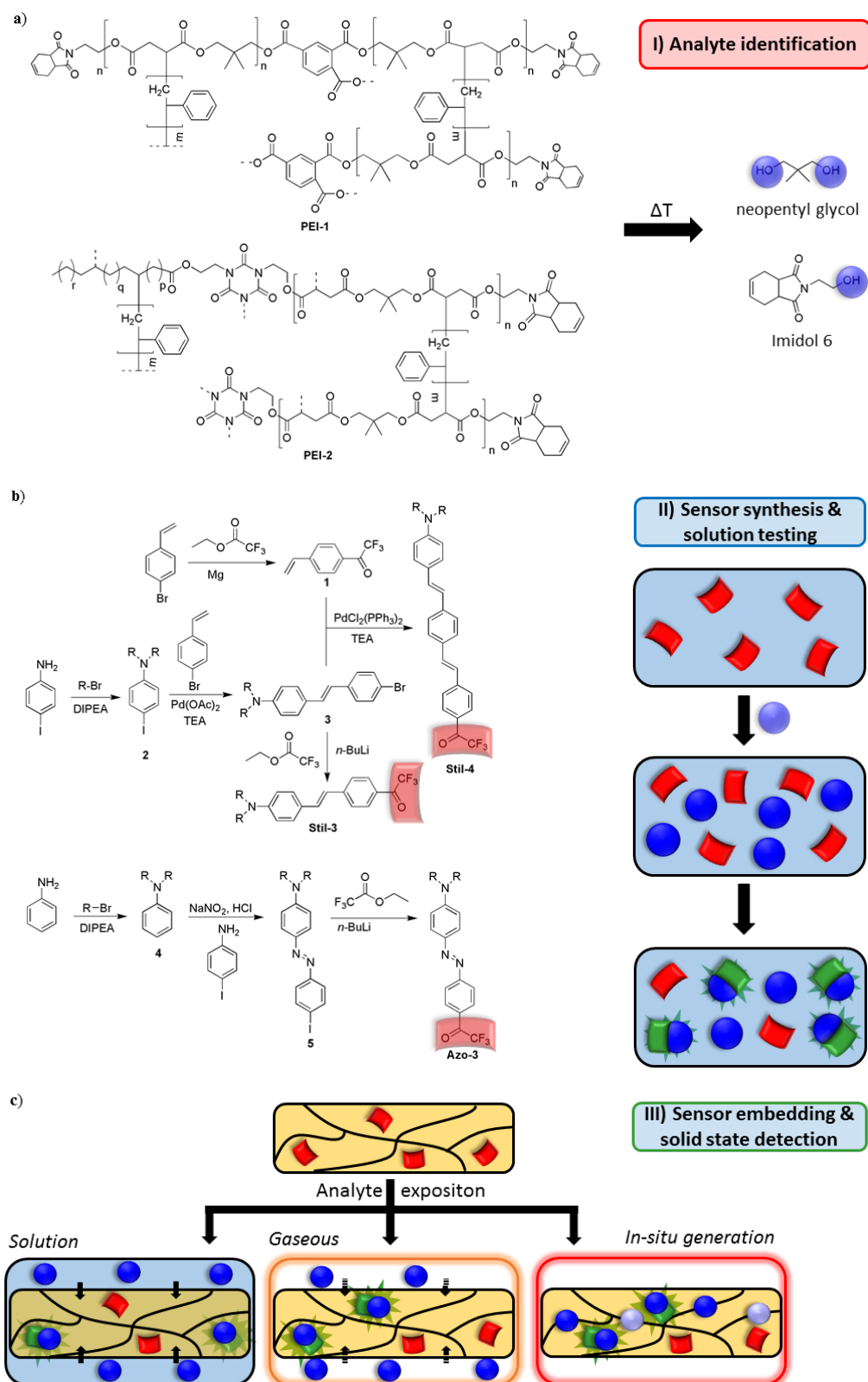
Scheme 1 To develop a suitable sensor system to monitor PEI degradation a) alcoholic degradation products, especially NPG, were found as main analytes during thermal degradation of **PEI-1** and **PEI-2**. Subsequently the alcohol sensitive sensor molecules **Stil-3**, **Stil-4** and **Azo-3** were synthesized and sensor response was tested in solution detected by optical spectroscopy. Afterwards, sensor molecules were embedded within **PEI-1** and **PEI-2** and activated by storing the specimens in analyte solution, gaseous analyte atmosphere and finally by in-situ analyte generation through thermal degradation.

The thereby identified alcohols, especially neopentyl glycol (NPG) and Imidol 6, occurring as main degradation products, allow the application of trifluoroacetyl functionalized dye molecules, in particular the stilbene molecules **Stil-3** and **Stil-4**, and the azobenzene **Azo-3** (**Scheme 1b**).

The trifluoroacetyl group allows a nucleophilic attack of an alcohol whereby the emission wavelength of the corresponding hemiacetal formed during reaction is significantly blue-shifted and thus allows a discrimination between the activated and the virgin form[257-259].

The possible sensor molecules should be fully characterized in solution experiments to prove their responsivity towards nucleophilic analytes, especially NPG and Imidol 6, followed by solid state activation experiments.

Due to their suitability in radically cross-linked polymers and their high thermal stability, trifluoroacetyl functionalized stilbenes and azobenzenes constitute promising optical chemosensors to monitor long-term thermal PEI degradation by optical spectroscopy[260-263]. Additionally the sensor molecules has to withstand the processing conditions of the PEI resins, which are cured at up to 140 °C for 3 h.

Sensor activation in solid state should be demonstrated by model experiments using a model poly(styrene-*co*-divinylbenzene) (**PS/DVB**) resin synthesized by free radical polymerization. Subsequently, the sensor molecules **Stil-3**, **Stil-4** and **Azo-3** should be embedded within **PEI-1** and **PEI-2** and the activation conditions should be increasingly refined in order to demonstrate sensor activation under most realistic conditions (**Scheme 1c**). Thus, specimens should be first stored in aqueous *n*-butylamine (*n*-BuA) solution, whereby a fast sensor activation should be ensured by an excess of analyte and the strong nucleophilicity of the analyte. Afterwards, sensor activation within **PEI-1** and **PEI-2** should be demonstrated by exposure to an excess of gaseous NPG, the later main analyte. Finally, sensor activation should be triggered by thermal stress, leading to PEI degradation and thereby in-situ generating alcoholic degradation products.

3. Results and Discussion

3.1. Analyte determination by thermal degradation experiments

Before a suitable sensor for the detection of thermal degradation of poly(ester imides) (PEI)s could be developed, identification of possible analytes was required. Thus, various PEIs were thermally degraded and the resulting degradation products were analyzed.

3.1.1. Investigated PEIs

The chemical structure of the two cured resins **PEI-1** and **PEI-2** and the two corresponding pre-condensates **PEI-1PC** and **PEI-2PC** is presented in **Figure 23** and **Figure 24**.

PEI-1PC is synthesized by a polycondensation of the trivalent trimellitic anhydride (TMA), neopentyl glycol (NPG), maleic acid and Imidol 6. **PEI-1PC** is dissolved in styrene and the double bond introduced into the polymer by the maleic acid serves as a cross-linker during the radical resin curation yielding **PEI-1**.
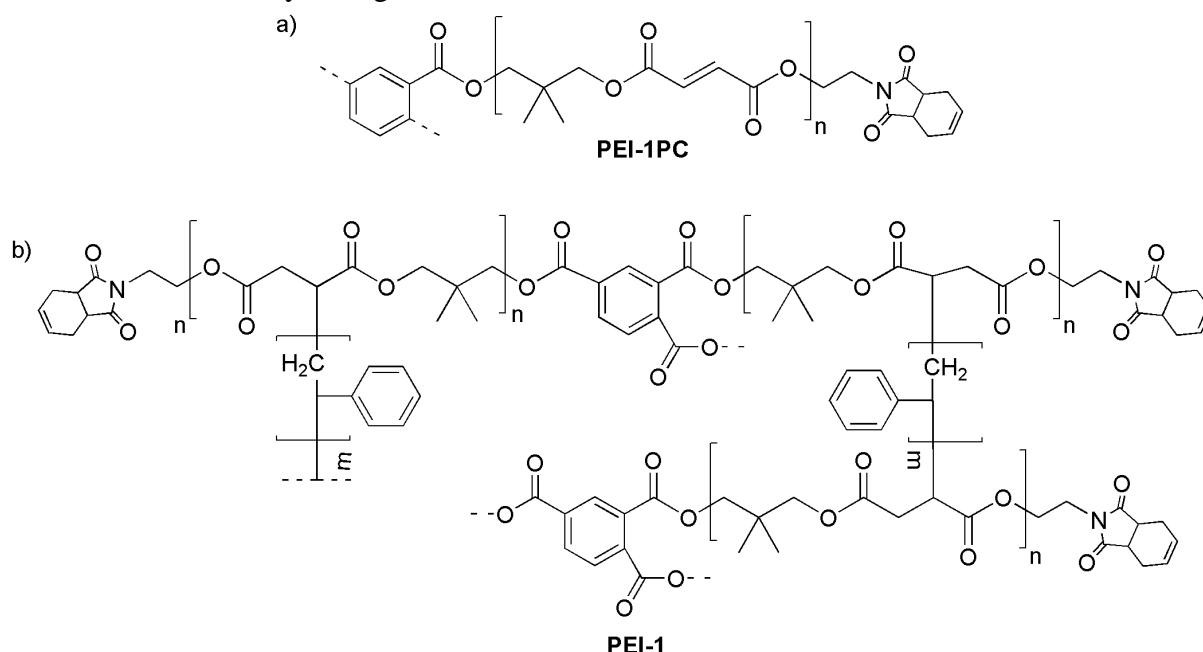

Figure 23 Chemical structure of the a) pre-condensed **PEI-1PC** and the b) corresponding cured resin **PEI-1**.

In **PEI-2PC** the trivalent 1,3,5-tris(2-hydroxyethyl)isocyanurate (THEIC) was reacted together with maleic acid, NPG, an unsaturated fatty acid and Imidol 6. Likewise **PEI-1**, **PEI-2** is synthesized by dissolving **PEI-2PC** in styrene and performing a radical cross-linking. The detailed curing process together with the characterization is given in the Experimental part 4.4. and in the Appendix 7.1. (**Figure A1** to **Figure A11**). **PEI-1** and **PEI-2** both showed high thermal stability as demonstrated by the TGA curves in **Figure A10** and **Figure A11**, respectively. However, in both cases the cross-linked PEI was slightly less thermally stable compared to the corresponding pre-condensate. **PEI-1** showed a maximum decomposition rate at 405 °C whereas **PEI-2** showed a maximum decomposition rate at 420 °C, thus having a slightly higher thermal stability.
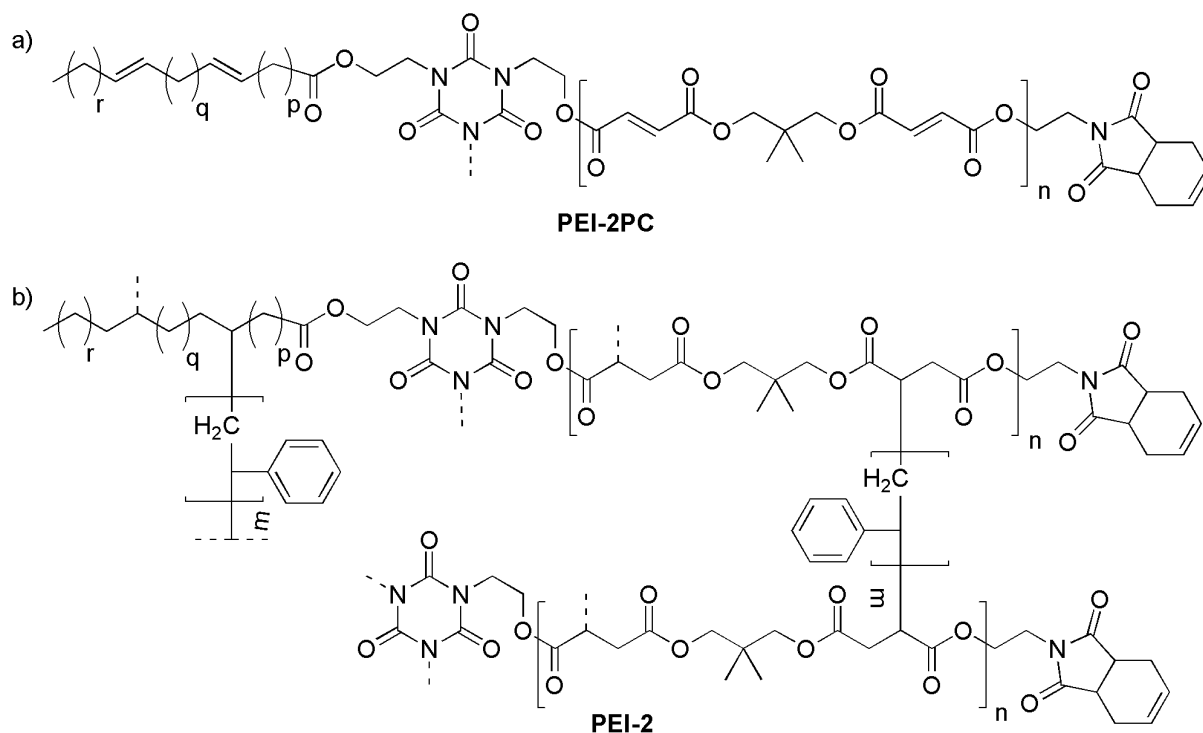
Figure 24 Chemical structure of the a) pre-condensed **PEI-2PC** and the b) corresponding cured resin **PEI-2**.

3.1.2. Thermal degradation experiments

The long-term thermal degradation of **PEI-1PC**, **PEI-1**, **PEI-2PC** and **PEI-2** was investigated under moderate temperatures, to which the resins are also exposed during their application as coating material. **PEI-1** and **PEI-2** belong to thermal class H, thus are designed to withstand temperatures up to 180 °C. Due to their high thermal stability, thermal degradation at 180 °C was expected to be slow and thus additionally degradation at 200 °C and 220 °C was tested. Degradation was investigated under oxygen, thus the thermal-oxidative degradation mechanism was promoted as it is also expected for application issues. The degradation experiments were performed with a self-built apparatus and the setup as well as the mode of operation are described in section 4.2. and **Figure 72**. Thermal degradation was investigated over a period of 5000 h and additionally after 500 h, 1000 h and 3000 h the trapped gaseous degradation products were extracted from the adsorption column and analyzed by ^{1}H-NMR spectroscopy and ESI-TOF-MS. The amounts extracted after several degradation intervals are summarized in **Table 5** and **Table 6**.

Table 5 Amounts of degradation products of **PEI-1PC** and **PEI-1** extracted from the adsorption column after distinct time intervals. Values are given in mg.

	PEI-1PC			PEI-1		
	180 °C	200 °C	220 °C	180 °C	200 °C	220 °C
500 h	26.6	103.1	111.0	21.2	65.7	163.4
1000 h	4.2	68.4	82.0	14.9	67.2	73.7
3000 h	5.7	59.8	74.9	29.5	56.1	71.7
5000 h	3.2	4.1	74.9	14.3	10.7	66.3

35

There was a tendency for higher temperatures to lead to higher extract quantities, i.e. an increased degradation processes. In addition, the largest extract quantity was usually obtained after 500 h and in the later degradation periods the quantities were significantly reduced.

Table 6 Amounts of degradation products of **PEI-2PC** and **PEI-2** extracted from the adsorption column after distinct time intervals. Values are given in mg.

	PEI-2PC			PEI-2		
	180 °C	200 °C	220 °C	180 °C	200 °C	220 °C
500 h	130.5	146.3	21.4	49.9	106.5	198.2
1000 h	7.7	62.8	65.7	6.9	77.8	69.8
3000 h	5.1	54.5	75.4	13.5	48.6	51.0
5000 h	3.9	3.4	47.9	4.0	6.6	54.1

Especially with regard to the realistic conditions at 180 °C, some observations should be mentioned. The pre-condensates degraded more slowly than the corresponding cured resin, which confirmed the results from the TGA measurements. Furthermore, the amount of degradation products collected in the interval from 500 h to 1000 h was less than the amount collected in the interval from 1000 h to 3000 h. This might indicate a different degradation mechanism at moderate temperatures.

For the specimens **PEI-1** and **PEI-2** the mass loss was monitored by weighing after the targeted time interval was accomplished and the results are summarized in **Figure 25**. For both PEIs the fastest and highest mass loss was observed when degradation was done at 220 °C. As **PEI-1PC** and **PEI-2PC** did not keep their shape after exposition to higher temperatures, resulting in sintering with the weighing boats on which the specimen were inserted into the glass tube, weight monitoring was not possible for the uncured resins. A strong initial mass loss was also detected for 200 °C and 180 °C, whereas at 180 °C the slowest decrease was observed. When **PEI-1** and **PEI-2** were degraded at 220 °C, after 3000 h hardly any mass loss was observed which indicated that the temperature was high enough to induce cross-linking and cyclization process leading to stable char formation[72]. Furthermore, a darkening of the specimen was observed which was less distinct for specimens aged at 180 °C and strong for specimens stored at 220 °C.
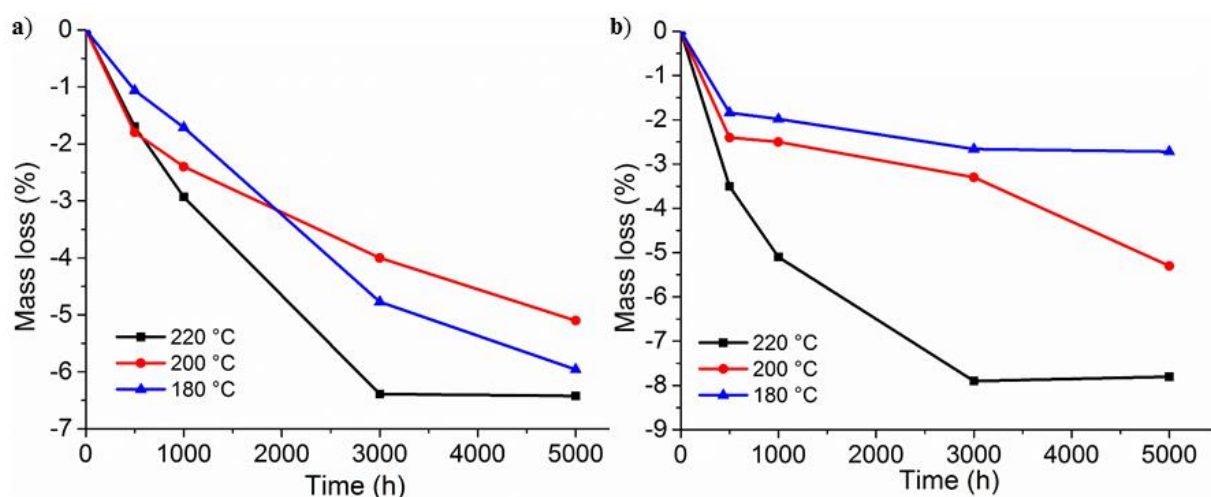

Figure 25 Mass loss of the specimens **PEI-1** and **PEI-2** monitored during the long-term thermal degradation experiments at different temperatures.

Overall, the mass loss curves for degradation at 180 °C and 200 °C showed similar trends while the curves for degradation at 220 °C showed significant different progressions, hinting at different degradation pathways. The comparison of the different mass loss curves for **PEI-1** and **PEI-2** also allows statements about their thermal stability. For **PEI-1** mass losses of 6.4 %, 5.1 % and 6.0 % were measured when the specimen was degraded at 220 °C, 200 °C and 180 °C, respectively. **PEI-2** showed mass losses of 7.8 %, 5.3 % and 2.7 % when stored at 220 °C, 200 °C and 180 °C, respectively. Thus, the degradation pattern of **PEI-2** showed a stronger temperature dependency, but in terms of long-term stability at application temperature of 180 °C, **PEI-2** was proven to be more suitable.

However, a safe application of the PEI-coatings is guaranteed up to 30 % mass loss, which was not achieved for any of the investigated resins even at 220 °C, which was 40 °C above their recommended application temperature.

3.1.3. Analyte detection by ^{1}H-NMR spectroscopy

Subsequently, the degradation extracts, which were collected during the thermal degradation experiments, were further analyzed to identify formed thermal degradation products and calculate their amount. The extracts were a highly complex mixture of different products formed during the resin degradation, thus the analysis was focused on those compounds, potentially serving as target molecules for a sensor molecule.

^{1}H-NMR spectroscopy was used as main analytic tool for analyte identification and qualification. Quantification was done by addition of an external standard, 1,3,5-trioxane, serving as reference for the calculation. ^{1}H-NMR spectra of the degradation extracts are presented in the Appendix 7.1. and the calculated amounts of alcoholic degradation products are summarized in **Table 7** to **Table 10**. All values refer to the collected extract from the decomposition of specimens with a weight of 5 g (compare Experimental part 4.2.).

Table 7 NPG and Imidol 6 amounts for the thermal degradation of **PEI-1PC** calculated by ^{1}H-NMR spectroscopy using 1,3,5-trioxane as external standard. Upper values are given in mg, bottom values are given in mmol.

	PEI-1PC					
	180 °C		200 °C		220 °C	
	NPG	Imidol 6	NPG	Imidol 6	NPG[5]	Imidol 6[5]
500 h	1.52, 0.015[1]	6.57, 0.034[1]	10.40, 0.100[3]	6.19, 0.032[3]	8.97, 0.086[4]	0.37, 0.002[4]
1000 h	0.57, 0.005[1]	0.19, < 0.001[1]	4.88, 0.047[3]	0.18, < 0.001[3]	4.87, 0.047[4]	0.02, < 0.001[4]
3000 h	1.88, 0.018[1]	0.04, < 0.001[1]	4.22, 0.040[3]	n.d.[3]	11.76, 0.113[3]	n.d.[3]
5000 h	3.18, 0.031[2]	0.07, < 0.001[2]	2.59, 0.025[1]	n.d.[1]	9.24, 0.089[3]	n.d.[3]

1,3,5-Trioxane was added as internal reference for analyte calculations and the following amounts were used:
[1]0.35 mg / 3.9·10^-3 mmol, [2]0.175 mg / 1.94·10^-3 mmol, [3]1.8 mg / 0.02 mmol, [4]0.90 mg / 0.01 mmol, [5]corrected with a factor of 0.90 due to contamination in the adsorption material.

Exemplarily, the ^{1}H-NMR spectra of **PEI-2** degraded at 180 °C are shown in **Figure 26**. The investigated PEIs showed a constant release of NPG. Furthermore, Imidol 6 was detected within the first 1000 h, in particular a greater amounts within the first 500 h.

Table 8 NPG and Imidol 6 amounts for the thermal degradation of **PEI-1** calculated by ^{1}H-NMR spectroscopy using 1,3,5-trioxane as external standard. Upper values are given in mg, bottom values are given in mmol.

	PEI-1					
	180 °C		200 °C		220 °C	
	NPG	Imidol 6	NPG	Imidol 6	NPG[5]	Imidol 6[5]
500 h	2.00, 0.019[1]	1.43, 0.007[1]	4.51, 0.043[3]	0.86, 0.004[3]	4.60, 0.044[3]	0.88, 0.005[3]
1000 h	3.24, 0.031[1]	0.20, 0.001[1]	3.63, 0.035[3]	n.d.[3]	4.39, 0.044[3]	n.d.[3]
3000 h	1.40, 0.013[4]	n.d.[4]	1.16, 0.011[3]	n.d.[3]	3.83, 0.037[3]	n.d.[3]
5000 h	1.05, 0.010[3]	n.d.[3]	1.04, 0.010[1]	n.d.[1]	n.d.[3]	n.d.[3]

1,3,5-Trioxane was added as reference for analyte calculations and the following amounts were used: [1]0.35 mg / $3.9 \cdot 10^{-3}$ mmol, [2]0.175 mg / $1.94 \cdot 10^{-3}$ mmol, [3]1.8 mg / 0.02 mmol, [4]0.90 mg / 0.01 mmol, [5]corrected with a factor of 0.90 due to contamination in the adsorption material.

Table 9 NPG and Imidol 6 amounts for the thermal degradation of **PEI-2PC** calculated by ^{1}H-NMR spectroscopy using 1,3,5-trioxane as external standard. Upper values are given in mg, bottom values are given in mmol.

	PEI-2PC					
	180 °C		200 °C		220 °C	
	NPG	Imidol 6	NPG	Imidol 6	NPG[5]	Imidol 6[5]
500 h	1.78, 0.103[1]	27.46, 0.141[1]	19.16, 0.184[3]	14.25, 0.073[3]	2.05, 0.002[3]	1.32, 0.007[3]
1000 h	1.13, 0.011[1]	0.73, 0.004[1]	4.02, 0.039[3]	0.25, 0.001[3]	3.99, 0.038[3]	0.25, < 0.001[3]
3000 h	3.52, 0.034[1]	0.76, 0.004[1]	4.82, 0.046[3]	0.18, < 0.001[3]	10.16, 0.097[3]	0.72, 0.004[3]
5000 h	1.50, 0.014[2]	0.08, < 0.001[2]	0.97, 0.009[1]	0.27, 0.001[1]	7.84, 0.076[3]	0.23, < 0.001[3]

1,3,5-Trioxane was added as reference for analyte calculations and the following amounts were used: [1]0.35 mg / $3.9 \cdot 10^{-3}$ mmol, [2]0.175 mg / $1.94 \cdot 10^{-3}$ mmol, [3]1.8 mg / 0.02 mmol, [4]0.90 mg / 0.01 mmol, [5]corrected with a factor of 0.90 due to contamination in the adsorption material.

A large amount of degradation products that were found could be traced back to the production of the resins, including solvents and stabilizers and they also predominantly were trapped within the first 1000 h. All ^{1}H-NMR spectra show that, in addition to the two main analytes identified, a number of other aliphatic and aromatic compounds, including TMA and maleic acid or fumaric acid respectively, were formed during thermal degradation. Due to the complexity of

the degradation extract and small analyte amounts together with partly very small sample quantities available, a precise quantification was not expedient. For **PEI-2PC** and **PEI-2** no THEIC was identified as degradation product, which is due to its outstanding thermal stability resulting in an improvement of the thermal properties of **PEI-2** compared to **PEI-1**[180].

Table 10 NPG and Imidol 6 amounts for the thermal degradation of **PEI-2** calculated by ^{1}H-NMR spectroscopy using 1,3,5-trioxane as external standard. Upper values are given in mg, bottom values are given in mmol.

	PEI-2					
	180 °C		200 °C		220 °C	
	NPG	Imidol 6	NPG	Imidol 6	NPG[5]	Imidol 6[5]
500 h	1.49, 0.014[1]	6.17, 0.032[1]	7.49, 0.072[3]	10.37, 0.053[3]	9.65, 0.093[3]	13.97, 0.072[3]
1000 h	2.09, 0.020[1]	0.23, 0.001[1]	6.61, 0.063[3]	0.27, 0.001[3]	4.28, 0.041[3]	n.d.[3]
3000 h	2.43, 0.023[4]	n.d.[4]	3.71, 0.036[3]	n.d.[3]	7.07, 0.068[3]	n.d.[3]
5000 h	1.44, 0.013[2]	n.d.[2]	0.65, 0.006[1]	n.d.[1]	4.67, 0.045[3]	n.d.[3]

1,3,5-Trioxane was added as reference for analyte calculations and the following amounts were used: [1]0.35 mg / 3.9·10^{-3} mmol, [2]0.175 mg / 1.94·10^{-3} mmol, [3]1.8 mg / 0.02 mmol, [4]0.90 mg / 0.01 mmol, [5]corrected with a factor of 0.90 due to contamination in the adsorption material.
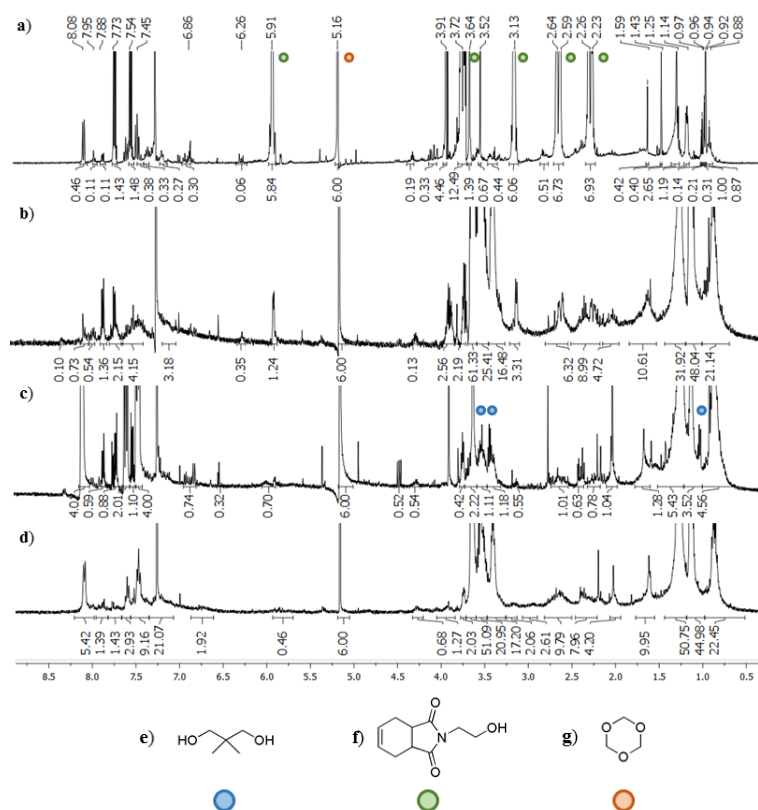
Figure 26 ^{1}H-NMR spectra of the degradation extracts of **PEI-2** degraded at 180 °C after a) 500 h, b) 1000 h, c) 3000 h and d) 5000 h recorded in CDCl$_3$ and the structures of the main analytes e) NPG and f) Imidol 6 with g) 1,3,5-trioxane used as reference for calculation.

3.1.4. Analyte detection by ESI-TOF-MS

The main analytes were analyzed by ESI-TOF-MS. To facilitate analyte detection, preliminary tests were carried out to separate the complex degradation extract by means of HPLC. Therefore, a monomer blend of 0.2 mg each of NPG, Imidol 6, TMA, THEIC and fumaric acid was prepared, separated by HPLC which was coupled to an ESI-TOF-MS thus allowed a subsequent detection of the separated monomers (**Figure 27**). For the measuring procedure the sample requirements for HPLC and ESI-TOF-MS were taken into account and different methods were tested. Although salt addition supports analyte ionization in MS, it should be avoided to protect the HPLC column. Therefore, a suitable method has turned out to be methanol as solvent and MS detection in negative mode. Methanol achieved sufficient separation efficiency and, in addition, the polar analytes, in particular alcohols and carboxylic acids, allowed good detection without salt addition.
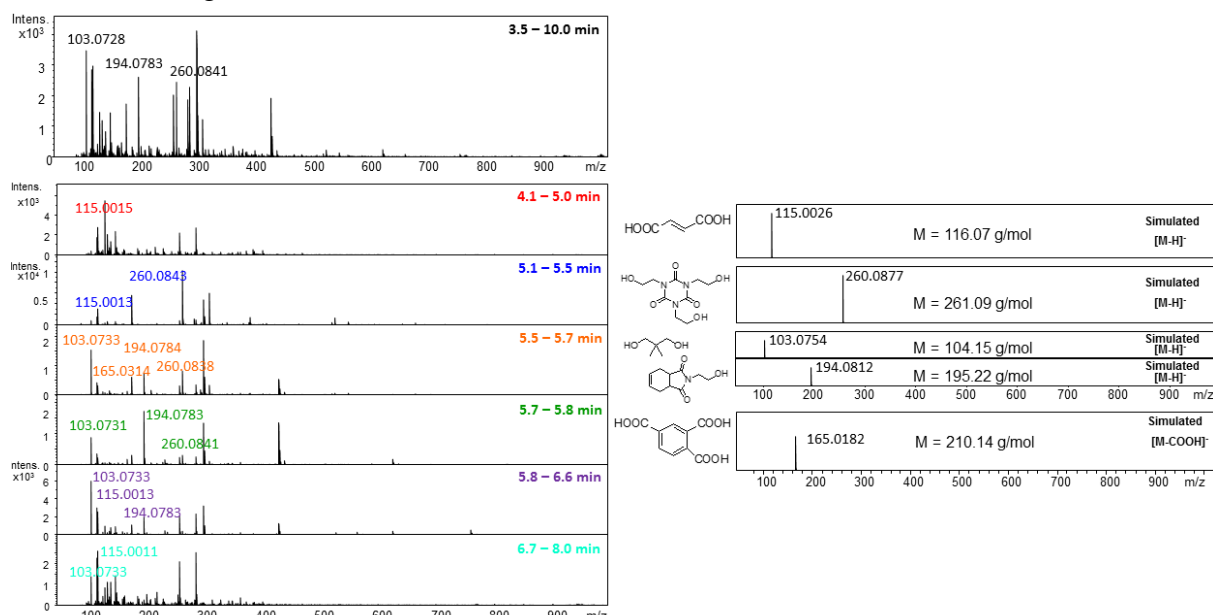
Figure 27 ESI-TOF-MS spectra of a monomer blend of NPG, Imidol 6, TMA, THEIC and fumaric acid after separation by HPLC.

The first detected analyte was fumaric acid after 4.1 min and the *m/z* values were in good accordance with the simulated pattern for [M-H]⁻. After 5 min THEIC could be detected matching the simulated [M-H]⁻ molecule ion. NPG and Imidol 6 were detected after 5.5 min, also in good accordance with the corresponding simulated [M-H]⁻ molecule ion. Finally, TMA was detected as [M-COOH]⁻ after 5.7 min. However, while NPG, Imidol 6 and THEIC were easily detectable with the chosen method, it was less sensitive for the detection of fumaric acid and TMA.

The actual analyte amounts were significantly lower in the degradation extracts, yet they could partially be detected with the developed HPLC/ESI-TOF-MS method as demonstrated in **Figure 28**. Due to their low amounts and lower sensitivity compared to other analytes, TMA and fumaric acid could not be detected by NMR spectroscopy. However, in ESI-TOF-MS measurements both substances were detectable. Neither for **PEI-2PC** nor for **PEI-2** THEIC was identified, proving the observations from NMR spectroscopy. Thus ESI-TOF-MS could be used to additionally confirm the results from the ¹H-NMR spectroscopy and the measured spectra are shown in Appendix 7.1.
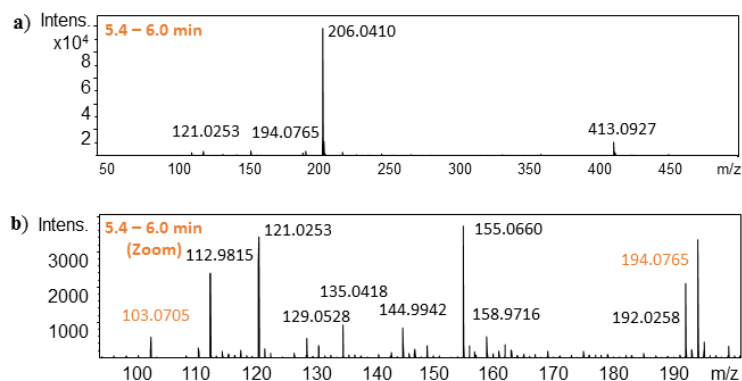
Figure 28 ESI-TOF-MS spectra of the degradation extract of **PEI-2** at 220 °C after 500 h at a) the time interval 5.4 to 6.0 min and b) the zoomed spectra showing the molecule ion signals of NPG and Imidol 6.

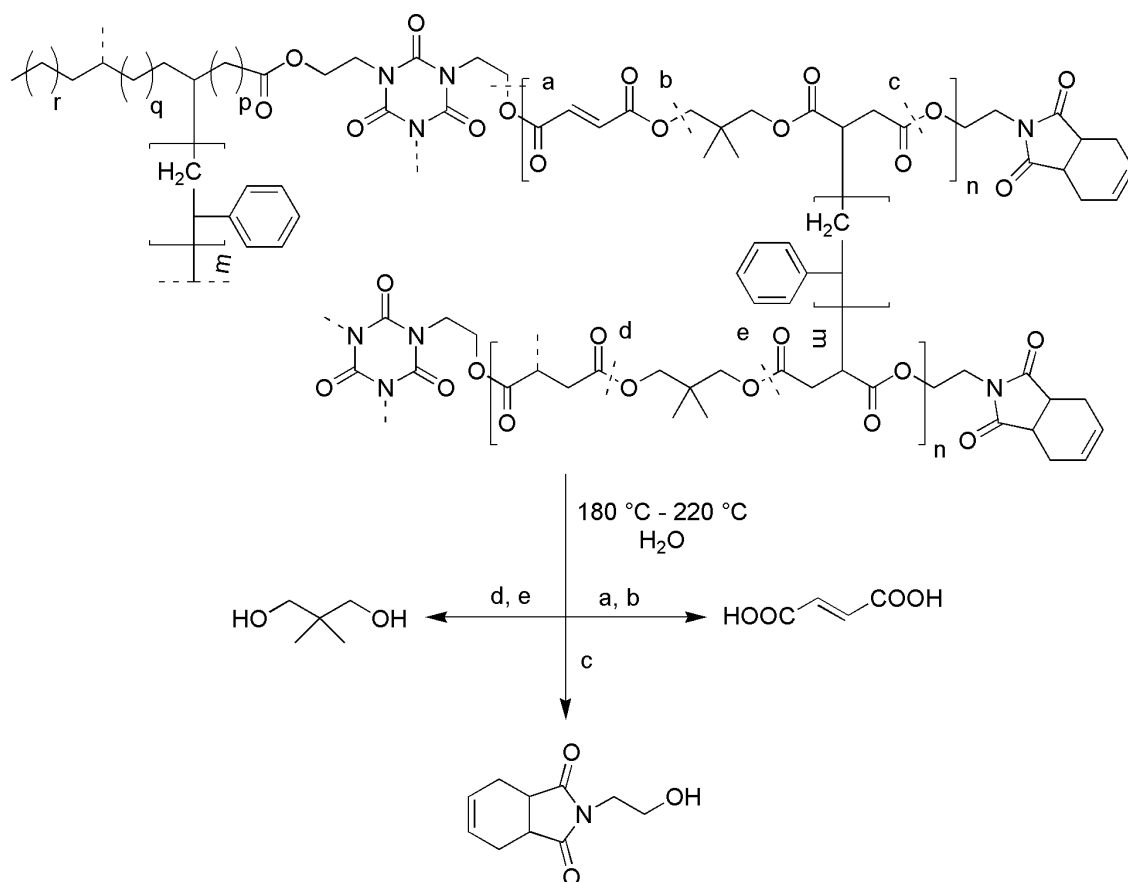### 3.1.5. Postulated degradation mechanism for analyte formation

Based on the results from ^{1}H-NMR spectroscopy and ESI-TOF-MS, the degradation mechanisms shown in **Scheme 2** and **Scheme 3** were postulated for the analyte release from **PEI-1** and **PEI-2**. For both, the pre-condensates and the cured PEIs, NPG was identified as the main analyte, suggesting the cleavage of the ester bond as the weakest link. Alcoholic decompositions products, in particular NPG and Imidol 6, were found to be more abundant, while acids were only observed in small amounts. The identification of TMA in the degradation extracts of **PEI-1** together with the absence of THEIC in the decomposition extracts of **PEI-2** suggests a higher thermal stability for **PEI-2**. This observation was confirmed in TGA measurements (**Figure A10** and **Figure A11**).
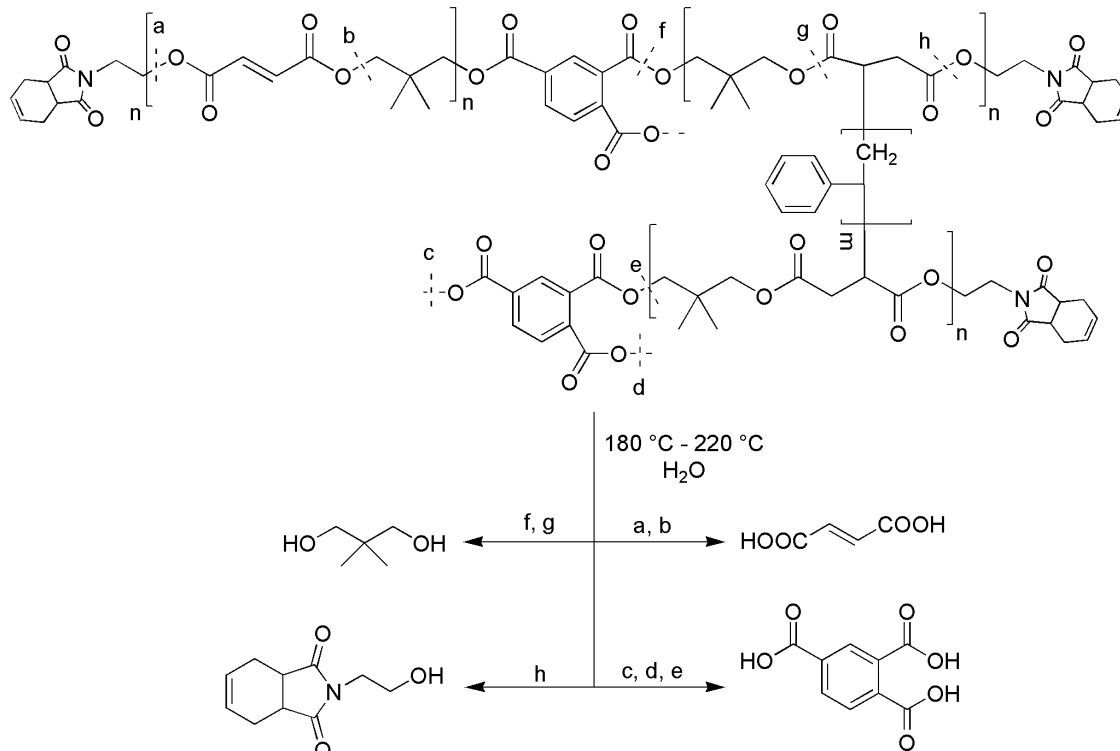
Scheme 2 Postulated degradation mechanism of **PEI-1** triggering the release of the main analytes NPG and Imidol 6.

Further, ^{1}H-NMR spectroscopy suggests that for the cured resins **PEI-1** and **PEI-2** also aromatic olefins, presumably styrene and derivatives, were formed. However, due the number

41

of different resonances in the aromatic region, a quantification and qualification was not possible by means of NMR spectroscopy. Additionally, identification of these compounds using mass spectroscopy was also not possible due to the lack of ionization by the chosen ESI-TOF-MS method.

Scheme 3 Postulated degradation mechanism of **PEI-2** triggering the release of the main analytes NPG and Imidol 6.

A comparison of the IR spectra recorded before and after 5000 h of thermal aging revealed great changes at wavenumbers above 3000 cm^{-1}, thus indicating the formation of aromatic structures, presumably by cyclization reactions. Furthermore, the broadness of the signals together with the wavenumbers above 3500 cm^{-1} suggest the formation of hydroxyl and carboxyl groups within the residue. The IR spectra are shown in **Figure A35** to **Figure A38**.

In summary, a variety of degradation products were found, whereas a complete identification and quantification was not possible. However, because of the amounts of alcohol, in particular NPG and Imidol 6, released during the PEI decomposition, alcohols were chosen as main analyte to monitor the thermal degradation of **PEI-1** and **PEI-2**.

3.2. Synthesis of the sensor molecules Stil-3, Stil-4 and Azo-3

Trifluoroacetyl functionalized dyes, **Stil-3**, **Stil-4** and **Azo-3**, were selected as promising suitable sensor molecules. The trifluoroacetyl group was of importance as it selectively reacts with nucleophilic analytes, including alcohols. Consequently, a shortening of the conjugated system induced a shift of the absorption and emission maxima which was easily detectable by UV/Vis- and fluorescence spectroscopy.

As shown in **Scheme 4**, the synthesis of **Stil-3** and **Stil-4** was similar and proceeded via the same intermediates. The detailed experimental procedure together with a complete characterization of all sensor molecules is given in the Experimental part 4.3. and the Appendix 7.2., respectively.

First, the amine protons of *p*-iodoaniline were substituted by hexyl-chains using 1-bromhexane and *N,N*-diisopropylethylamine (DIPEA) in DMF yielding **2** with a yield of 78 %. A complete substitution was required as the primary amine would interfere with the trifluoroacetyl sensor group. Furthermore, the dihexyl substitution was essential as it guaranteed the subsequent solubility of sensor molecules in the organic PEI resins. In the next step, the stilbene moiety was introduced by a Heck reaction of **2** with 4-bromostyrene using palladium(II)acetate as catalyst generating **3** with a yield of 39 %. Subsequently, **3** was reacted with ethyl trifluoroacetate and *n*-butyllithium (*n*-BuLi) to give **Stil-3** with a yield of 84 %.
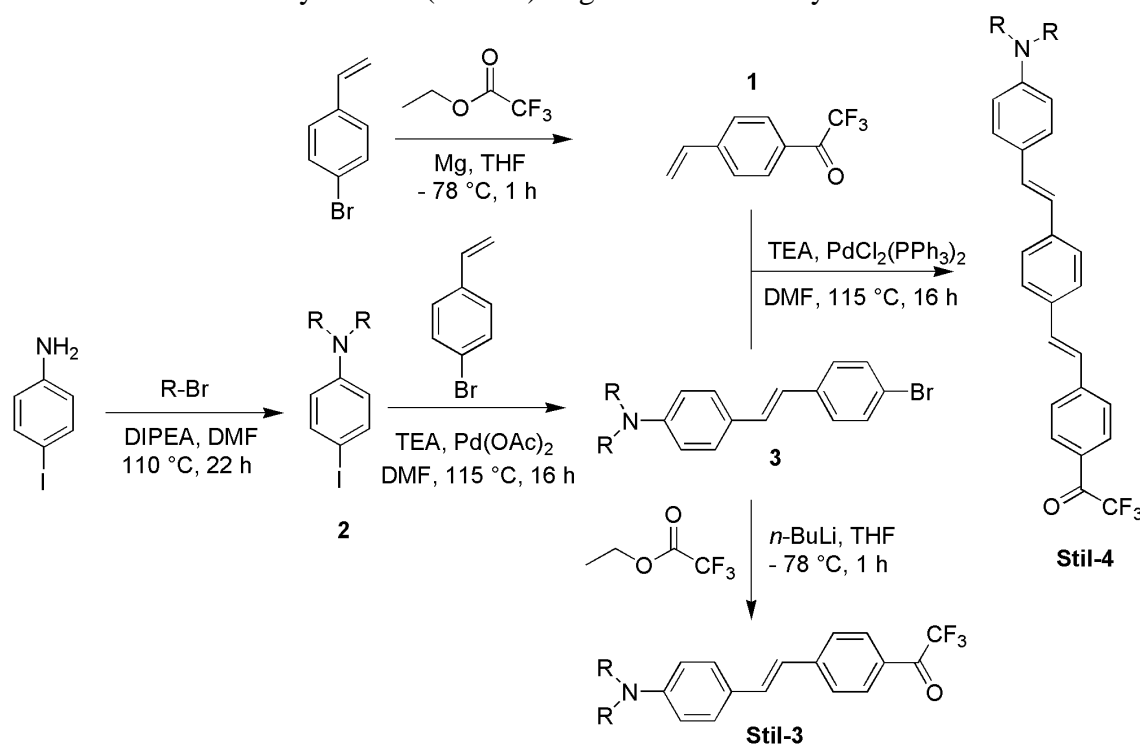
Scheme 4 Synthetic pathway of the trifluoroacetyl functionalized stilbene sensor molecules **Stil-3** and **Stil-4** (R = –C_6H_{13}).

The successful synthesis of **2**, **3** and **Stil-3** was proven by NMR-spectroscopy and the ^{1}H-NMR spectra are presented in **Figure 29**. By comparing the ^{1}H-NMR spectrum of **2** (**Figure 29a**) with the ^{1}H-NMR spectrum of **3** (**Figure 29b**) the successful stilbene formation was demonstrated by the additional protons H_{12} and H_{13} at 6.61 ppm and 6.93 ppm originating from the internal double bond. Additionally, protons H_{15} and H_{16} at 7.31 to 7.43 ppm, characteristic for aromatic protons, confirmed the attachment of the second benzene ring. The number of protons in **Figure 29c** remained constant, but due to the substitution of the bromine by the trifluoroacetyl functionality in the monostyryl stilbene **Stil-3**, the resonance of H_{16} was significantly shifted to 8.01 ppm.
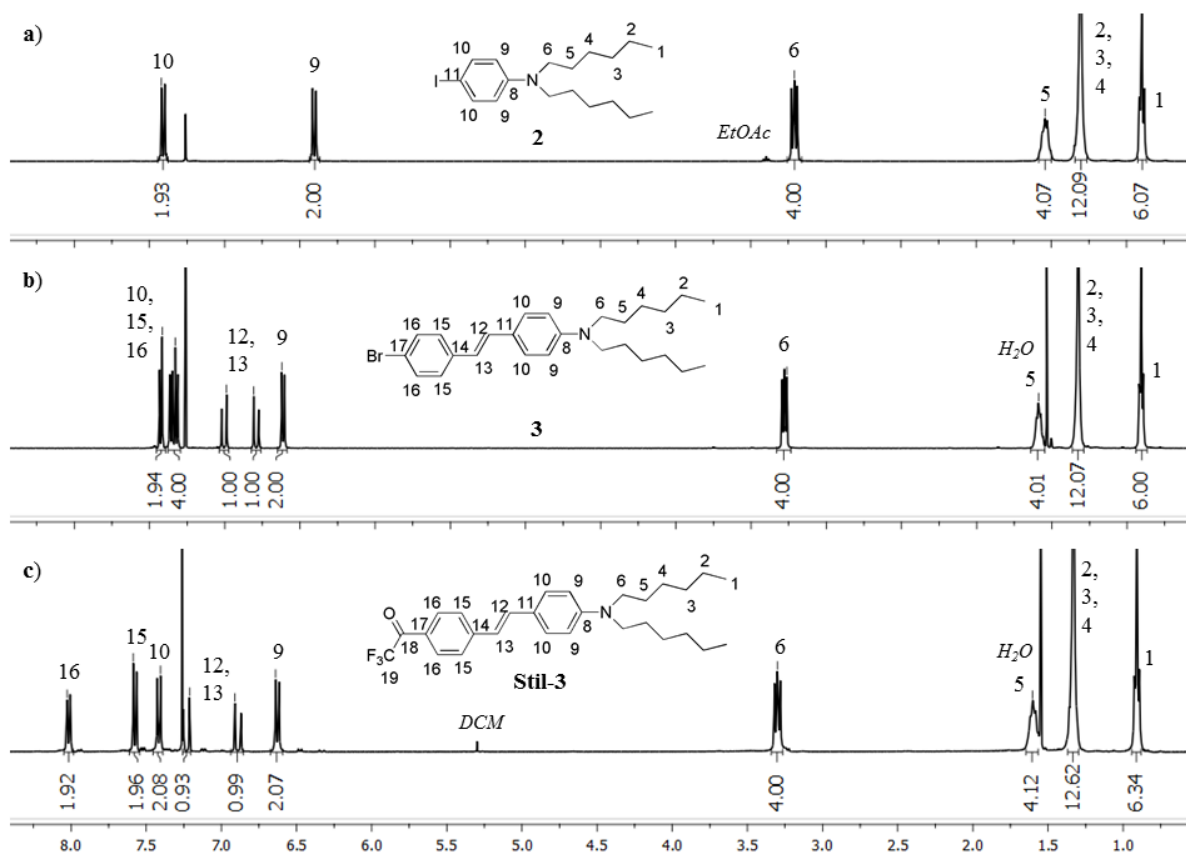
Figure 29 ¹H-NMR spectra of a) **2**, b) **3** and c) **Stil-3** measured in CDCl₃.

As shown in **Scheme 4**, the synthesis of the distyryl stilbene **Stil-4** required two additional reaction steps. First, 4-bromostyrene was substituted with the trifluoroacetyl group by a Grignard reaction yielding **1** with a yield of 34 %. The remaining double bond enabled a second Heck coupling with **3** and dichlorobis-(triphenylphosphine)-palladium(II) as catalyst which generated **Stil-4** with a yield of 19 %. ¹H-NMR spectra of **1** and **Stil-4** are presented in **Figure 30**.
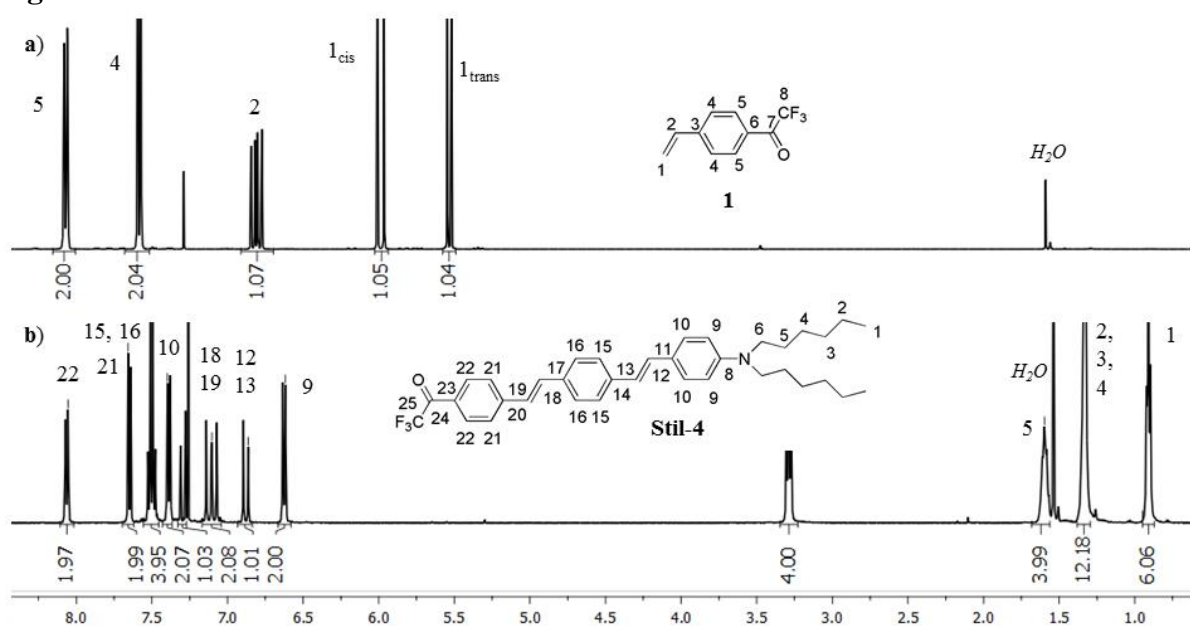
Figure 30 ¹H-NMR spectra of a) **1** and b) **Stil-4** measured in CDCl₃.

The characteristic doublets at 5.49 ppm and 5.96 ppm of $H_{1,cis}$ and $H_{1,trans}$ together with the doublet of doublets of H_2 at 6.79 ppm of the terminal vinyl group and the two aromatic resonances of H_4 and H_5 at 7.56 ppm and 8.05 ppm proved the successful synthesis of the Grignard compound **1**. The appearance of six additional protons in the ^{1}H-NMR spectrum of **Stil-4** compared with the spectrum of **Stil-3** (**Figure 29c**) verified the insertion of the additional styryl unit. Due to the lack of additional protons, the attachment of the trifluoroacetyl group to **Stil-3** and **Stil-4** was proven by ^{19}F-NMR spectroscopy (**Figure 31**).
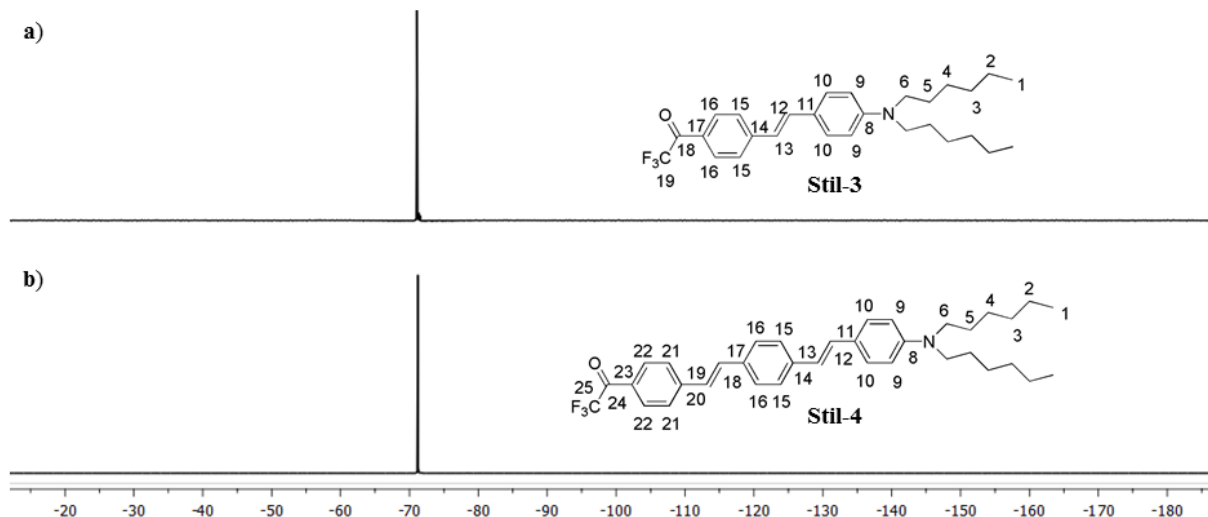
Figure 31 ^{19}F-NMR spectra of a) **Stil-3** and b) **Stil-4** measured in CDCl$_3$.

Despite the similar structure, the synthesis of **Azo-3** required an adaption of the synthetic pathway to allow the insertion of the azo group as shown in **Scheme 5**.
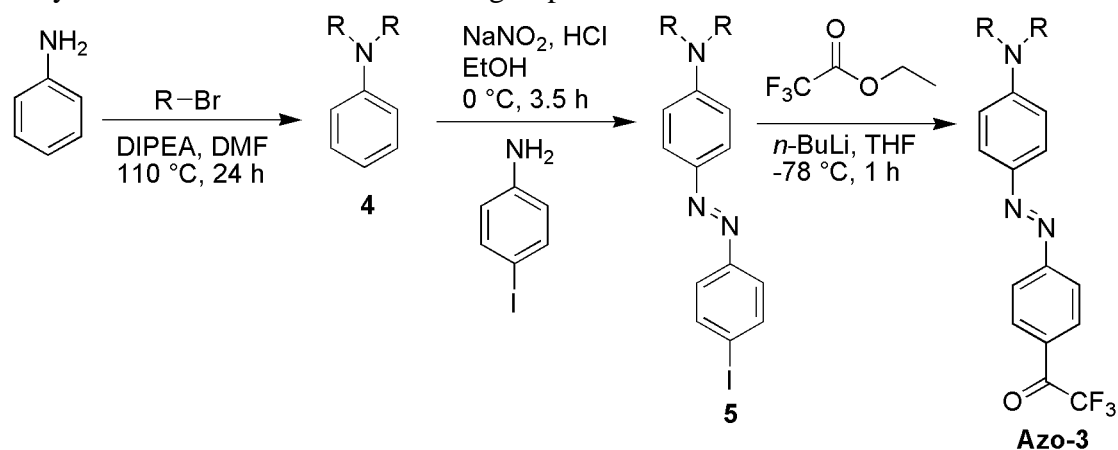
Scheme 5 Synthetic pathway of the trifluoroacetyl functionalized azo benzene sensor molecule **Azo-3** (R = –C$_6$H$_{13}$).

First, **4** was synthesized with a yield of 94 % by the reaction of aniline with 1-bromohexane to ensure the solubility of the later sensor molecule in the PEI-matrix. Again, a complete reaction was essential to exclude subsequent cross-reaction of the unsubstituted aniline with the trifluoroacetyl group. In the next step an azo coupling was performed by the reaction of **4** with *p*-iodoaniline and NaNO$_2$ under the addition of HCl yielding the azo benzene **5** with a yield of 10 %. Subsequently, **5** was reacted with ethyl trifluoroacetate and *n*-butyllithium (*n*-BuLi) to give **Azo-3** with a yield of 22 %. The successful synthesis of **4**, **5** and **Azo-3** was proven by

NMR-spectroscopy and the ^{1}H-NMR spectra are presented in **Figure 32**. The successful azo coupling was proven by the additional resonances H_{15} and H_{16} of the attached aromatic ring depicted in **Figure 32b**. The substitution of the iodine with the trifluoroacetyl group was confirmed by the shift of protons H_{16} from 7.80 ppm to 8.16 ppm and by the ^{19}F-NMR spectra shown in **Figure 33**.
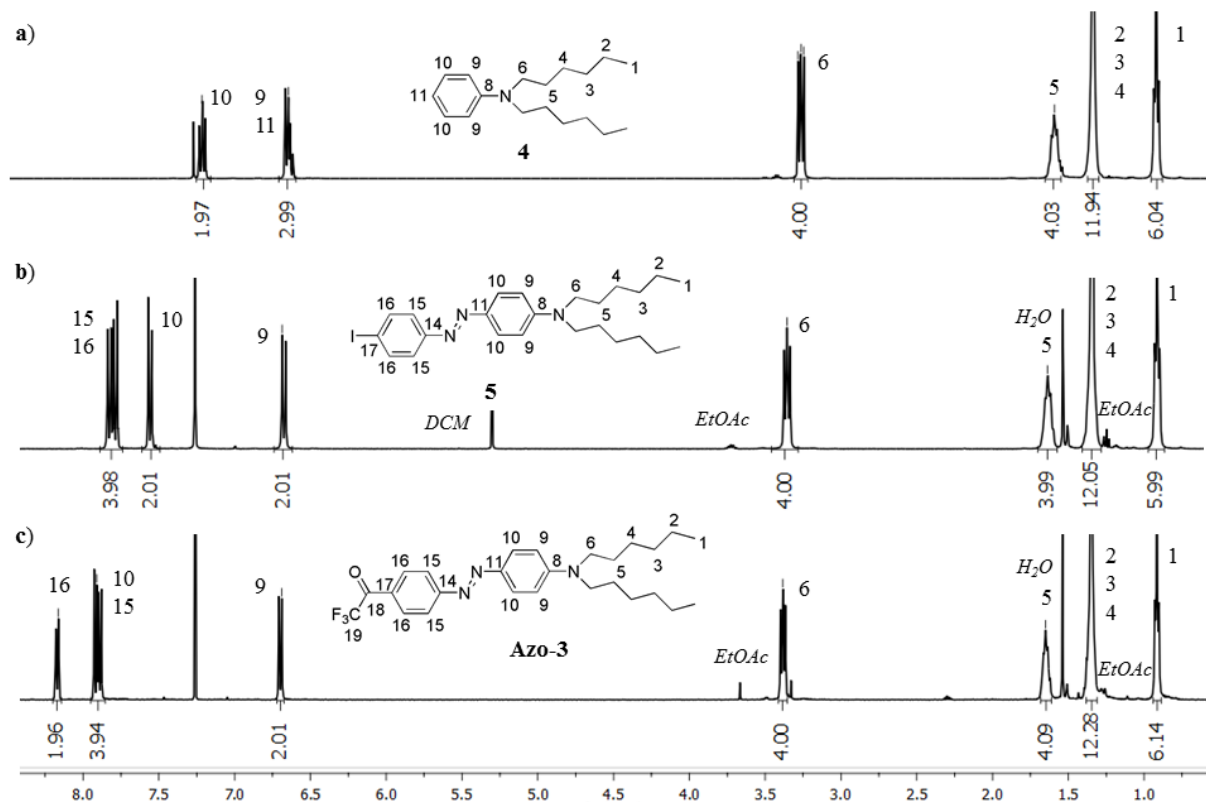

Figure 32 ^{1}H-NMR spectra of a) **4**, b) **5** and c) **Azo-3** measured in CDCl$_3$.
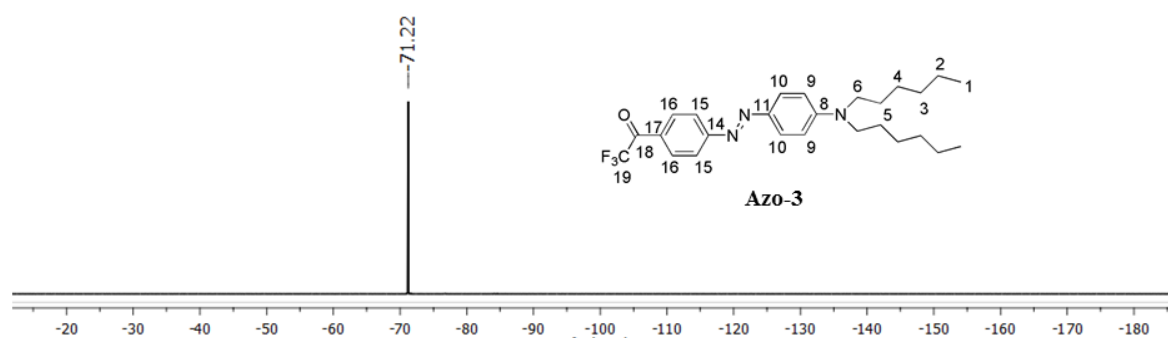
Figure 33 ^{19}F-NMR spectrum of **Azo-3** measured in CDCl$_3$.

3.3. Preliminary investigations to determine the suitability as sensor molecules
3.3.1. Optical properties of the sensor molecules

The optical properties of all sensor molecules are determined by their electron donor-acceptor system[259]. The alkylamino group is acting as electron donor and additionally providing the dyes with a lipophilic character to ensure their solubility in the PEI-resins. Due to the electron-withdrawing effect of the carbonyl group and the trifluoromethyl substituent, the trifluoroacetyl functionality acts as electron acceptor. Furthermore, the nucleophilicty of the carbonyl carbon is highly increased, thus enabling the nucleophilic addition of alcohols as sensor activation

reaction. The disubstitution with an electron donor and acceptor group at the 4 and 4' positions of the phenyl rings, induces a strong polarization within the molecule. This causes a strong influence of the solvent polarity towards the emission spectra in addition with significantly reducing *cis-trans* isomerization due to an increase of both, the energy level of the ground and excited state[264].

Before the sensor molecules **Stil-3**, **Stil-4** and **Azo-3** were embedded in the actual PEI-matrix, pre-experiments were performed to explore their potential suitability as alcohol sensors. In solution experiments it was possible to investigate the sensor activation and the resulting optical indication without hindered diffusion. The optical properties of all sensor molecules were determined by UV/Vis- and fluorescence spectroscopy and were in accordance with literature[258, 265]. The corresponding spectra are shown in **Figure 34** and **Figure 35**, respectively. Despite the elongation of the conjugated system in **Stil-4**, the absorption maximum, which is originating from the n $\rightarrow$ π* transition, of both, **Stil-3** and **Stil-4**, was located at 442 nm (**Figure 34a** and **Figure 34b**). However, the second absorption maximum of the π $\rightarrow$ π* transition from the distyryl dye was significantly shifted to longer wavelengths from 299 nm to 338 nm. **Azo-3** showed an absorption maximum at 481 nm, originating from the n $\rightarrow$ π* transition, and a second absorption maximum from the π $\rightarrow$ π* transition at 288 nm.
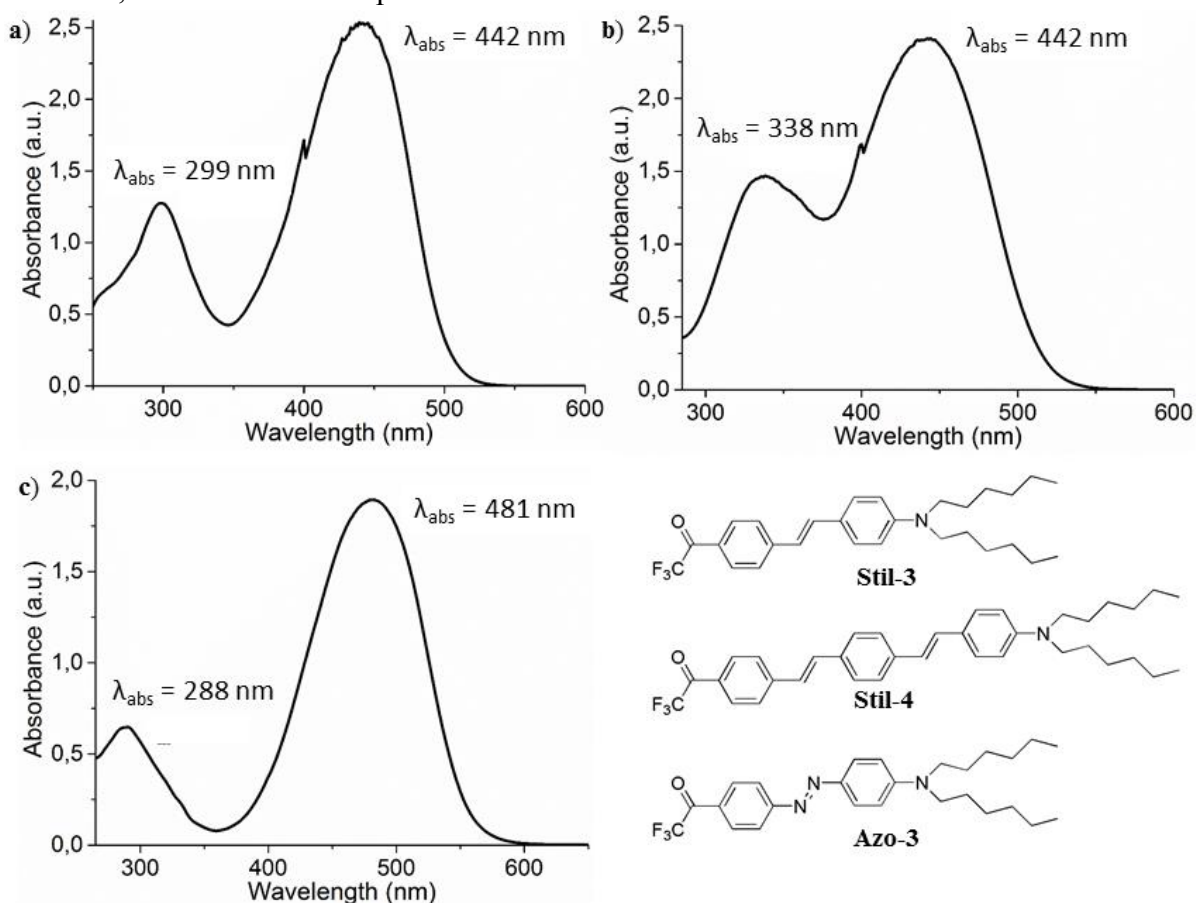

Figure 34 UV/Vis spectra of a) **Stil-3** (c = 0.09 µmol/mL), b) **Stil-4** (c = 0.06 µmol/mL) and c) **Azo-3** (c = 0.05 µmol/mL) recorded in dioxane.

Stil-3 showed an emission maximum at 557 nm (**Figure 35**), while the elongation of the conjugated system in **Stil-4** caused a shift of the emission maximum to longer wavelengths at 603 nm (**Figure 35**). Although its similar structure compared with the stilbene dyes, **Azo-3**

proved to be non-fluorescent. Azobenzenes are known to feature low fluorescence behavior because photoisomerization in the excited state causes a change in the direction of a lone pair of one nitrogen atom, consequently triggering a quenching effect[266].
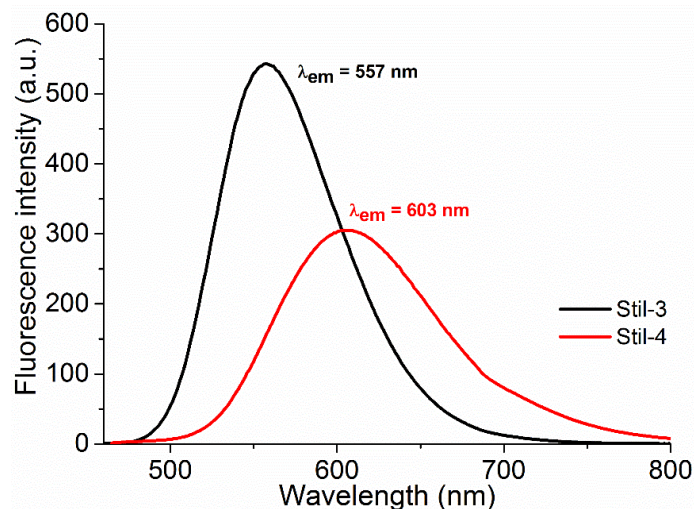

Figure 35 Fluorescence spectra of **Stil-3** (c = 0.0075 µmol/mL, λ_{ex} = 442 nm) and **Stil-4** (c = 0.0075 µmol/mL λ_{ex} = 448 nm) recorded in dioxane.

3.3.2. Sensor activation of Stil-3

To trigger the activation of the sensor molecules, **Stil-3**, **Stil-4** and **Azo-3** were exposed to a solution of dioxane containing an excess of the later main analyte NPG and subsequently the alcohol caused a hemiacetal formation by attacking the highly nucleophilic carbon from the trifluoroacetyl group. The nucleophile addition caused a shortening of the conjugated system and therefore led to a blue shift of the absorption and emission maxima. Thus, sensor activation was monitorable by UV/Vis and fluorescence spectroscopy.

The UV/Vis and fluorescence spectra for the activation of **Stil-3** were in accordance with literature[258] and are depicted in **Figure 36**. A decrease of the virgin absorption maximum at 442 nm together with the formation of a new absorption maximum at 366 nm within 14 days proved the successful activation of **Stil-3** by NPG (**Figure 36a**). Irrespective of the solvent, **Stil-3** showed a spontaneous decrease in the absorption intensity at the beginning of the measurement, which was also observed in reference measurements without the addition of NPG (**Figure 36b**). The cause of this will be explained by the results from the density functional studies in part 3.4.1. All further changes which occurred in samples which contained alcohol were attributed to the activation reaction.

The results of the corresponding fluorescence experiments are shown in **Figure 36c** and **Figure 36d**. Excitation of the virgin **Stil-3** was done at 442 nm, giving a strong emission at 588 nm. When the hemiacetal of **Stil-3** was excited at 366 nm, a weak emission at 588 nm together with a second emission maximum at 415 nm from the $\pi \rightarrow \pi^*$ transition was observable. After exposition to NPG, the virgin emission maximum was decreasing while the emission maximum at 415 nm was slightly shifted to 430 nm and its intensity increased. Again, reference measurements showed initial changes of the fluorescence but an overall change within 14 days was not observable, thus the sensor activation could also be proven by fluorescence spectroscopy. All observed UV/Vis and fluorescence maxima were in good accordance with literature[258]. Reference samples showed fluorescence intensities approximately three times

higher compared with the samples containing NPG. This is caused by the increased solvent polarity, which is lowering the quantum yield of both, the non-activated and the activated **Stil-3**, and is also described in literature[258].
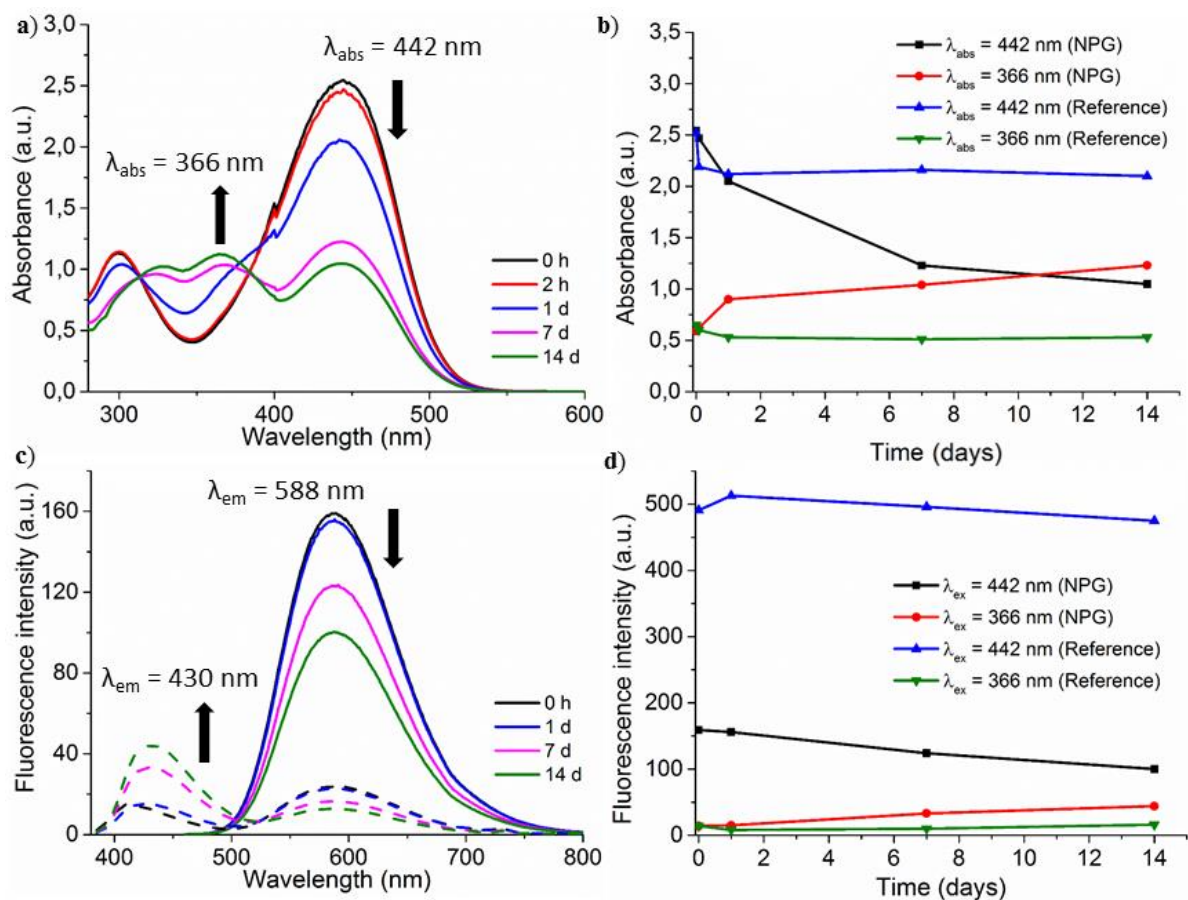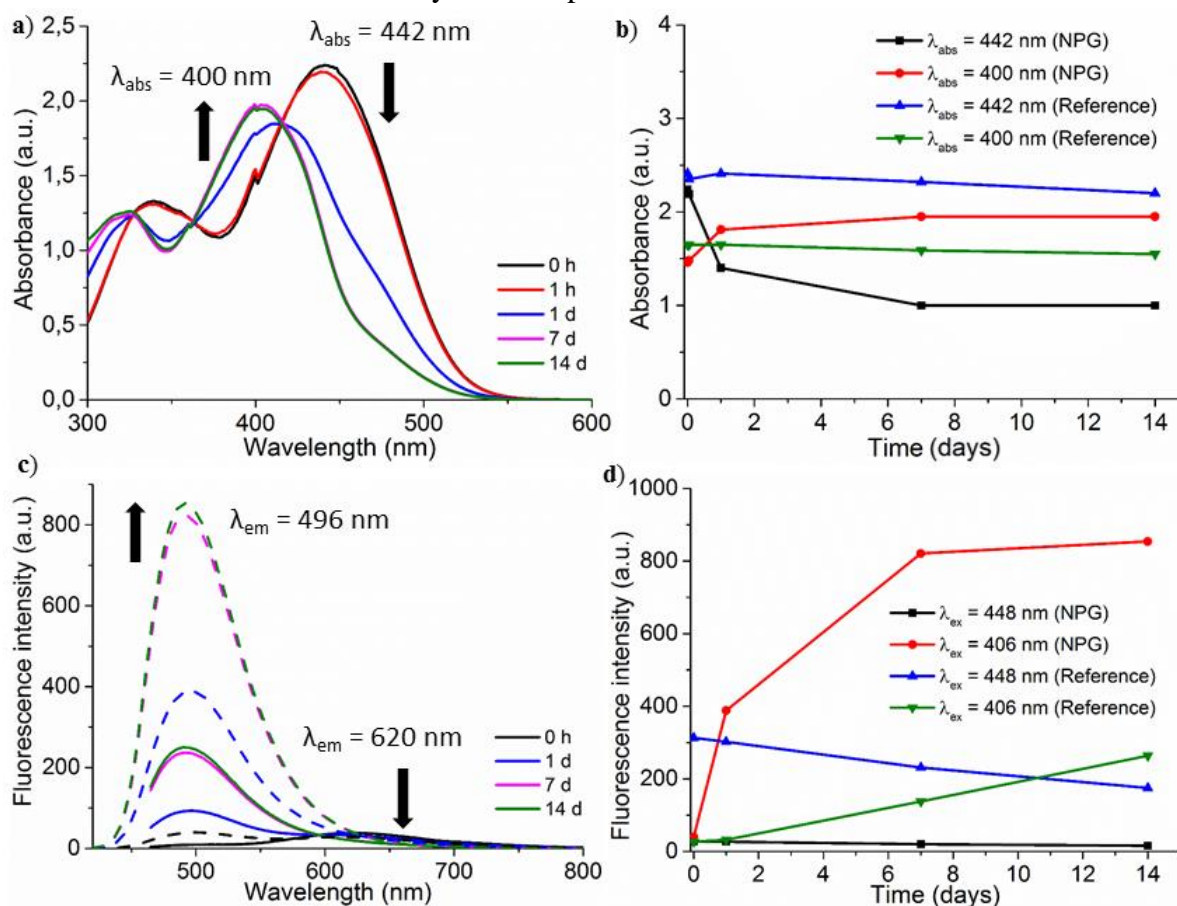

Figure 36 a) UV/Vis spectra of **Stil-3** ($c = 0.09\,\mu mol/mL$) with b) the corresponding plot of the absorption maxima *vs*. time, and c) fluorescence spectra of **Stil-3** ($c = 0.0075\,\mu mol/mL$, $\lambda_{ex,1} = 442$ nm, $\lambda_{ex,2} = 366$ nm) with d) the corresponding plot of the fluorescence maxima *vs*. time. All spectra were recorded in dioxane and sensor activation was triggered by neopentyl glycol (1 mmol/mL).

3.3.3. Sensor activation of Stil-4

All determined absorption and emission maxima for the activation of **Stil-4** were in good accordance with literature[258] and the corresponding UV/Vis and fluorescence spectra are shown in **Figure 37**. In the UV/Vis spectra a decrease of the virgin absorption maximum at 442 nm was observable, together with the formation of a new absorption maximum at 400 nm (**Figure 37a**). In contrast to **Stil-3**, no changes of the absorption maximum within the first hours were observable when no NPG was present (**Figure 37b**).

However, fluorescence investigations of the reference samples, showed a decrease of the virgin emission maximum of **Stil-4** at 620 nm after excitation at 448 nm. At the same time, when excited at 406 nm, an increase of the emission maximum at 496 nm for the activated form was observable. This observation was explained by the slow reaction of **Stil-4** with humidity, which is a potential competitive reaction leading to a diol formation[257]. Due to the stronger nucleophilicity of alcohols compared with water, the diol formation was suppressed in the presence of NPG but could take place in reference experiments. **Stil-4** showed a fast reaction towards NPG and was almost completely activated after 1 day. In contrast, **Stil-3** was not

completely activated even after 14 days, thus the lower reactivity is explaining why the slow diol formation was not observed in reference experiments of **Stil-3**. Again, samples with NPG showed significantly lower fluorescence intensities of **Stil-4** due to the quantum yield decrease when the polarity is increased[258].

A comparison of **Stil-3** and **Stil-4** showed a huge difference in their activation process as monitored by fluorescence spectroscopy. The virgin **Stil-3** showed a strong fluorescence intensity while its activated form showed only a weak emission intensity. **Stil-4** showed weak emission when excited in its virgin form, but a strong signal when excited in its hemiacetal form. This observation was explained by the high quantum yield of **Stil-3** in its trifluoroacetyl form and **Stil-4** in its hemiacetal form and the low quantum yields of **Stil-3** in its hemiacetal form and **Stil-4** in its trifluoroacetyl form in polar solutions[258].

Figure 37 a) UV/Vis spectra of **Stil-4** ($c = 0.06\,\mu mol/mL$) with b) the corresponding plot of the absorption maxima *vs*. time, and c) fluorescence spectra of **Stil-4** ($c = 0.0075\,\mu mol/mL$, $\lambda_{ex,1} = 448$ nm, $\lambda_{ex,2} = 406$ nm) with d) the corresponding plot of the fluorescence maxima *vs*. time. All spectra were recorded in dioxane and sensor activation was triggered by neopentyl glycol (1 mmol/mL).

3.3.4. Sensor activation of Azo-3

The UV/Vis spectra of **Azo-3** were in good accordance with literature[257] and are shown in **Figure 38a**. Upon exposition towards NPG, sensor activation was observed by a decrease of the absorption maximum at 481 nm and a shoulder formation of an additional absorption maximum at 430 nm. Reference experiments showed no formation of an additional absorption maximum, therefore diol formation could be excluded (**Figure 38b**). **Azo-3** showed fast reaction kinetics as **Stil-4** and sensor activation was almost completed after 1 day. Due to

photoisomerization processes in the excited state causing a quenching effect, **Azo-3** was non-fluorescent and additional characterization of its activation with fluorescence spectroscopy was not possible[266].
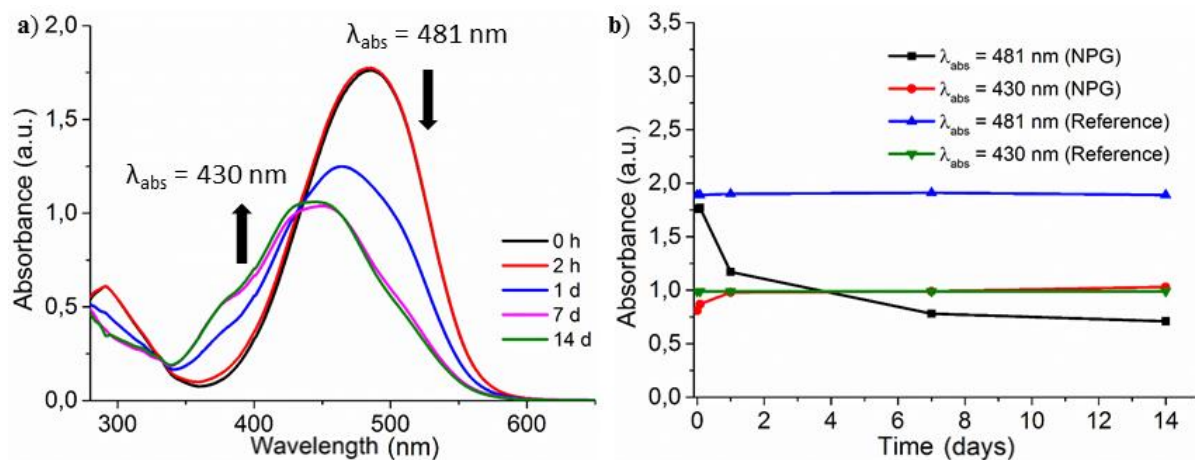

Figure 38 a) UV/Vis spectra of **Azo-3** ($c = 0.05\,\mu mol/mL$) and b) the corresponding plot of the absorption maxima *vs.* time. All spectra were recorded in dioxane and sensor activation was triggered by neopentyl glycol (1 mmol/mL).

In preliminary experiments, all three potential sensor molecules **Stil-3**, **Stil-4** and **Azo-3** could be activated by the addition of NPG and the activation could be followed by optical spectroscopy.

However, in an initial assessment of sensor applicability in solid PEI resins, the two stilbene dyes were found to have a higher chance of successful applicability. Due to the farther apart maxima of non-activated and activated sensor in fluorescence spectroscopy compared to UV/Vis spectroscopy, a differentiation of both forms was facilitated in fluorescence investigations.

Only **Stil-3** showed absorption maxima which were far enough apart to enable a possible detection by UV/Vis spectroscopy. The extension of the conjugated system in **Stil-4**, on the one hand led to a worsening of the resolution by shifting the absorption maximum of the activated form from 366 nm up to 400 nm and thus closer to the virgin absorption maximum at 442 nm. On the other hand, the longer conjugated system increased the absorption intensity of the hemiacetal and thus potentially allowed an enhanced detection of the hemiacetal form. Preliminary experiments of the cured PEI resins for the estimation of their optical properties showed strong self-absorption, which would lead to interference with the dye signals and a test specimen of **PEI-1** with **Azo-3** showed that a differentiation of the sensor and the resin absorption was not possible (**Figure A50**). The interference of the sensor molecules with the intrinsic resin fluorescence was significantly lower. All solid state investigations will be discussed in detail in part 3.5.

Thus both, better resolution and less interference with the resin matrix, made fluorescence spectroscopy the method of choice for monitoring polymer degradation. Further, **Azo-3** can be regarded as less suitable due to its non-fluorescent properties.

3.4. Full characterization of Stil-3 and Stil-4 in solution

The two dyes **Stil-3** and **Stil-4** proved to be more suitable and thus were investigated in detail regarding their properties in solution and their reactivity towards different analytes.

51

3.4.1. Density functional studies of Stil-3 and Stil-4

Density functional studies (DFT) were carried out to analyze the structural and electronic properties of **Stil-3** and **Stil-4**. First, the optimized geometric structures of the trifluoroacetyl and hemiacetal form of **Stil-3** and **Stil-4** were simulated using Gaussian 09 at B3LYP/6-31G** level of theory. The results are shown in **Figure 39**.
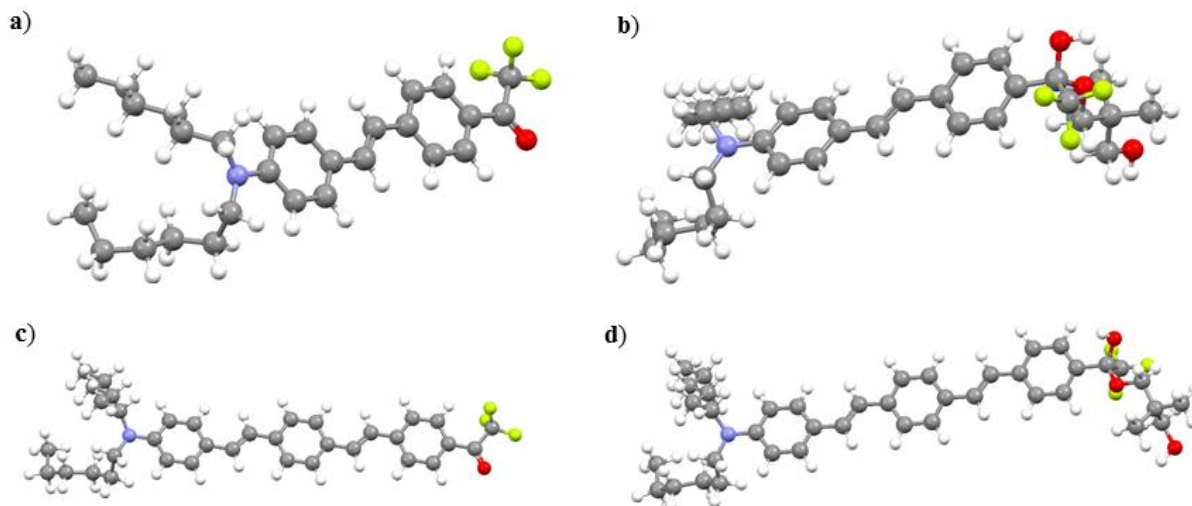
Figure 39 Optimized geometric structures of a) the trifluoroacetyl and b) the hemiacetal form of **Stil-3** and of c) the trifluoroacetyl and d) the hemiacetal form of **Stil-4** calculated by DFT studies.

All molecules showed a planar conformation with respect to each other phenyl rings and the dihedral angle between the phenyl rings was 2.37°. It was not possible to simulate a *cis*-form of either **Stil-3** or **Stil-4** in the trifluoroacetyl or in the hemiacetal form and thus all four molecules were assumed to occur only in their *trans*-form.

The simulated optimized geometric structures were used to calculate the electron density distribution of the HOMO and LUMO of the trifluoroacetyl and hemiacetal form of **Stil-3** and **Stil-4** by the DFT/B3LYP method and the obtained energy level diagram is shown in **Figure 40a**. The HOMO orbitals of both sensor molecules were delocalized over the phenyl rings and the LUMO orbitals were delocalized over the trifluoroacetyl and phenyl groups. Thus a partial electron density transfer from the phenyl groups from the HOMO to the trifluoroacetyl group in the LUMO was assumed. This charge transfer was stronger in the trifluoroacetyl forms of **Stil-3** and **Stil-4** compared with their corresponding hemiacetal forms and thus suggested intramolecular charge transfer for the virgin sensor molecules. The simulations demonstrated an especially strong intramolecular charge transfer (ICT) for **Stil-4** due to its longer conjugated system as shown in **Figure 40b**.

The results of the simulations were in accordance with the experimental results discussed in the previous part. For both dyes the energy gap between HOMO and LUMO increased after the hemiacetal formation, which consequently led to a blue shift as observed during sensor activation. The calculated difference of the energy gap between the trifluoroacetyl and the hemiacetal form of **Stil-3** was 0.66 eV and thus bigger than for **Stil-4** with 0.48 eV. Consequently, the absorbance and emission maximum of **Stil-3** were stronger blue shifted to λ_{abs} = 366 nm and λ_{em} = 430 nm compared to **Stil-4** with λ_{abs} = 400 nm and λ_{em} = 496 nm. Furthermore, the slow activation of the reference sample of **Stil-4** without addition of NPG was

assumed to not only result from diol formation but additionally from the strong intramolecular charge transfer, which only was found in simulations of the trifluoroacetyl form.
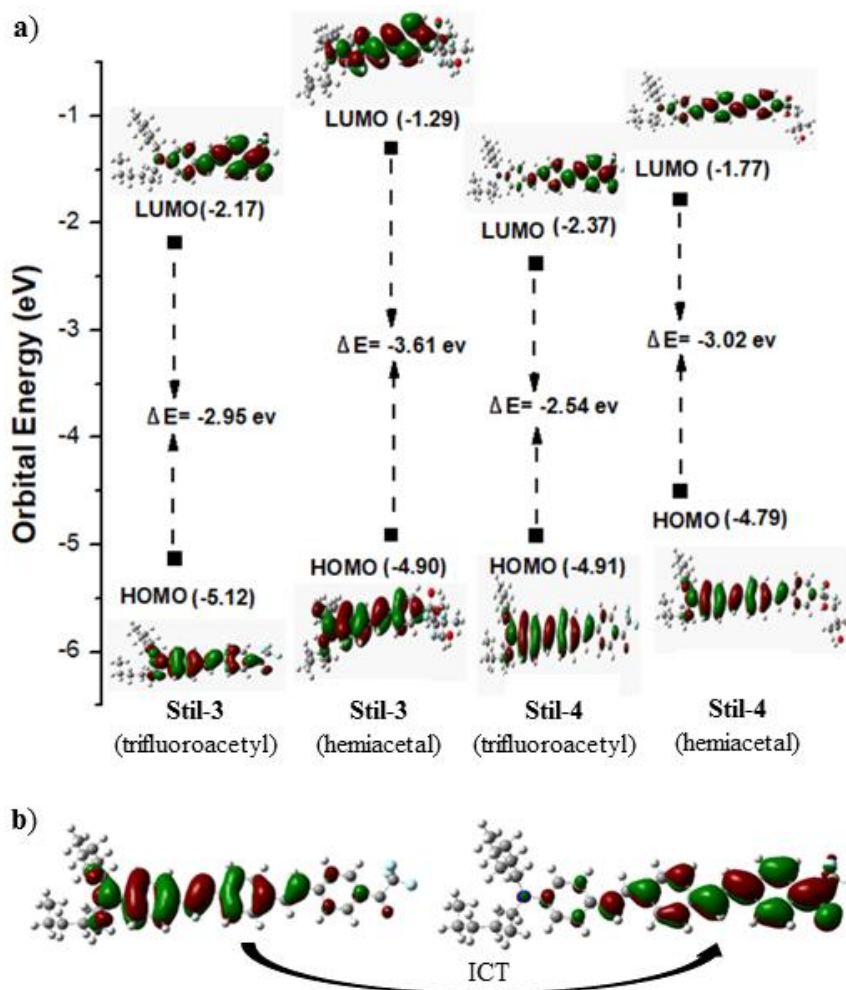

Figure 40 a) Energy level diagram of the molecular orbitals of **Stil-3** and **Stil-4** in their trifluoroacetyl and hemiacetal form calculated with the DFT/B3LYP method and b) the intramolecular charge transfer from the phenyl rings into the trifluoroacetyl group in **Stil-4**.

In the next step, the results were used to simulate the UV/Vis spectra of **Stil-3** and **Stil-4** with the CAM-B3LYP and the B3LYP model. The simulated spectra are shown in **Figure 41** together with experimental spectra for comparison. For all cases the experimental absorption maxima were found to lie between both absorption maxima calculated with the different models. However, while for the trifluoroacetyl form of **Stil-3** (**Figure 41a**) and the hemiacetal form of **Stil-4** (**Figure 41d**) experimental and simulated UV/Vis spectra were of similar shape, for activated **Stil-3** (**Figure 41b**) and virgin **Stil-4** (**Figure 41c**) the spectra showed significant differences. In case of the activated **Stil-3** this was explained by the incomplete conversion into the hemiacetal, which consequently resulted in the remaining absorption maximum at 440 nm of non-activated **Stil-3** in the experimental spectrum. For the simulation of the virgin **Stil-4**, the strong intramolecular charge transfer from the phenyl rings to the trifluoroacetyl group led to deviations for the B3LYP model.

It should be noted that experimental spectra were recorded in 1,4-dioxane while the simulations were done in THF. Due to the similar polarity of the solvents ($E_T(30)_{1,4\text{-dioxane}} = 36.0$ kcal/mol[267] and $E_T(30)_{THF} = 37.4$ kcal/mol[267]) the solvent influence was negligible as demonstrated by the

UV/Vis spectra in **Figure A51**. The approximation of the simulated spectra to the experimental spectra could have been sophisticated by increasing the calculation steps, but due to the additional time effort and the low benefit, this was not done.
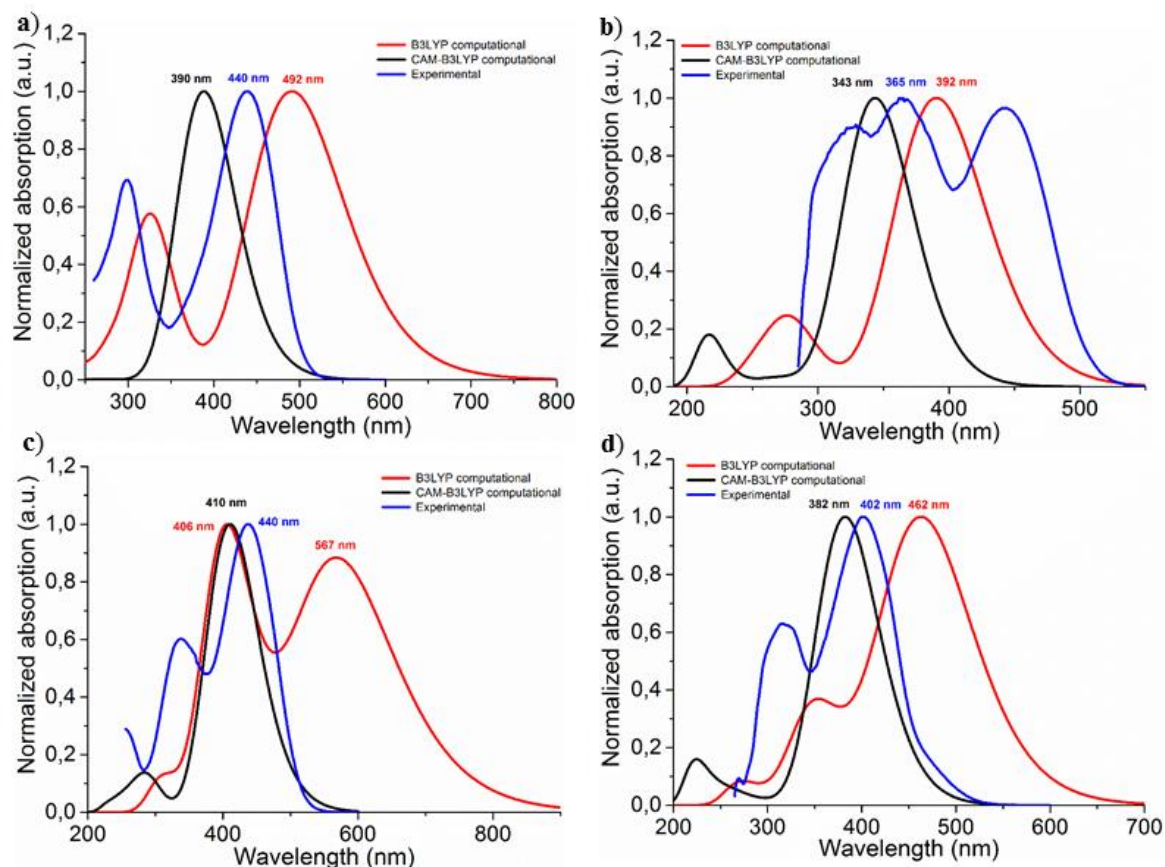

Figure 41 Experimental and simulated spectra of a) the non-activated and the b) activated **Stil-3** together with c) the non-activated and the d) activated **Stil-4**. Experimental spectra were recorded in 1,4-dioxane and simulations were done using TD-DFT at B3LP and CAM-B3LYP levels in THF.

3.4.2. Concentration series of Stil-3 and Stil-4

For further activation experiments in solution it was necessary to determine the linear range of UV/Vis absorption and fluorescence to avoid measuring errors due to exceeding the concentration limit of **Stil-3** and **Stil-4**. The concentration plots are shown in **Figure 42** and all corresponding spectra are shown in **Figure A52**. Linear absorption of **Stil-3** was found for concentrations up to 0.08 µmol/mL and for **Stil-4** for concentrations up to 0.06 µmol/mL. **Stil-3** showed linear fluorescence behavior up to 0.008 µmol/mL and **Stil-4** for concentrations up to 0.0075 µmol/mL. With regard to the later application as sensor molecule within a PEI coating in an electric motor, fluorescence spectroscopy proved to be advantageous since the required sensor amounts were significantly lower, thus having lower production costs.
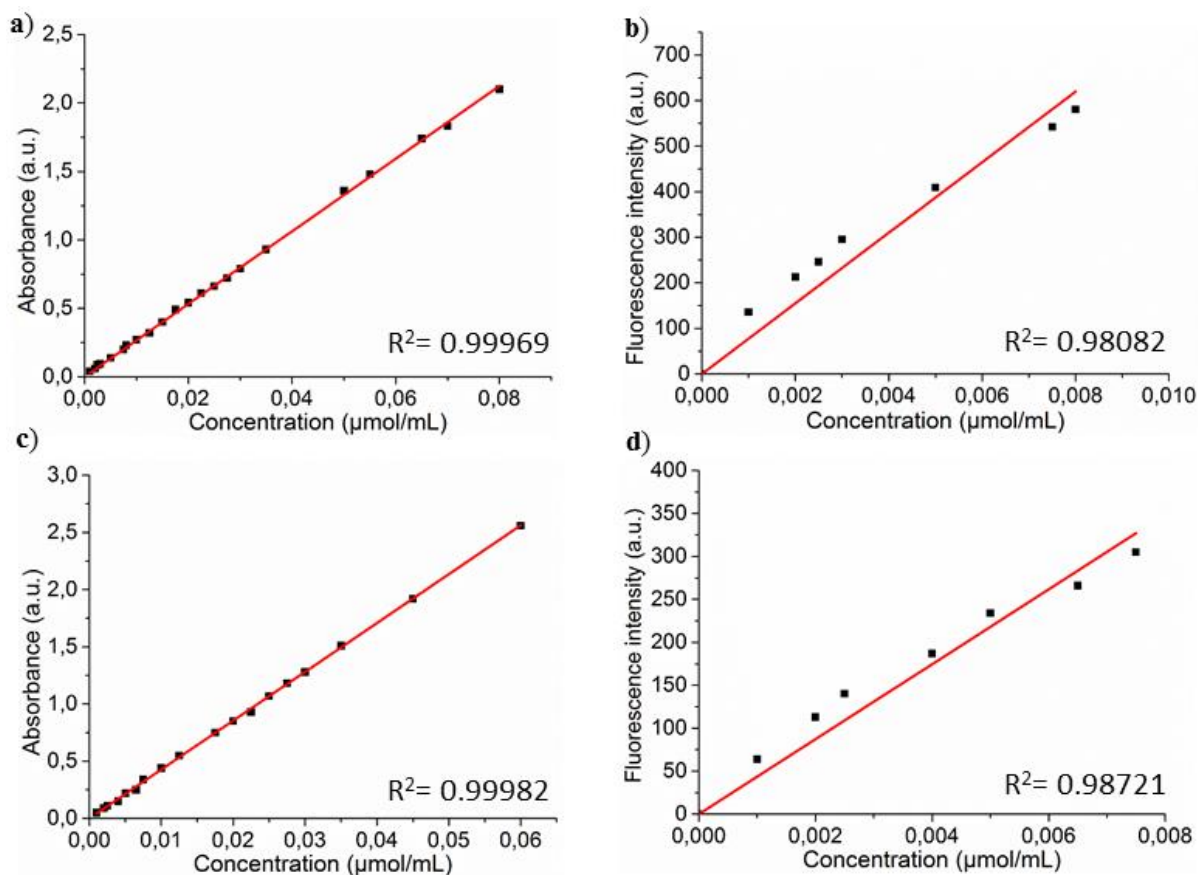
Figure 42 Linear plots of the concentrations series from the a) UV/Vis and b) fluorescence spectra of **Stil-3** and from the c) UV/Vis and d) fluorescence spectra of **Stil-4** recorded in dioxane.

3.4.3. Sensor activation of Stil-3 and Stil-4 with different analytes

In part 3.3.3. the activation of **Stil-3** and **Stil-4** by NPG, the later main analyte, was already proven. The next step was to investigate the influence of the analyte structure and the analyte concentration towards the kinetics of the sensor activation. Additionally, the sensor was stored in solution to get indications of its long-term suitability.

The activation of **Stil-3** was evaluated by exposition to *n*-butylamine (*n*-BuA), 1,4-butanediol (1,4-BuOH), methanol, NPG, 1-butanol (1-BuOH), *tert*-butanol (*t*-BuOH) and Imidol 6. Sensor activation was monitored by the emission decrease of the virgin form and the corresponding plots are shown in **Figure 43**. Selected emission spectra are shown in **Figure A53**.

n-BuA, 1,4-BuOH and MeOH triggered a sensor activation within minutes (**Figure 43a**) while NPG, 1-BuOH, *t*-BuOH and Imidol 6 only showed emission changes after several days of analyte exposition (**Figure 43b**). The fastest activation of **Stil-3** was achieved by *n*-BuA which accomplished maximum activation after 50 minutes. With a concentration of 8.4 nmol/mL, the amount of analyte was significantly lower compared to the concentrations used for alcoholic analytes which were 0.5 mmol/mL and 1 mmol/mL. When a *n*-BuA concentration of 16.8 nmol/mL was used, maximum conversion was also reached after 50 minutes but the initial activation kinetics were accelerated and higher conversions were achieved. Also for MeOH and 1,4-BuOH a fast activation was observed within the first 50 minutes, but the maximum conversion was reached only after approximately 14 days (see insert **Figure 43a**). Again, for higher concentrations higher conversions were achieved.
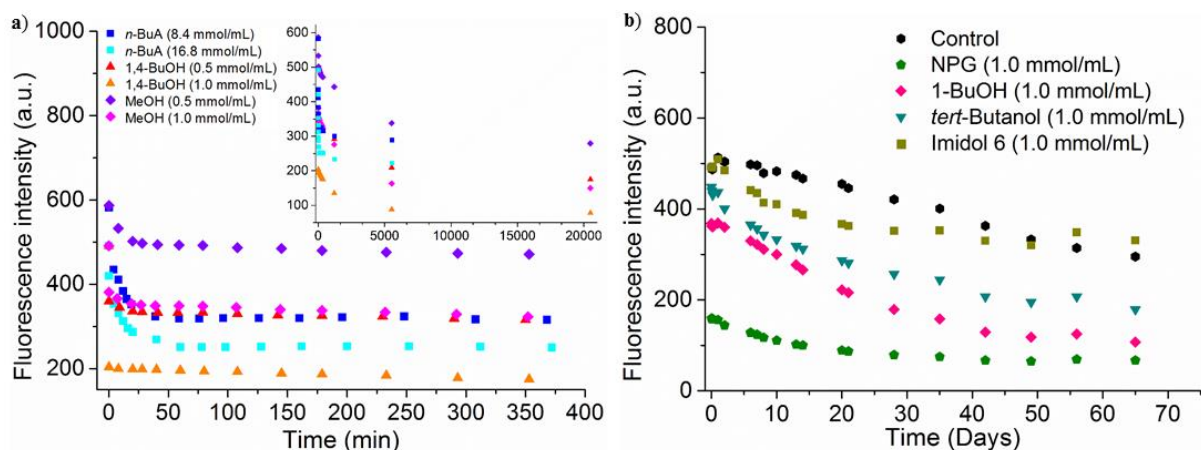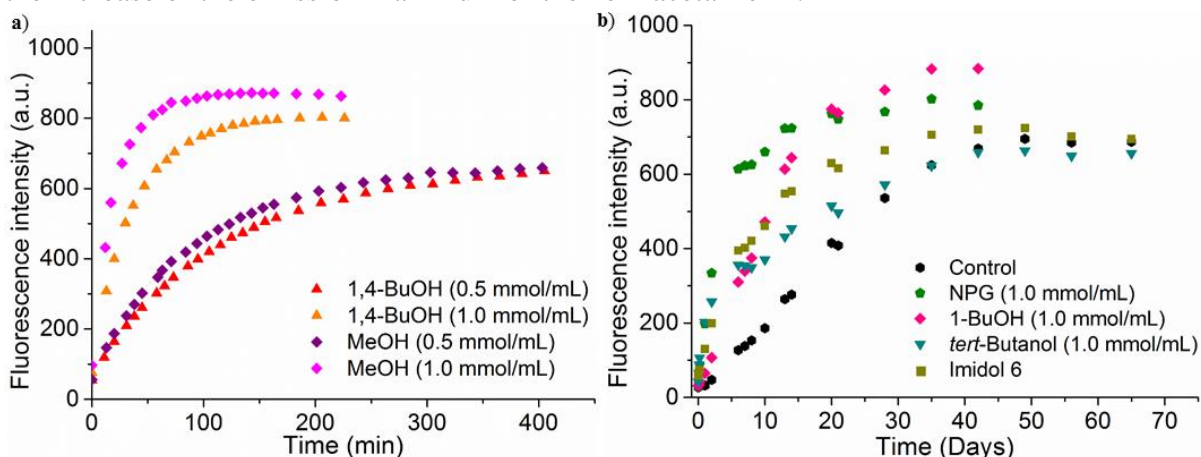
Figure 43 Sensor activation of **Stil-3** by a) fast activating analytes *n*-butylamine, 1,4-butanediol and methanol in different concentrations (long timescale in insert) and by b) slow activating analytes neopentyl glycol, 1-butanol, *tert*-butanol and Imidol 6 in dioxane ($c_{\text{Stil-3}}$ = 7.5 µmol/L, λ_{ex} = 442 nm).

The activation by the other analytes was significantly slower and maximum conversion was reached after 42 days for NPG, after 49 days for 1-BuOH and Imidol 6 and after 65 days for *t*-BuOH. The slow emission decrease of **Stil-3** in dioxane without addition of analyte in the control experiment was attributed to diol formation and the intramolecular charge transfer exclusively observed for the trifluoroacetyl form in DFT simulations.

The same experiments were conducted for **Stil-4** and the results are summarized in **Figure 44**. Selected emission spectra are shown in **Figure A54**. The sensor activation was monitored by the increase of the emission maximum of the hemiacetal form.

Figure 44 Sensor activation of **Stil-4** by a) fast activating analytes 1,4-butanediol and methanol in different concentrations and by b) slow activating analytes neopentyl glycol, 1-butanol, *tert*-butanol and Imidol 6 in dioxane ($c_{\text{Stil-4}}$ = 7.5 µmol/L, λ_{ex} = 406 nm).

Due to the fast activation of **Stil-4**, for *n*-BuA a kinetic profile could not be determined since even concentrations of 8.4 mmol/mL led to a maximum conversion within seconds. The alcoholic analytes showed faster kinetics compared to **Stil-3**. 1,4-BuOH and MeOH triggered the fastest activation and maximum conversion was achieved after 85 min and 150 min for 1 mmol/mL analyte concentrations and after 400 min for 0.5 mmol/mL analyte concentrations. For higher analyte concentrations the maximum sensor conversion was found to be higher. For NPG the maximum conversion was reached after 35 days, for 1-BuOH and Imidol 6 after

42 days and for *t*-BuOH after 49 days. Emission changes were observed for the control experiment without analyte, which were stronger compared to **Stil-3**. This observation was explained by the faster diol formation and by the strong intramolecular charge transfer of the trifluoroacetyl form of **Stil-4**.

The analyte structure, in particular functionality and steric hinderance, was found to have a major influence on sensor activation. For both sensor molecules *n*-BuA showed the fastest activation due to its higher nucleophilicity compared with alcohols. Because of its bifunctionality, 1,4-BuOH triggered a faster activation than MeOH, because same analyte concentrations provided a double amount of hydroxyl groups. For the same reason NPG triggered a faster activation than 1-BuOH, followed by Imidol 6 and *t*-BuOH, which had the highest steric demand of all analytes. Towards all analytes **Stil-4** showed the faster activation kinetics compared with **Stil-3**. However, in solution experiments both sensor molecules were proved to be suitable for further investigations regarding their applicability in solid PEI resins.

3.5. Sensor detection in solid state

The PEI resins are a complex matrix with intrinsic optical properties, showing UV/Vis absorption and fluorescence. Thus, interference with the sensor molecules is expected and before **Stil-3** and **Stil-4** were embedded in their actual PEI matrix, their suitability was tested in the poly(styrene-*co*-divinylbenzene) (**PS/DVB**) model resin.

3.5.1. Sensor testing in PS/DVB
3.5.1.1. Synthesis of PS/DVB and sensor embedding

PEIs were cured with styrene as comonomer and thus **PS/DVB** with closely similar structure has served as model resin without the presence of fluorescent groups. Specimen preparation was done by curing styrene with 4 mol% of divinylbenze and 1 mol% of 2,2'-azobis(2-methylpropionitrile) (AIBN) in a teflon mould at 78 °C for 3 hours. Sensor embedding was done by dissolving the dye in the reaction mixture before filling the teflon moulds. The experimental procedure together with the characterization is given in the Experimental part 4.4.

Thermal sensor stability was demonstrated by differential scanning calorimetry (DSC) (**Figure A55**) and by UV/Vis and fluorescence spectroscopy of dye samples which previously were exposed to thermal load (**Figure A56**).

Stil-3 showed a strong emission at 540 nm and the emission maximum of **Stil-4** was detected at 560 nm (**Figure 45**). Compared with the solution experiments both fluorescence maxima shifted to smaller wavelengths whereas the shift of **Stil-4** was stronger and despite its longer conjugated system its emission maximum in **PS/DVB** was observed close to the emission maximum of **Stil-3**. A reference sample without dye was non-fluorescent and thus fluorescence spectroscopy allowed interference-free sensor detection. However, **PS/DVB** showed strong absorption at wavelengths below 400 nm (**Figure A57**), therefore optical investigations were focused on fluorescence spectroscopy. Consequently, sensor activation in **PS/DVB** was used as proof of concept for activation and detection of **Stil-3** and **Stil-4** in solid state.
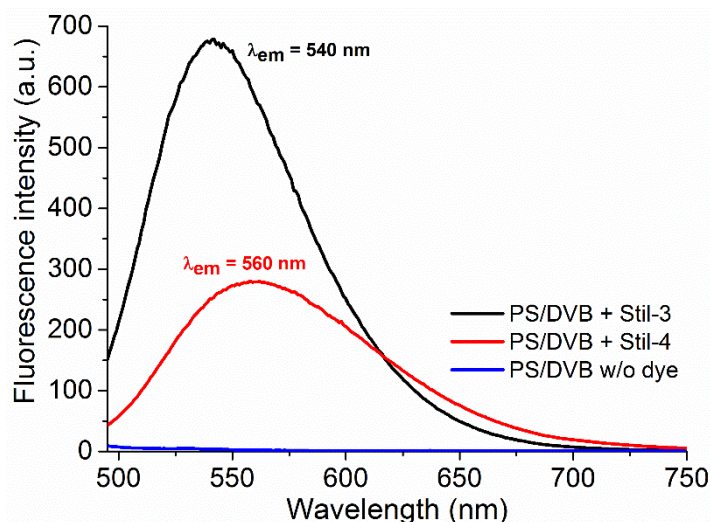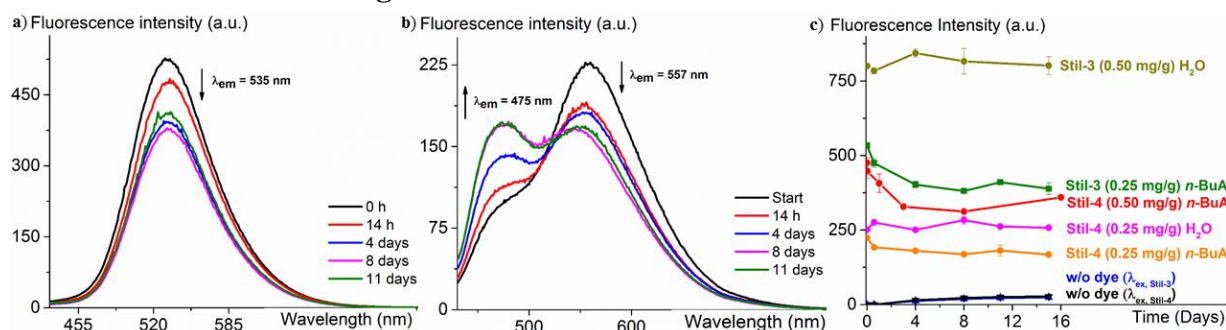
Figure 45 Emission spectra of **Stil-3** ($c = 0.50$ mg/g resin, $\lambda_{ex} = 414$ nm) and **Stil-4** ($c = 0.25$ mg/g resin, $\lambda_{ex} = 409$ nm) embedded within **PS/DVB** and emission spectrum of **PS/DVB** ($\lambda_{ex} = 414$ nm) without dye.

3.5.1.2. Sensor activation in PS/DVB

Due to hindered analyte diffusion, sensor activation was assumed to be slow in solid state compared to previous solution experiments. Therefore, *n*-BuA was used as analyte because it showed the fastest activation in solution experiments and thus was expected to trigger sensor activation in reasonable timescales. Specimens containing **Stil-3** and **Stil-4** were stored in aqueous *n*-BuA solution and their fluorescence properties were measured frequently. The results are summarized in **Figure 46**.

Figure 46 Emission spectra of a) **Stil-3** ($c = 0.25$ mg/g resin, $\lambda_{ex} = 414$ nm) and b) **Stil-4** ($c = 0.25$ mg/g resin, $\lambda_{ex} = 409$ nm) embedded within **PS/DVB** and exposed to *n*-BuA solution (1.5 mmol/mL) and c) plot of the fluorescence intensities *vs*. time together with corresponding control experiments.

The emission maximum at 535 nm of the trifluoroacetyl form of **Stil-3** decreased by 27 % when a concentration of $c = 0.25$ mg/g resin was used (**Figure 46c**). For a specimen with **Stil-4** at a concentration of $c = 0.50$ mg/g resin, the decrease of the emission maximum at 557 nm by 24 % was accompanied by the appearance of a second emission maximum of the corresponding, highly fluorescent hemiaminal form at 475 nm.

As observed in solution experiments, the activation of **Stil-4** was faster compared to **Stil-3**. Maximum conversion was reached after 3 days for **Stil-4** and after 8 days for **Stil-3**, thus being significantly slower compared to sensor activation in solution. To exclude matrix / solvent interactions, reference specimens without dye were stored in *n*-BuA solution and excitation at

the excitation maximum of **Stil-3** and **Stil-4** showed only negligible changes in the emission intensity. Furthermore **PS/DVB** specimens which contained either **Stil-3** or **Stil-4** were stored in water and the overall changes in fluorescence spectroscopy were only -1 % and 2 %, thus significantly smaller. Therefore, the fluorescence changes in the actual specimen were attributed to the sensor activation. However, the extent of activation was slower compared to solution experiments, which can be explained by the poor water diffusion in **PS/DVB**[268]. This consequently led to predominant sensor activation at the surface of the specimen while the sensor molecules in bulk were not accessible for the analyte.

3.5.2. Sensor testing in PEI-1
3.5.2.1. Curing of PEI-1 and sensor embedding

The preparation of **PEI-1** specimen required the mixing of two components **PEI-1A** and **PEI-1B** in a 50/50 (w%) ratio and the reaction mixture was subsequently cured at 80 °C for 50 min, followed by 5 min at 140 °C in a teflon mould. Sensor embedding was done by dissolving either **Stil-3** or **Stil-4** in the reaction mixture before it was transferred into the teflon mould. The experimental procedure together with the characterization is given in the Experimental part 4.4. The linear emission concentration of **Stil-3** and **Stil-4** was determined up to 1 mg dye/g resin, which consequently was used to have the largest possible sensor quantity available. The results are presented in **Figure A58** together with the concentrations series measured with the spectro2guide, a handheld device which should server as inline detection device during application.
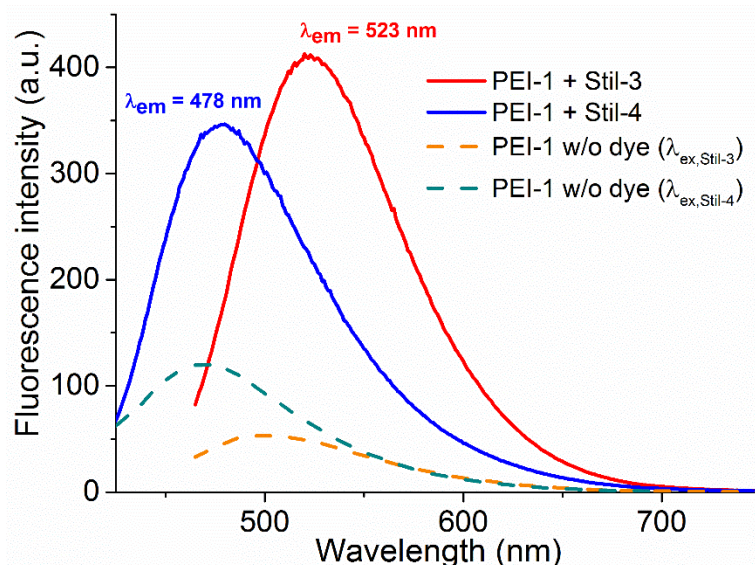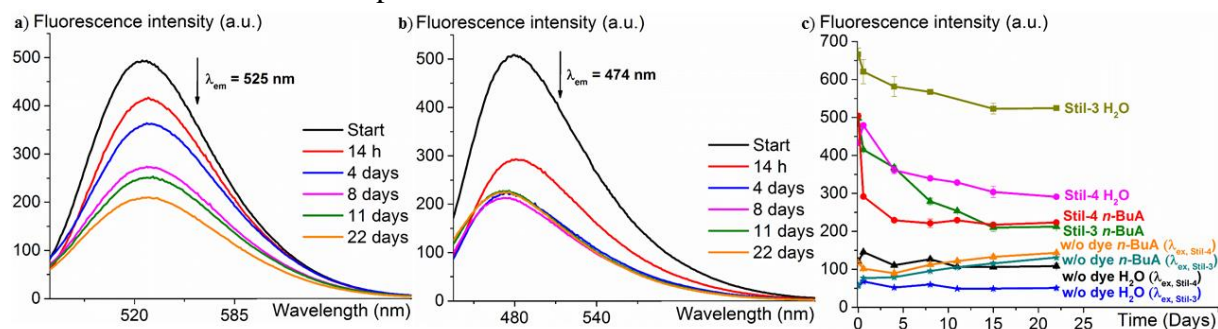

Figure 47 Emission spectra of **Stil-3** (c = 1 mg/g resin, λ_{ex} = 447 nm) and **Stil-4** (c = 1 mg/g resin, λ_{ex} = 410 nm) embedded within **PEI-1** and emission spectrum of **PEI-1** ($\lambda_{ex,Stil-3}$ = 447 nm, $\lambda_{ex,Stil-4}$ = 410 nm) without dye.

The emission maximum of **Stil-3** was found at 523 nm (**Figure 47**), thus slightly shifted to smaller wavelength compared with **PS/DVB**. The emission maximum of **Stil-4** was again significantly shifted to smaller wavelength at 478 nm. This strong effect was attributed to molecular interactions of the long conjugated system with the aromatic structures of the resin matrix and further investigations are described in chapter 3.5.4. **Figure 47** also displays the intrinsic fluorescence of **PEI-1** after the excitation at the excitation maxima of **Stil-3** and **Stil-4**.

Because the emission maximum of **PEI-1** was close to the emission maximum of **Stil-4** in **PEI-1** (compare with **Figure A59**), an interference was likely whereas the interference with **Stil-3** was significantly lower and thus allowed better sensor detection. Nevertheless, fluorescence spectroscopy proved to be the more suitable detection method compared to UV/Vis spectroscopy (**Figure A60**).

3.5.2.2. Sensor activation in PEI-1 by *n*-BuA

To investigate sensor activation in **PEI-1**, the specimens were stored in an aqueous *n*-BuA solution which triggered the hemiaminal formation in reasonable time. Sensor activation was followed by fluorescence spectroscopy and the results are summarized in **Figure 48**. Both sensors showed a decrease of 56 % for the virgin emission maxima located at 525 nm for **Stil-3** and at 474 nm for **Stil-4**. Again, **Stil-4** reached its maximum conversion after 4 days and thus faster than **Stil-3** which took 15 days. For **PEI-1** the appearance of a second emission maximum of the corresponding hemiaminal form was not observed, which is attributed to the interference with the intrinsic resin absorption and fluorescence in the area concerned.

Figure 48 Emission spectra of a) **Stil-3** (c = 1 mg/g resin, λ_{ex} = 447 nm) and b) **Stil-4** (c = 1 mg/g resin, λ_{ex} = 410 nm) embedded within **PEI-1** and exposed to *n*-BuA solution (1.5 mmol/mL) and c) plot of the fluorescence intensities *vs*. time together with corresponding control experiments.

In control experiments, for both dyes a slow reaction with water was observed which led to the diol formation and thus to a decrease of the emission intensity of 21 % for **Stil-3** and of 23 % for **Stil-4**. This assumption was proven by the reference samples without dye, because they did not show a decrease of their intrinsic emission intensity. The reason for the enhanced diol formation, which was not observed for **PS/DVB**, is the better diffusion of water within **PEI-1**[269]. Because of the better diffusion, sensor molecules within the bulk material were better accessible and thus in **PEI-1** higher sensor conversions were achieved than in **PS/DVB**. An exposition of **PEI-1** specimen without dye to *n*-BuA solution only led to a slight increase of the intrinsic fluorescence.

Therefore, activation of **Stil-3** and **Stil-4** embedded in **PEI-1** was successfully demonstrated by using the highly nucleophilic *n*-BuA analyte. However, it should be noted that the occurrence of water in the later application of PEI coated devices is unlikely and diol formation will play a subordinated role. Furthermore, specimen with **Stil-3** and **Stil-4** maintained their fluorescence intensities when they were stored under ambient conditions, thus intramolecular charge transfer was not observed in solid state.

3.5.2.3. Sensor activation in PEI-1 by neopentyl glycol

In a next step, the reactivity towards the later main analyte NPG was tested. As sensor activation was expected to be slow when triggered by NPG release during thermal degradation, first specimens of **PEI-1** with **Stil-3** and **Stil-4** were exposed to a gaseous NPG atmosphere. Specimens were attached in the inner part of the lid of a petri dish and the lower part was covered with NPG. The petri dish was placed in a sand bath at 180 °C and consequently the NPG evaporated while the thermal load on **PEI-1** was reduced due to the distance from the sand bath. The procedure prevented the thermal aging of **PEI-1** which would have distorted sensor detection. Due to the high analyte excess, sensor reaction was observed on reasonable timescales.

The results for the measurements of **PEI-1** with **Stil-3** are shown in **Figure 49**. The emission maximum at 525 nm decreased by 26 % in the cause of 30 days. In a control experiment a similarly treated specimen of **PEI-1** without dye showed a minor emission increase. A second control experiment of **PEI-1** with **Stil-3** in the absence of NPG, showed only a minor decrease of fluorescence by 4 % and proved the thermal stability of the sensor molecule. Thus the successful activation and detection of **Stil-3** within **PEI-1** was demonstrated. Results of the corresponding experiments for **Stil-4** are presented in **Figure 50**.
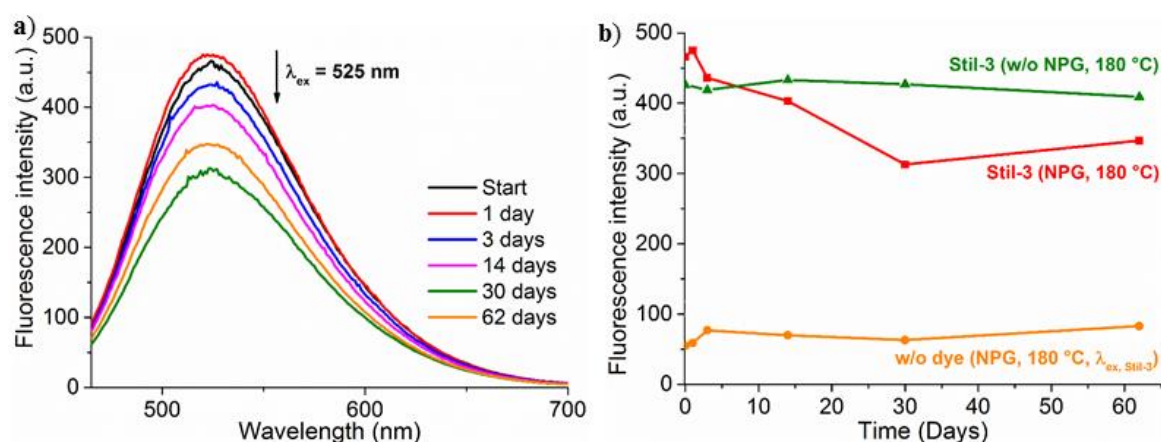
Figure 49 Emission spectra of a) **Stil-3** (c = 1 mg/g resin, λ_{ex} = 447 nm) embedded within **PEI-1** exposed to gaseous neopentyl glycol atmosphere and b) plot of the fluorescence intensities *vs.* time together with corresponding control experiments.
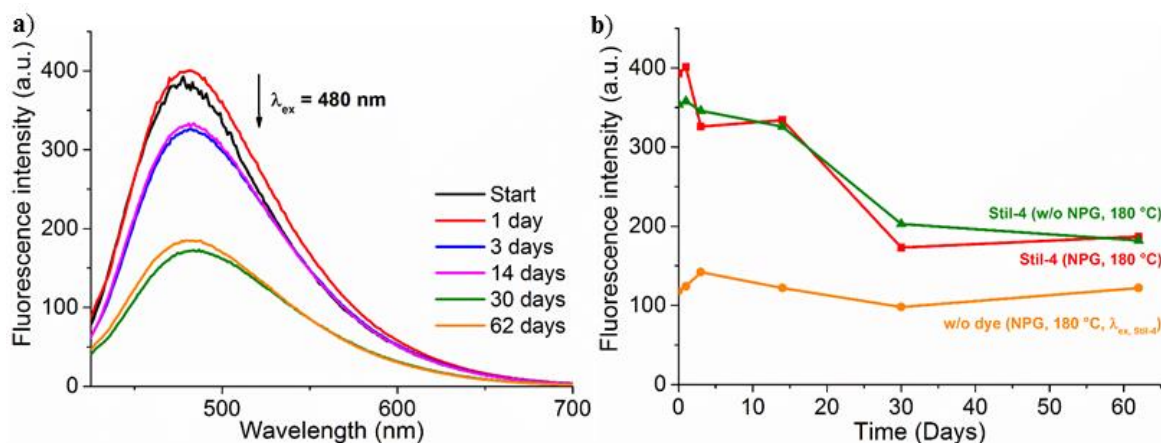

Figure 50 Emission spectra of a) **Stil-4** (c = 1 mg/g resin, λ_{ex} = 410 nm) embedded within **PEI-1** exposed to gaseous neopentyl glycol atmosphere and b) plot of the fluorescence intensities *vs.* time together with corresponding control experiments.

A fast initial emission decrease for the emission maximum at 480 nm was observed. However, also the control experiment with **PEI-1** that contained **Stil-4** and which was not exposed to an excess of NPG showed the same tendencies. A decomposition of **Stil-4** is unlikely as it exhibits higher thermal stability compared to **Stil-3**. Thus it was concluded that the thermal load was high enough to partially trigger resin decomposition, which consequently led to the activation of the highly sensitive **Stil-4** sensor by released alcoholic degradation products.

3.5.2.4. Sensor activation in PEI-1 by thermal degradation

In the last step, in-situ sensor activation of **Stil-3** and **Stil-4** in **PEI-1** was done by generating the alcoholic analytes, in particular NPG, through thermal degradation of the resin matrix. Polymer degradation was triggered by storing the specimen in a sand bath heated at 180 °C.

The activation of **Stil-3** was monitored by fluorescence spectroscopy and the results are summarized in **Figure 51**. The emission maximum at 525 nm was constantly decreasing, but compared to previous conducted experiments, the sensor activation was slow and still not completed after 80 days at 180 °C. Especially within the first 30 days, an emission decrease of 27 % was observed which was in accordance with the results from the degradation experiments in part 3.1. **PEI-1** showed a fast mass loss within the first 20 days (**Figure 25**), which was predominantly caused by the release of NPG and Imidol 6 and thus provided large amounts of alcoholic analytes, which consequently triggered the activation of **Stil-3**.

For similarly treated control specimen of **PEI-1** without dye, only a slight increase of the fluorescence intensity was observed when the control specimen was exited at the excitation maximum of **Stil-3**. Therefore, the in-situ activation and detection of **Stil-3** in **PEI-1** was demonstrated.
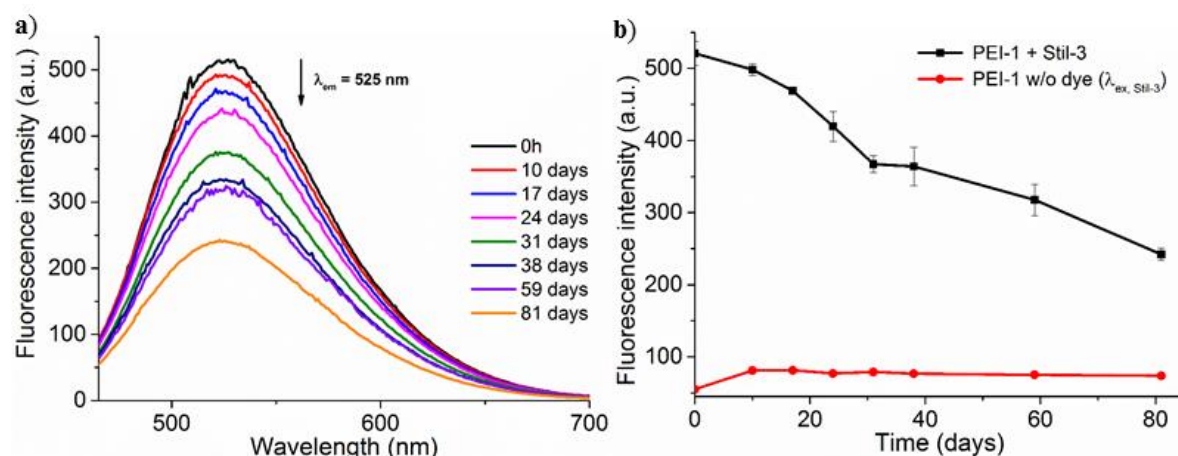

Figure 51 Emission spectra of a) **Stil-3** (c = 1 mg/g resin, λ_{ex} = 447 nm) embedded within **PEI-1** and thermally aged at 180 °C and b) plot of the fluorescence intensities *vs*. time together with the corresponding control experiment.

The results for the thermal activation of **Stil-4** in **PEI-1** are presented in **Figure 52**. A strong decrease by 56 % of the emission maximum at 482 nm within the first 20 days was observed. As already mentioned, this was in accordance with the results from the thermal degradation investigations. Again, **Stil-4** showed significantly faster activation kinetics compared to **Stil-3** and a maximum conversion was almost reached after 80 days. For similarly treated control specimen of **PEI-1** without dye, only a slight increase of the fluorescence intensity was

observed when exited at the excitation maximum of **Stil-4**. Therefore, the in-situ activation and detection of **Stil-4** in **PEI-1** was demonstrated.

Furthermore, thermal activation experiments of **Stil-3** and **Stil-4** embedded within **PEI-1** were accompanied by measurements with the spectro2guide and the results are shown in **Figure A61**.
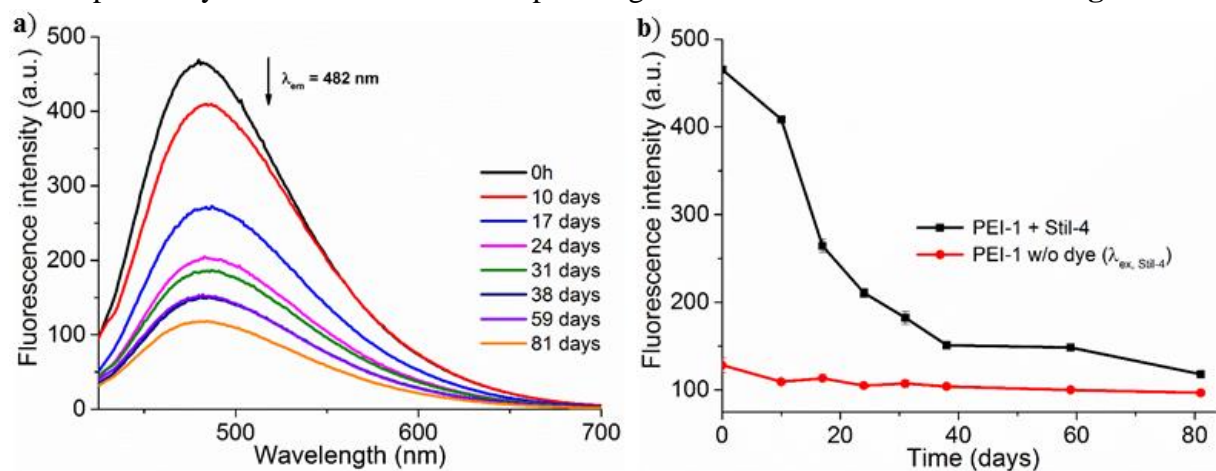

Figure 52 Emission spectra of a) **Stil-4** (c = 1 mg/g resin, λ_{ex} = 410 nm) embedded within **PEI-1** and thermally aged at 180 °C and b) plot of the fluorescence intensities *vs.* time together with the corresponding control experiment.

3.5.3. Sensor testing in PEI-2
3.5.3.1. Curing of PEI-2 and sensor embedding

The single-component system, **PEI-2A** was directly transferred in teflon moulds and curing was done at 150 °C for 3 hours which yielded **PEI-2** specimen. Sensor embedding was done by either dissolving **Stil-3** or **Stil-4** in **PEI-2A** before it was transferred into the teflon mould. The experimental procedure together with the characterization is given in the Experimental part 4.4. The linear emission concentration of **Stil-3** and **Stil-4** was determined up to 0.25 mg dye/g resin, which consequently was used to have the largest possible sensor quantity available and the results are presented in **Figure A62**.
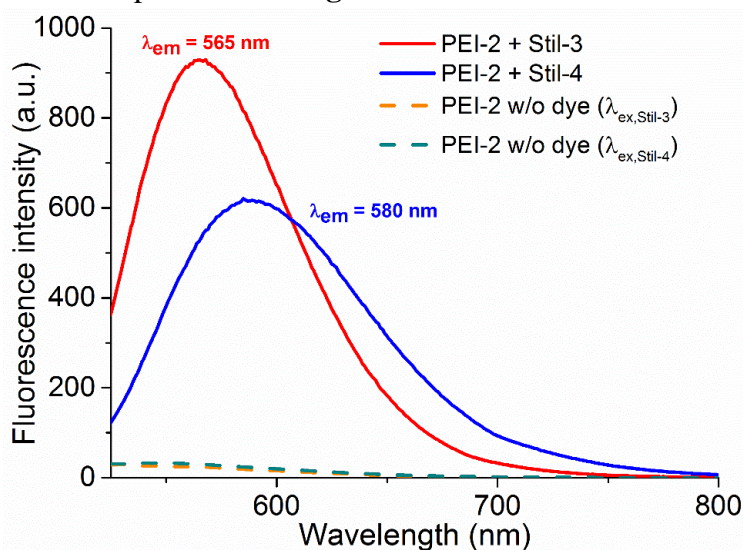
Figure 53 Emission spectra of **Stil-3** (c = 0.25 mg/g resin, λ_{ex} = 510 nm) and **Stil-4** (c = 0.25 mg/g resin, λ_{ex} = 500 nm) embedded within **PEI-2** and emission spectrum of **PEI-2** ($\lambda_{ex,Stil-3}$ = 510 nm, $\lambda_{ex,Stil-4}$ = 500 nm) without dye.

The emission maximum of **Stil-3** was found at 565 nm (**Figure 53**), thus it is slightly shifted to longer wavelengths compared to **PEI-1**. The emission maximum of **Stil-4** again was significantly shifted to a longer wavelength at 580 nm, and again was stronger affected by the different matrix compared to **Stil-3**. **Figure 53** also displays the intrinsic fluorescence of **PEI-2** after the excitation at the excitation maxima of **Stil-3** and **Stil-4**. Because the emission maxima of both sensor molecules were shifted to longer wavelengths, almost no fluorescence interferences with **PEI-2** were observed although it is showing a stronger intrinsic fluorescence than **PEI-1** (compare with **Figure A63**).

3.5.3.2. Sensor activation in PEI-2 by *n*-BuA

To investigate sensor activation in **PEI-2**, the specimens were stored in an aqueous *n*-BuA solution which triggered the hemiaminal formation in reasonable time. Sensor activation was followed by fluorescence spectroscopy and the results for **Stil-3** are summarized in **Figure 54**. **Stil-3** showed a decrease of the virgin emission intensity by 17 % within 14 days when excited at 510 nm. The same conversion was observed for a control experiment in which **Stil-3** was embedded within **PEI-2** and subsequently stored in water. However, diol formation was slow and took 63 days. During the decrease of the virgin emission intensity, a second emission maximum emerged at 460 nm. As this was not observed in control experiments, this was attributed to the emission of the hemiaminal form. It should be noted that before the emission maximum of the hemiaminal form increased, within the first day an initial decrease was observed. This was also detected for the control experiment of a **PEI-2** in *n*-BuA, which in turn did not further increased afterwards but nevertheless interferes with the detection of the hemiaminal form.

This observation together with the strong intrinsic fluorescence of **PEI-2** when excited at the excitation maximum of the hemiaminal form, confirmed the monitoring of the trifluoroacetyl as the more reliable detection method.
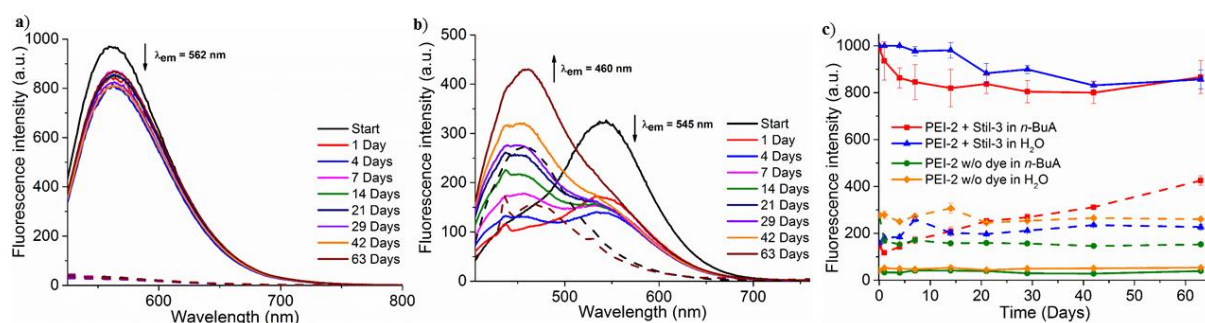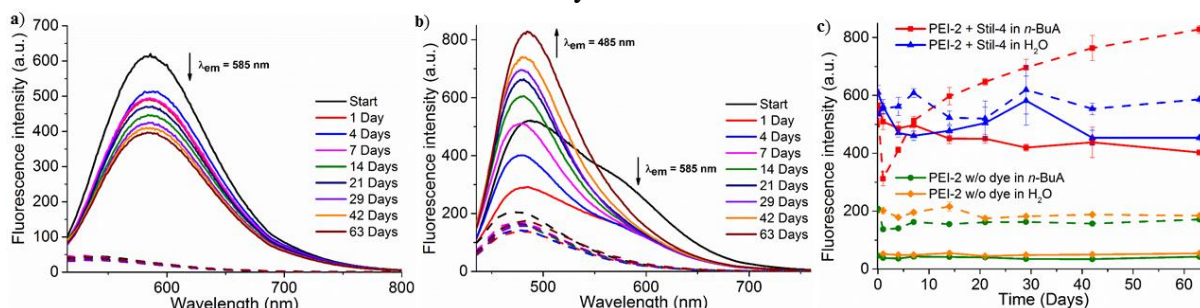

Figure 54 Emission spectra of a) **Stil-3** (c = 0.25 mg/g resin) excited at a) λ_{ex} = 510 nm) and b) λ_{ex} = 390 nm embedded within **PEI-2** and exposed to *n*-BuA solution (1.5 mmol/mL) and c) plot of the fluorescence intensities *vs*. time together with corresponding control experiments (solid lines: λ_{ex} = 510 nm, dashed lines: λ_{ex} = 390 nm).

The results for the activation of **Stil-4** in **PEI-2** by *n*-BuA are summarized in **Figure 55**. A decrease of the emission maximum at 585 nm was observed together with an appearance of a second emission maximum at 485 nm. For a control experiment of **PEI-2** without dye in *n*-BuA again an initial decrease of the emission maximum was observed when excited at 420 nm. While during further measurements the control experiments did not show fluorescence changes, for the actual sample a strong increase of the fluorescence intensity was observed and indicated

the hemiaminal formation. Similar as in preliminary solution experiments, due to the high intensity of the emission maximum at 485 nm, after 4 days the virgin emission maximum at 585 nm was no longer detectable. Compared with **Stil-3**, **Stil-4** showed a stronger emission decrease by 26 % when stored in water. The activation of **Stil-3** and **Stil-4** in **PEI-2** by aqueous *n*-BuA solution was demonstrated, whereby **Stil-3** proved to be more suitable due to interferences of **PEI-2** with the trifluoroacetyl and the hemiaminal of **Stil-4**.

Figure 55 Emission spectra of a) **Stil-4** (c = 0.25 mg/g resin) excited at a) λ_{ex} = 500 nm) and b) λ_{ex} = 420 nm embedded within **PEI-2** and exposed to *n*-BuA solution (1.5 mmol/mL) and c) plot of the fluorescence intensities *vs*. time together with corresponding control experiments (solid lines: λ_{ex} = 500 nm, dashed lines: λ_{ex} = 420 nm).

3.5.3.3. Sensor activation in PEI-2 by neopentyl glycol

Sensor activation of **Stil-3** and **Stil-4** within **PEI-2** was tested similarly as previously described in part 3.5.2.3., and the results are presented in **Figure 56** and **Figure 57**. For **Stil-3** the emission maximum at 565 nm was only slightly decreasing while a strong increase of an emission maximum at 470 nm was observed. As this phenomenon was also observed in control experiments a quantification of sensor conversion was difficult.
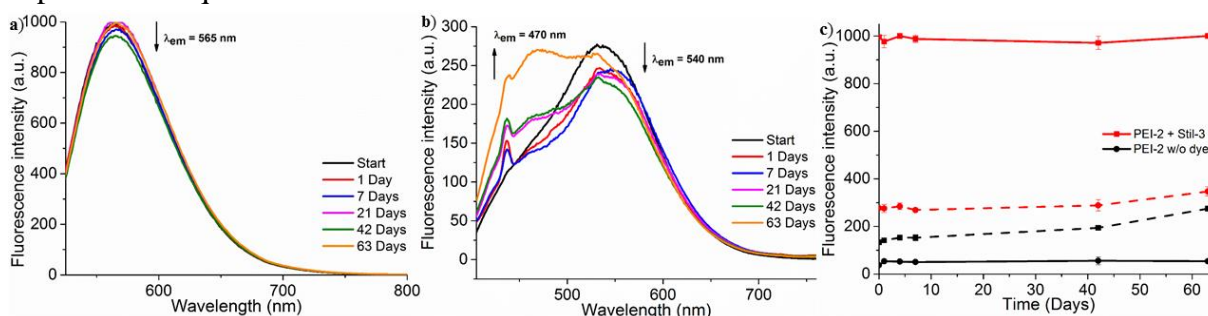

Figure 56 Emission spectra of **Stil-3** (c = 0.25 mg/g resin) excited at a) λ_{ex} = 510 nm and b) λ_{ex} = 390 nm embedded within **PEI-2** exposed to gaseous neopentyl glycol atmosphere and b) plot of the fluorescence intensities *vs*. time together with corresponding control experiment.

Stil-4 showed faster sensor activation, which was monitored by a constant decrease of the emission maximum at 585 nm. However, the activation was slower than for the corresponding experiments conducted in *n*-BuA solution which was in accordance with observation made for **PEI-1**. The strong intrinsic resin fluorescence together with emission changes observed for the control specimen excited at 420 nm made the monitoring of the virgin form the more suitable method.
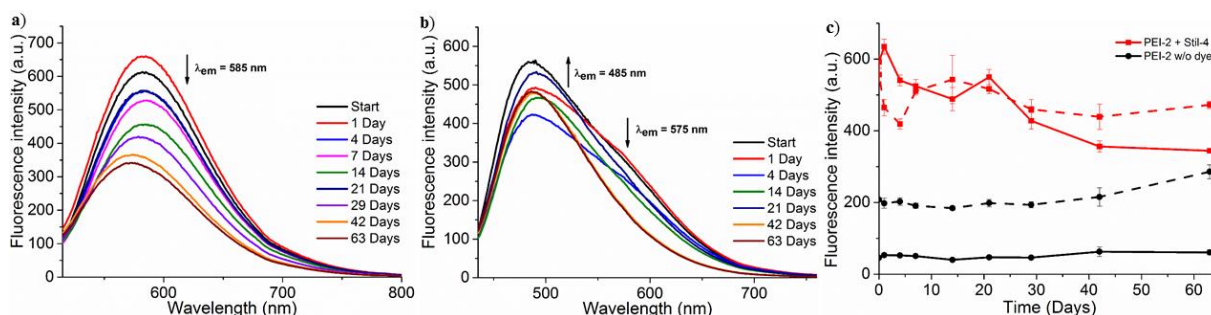
Figure 57 Emission spectra of **Stil-4** (c = 0.25 mg/g resin) excited at a) λ_{ex} = 500 nm and b) λ_{ex} = 420 nm embedded within **PEI-2** exposed to gaseous neopentyl glycol atmosphere and b) plot of the fluorescence intensities *vs.* time together with corresponding control experiment.

3.5.3.4. Sensor activation in PEI-2 by thermal degradation

In a last step, in-situ sensor activation of **Stil-3** and **Stil-4** in **PEI-2** was done by generating the alcoholic analytes, in particular NPG, through thermal degradation of the resin matrix. Polymer degradation was triggered by storing the specimen in a sand bath heated at 180 °C.

The emission maximum of **Stil-3** at 565 nm was initially decreasing by 6 % and afterwards was not significantly changing during 59 days (**Figure 58**). After 81 days the emission decreased by 29 %. This was in good accordance with the degradation experiments, in which a mass loss, thus formation of alcoholic analytes, of **PEI-2** was only observed in the initial stage while at 180 °C only minor mass loss was detected after the first degradation interval.

Furthermore, the consistency of **Stil-3** proved the thermal stability within the resin matrix and thus was an additional proof that for **PEI-1** samples the changes can be attributed to the activation process. In the control experiment no fluorescence changes of **Stil-3** were detected, and thus the matrix was not affected by the experimental conditions and the observed emission changes were attributed to hemiacetal formation.
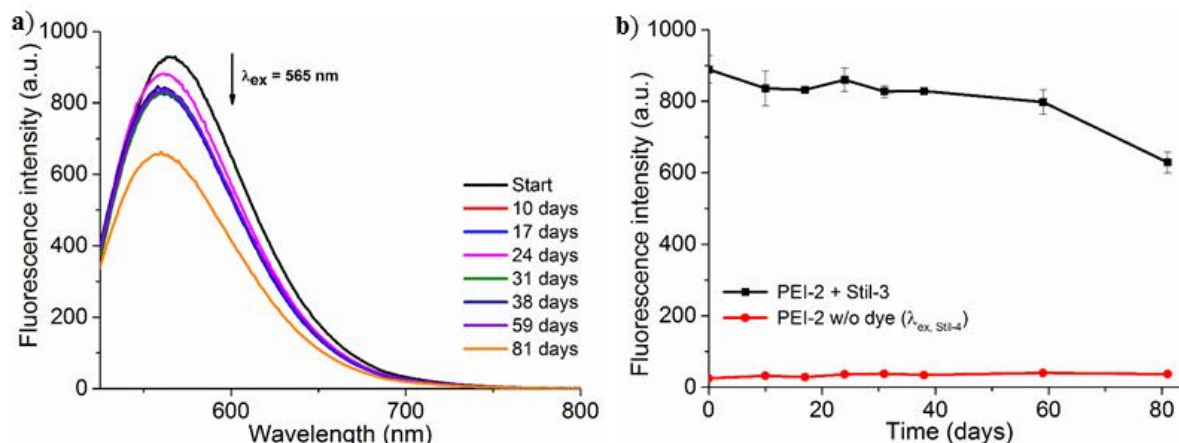

Figure 58 Emission spectra of a) **Stil-3** (c = 0.25 mg/g resin, λ_{ex} = 510 nm) embedded within **PEI-2** and thermally aged at 180 °C and b) plot of the fluorescence intensities *vs.* time together with the corresponding control experiment.

With 60 % **Stil-4** showed a stronger decrease of the emission maximum at 578 nm, which was in accordance with previous experiments which demonstrated a higher sensitivity for the distyryl dye (**Figure 59**). Control experiment also showed no fluorescence changes for the resin matrix and thus sensor activation of **Stil-4** within **PEI-2** was demonstrated.

Furthermore, thermal activation experiments of **Stil-3** and **Stil-4** embedded within **PEI-2** were accompanied by measurements with the spectro2guide and the results are shown in **Figure A64**.
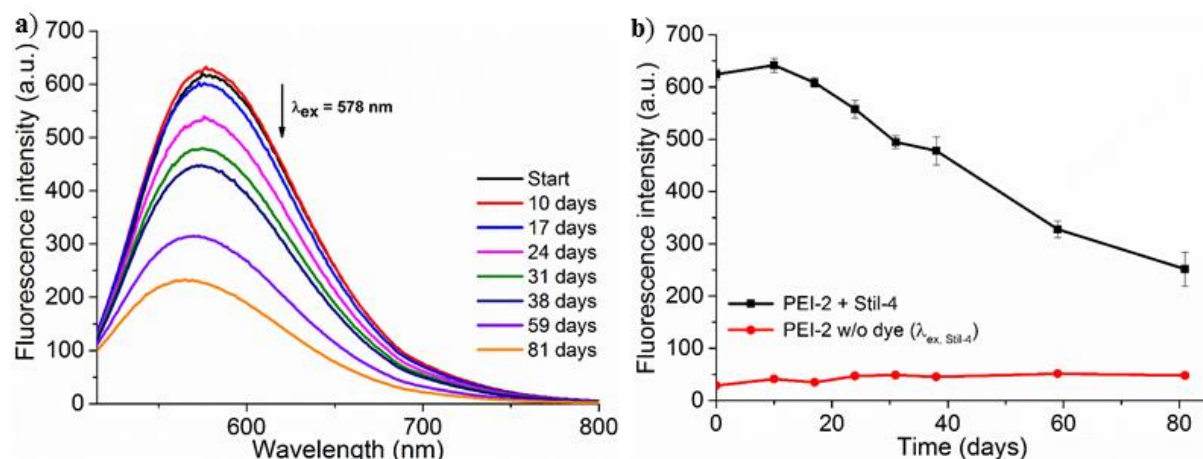

Figure 59 Emission spectra of a) **Stil-4** ($c = 0.25$ mg/g resin, $\lambda_{ex} = 500$ nm) embedded within **PEI-2** and thermally aged at 180 °C and b) plot of the fluorescence intensities *vs*. time together with the corresponding control experiment.

3.5.4. Investigation of the matrix influences

Sensor testing in solution and in different PEI resins showed a strong matrix influence on the emission properties of **Stil-3** and **Stil-4**. Strong polarity effects, leading to different absorption and emission maxima and different fluorescence quantum yields, are described in literature[258, 270]. It was assumed that additionally due to strong interactions between sensor molecule and matrix, especially π-π–stacking, molecular rearrangements and microphase separation or excimer formation could occur. Because of the extended conjugated system, it was assumed that these interactions are particularly strong in **Stil-4**.

3.5.4.1. Sensor embedding within PEI-3

Both sensor molecules were embedded within **PEI-3** and the experimental procedure is described in the Experimental part 4.4. Concentration series were determined and the corresponding plots are presented in **Figure A65** and the emission spectrum of **PEI-3** without dye is shown in **Figure A66**.

PEI-3 had the similar structure as **PEI-1** but the comonomer for the cross-linking process was substituted by methyl methacrylate (MMA). Consequently, due to the absence of the polystyrene within the PEI matrix, a strong decrease of the interactions between phenyl rings of the sensor molecules and the PEI resin was expected. The results of the fluorescence investigations are shown in **Figure 60**. For comparison, other matrices which had been investigated, are also displayed. Both dyes showed shifts of the emission maxima when embedded in different matrices. However, for **Stil-3** the emission maximum in **PEI-2** and **PEI-3** was similar to the emission maximum in dioxane. At same concentrations, the fluorescence intensity of virgin **Stil-3** is higher in **PEI-2**. In **PS/DVB** the emission maximum was slightly blue-shifted to 540 nm and the fluorescence intensity was similar to the **PEI-3** specimen even though the concentration was only 0.25 mg dye/resin.

For **Stil-4** the emission maxima were slightly shifted to smaller wavelengths from 608 nm in dioxane to 585 nm in **PEI-2** and 560 nm in **PS/DVB**. In **PEI-3** the emission maximum was

strongly shifted to 486 nm and the strongest shift was also identified in **PEI-3** where the emission maximum was observed at 479 nm.

These observations allowed some conclusion about possible interactions between the sensor molecules embedded within the different matrices. First, the influences were significantly stronger for **Stil-4** than for **Stil-3**, especially when **PEI-1** and **PEI-3** were used as matrix. **Stil-3** showed similar emission maxima in **PEI-2** and **PEI-3** whereas **Stil-4** showed similar emission maxima for **PEI-1** and **PEI-3**. Thus it was concluded that π-π interactions between the dye and the matrix cannot explain the significant shifts of the emission maxima. Although greater agreement was expected in **PEI-1** and **PEI-2**, the observed deviation could be related to the dimeric fatty acid which was used in **PEI-2** and served as spacer molecule to provide the cured resin with more flexibility. As **Stil-4** showed a worse solubility in **PEI-1** and **PEI-3** compared to **Stil-3** it was assumed that in these resins, **Stil-4** was affected by microphase separation and aggregation which was enabled by the alignment of the sensor molecules due to their long conjugated system. Due to the better solubility in **PEI-2** together with the more flexible network, this phenomenon was not observed in this case. Further investigation were carried out by means of fluorescence lifetime measurements.
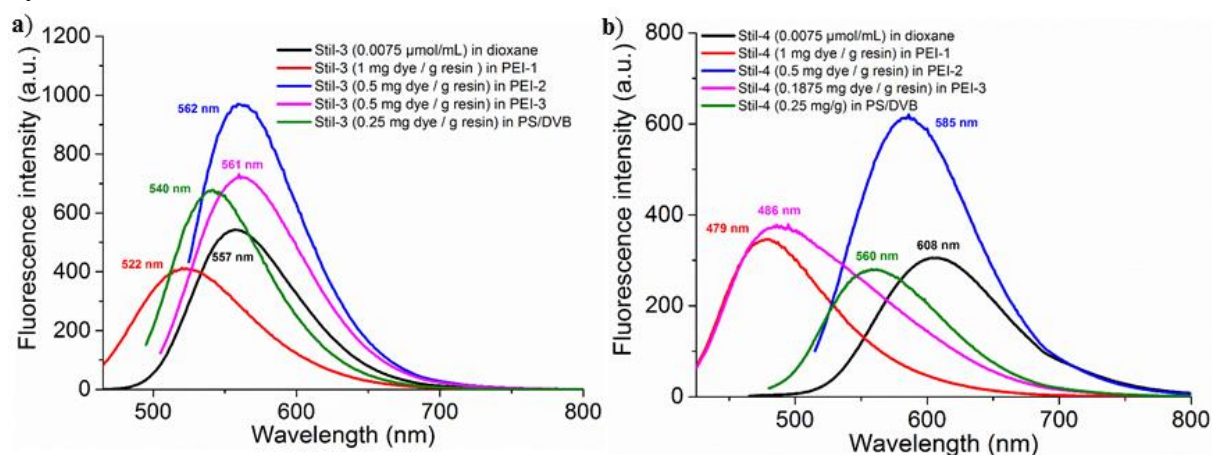

Figure 60 Emission spectra of a) **Stil-3** and b) **Stil-4** in dioxane and embedded within **PEI-1**, **PEI-2**, **PEI-3** and **PS/DVB**.

3.5.4.2. Fluorescence lifetime measurements in PEI-1

To confirm the assumption that **Stil-4** tends to stronger aggregate due to its longer conjugated system and poorer solubility in the resin compared to **Stil-3**, time-resolved fluorescence spectroscopy was performed. Hence, concentrations of **Stil-3** and **Stil-4** in **PEI-1** were prepared and the concentration influence of the dye concentrations towards the fluorescence lifetime was investigated.

The results for the concentration series of **Stil-3** are presented in **Figure 61**. The fluorescence decay curves showed only slight differences with increasing concentrations. However, when the fluorescence decay curves were plotted against the concentration, the decay kinetics revealed concentration issues and a highly complex sample behavior. While for simple fluorophores usually a monoexponential decay is observed, the fit for both dyes in **PEI-1** allowed the determination of three time components. For **Stil-3** and **Stil-4**, one time component was below a picosecond and therefore difficult to resolve. Additionally, **Stil-3** showed a nearly constant time component τ_1 with a fluorescence decay time of 1.6 to 1.7 ns and third

fluorescence decay with τ_2. τ_2 was decreasing from 4 ns to 3 ns with increasing concentration and reached its minimum at a concentration of 0.75 mg/g resin.
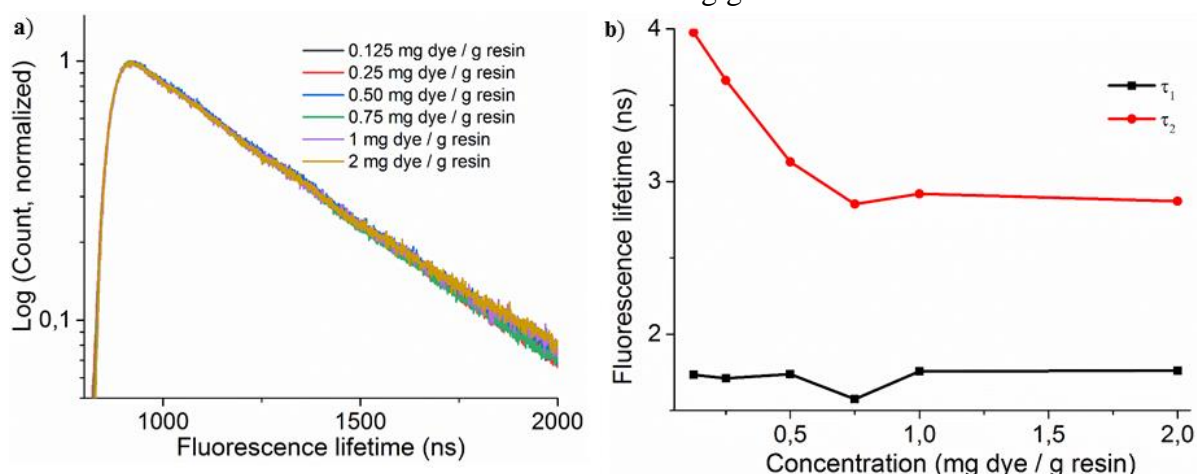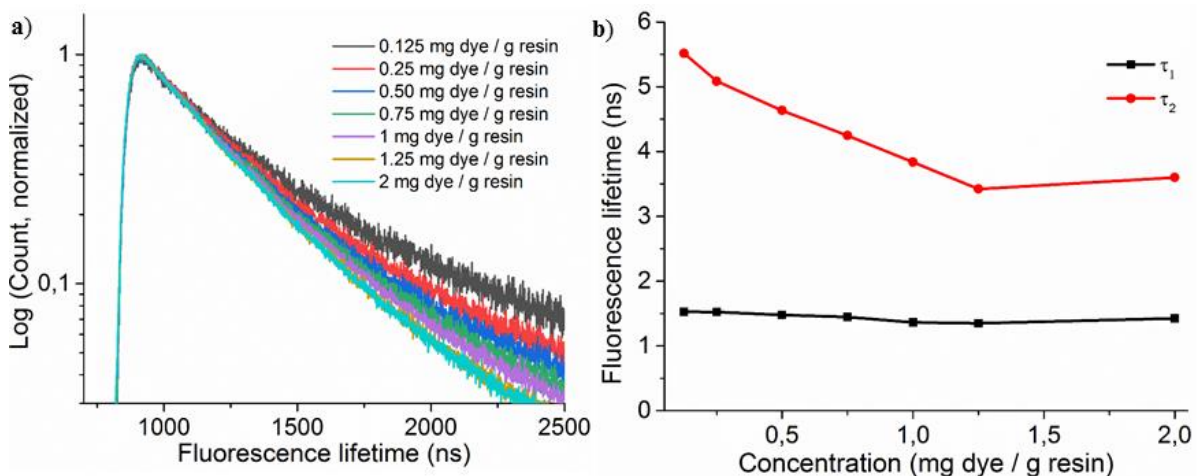

Figure 61 a) Fluorescence decay of **Stil-3** embedded within **PEI-1** at different concentrations and b) the plotted fluorescence lifetimes *vs.* dye concentration.

The concentration effect observed for **Stil-4** within **PEI-1** was significantly stronger and is shown in **Figure 62**. Obviously, the decay curves do not show any concentration dependence for fast decay kinetics, but are decreasing faster for longer lifetimes with increasing concentration until they finally reach a constant value. This observation was proven by plotting the decay kinetics which again gave a constant τ_1 with 1.4 to 1.5 ns, while τ_2 was decreasing from 5.5 to 3.5 ns for concentrations exceeding 1.25 mg/g resin.

Figure 62 a) Fluorescence decay of **Stil-4** embedded within **PEI-1** at different concentrations and b) the plotted fluorescence lifetimes *vs.* dye concentration.

Summarized, for both dyes a concentration dependency of the fluorescence lifetime in **PEI-1** was observed, whereas concentration influences were significantly stronger for **Stil-4**. This supports the assumption that the fluorescence behavior is influenced by an aggregation of the dyes, which should be supported with increasing concentration. The aggregation is much stronger for **Stil-4**, which leads to stronger differences in the emission spectra. However, as **Stil-4** showed a similar fluorescence behavior within **PEI-1** with a concentration of 1 mg/g resin and within **PEI-3** with a concentration of 0.1875 mg/g resin (compare with **Figure 60b**) but a strong deviation to **PEI-2** with a concentration of 0.5 mg/g resin, additionally

interactions between the resin and the sensor molecules are likely. Thus, a complex fluorescence pattern of **Stil-3** and **Stil-4** within the poly(ester imides) is assumed.

3.5.5. Sensor embedding within a supramolecular polyurethane (PU) network

Beyond the actual project, the final part will examine the investigation of the developed sensor system in polyurethanes (PUs). Like PEIs, PUs are an outstanding material class that fill a wide range of applications in industry. Their facile synthesis and easily adaptable structural characteristics make PUs a versatile polymer class that is used as thermoplastic, thermosetting and elastomeric material and, among others, is used for protective coatings[271-272]. Due to its excellent thermal insulating properties together with its ageing-resistance, lightweight and good processing abilities, one of its main applications is the construction sector[273]. Additionally, PUs are often used for the development of smart materials, which show stimuli-responsive behavior and, for example, are able to detect and store external forces, e.g. mechanically applied stress, providing the polymer with an intrinsic damage sensing system[274]. Furthermore, because of their self-healing ability due to strong hydrogen bonding, in recent years supramolecular PU networks have received much attention in research[275-276]. Together with their tendency to release amines and alcoholic degradation products when they undergo thermal degradation, PUs constitute a promising matrix for the developed sensor system[277-279].

3.5.5.1. Synthesis of PU-1

PU-1 was synthesized by a polyaddition of poly(tetrahydrofuran) (PTHF), 1,4-butanediol (1,4-BuOH) and 4,4-methylendi(phenylisocyante) (MDI) in THF at room temperature. The polymerization was catalyzed by diazabicyclo[5.4.0]undec-7-ene (DBU) acting as non-nucleophilic base. The exact experimental procedure of **PU-1** is described in the Experimental part 4.4. together with a complete characterization (Appendix 7.4.). A full conversion was proven by the absence of isocyanate groups in the IR spectra (**Figure A69**).

The challenge was the embedding of the sensor molecules within **PU-1**. Whereas in the pre-condensed PEIs, the alcohol was already inserted into the polymer and the curing was done via a free radical process, the alcohol concentration in the reaction mixture of **PU-1** was very high. The polyaddition follows a step-growth mechanism, which is characterized by initial oligomer formation that only form the polymer at very high conversion rates. Thus, the sensor molecule was added at the latest possible time, at low alcohol concentration, before the increasing viscosity of **PU-1** prevented further stirring.

However, the procedure was only possible for **Stil-3**, because due to its high reactivity towards alcohols, in particular 1,4-BuOH, **Stil-4** was already activated and was not suitable for an application within **PU-1**. Fluorescence experiments of a specimen of **PU-1** with **Stil-3** revealed good accordance with solution experiments and the sensor showed an emission maximum at 572 nm (**Figure 63**). As **PU-1** is non-fluorescent, control experiments of a specimen without dye did not show any interference and thus **PU-1** was considered as suitable matrix to detect sensor activation of **Stil-3**. A concentration series of **Stil-3** within **PU-1** was prepared and is shown in **Figure A71**.
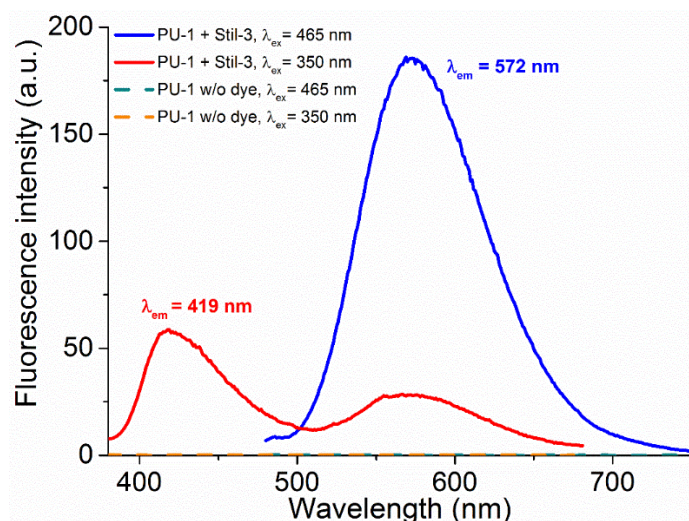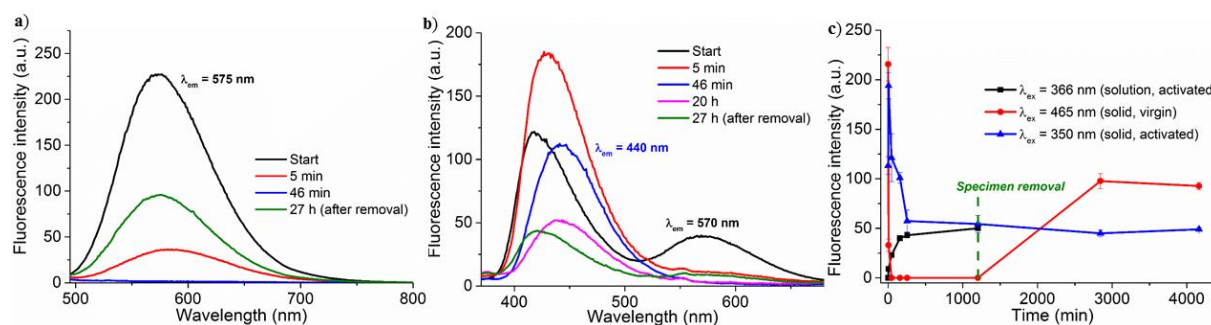
Figure 63 Emission spectra of **Stil-3** (c = 0.033 mg/g resin) embedded within **PU-1** and excited at λ_{ex1} = 465 nm and λ_{ex2} = 350 nm together with reference samples of **PU-1** without dye.

3.5.5.2. Sensor activation of Stil-3 within PU-1 by alcohols

Subsequently, sensor activation was tested by exposing specimens of **PU-1** with **Stil-3** to MeOH and a solution of 1,4-BuOH in ACN (1 mmol/mL) and the results are summarized in **Figure 64** and **Figure 65**. In both experiments a fast sensor activation was observed after minutes and was monitored by a decrease of the virgin emission maxima together with the formation of second emission maxima of the hemiacetal.

Figure 64 Emission spectra of **Stil-3** (c = 0.033 mg/g resin) embedded within **PU-1** exposed to MeOH excited at a) λ_{ex1} = 465 nm and at b) λ_{ex2} = 350 nm and c) plot of the fluorescence intensities *vs.* time together with corresponding storage solution measurements.

As in solution experiments, the hemiacetal with 1,4-BuOH showed a weaker emission which was attributed to its lower fluorescence quantum yield. Surprisingly, the fluorescence intensity of the hemiacetal was decreasing after an initial increase after exposure to both analytes. This was due to sensor leaching in MeOH and ACN, which was demonstrated by fluorescence spectroscopy of the storage solution. In both cases, the hemiacetal was found in the storage solution and its intensity increased until an equilibrium of **Stil-3** in **PU-1** and solution had been established as represented by the black lines in **Figure 64c** and **Figure 65c**. At the same time the equilibrium was reached, the emission intensity of **Stil-3** within **PU-1** also reached its maximum. Additionally, after the specimens were removed from the analyte solution and were stored in vacuum for 1 day, the emission of the trifluoroacetyl form was recovered which is demonstrated by the measured values presented by the green line in **Figure 64c** and **Figure 65c**.

However, the initial intensity was not reached due to the partial sensor leeching in MeOH and ACN.
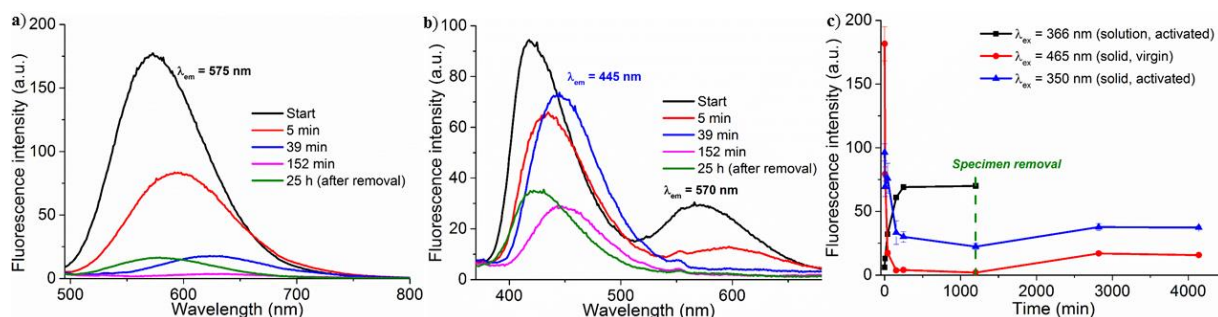

Figure 65 Emission spectra of **Stil-3** ($c = 0.033$ mg/g resin) embedded within **PU-1** and exposed to 1,4-BuOH (1 mmol/mL in ACN) excited at a) $\lambda_{ex1} = 465$ nm and at b) $\lambda_{ex2} = 350$ nm and c) plot of the fluorescence intensities *vs.* time together with corresponding storage solution measurements.

3.5.5.3. Sensor activation of Stil-3 within PU-1 by *n*-BuA

The fluorescence recovery of the trifluoroacetyl form in the dynamic supramolecular **PU-1** was an interesting observation that was further investigated. To overcome the problem of sensor leeching, again aqueous *n*-BuA solution was used and no leeching was observed after 20 days of exposition. Furthermore, the concentration influence of both, dye and analyte, towards the repeatable switching of **Stil-3** within **PU-1** was examined. Fast activation kinetics were found for the three sensor concentrations 0.033, 0.025 and 0.009 mg dye/g resin and all three *n*-BuA concentrations 0.1, 0.2 and 0.3 mmol/mL and the results are summarized in **Figure 66**, **Figure 67** and **Figure 68**.
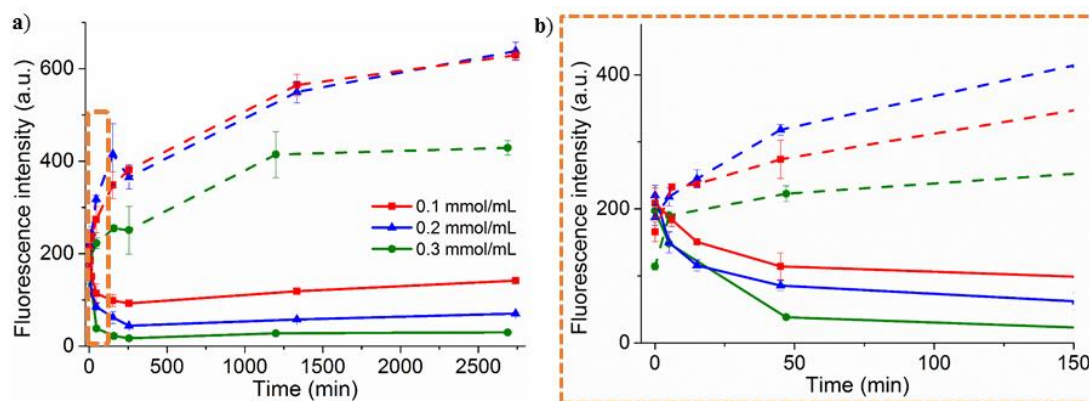
Figure 66 a) Plot of the fluorescence intensities *vs.* time of **Stil-3** ($c = 0.033$ mg/g resin) embedded within **PU-1** and exposed to different concentrations of aqueous *n*-BuA excited at $\lambda_{ex1} = 465$ nm ($\lambda_{em} = 575$ nm, solid) and at $\lambda_{ex2} = 350$ nm ($\lambda_{em} = 425$ nm, dashed) and b) the zoomed inlet for the initial activation process.

In all cases, monitoring of the trifluoroacetyl form by excitation at 465 nm showed faster decay kinetics as well as higher maximum conversions with increasing *n*-BuA concentration. However, by monitoring the hemiaminal form of **Stil-3** by excitation at 350 nm, highest maximum conversions were found for either 0.1 mmol/mL or 0.2 mmol/mL *n*-BuA concentrations, whereas in all cases specimens stored at a concentration of 0.3 mmol/mL showed the weakest emission. This was explained by the control experiments of **PU-1** without dye, which were stored in *n*-BuA, and showed no changes when excited at 465 nm but slight changes when excited at 350 nm after 2 days of exposition (**Figure A72**).
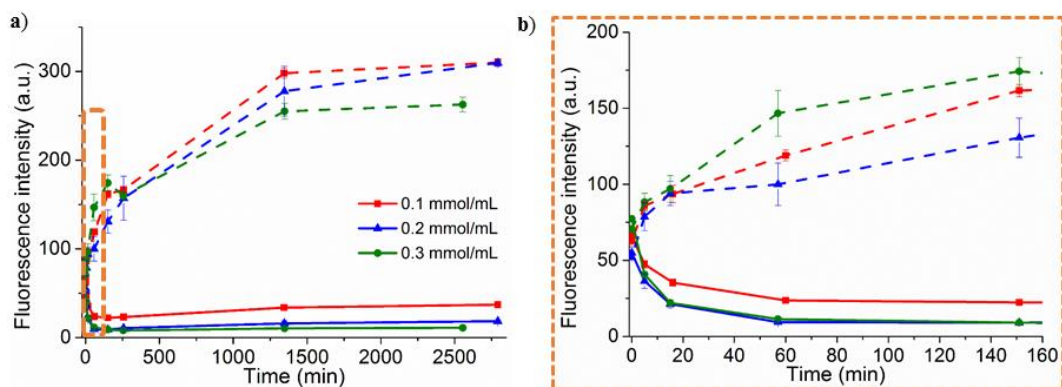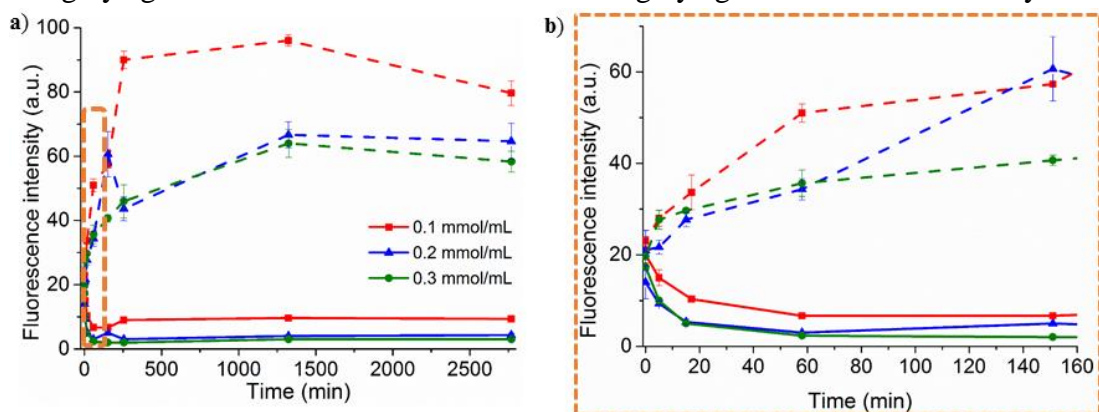
72

Figure 67 a) Plot of the fluorescence intensities *vs.* time of **Stil-3** ($c = 0.025$ mg/g resin) embedded within **PU-1** and exposed to different concentrations of aqueous *n*-BuA excited at $\lambda_{ex1} = 465$ nm ($\lambda_{em} = 575$ nm, solid) and at $\lambda_{ex2} = 350$ nm ($\lambda_{em} = 425$ nm, dashed) and b) the zoomed inlet for the initial activation process.

Thus, observation of the virgin emission maxima was the more suitable method. Overall, the sensor response time in **PU-1** was significantly faster compared to the poly(ester imides). Furthermore, at lower dye concentrations the maximum conversion was reached faster. For a concentration of 0.009 mg dye/g resin maximum conversion was observed after 160 min, 0.025 mg dye/g resin after 1300 min and for 0.033 mg dye/g resin after almost 2 days.

Figure 68 a) Plot of the fluorescence intensities *vs.* time of **Stil-3** ($c = 0.009$ mg/g resin) embedded within **PU-1** and exposed to different concentrations of aqueous *n*-BuA excited at $\lambda_{ex1} = 465$ nm ($\lambda_{em} = 575$ nm, solid) and at $\lambda_{ex2} = 350$ nm ($\lambda_{em} = 425$ nm, dashed) and b) the zoomed inlet for the initial activation process.

3.5.5.4. Repeated sensor activation of Stil-3 in PU-1

As observed for the activation with alcohols, it was attempted to exploit the dynamic supramolecular **PU-1** by performing repeated sensor activation of **Stil-3**. Therefore, specimens were alternately stored in aqueous *n*-BuA solution for 2 days and subsequently removed from the solution and stored in vacuum for 2 days. After each cycle, the specimen was measured by fluorescence spectroscopy to check the degree of activation or deactivation. In total, 10 cycles were recorded (5 in aqueous *n*-BuA solution and 5 in vacuum). The results are summarized in **Figure 69**, **Figure 70** and **Figure 71**. For all measurements, the trifluoroacetyl form was recovered after 10 cycles at almost the same intensity as before the start of repeated activation. Sensor leeching was not observed in the cause of 20 days.
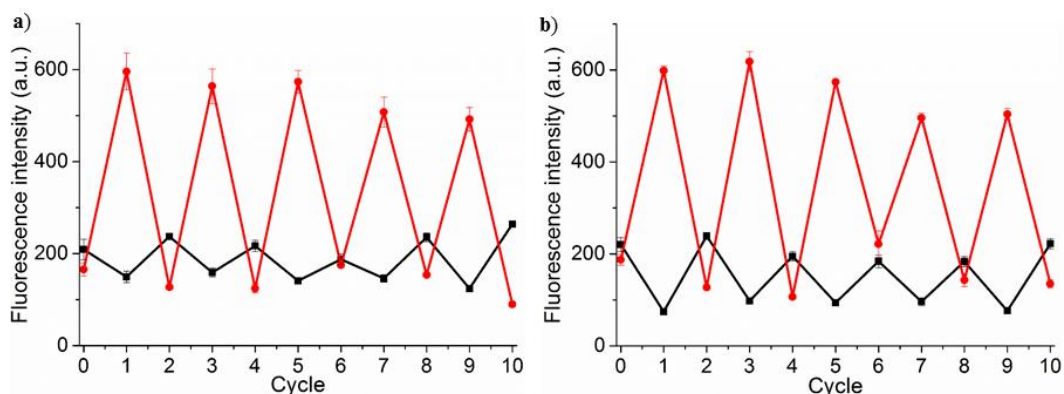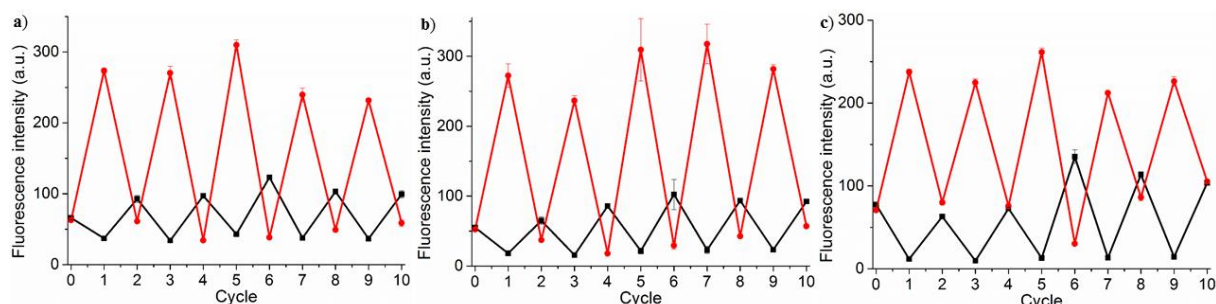
Figure 69 a) Cycled sensor activation and deactivation of **Stil-3** ($c = 0.033$ mg dye/g resin) by alternating exposing the specimen to aqueous *n*-BuA solution with a concentration of a) 0.1 mmol/mL and b) 0.2 mmol/mL (uneven cycle number) and vacuum (even cycle number). Each cycle lasted 2 days and excitation was done at $\lambda_{ex1} = 465$ nm ($\lambda_{em} = 575$ nm, black) and at $\lambda_{ex2} = 350$ nm ($\lambda_{em} = 425$ nm, red).

Figure 70 a) Cycled sensor activation and deactivation of **Stil-3** ($c = 0.025$ mg dye/g resin) by alternating exposing the specimen to aqueous *n*-BuA solution with a concentration of a) 0.1 mmol/mL, b) 0.2 mmol/mL and c) 0.3 mmol/mL (uneven cycle number) and vacuum (even cycle number). Each cycle lasted 2 days and excitation was done at $\lambda_{ex1} = 465$ nm ($\lambda_{em} = 575$ nm, black) and at $\lambda_{ex2} = 350$ nm ($\lambda_{em} = 425$ nm, red).

As at this concentration also the fastest sensor response was observed, the low dye concentration is best suited for repeated sensor activation, whereas the analyte concentration does not have a significant influence. The results show that **Stil-3** embedded within **PU-1** is a suitable sensor for the detection of amines even after repeated activation.
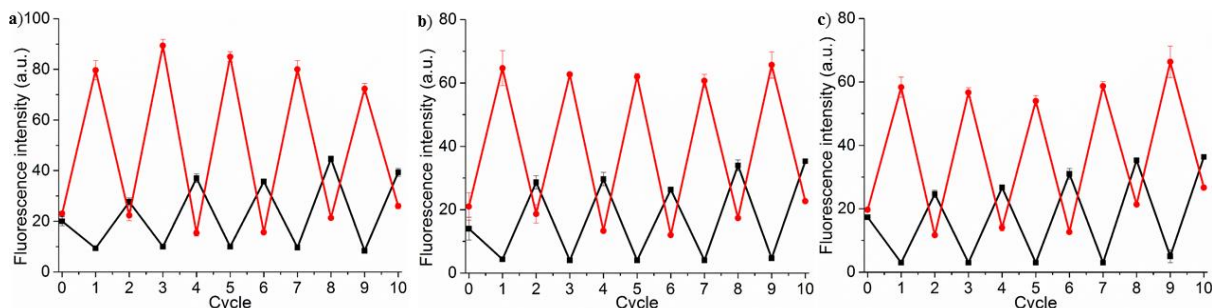

Figure 71 a) Cycled sensor activation and deactivation of **Stil-3** ($c = 0.009$ mg dye/g resin) by alternating exposing the specimen to aqueous *n*-BuA solution with a concentration of a) 0.1 mmol/mL, b) 0.2 mmol/mL and c) 0.3 mmol/mL (uneven cycle number) and vacuum (even cycle number). Each cycle lasted 2 days and excitation was done at $\lambda_{ex1} = 465$ nm ($\lambda_{em} = 575$ nm, black) and at $\lambda_{ex2} = 350$ nm ($\lambda_{em} = 425$ nm, red).

4. Experimental part
4.1 Materials and methods
All solvents were purchased in technical grade and were distilled before usage. Dry tetrahydrofuran (THF) and dry *N,N*-dimethylformamide (DMF) were taken from a solvent-purification-system (SPS) MB-SPS-800 from MBraun equipped with a MB-KOL-A and a MB-KOL-M (Type 2 and 3) column. All reactions were conducted under dry nitrogen atmosphere using Schlenk techniques unless otherwise noted.

4-Bromostyrene (99 %), 4-iodoaniline (99 %), tri(*o*-tolyl)phosphine (98+ %), magnesium sulfate (99 %), calcium hydride (coarse powder 92 %) were purchased from Alfa Aesar. Ethyl trifluoroacetate (99 %), 1-bromohexane (98 %), *N,N*-diisopropylethylamine (DIPEA) (99 %), *n*-butyllithium solution (*n*-BuLi) (1.6 M in cyclohexane), sodium nitrite (reagent plus), magnesium turnings (4+30 mesh 99.98 %), triethylamine (TEA) (99 %), dichlorobis-(triphenylphosphine)-palladium(II) (99.9 %), styrene (99 %, stabilized with hydroquinone), divinylbenzene (55 %), 2,2'-azobis(2-methylpropionitrile) (AIBN) (98 %), poly(tetrahydrofuran) (PTHF) (M_n = 2900 g/mol), poly(ethylene glycol) (PEG) (M_n = 1500 g/mol, M_n = 3350 g/mol), 1,4-butanediol (98 %) and 1,2-ethanediol (99.8 %) were bought from Sigma Aldrich. Palladium(II)acetate (99 %) was purchased from Carbolution Chemicals. Aniline (for synthesis), sodium (in mineral oil) and 1,3,5-trioxane were bought from Merck. 4,4-Methylendi(phenylisocyante) (MDI) (> 97 %) was acquired from TCI and 1,8-diazabicyclo[5.4.0]undec-7-ene (DBU) (98 %) was purchased from Fluka. Sodium bicarbonate, sodium hydroxide (99 %) and hydrochloric acid (37 %) were bought from Gruessing. $(NH_4)_6Mo_7O_{24}\cdot 4H_2O$ and $Ce(SO_4)_2\cdot 4H_2O$ were acquired from VEB and sodium sulfate and sodium chloride were purchased from Roth. Amberlite® XAD-4 was bought from abcr. HPLC-grade methanol and HPLC-grade acetonitrile (ACN) were purchased from VWR-BDH Prolabo. Deuterated chloroform ($CDCl_3$) was bought from Chemotrade.

^{1}H-NMR-, ^{13}C-NMR- and ^{19}F-NMR spectra were recorded either on an Agilent Varian Gemini 200 (400 MHz) or on an Agilent Varian Unity Inova (500 MHz) spectrometer at 27 °C using deuterated chloroform ($CDCl_3$). All chemical shifts (δ) were given in parts per million (ppm) and were referred to the solvent signal of $CDCl_3$ (7.26 ppm (^{1}H-NMR), 77.0 ppm (^{13}C-NMR)). Values of coupling constants J are given in Hertz (Hz). Evaluation of all NMR data was done using MestReNova software (version 6.0.2-5475).

UV/Vis absorbance spectra of dissolved sensor molecules were recorded on a Perkin Elmer UV/VIS Lambda 365 spectrometer. For sensor activation in solution the analyte was transferred into a cuvette and subsequently dissolved in dioxane. Typically a stock-solution of either 1 mg **Stil-3** or **Stil-4** in 1 mL dioxane was prepared and the required amount was transferred into a cuvette containing the analyte. UV/Vis measurements were immediately started after sensor addition. The total solvent volume for all UV/Vis measurements was 3 mL. For solid-state measurements, the spectrometer was equipped with a Lambda 365 Integrating sphere.

Fluorescence spectra of both, dissolved and embedded sensor molecules, were recorded on an Agilent Technologies Cary Eclipse Fluorescence Spectrophotometer. In all experiments the detector voltage was set to 500 V. In solid state measurements three different positions on the

specimen were measured and measurement errors were indicated by error bars. Selected measurements were additionally performed with the spectro2guide from BYK Gardner, a handheld device which should be used for inline measurements during application. For sensor activation in solution the analyte was transferred into a cuvette and subsequently dissolved in dioxane. Typically a stock-solution of either 1 mg **Stil-3** or **Stil-4** in 1 mL dioxane was prepared and the required amount was transferred into a cuvette containing the analyte. Fluorescence measurements were immediately started after sensor addition. The total solvent volume for all fluorescence measurements was 3 mL. UV/Vis- and fluorescence measurements were performed using quartz glass cuvettes with a diameter of 10 mm from Helma Analytics.

Fluorescence lifetime measurements were performed with a Hamamatsu R5900 16-channel MA photomultiplier tube (PMT) with 16 separate output (anode) elements and a common cathode and dynode system (PML-16C, Becker&Hickl, Berlin, Germany)[280-283]. The polychromator was equipped with a 300 grooves/mm grating resulting in a spectral bandwith of the PML-16C of approximately 12.5 nm/channel. A 405 nm pulsed laser diode (LDH-405, Picoquant, Berlin) and a 470 nm pulsed laser diode (LDH-470, Picoquant, Berlin) were used for excitation.

ATR-IR measurements were recorded on Bruker Tensor VERTEX 70 by using an ATR Golden Gate Diamond Unit for solid-state investigations.

HPLC measurements were performed on a VWR Hitachi Chromaster on an Atlantis T3 (5.0 µm, 4.6 mm x 250 mm) C18 reversed column. A flow rate of 0.8 mL/min and an injection volume of 10 µL were used. Analyte detection was done by an UV/Vis detector. For sample preparation HPLC-solvent was used with sample concentrations of 1 mg/mL.

ESI-TOF-MS measurements were performed on a Bruker Daltonics microTOF spectrometer, using direct injection with a flow rate of 180 µL/h in positive and negative mode. For sample preparation HPLC-grade methanol was used with sample concentrations of 0.5 mg/mL without addition of salt.

For HPLC / ESI-TOF-MS coupling a solution with a concentration of 1 mg/mL was prepared and subsequently 10 µL were injected on the HPLC column. The flow rate was set to 0.5 mL/min.

High-resolution mass spectroscopy was performed with a TripleToF 6600-1 mass spectrometer (AB Sciex), which was equipped with an ESI-DuoSpray-Ion-Source in positive mode and was controlled by Analyst 1.7.1 TF software (AB Sciex).

GPC measurements were done with a Viscotek GPCmax VE 2001 from Viscotek on a CLM3008 Tguard precolumn and a CLM3011 main column at 30 °C. Sample concentrations of 5 mg/mL in THF were used and the flow rate was set to 1 mL/min with an injection volume of 100 µL. Detection was done by either a RI-detector VE 3580 from Viscotek or with an UV-detector model no. 2600 from Viscotek at 35 °C. For molecular weight determination an external calibration with polystyrene standards (1000 g/mol to 115000 g/mol) was done.

TGA measurements were performed on a TGA Netzsch T210, using sample amounts of 5 mg. Measurements were done under a flow of nitrogen (20 mL/min) and a heating rate of 5 K/min.

DSC measurements were performed on a Netzsch Phoenix DSC 204 F1. Typically, 5 mg of the sample were weighed into alumina pans. The measurements were performed in the temperature range from 30 °C to 300 °C using a heating rate of 10 K/min and a cooling rate of 20 K/min.

Thin-layer chromatography (TLC) was performed on either Merck silica gel 60 or Macherey-Nagel ALUGRAM® ALOX N/UV254 sheets. Spots on TLC plates were visualized under UV light (254 nm or 366 nm) or by using the oxidizing agent "blue stain" composed of $(NH_4)_6Mo_7O_{24} \cdot 4H_2O$ (2.5 g) and $Ce(SO_4)_2 \cdot 4H_2O$ (1 g) dissolved in distilled water (90 mL) and concentrated H_2SO_4 (6 mL). For column chromatography either Merck Kieselgel 60 (230 – 400 mesh) or neutral aluminium oxide (Brockmann I Typ 507, 150 mesh) from Sigma Aldrich was used.

Density functional theory (DFT) studies and time dependent density functional theory (TD-DFT) studies were performed in THF using the polarized continuum model (CPCM) of the Gaussian 09 software. Investigated structures were optimized using B3LYP. For all calculations the 6-31G** basis set for C, H, N and S was used.

4.2. Execution of the long-term thermal degradation experiments

For degradation experiments a self-built apparatus was used, which was designed for long-term investigations. The apparatus is shown in **Figure 72**. A sand bath (7) on a hoist (8) was equipped with four glass pipes (4). Each glass tube was connected to a compressor (9) (EKOM DK50 Plus S/M), allowing to flush the gaseous degradation products into the adsorption columns (6) which were mounted at the outlet of the tube. The gas flow was controlled by a gas flow controller (2) and an overpressure valve (1) was attached to avoid bursting of the apparatus.

In total, eight glass tubes were distributed on two sand baths, allowing to run eight samples at two different temperatures at the same time. For degradation experiments, **PEI-1** and **PEI-2** were cured in a teflon-mould (50 mm x 10 mm x 10 mm), yielding specimen with a weight of 5 g which were placed on a weighing boat. Both non cross-linked pre-condensates **PEI-1PC** and **PEI-2PC** were directly weighed (5 g) into the weighing boat. The weighing boats containing the specimen were then stored in a glass-tube which was placed in the sand-bath for continuously heating the samples at 180 °C, 200 °C and 220 °C. Before starting the apparatus, each adsorption column was filled with Amberlite® XAD-4 (50 g) which was thoroughly washed with distilled water and acetone before loading. By applying a constant flow of oxygen (4 mL/min), gaseous degradation products were flushed into the adsorption column.

All adsorbed degradation products were collected after 500 h, 1000 h, 3000 h and 5000 h by removing the Amberlite® XAD-4 from the adsorption column and subsequently washing the adsorption material thoroughly with acetone. Before the restart of the apparatus the columns were reloaded with fresh Amberlite® XAD-4. Quantification of degradation products was done

by ^{1}H-NMR spectroscopy, using 1,3,5-trioxane (0.175 mg / 1.94 µmol to 1.80 mg / 0.02 mmol) as external standard.

1. Overpressure valve
2. Gas flow controller
3. Adapter
4. Glas pipe
5. Adapter
6. Column
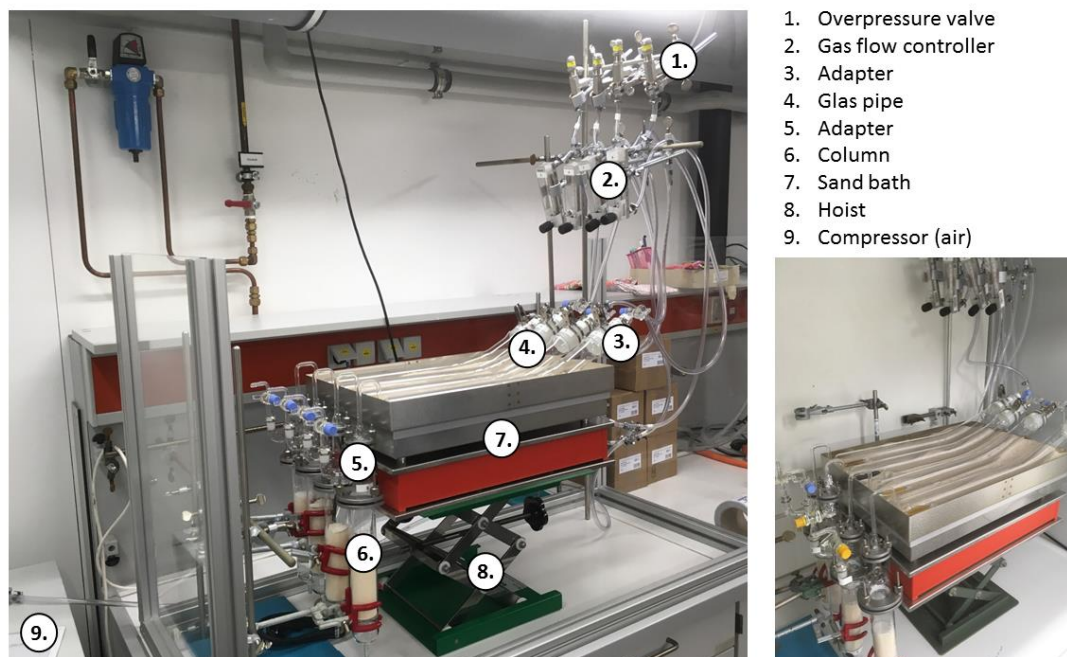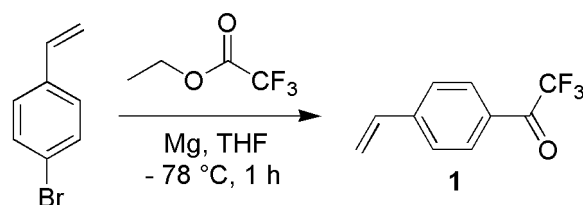7. Sand bath
8. Hoist
9. Compressor (air)

Figure 72 The two self-built apparatuses used for long-term thermal degradation of poly(ester imide) specimen.

4.3. Synthesis of the sensor molecules
4.3.1. Synthesis of 2,2,2-trifluoro-1-(4-vinylphenyl)ethan-1-one (1)

Scheme 6 Synthesis of 2,2,2-trifluoro-1-(4-viniylphenyl)ethan-1-one (**1**).

Synthesis of **1** was done according to the literature[284]. A two-neck flask was charged with Mg-turnings (1.82 g, 75.0 mmol, 1.5 eq.) and dry THF (50 mL) was added. Afterwards 4-bromostyrene (6.50 mL, 50.0 mmol, 1.0 eq.) was added via syringe and the reaction was initiated by hand warmth. The reaction mixture turned yellow, was allowed to cool down to room temperature and was stirred for 1 h. After addition of dry THF (5 mL) the reaction mixture was cooled down to -78 °C. Ethyl trifluoroacetate (9.0 mL, 75.0 mmol, 1.5 eq.) was added dropwise via syringe and the reaction was allowed to run for 1 h at -78 °C. After the solution was warmed up to 0 °C, 1 M HCl (100 mL) was slowly added and the reaction mixture was extracted with ethyl acetate (3 x 100 mL). The combined organic phases were washed with brine and dried over MgSO$_4$. The solvent was removed under vacuum and the crude product was purified by column chromatography using pentane / diethyl ether (50:1, R_f = 0.4) and isolated as a colorless oil.

Characterization of **1**:
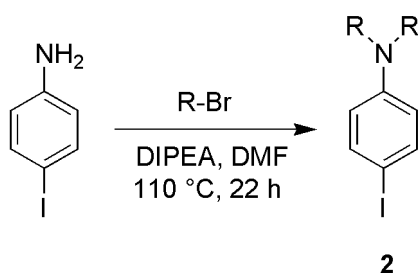Yield: 0.34 g, 1.70 mmol, 34 %

^{1}H-NMR (CDCl$_3$, 400 MHz, δ): 5.49 (d, J = 10.9 Hz, 1H, H-1a), 5.96 (d, J = 17.6 Hz, 1H, H-1b), 6.79 (dd, J = 17.6 Hz, J = 10.9 Hz, 1H, H-2), 7.56 (m, 2H, H-4), 8.05 (m, 2H, H-5).
^{13}C-NMR (CDCl$_3$, 100 MHz, δ): 116.9 (C-1), 118.7 (C-8), 126.9 (C-6), 129.2 (C-4), 130.7 (C-5), 135.6 (C-2), 144.7 (C-3), 180.1 (C-7).
^{19}F-NMR (CDCl$_3$, 376 MHz, δ): -71.4 (s, 3F).
IR (ATIR): v_{max} (cm^{-1}) = 3074 (w), 1712 (s), 1603 (s), 1339 (w), 1199 (s), 1170 (s), 1141 (m), 856 (m).

4.3.2. Synthesis of *p*-iodo-*N,N*-dihexylaniline (2)

Scheme 7 Synthesis of *p*-iodo-*N,N*-dihexylaniline (**2**) (R = –C$_6$H$_{13}$).

Synthesis of **2** was done according to the literature[285]. A mixture of *p*-iodoaniline (7.58 g, 34.62 mmol), 1-bromohexane (17.0 mL, 20.0 g, 121.16 mmol, 3.5 eq.), *N,N*-diisopropylethylamine (20.68 mL, 121.16 mmol, 3.5 eq.) and DMF (15 mL) was stirred at 110 °C for 22 h. After cooling to room temperature, the reaction mixture was poured on distilled water (100 mL) and the product was extracted with chloroform (3 x 75 mL). The combined organic phase was washed with distilled water (2 x 75 mL) and dried over MgSO$_4$. The obtained oil was purified by flash chromatography on silica gel using hexane / ethyl acetate (19:1, R_f = 0.9) as the eluent, yielding **2** as a yellow liquid after solvent evaporation.

Characterization of **2**:
Yield: 10.41 g, 27.10 mmol, 78 %

^{1}H-NMR (CDCl$_3$, 400 MHz, δ): 0.89 (t, J = 6.7 Hz, 6H, H-1), 1.30 (m, 12H, H-2 + H-3 + H-4), 1.54 (m, 4H, H-5), 3.21 (m, 4H, H-6), 6.40 (m, 2H, H-9), 7.42 (m, 2H, H-10).
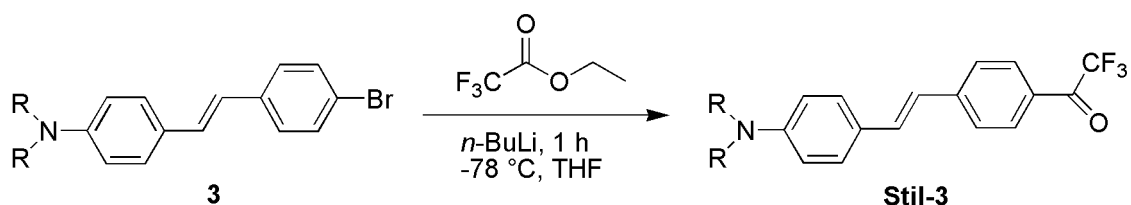^{13}C-NMR (CDCl$_3$, 100 MHz, δ): 14.2 (C-1), 22.8 (C-2) 27.0 (C-4), 27.2 (C-5), 31.9 (C-3), 51.2 (C-6), 75.5 (C-11), 114.2 (C-9), 137.8 (C-10), 147.8 (C-8).
IR (ATIR): v_{max} (cm^{-1}) = 3086 (w), 2954 (s), 2925 (s), 2855 (s), 1587 (s), 1496 (s), 1367 (m), 1193 (m).

4.3.3. Synthesis of 4-bromo-4'-(dihexylamino)stilbene (3)
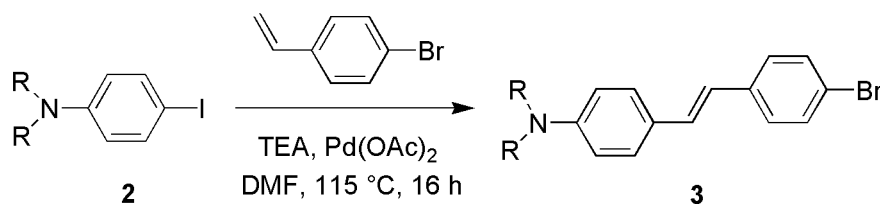
Scheme 8 Synthesis of 4-bromo-4'-(dihexylamino)stilbene (**3**) (R = –C$_6$H$_{13}$).

Synthesis of **3** was done according to the literature[285]. A mixture of **2** (9.0 g, 23.4 mmol), 4-bromostyrene (3.78 ml, 29.25 mmol, 1.25 eq.), palladium(II)diacetate (57.78 mg, 0.26 mmol, 0.011 eq.), tri-*o*-tolylphosphine (150.84 mg, 0.495 mmol, 0.021 eq.) and triethylamine (19.26 mL, 138.06 mmol, 5.9 eq.) was dissolved in dry DMF (30 mL) and refluxed at 115 °C under nitrogen for 16 h. To the cooled solution distilled water (50 mL) and chloroform (50 mL) were added and the aqueous layer was extracted with chloroform (3 x 50 mL). The combined organic layer was washed with distilled water (3 x 75 mL) and dried over Mg$_2$SO$_4$. The crude product was purified by column chromatography on silica gel using hexane / chloroform (2:1, R_f = 0.8) as the eluent and afterwards was recrystallized from methanol yielding **3** as yellow crystals which were isolated by vacuum filtration.

Characterization of **3**:
Yield: 4.00 g, 9.05 mmol, 39 %

^{1}H-NMR (CDCl$_3$, 400 MHz, δ): 0.91 (m, 6H, H-1), 1.32 (m, 12H, H-2 + H-3 + H-4), 1.59 (m, 4H, H-5), 3.28 (m, 4H, H-6), 6.61 (d, *J* = 8.9 Hz, 2H, H-9), 6.77 – 7.02 (m, 2H, H-11 + H-12), 7.31 – 7.43 (m, 6H, H-10 + H-14 + H-15).
^{13}C-NMR (CDCl$_3$, 100 MHz, δ): 14.2 (C-1), 22.8 (C-2), 27.0 (C-4), 27.4 (C-5), 31.9 (C-3), 51.2 (C-6), 111.8 (C-9), 120.0 (C-17), 122.4 (C-11), 124.2 (C-10), 127.5 (C-12), 128.0 (C-13), 129.8 (C-15), 131.7 (C-16), 137.5 (C-14), 148.2 (C-8).
IR (ATIR): ν$_{max}$ (cm^{-1}) = 3038 (w), 2955 (s), 2924 (s), 2853 (s), 1601 (s), 1516 (s), 1364 (m), 1182 (s), 819 (s).
UV/Vis (diethyl ether): λ$_{max}$ = 365 nm.
Fluorescence (diethyl ether): λ$_{ex,max}$ = 365 nm, λ$_{em,max}$ = 418 nm.

4.3.4. Synthesis of 4-trifluoracetyl-4'-(dihexylamino)stilbene (Stil-3)

Scheme 9 Synthesis of 4-trifluoroacetyl-4'-(dihexylamino)stilbene (**Stil-3**) (R = –C$_6$H$_{13}$).

Synthesis of **Stil-3** was done according to the literature[285]. **3** (250.0 mg, 0.55 mmol) was dissolved in dry tetrahydrofuran (5 mL) and cooled to -78 °C using methanol / liquid nitrogen as the cooling agent. To the stirred solution a 1.6 M solution of *n*-butyllithium in hexane

(387.5 µl, 0.65 mmol, 1.1 eq.) was added and stirring was continued for further 30 min. Then, ethyl trifluoroacetate (70.0 µL, 0.85 mmol, 1.03 eq.) was added and the solution was stirred for another 60 min. The solution was warmed up to room temperature and methanol (1 mL) was added followed by the addition of diethyl ether (20 mL). The orange solution was washed once with 1 M HCl (3 mL) and saturated NaHCO$_3$ solution (3 mL) and twice with distilled water (2 x 15 mL). After drying over MgSO$_4$ and evaporation to dryness, the orange oil was purified by column chromatography using neutral Al$_2$O$_3$ and hexane / dichloromethane (2:1, R_f = 0.4) as the eluent. The eluent was then changed to hexane / dichloromethane (1:1, R_f = 0.6) and further to dichloromethane / methanol (100:1, R_f = 1) yielding **Stil-3** as orange crystals after solvent evaporation.

Characterization of **Stil-3**:
Yield: 0.85 g, 1.84 mmol, 84 %

^{1}H-NMR (CDCl$_3$, 400 MHz, δ): 0.91 (t, J = 6.8 Hz, 6H, H-1), 1.33 (m, 12H, H-2 + H-3 + H-4), 1.60 (m, 4H, H-5), 3.30 (m, 4H, H-6), 6.64 (d, J = 8.9 Hz, 2H, H-9), 6.91 (d, J = 16.2 Hz, 2H, H-12), 7.22 (d, J = 16.2 Hz, 2H, H-13), 7.42 (d, J = 8.8 Hz, 2H, H-10), 7.57 (d, J = 8.5 Hz, 2H, H-15), 8.01 (d, J = 7.9 Hz, 2H, H-16).
^{13}C-NMR (CDCl$_3$, 100 MHz, δ): 14.2 (C-1), 22.9 (C-2), 27.0 (C-4), 27.4 (C-5), 31.9 (C-3), 51.2 (C-6), 111.5 (C-9), 121.3 (C-7), 125.9 (C-12), 128.6 (C-13), 130.9 (C-15), 134.0 (C-16), 146.1 (C-14), 148.9 (C-8), 179.8 (C-18).
^{19}F-NMR (CDCl$_3$, 376 MHz, δ): -71.1 (s, 3F).
HR-MS (ESI): m/z calculated for [C$_{28}$H$_{36}$F$_3$NO] = 459.2749; simulated [M+H]$^+$ = 460.2822, found [M+H]$^+$ = 460.2817 and simulated [M+H$_3$O]$^+$ = 478.2927, found [M+H$_3$O]$^+$ = 478.2932.
IR (ATIR): ν$_{max}$ (cm^{-1}) = 3037 (w), 2954 (m), 2927 (s), 2855 (m), 1697 (s), 1580 (s), 1520 (s), 1359 (m), 1164 (s), 1128 (s).
UV/Vis (dioxane): λ$_{max}$ (ε) = 440 nm (26500).
Melting point: 43 °C

4.3.5. Synthesis of 1-[4-(2-(4-[2-(4-dihexylaminophenyl)-vinyl]-phenyl)-vinyl)-phenyl]-2,2,2,-trifluoroethanone (Stil-4)
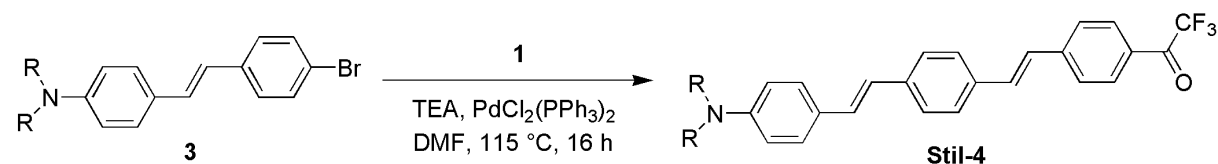
Scheme 10 Synthesis of 1-[4-(2-(4-[2-(4-dihexylaminophenyl)-vinyl]-phenyl)-vinyl)-phenyl]-2,2,2-trifluoroethanone (**Stil-4**) (R = –C$_6$H$_{13}$).

Synthesis of **Stil-4** was done according to the literature[258]. A two-neck flask was charged with **3** (2.0 g, 4.52 mmol, 1.15 eq.), **1** (788.64mg, 3.94 mmol) and dichlorobis-(triphenylphosphine)-palladium(II) (74.66 mg, 0.10 mmol, 0.027 eq.). The reactants were dissolved in triethylamine (15.0 mL, 108.0 mmol, 27.4 eq.) and dry DMF (16 mL). The reaction mixture was stirred at 115 °C for 16 h. The solution was allowed to cool down and water (50 mL) was added. The aqueous layer was extracted with DCM (3 x 50 mL) and the combined organic layers were

washed with distilled water (3 x 100 mL). After the organic layer was dried with $MgSO_4$ the solvent was removed under vacuum and the crude product was purified by column chromatography on neutral Al_2O_3 using hexane / ethyl acetate (2:1, $R_f = 0.5$) as the eluent, yielding **Stil-4** as red crystals after solvent evaporation.

Characterization of **Stil-4**:
Yield: 0.41 g, 0.73 mmol, 19 %

^{1}H-NMR (CDCl$_3$, 400 MHz, δ): 0.91 (m, 6H, H-1), 1.33 (m, 12H, H-2 + H-3 + H-4), 1.60 (m, 4H, H-5), 3.29 (m, 4H, H-6), 6.62 (d, $J = 8.9$ Hz, 2H, H-9), 6.90 - 7.31 (m, 4H, H-12 + H-13 + H-18 + H-19), 7.40 (d, $J = 8.8$ Hz, 2H, H-10), 7.51 (m, 4H, H-15 + H-16), 7.64 (d, $J = 8.5$ Hz, 2H, H-21), 8.07 (d, $J = 7.9$ Hz, 2H, H-22).

^{13}C-NMR (CDCl$_3$, 100 MHz, δ): 14.2 (C-1), 22.8 (C-2), 27.0 (C-4), 27.5 (C-5), 31.9 (C-3), 51.2 (C-6), 111.8 (C-9), 123.0 (C-15), 124.3 (C-11), 125.9 (C-16), 126.5 (C-13), 126.8 (C-18), 127.6 (C-19), 128.1 (C-12), 128.4 (C-22), 129.9 (C-21), 130.9 (C-10), 133.3 (C-23), 134.4 (C-14), 139.3 (C-17), 144.9 (C-20), 148.2 (C-8).

^{19}F-NMR (CDCl$_3$, 376 MHz, δ): -71.2 (s, 3H).

HR-MS (ESI): m/z calculated for [C$_{36}$H$_{42}$F$_3$NO] = 561.3218; simulated [M+H]$^+$ = 562.3291, found [M+H]$^+$ = 562.3280 and simulated [M+H$_3$O]$^+$ = 580.3397, found [M+H$_3$O]$^+$ = 580.3387.

IR (ATIR): ν$_{max}$ (cm^{-1}) = 3021 (w), 2955 (m), 2928 (s), 2858 (m), 1703 (s), 1605 (s), 1582 (s), 1519 (s), 1420 (w), 1168 (m), 1150 (s).

UV/Vis (dioxane): λ$_{max}$ (ε) = 438 nm (42700).

Melting point: 137 °C

4.3.6. Synthesis of *N*,*N*-dihexylaniline (4)
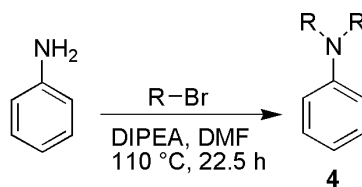
Scheme 11 Synthesis of *N*,*N*-dihexylaniline (**4**) (R = –C$_6$H$_{13}$).

Synthesis of **4** was done according to the literature[286]. A mixture of aniline (4.10 mL, 45.10 mmol), 1-bromohexane (17.0 mL, 121.16 mmol, 2.7 eq.), *N*,*N*-diisopropylethylamine (23.44 mL, 137.26 mmol, 3.0 eq.) and DMF (30 mL) was stirred at 110 °C for 22.5 h. After cooling to room temperature, the reaction mixture was poured in distilled water (50 mL) and was extracted three times with chloroform (3 x 50 mL). The combined organic phase was washed two times with distilled water (2 x 75 mL) and dried over Na$_2$SO$_4$. Subsequently, the solvent was removed and the resulting dark brown oil was purified by flash chromatography using silica gel and hexane / ethyl acetate (19:1, $R_f = 0.9$) as the eluent, yielding **4** as a yellow oil.
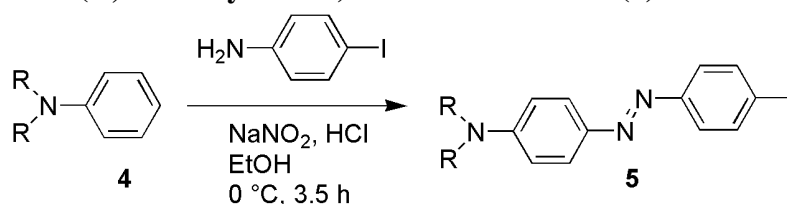
Characterization of **4**:
Yield: 11.14 g, 42.64 mmol, 95 %

^{1}H-NMR (CDCl$_3$, 400 MHz, δ): 0.91 (t, J = 6.7 Hz, 6H, H-1), 1.32 (m, 12H, H-2 + H-3 + H-4), 1.58 (m, 4H, H-5), 3.25 (m, 4H, H-6), 6.63 (m, 3H, H-9 + H-11), 7.21 (m, 2H, H-10).
^{13}C-NMR (CDCl$_3$, 100 MHz, δ): 14.2 (C-1), 22.9 (C-2) 27.0 (C-4), 27.4 (C-5), 31.9 (C-3), 51.2 (C-6), 111.8 (C-9), 115.2 (C-11), 129.3 (C-10), 148.4 (C-8).
IR (ATIR): v_{max} (cm^{-1}) = 3060 (w), 2955 (s), 2926 (s), 2856 (m), 1597 (m), 1503 (s), 1464 (w), 1367 (w).

4.3.7. Synthesis of 4-(*N,N*-dihexylamino)-4'-iodoazobenzene (5)

Scheme 12 Synthesis of 4-(*N,N*-dihexylamino)-4'-iodoazobenzene (**5**) (R = –C$_6$H$_{13}$).

Synthesis of **5** was done according to the literature[286]. 4-Iodoaniline (2.0 g, 9.13 mmol) was suspended in 6 M hydrochloric acid (12.17 mL) and cooled to 5 °C by means of an ice bath. Then, NaNO$_2$ (756.0 mg, 10.96 mmol, 1.2 eq.) dissolved in distilled water (5.8 mL) was added to the suspension and the resulting dispersion was added dropwise to a solution of **4** (2.24 g, 8.58 mmol, 0.94 eq.) in ethanol (45 mL) and concentrated hydrochloric acid (1.2 mL). The reaction mixture was stirred for 3.5 h in an ice bath at 0 °C and then allowed to warm up to room temperature. After stirring at room temperature for additional 1.5 h, the reaction mixture was extracted with chloroform (3 x 75 mL) and the combined organic phase was washed with distilled water (5 x 50 mL) and dried over Na$_2$SO$_4$. After solvent removal the resulting purple oil was purified by flash chromatography using silica gel and hexane / chloroform (3:1, R_f = 0.75) as the eluent, yielding **5** as red crystals which were recrystallized from MeOH for further purification.


Characterization of **5**:
Yield: 0.44 g, 0.90 mmol, 10 %

^{1}H-NMR (CDCl$_3$, 400 MHz, δ): 0.91 (m, 6H, H-1), 1.33 (m, 12H, H-2 + H-3 + H-4), 1.63 (m, 4H, H-5), 3.35 (m, 4H, H-6), 6.68 (d, J = 9.2 Hz, 2H, H-9), 7.56 (d, J = 8.6 Hz, 2H, H-10), 7.80 (m, 4H, H-10 + H-15 + H-16).
^{13}C-NMR (CDCl$_3$, 100 MHz, δ): 14.2 (C-1), 22.8 (C-2), 26.9 (C-4), 27.5 (C-5), 31.8 (C-3), 51.4 (C-6), 94.9 (C-17), 111.3 (C-9), 124.0 (C-10), 125.6 (C-15), 138.2 (C-16), 143.2 (C-11), 150.9 (C-17), 152.9 (C-8).
IR (ATIR): v_{max} (cm^{-1}) = 3055 (w), 2952 (s), 2855 (s), 1597 (s), 1512 (s), 1416 (w), 1167 (w).

4.3.8. Synthesis of 4-(*N,N*-dihexylamino)-4'-(trifluoroacetyl)azobenzene (Azo-3)
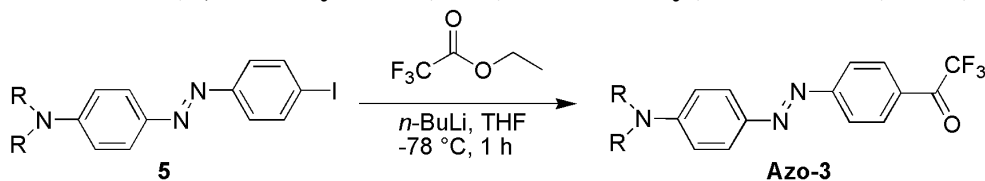
Scheme 13 Synthesis of 4-(*N,N*-dihexylamino)-4'-(trifluoroacetyl)azobenzene (**Azo-3**) (R = –C$_6$H$_{13}$).

Synthesis of **Azo-3** was done according to the literature[286]. **5** (250.0 mg, 0.50 mmol, 1.0 eq.) was dissolved and stirred in dry THF (7 mL) at -78 °C under argon atmosphere. A 1.6 M solution of *n*-butyl lithium in hexane (354.9 µL, 0.55 mmol, 1.1 eq.) was added dropwise to the reaction mixture. After 30 min ethyl trifluoroacetate (61.16 µL, 0.52 mmol, 1.03 eq.) was slowly added and the reaction mixture was continuously stirred for 1 h at -78 °C. The solution was warmed to room temperature, methanol (1 mL) was added, followed by the addition of diethyl ether (20 mL). Then, the solution was washed once with 1 M HCl (3 mL) and saturated NaHCO$_3$ solution (3 mL) and twice with distilled water (2 x 15 mL). The organic phase was dried over Na$_2$SO$_4$, and the solvent was removed. The crude product was purified by column chromatography using neutral Al$_2$O$_3$ and hexane / chloroform (2:1, R_f = 0.1) as the eluent to yield **Azo-3** as dark red crystals.

Characterization of **Azo-3**:
Yield: 49.7 mg, 0.11 mmol, 22 %

^{1}H-NMR (CDCl$_3$, 400 MHz, δ): 0.92 (m, 6H, H-1), 1.35 (m, 12H, H-2 + H-3 + H-4), 1.65 (m, 4H, H-5), 3.38 (m, 4H, H-6), 6.71 (d, *J* = 9.2 Hz, 2H, H-9), 7.91 (m, 4H, H-10 + H-15), 8.16 (d, *J* = 8.2 Hz, 2H, H-16).
^{13}C-NMR (CDCl$_3$, 100 MHz, δ): 14.2 (C-1), 22.8 (C-2), 27.0 (C-4), 27.5 (C-5), 31.8 (C-3), 51.5 (C-6), 111.4 (C-9), 115.8 (C-19), 122.6 (C-15), 126.5 (C-10), 129.3 (C-17), 131.5 (C-16), 143.6 (C-11), 151.9 (C-8), 157.7 (C-14).
^{19}F-NMR (CDCl$_3$, 376 MHz, δ): -71.2 (s, 3F).
IR (ATIR): ν_{max} (cm^{-1}) = 3080 (w), 2928 (s), 2859 (m), 1703 (s), 1593 (s), 1514 (m), 1315 (s), 1187 (s), 1130 (s), 938 (m).
UV/Vis (dioxane): λ_{max} = 482 nm.

4.4. Preparation of polymeric resins
4.4.1. Preparation of poly(styrene-*co*-divinylbenzene) (PS/DVB)
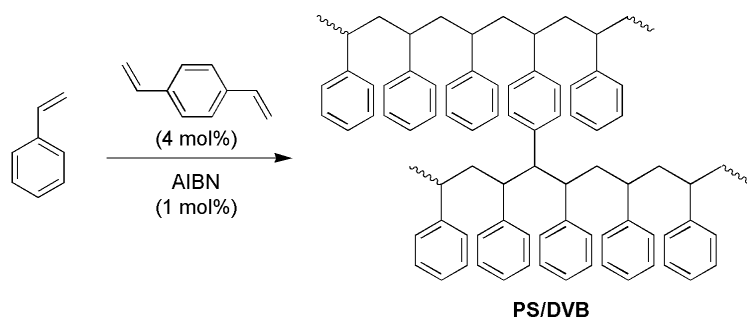
Scheme 14 Synthesis of poly(styrene-*co*-divinylbenzene) (**PS/DVB**).

Styrene and divinylbenzene (4 mol% referred to styrene) were mixed in a one-neck flask. Subsequently, AIBN (1 mol% referred to styrene) was dissolved in the reaction mixture. The required amount of **Stil-3** or **Stil-4** (**Table 11**) was dissolved in the reaction mixture (1 g), which subsequently was transferred into a teflon mould (25 mm x 10 mm x 2 mm) and was stored in an oven at 78 °C for 3 hours. During the curing process the teflon mould was covered with a watch glass to reduce the evaporation of styrene. After 3 hours the polymer was obtained as a transparent, glass-like specimen.

Characterization of **PS/DVB**:
Appearance: Solid, transparent, colorless
IR (ATIR): ν_{max} (cm^{-1}) = 3082 (w), 3059 (w), 3026 (m), 2920 (s), 2848 (w), 1601 (w), 1493 (s), 1451 (s), 697 (s).

Characterization of **PS/DVB** containing **Stil-3** (**Table 11**, entry 1):
Appearance: Solid, transparent, yellow
IR (ATIR): ν_{max} (cm^{-1}) = 3083 (w), 3060 (w), 3026 (m), 2921 (s), 2849 (w), 1601 (w), 1493 (s), 1451 (s), 697 (s).

Characterization of **PS/DVB** containing **Stil-4** (**Table 11**, entry 4):
Appearance: Solid, transparent, orange
IR (ATIR): ν_{max} (cm^{-1}) = 3083 (w), 3060 (w), 3026 (m), 2921 (s), 2849 (w), 1601 (w), 1493 (s), 1451 (s), 696 (s).

Table 11 Used sensor amounts and sensor concentrations for embedding **Stil-3** and **Stil-4** in **PS/DVB**.

Entry	Dye	m (mg)	n (µmol)	c (mg / g resin)
1	**Stil-3**	0.125	0.27	0.125
2	**Stil-3**	0.250	0.54	0.250
3	**Stil-3**	0.500	1.08	0.500
4	**Stil-4**	0.125	0.23	0.125
5	**Stil-4**	0.250	0.45	0.250
6	**Stil-4**	0.500	0.90	0.500

4.4.2. Synthesis of poly(ester imide) PEI-1

PEI-1A / PEI-1B
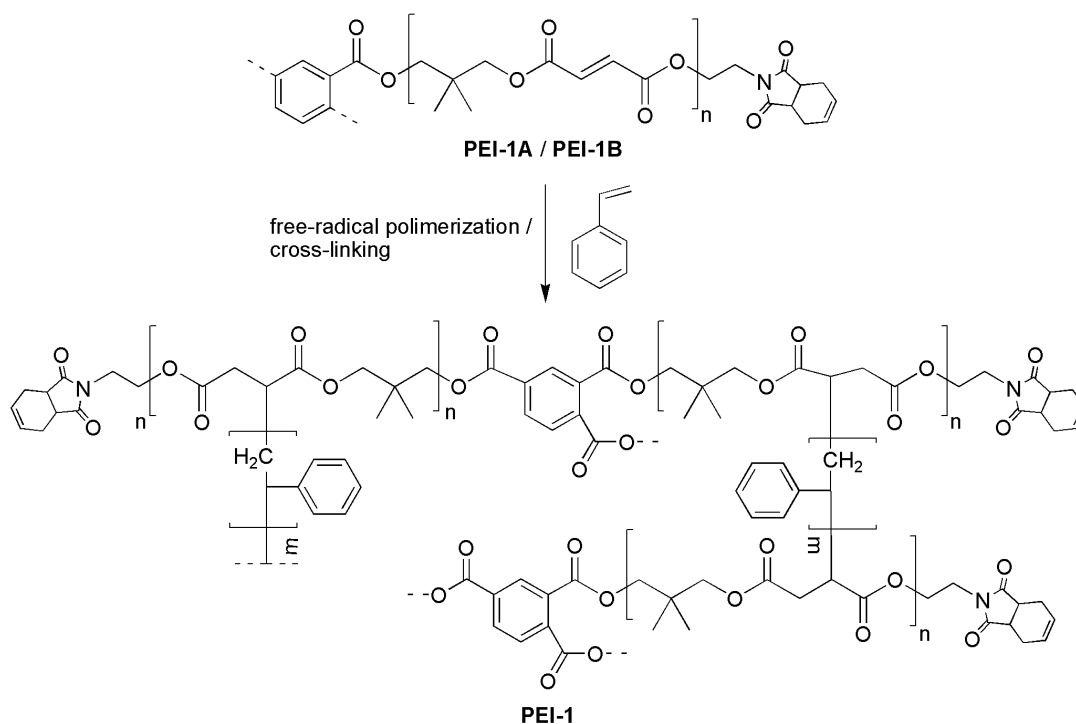
PEI-1

Scheme 15 Synthesis of a poly(ester imide) with trimellitic acid core structure and styrene as comonomer (**PEI-1**).

PEI-1 is a two-component system containing the pre-condensed **PEI-1PC**, a radical initiator and styrene. Curing was done according to the manufacturing protocol, by mixing both components **PEI-1A** and **PEI-1B** in a 50/50 (wt%) ratio. The required amount of **Stil-3**, **Stil-4** or **Azo-3** (**Table 12**) was dissolved in the reaction mixture (1 g), which subsequently was transferred into a teflon mould (25 mm x 10 mm x 2 mm) and cured by storing the teflon mould within a petri-dish in a pre-heated oven at 80 °C for 50 minutes, followed by 5 minutes at 140 °C. During the curing process the teflon mould was covered with a watch glass to reduce the evaporation of styrene. After cooling down, **PEI-1** was removed as a solid, transparent, brownish specimen.

Characterization of **PEI-1A**:
Appearance: Liquid, transparent, brown
IR (ATIR): ν_{max} (cm^{-1}) = 3444 (w), 3082 (w), 3058 (w), 2976 (w), 1723 (s), 1705 (s), 1603 (w), 1474 (m), 1257 (m), 1119 (m), 1021 (w), 700 (w), 536 (m).

Characterization of **PEI-1B**:
Appearance: Liquid, transparent, light brown
IR (ATIR): ν_{max} (cm^{-1}) = 3443 (w), 3083 (w), 3028 (w), 2965 (w), 1723 (s), 1704 (s), 1603 (w), 1398 (m), 1293 (m), 1119 (m), 1022 (m), 700 (w).

Characterization of **PEI-1**:
Appearance: Solid, transparent, light brown

IR (ATIR): ν_{max} (cm^{-1}) = 3481 (w), 3030 (w), 2963 (m), 1726 (s), 1703 (s), 1398 (w), 1258 (s), 1071 (s), 1013 (s), 793 (s).

Characterization of **PEI-1** containing **Stil-3** (**Table 12**, entry 7):
Appearance: Solid, transparent, yellowish
IR (ATIR): ν_{max} (cm^{-1}) = 3459 (w), 3031 (w), 2961 (w), 1725 (s), 1703 (s), 1452 (w), 1397 (m), 1241 (m), 1150 (m), 1022 (m).

Characterization of **PEI-1** containing **Stil-4** (**Table 12**, entry 15):
Appearance: Solid, transparent, orange
IR (ATIR): ν_{max} (cm^{-1}) = 3465 (w), 3031 (w), 2962 (w), 1725 (s), 1702 (s), 1453 (w), 1397 (m), 1243 (m), 1151(m), 1022 (m).

Characterization of **PEI-1** containing **Azo-3** (**Table 12**, entry 17):
Appearance: Solid, transparent, red
IR (ATIR): ν_{max} (cm^{-1}) = 3442 (w), 3032 (w), 2961 (w), 1703 (s), 1393 (w), 1247 (m), 1151 (m), 1018 (w), 702 (w).

Table 12 Used sensor amounts and sensor concentrations for embedding **Stil-3**, **Stil-4** and **Azo-3** in **PEI-1**.

Entry	Dye	m (mg)	n (µmol)	c (mg / g resin)
1	**Stil-3**	0.0625	0.14	0.0625
2	**Stil-3**	0.125	0.27	0.125
3	**Stil-3**	0.1875	0.41	0.1875
4	**Stil-3**	0.25	0.54	0.25
5	**Stil-3**	0.50	1.08	0.50
6	**Stil-3**	0.75	1.63	0.75
7	**Stil-3**	1.00	2.18	1.00
8	**Stil-3**	2.00	4.35	2.00
9	**Stil-4**	0.0625	0.11	0.0625
10	**Stil-4**	0.125	0.23	0.125
11	**Stil-4**	0.1875	0.34	0.1875
12	**Stil-4**	0.25	0.45	0.25
13	**Stil-4**	0.50	0.90	0.50
14	**Stil-4**	0.75	1.35	0.75
15	**Stil-4**	1.00	1.78	1.00
16	**Stil-4**	2.00	3.56	2.00
17	**Azo-3**	0.50	1.08	0.50

4.4.3. Synthesis of poly(ester imide) PEI-2
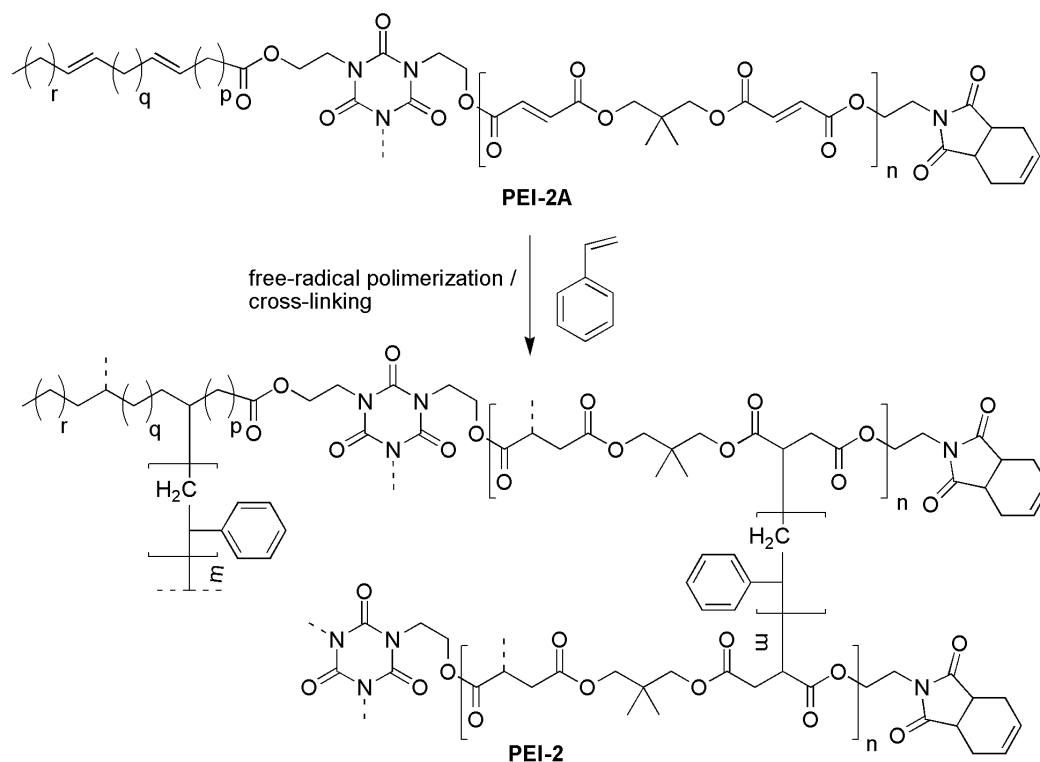
Scheme 16 Synthesis of a poly(ester imide) with 1,3,5-tris(2-hydroxyethyl)isocyanurate core structure and styrene as comonomer (**PEI-2**).

PEI-2 was a single-component system that contained the pre-condensed **PEI-2PC**, a radical initiator and styrene. Curing was done according to the manufacturing protocol. The required amount of **Stil-3** or **Stil-4** (**Table 13**) was dissolved in **PEI-2A** (1 g), which subsequently was transferred into a teflon mould (25 mm x 10 mm x 2 mm) and cured by storing the teflon mould within a petri-dish in a pre-heated oven at 140 °C for 3 hours. During the curing process the teflon mould was covered with a watch glass to reduce the evaporation of styrene. After cooling down, **PEI-2** was removed as a solid, transparent, yellowish specimen.

Characterization of **PEI-2A**:
Appearance: Liquid, slightly turbid, light brown
IR (ATIR): ν_{max} (cm^{-1}) = 3444 (w), 3082 (w), 3029 (w), 2927 (w), 1723 (s), 1703 (s), 1645 (w), 1450 (m), 1257 (m), 1152 (m), 1119 (w), 1021 (w), 700 (w).

Characterization of **PEI-2**:
Appearance: Solid, transparent, light brown
IR (ATIR): ν_{max} (cm^{-1}) = 3456 (w), 3028 (w), 2927 (w), 2854 (w), 1725 (s), 1700 (s), 1454 (w), 1397 (w), 1258 (m), 1151 (m), 1022 (m).

Characterization of **PEI-2** containing **Stil-3** (**Table 13**, entry 4):
Appearance: Solid, transparent, orange
IR (ATIR): ν_{max} (cm^{-1}) = 3457 (w), 3031 (w), 2927 (w), 2854 (w), 1725 (s), 1699 (s), 1457 (w), 1398 (m), 1256 (m), 1152 (s), 1022 (m).

Characterization of **PEI-2** containing **Stil-4** (**Table 13**, entry 12):

Appearance: Solid, transparent, deep orange

IR (ATIR): v_{max} (cm^{-1}) = 3463 (w), 3029 (w), 2927 (w), 2854 (w), 1723 (s), 1698 (s), 1456 (w), 1398 (m), 1255 (m), 1152 (s), 1022 (m).

Table 13 Used sensor amounts and sensor concentrations for embedding **Stil-3** and **Stil-4** in **PEI-2**.

Entry	Dye	m (mg)	n (µmol)	c (mg / g resin)
1	**Stil-3**	0.0625	0.14	0.0625
2	**Stil-3**	0.125	0.27	0.125
3	**Stil-3**	0.1875	0.41	0.1875
4	**Stil-3**	0.25	0.54	0.25
5	**Stil-3**	0.50	1.08	0.50
6	**Stil-3**	0.75	1.63	0.75
7	**Stil-3**	1.00	2.18	1.00
8	**Stil-3**	2.00	4.35	2.00
9	**Stil-4**	0.0625	0.11	0.0625
10	**Stil-4**	0.125	0.23	0.125
11	**Stil-4**	0.1875	0.34	0.1875
12	**Stil-4**	0.25	0.45	0.25
13	**Stil-4**	0.50	0.90	0.50
14	**Stil-4**	0.75	1.35	0.75
15	**Stil-4**	1.00	1.78	1.00
16	**Stil-4**	2.00	3.56	2.00

4.4.4. Synthesis of poly(ester imide) PEI-3

PEI-3 is a one-component system containing the pre-condensed PEI, a radical initiator and methyl methacrylate. Curing was done according to the manufacturing protocol. The required amount of **Stil-3** or **Stil-4** (**Table 14**) was dissolved in **PEI-3A** (1 g), which subsequently was transferred into a teflon mould (25 mm x 10 mm x 2 mm) and cured by storing the teflon mould within a petri-dish in a pre-heated oven at 150 °C for 2 hours. During the curing process the teflon mould was covered with a watch glass to reduce the evaporation of methyl methacrylate. After cooling down, **PEI-3** was removed as a solid, transparent specimen.
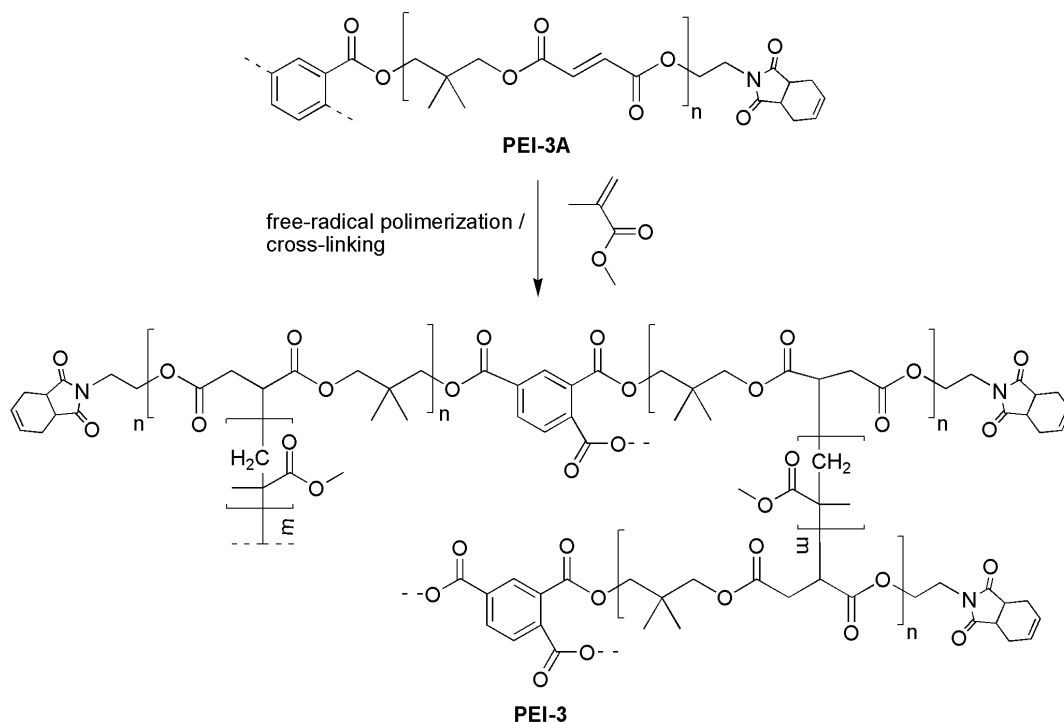
Scheme 17 Synthesis of a poly(ester imide) with trimellitic acid core structure and methyl methacrylate as comonomer (**PEI-3**).

Characterization of **PEI-3A**:
Appearance: Liquid, transparent, light brown
IR (ATIR): ν_{max} (cm^{-1}) = 3442 (w), 3044 (w), 2957 (w), 2889 (w), 1716 (s), 1638 (w), 1452 (w), 1257 (m), 1166 (m), 1026 (w), 657 (w).

Characterization of **PEI-3**:
Appearance: Solid, transparent, light brown
IR (ATIR): ν_{max} (cm^{-1}) = 3484 (w), 2952 (w), 2979 (w), 1721 (s), 1450 (w), 1397 (w), 1252 (m), 1149 (m).

Characterization of **PEI-3** containing **Stil-3** (**Table 14**, entry 4):
Appearance: Solid, transparent, orange
IR (ATIR): ν_{max} (cm^{-1}) = 3484 (w), 2945 (w), 2882 (w), 1722 (s), 1473 (w), 1395 (w), 1253 (m), 1148 (m).

Characterization of **PEI-3** containing **Stil-4** (**Table 14**, entry 9):
Appearance: Solid, transparent, yellowish
IR (ATIR): ν_{max} (cm^{-1}) = 3491 (w), 2951 (w), 2882 (w), 1721 (s), 1473 (w), 1395 (w), 1254 (m), 1149 (m).

Table 14 Used sensor amounts and sensor concentrations for embedding **Stil-3** and **Stil-4** in **PEI-3**.

Entry	Dye	m (mg)	n (µmol)	c (mg / g resin)
1	**Stil-3**	0.0625	0.14	0.0625
2	**Stil-3**	0.125	0.27	0.125
3	**Stil-3**	0.1875	0.41	0.1875
4	**Stil-3**	0.25	0.54	0.25
5	**Stil-3**	0.50	1.08	0.50
6	**Stil-4**	0.0625	0.11	0.0625
7	**Stil-4**	0.125	0.23	0.125
8	**Stil-4**	0.1875	0.34	0.1875
9	**Stil-4**	0.25	0.45	0.25
10	**Stil-4**	0.50	0.90	0.50

4.4.5. Synthesis of polyurethane PU-1
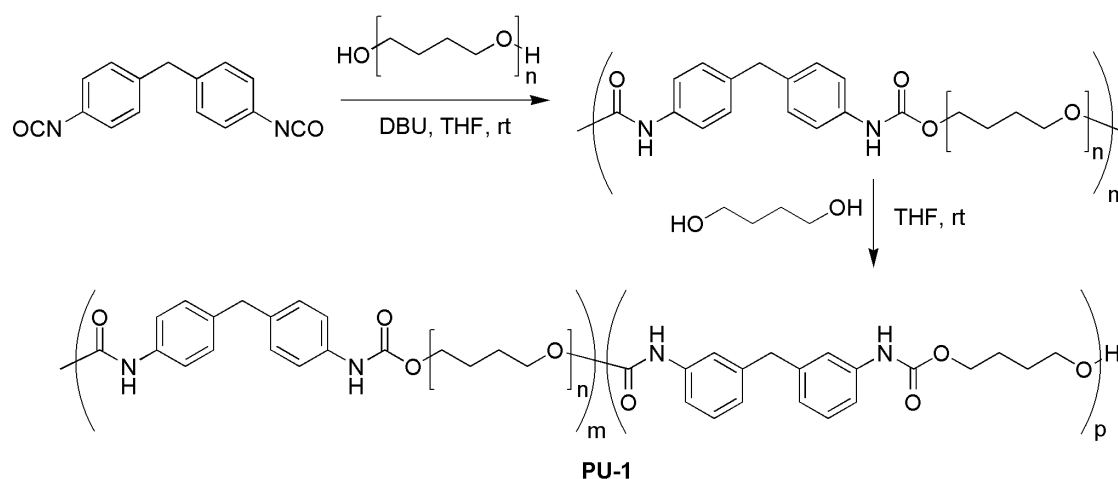
Scheme 18 Synthesis of polyurethane (**PU-1**).

The synthesis of **PU-1** was done according to the literature[274]. Bis(hydroxyl)-telechelic poly(tetrahydrofuran) **PTHF** (6.00 g, 2.06 mmol, M_n = 2900 g/mol) was dried at 50 °C under vacuum for two hours. 4,4-Methylendi(phenylisocyante) (1.04 g, 4.14 mmol) was dissolved in THF (3 mL) and was added to the **PTHF**, followed by the addition of THF (15 mL). After stirring the reaction mixture for 15 minutes at room temperature, two drops of 1,8-diazobicyclo[5.4.0]undec-7-ene were added. After 15 minutes 1,4-butanediol (183 µL, 2.07 mmol) dissolved in THF (1 mL) was added to the reaction mixture and condensation was allowed to proceed for further 15 minutes at room temperature. The transparent, colorless, viscous reaction mixture was then poured into a Petri dish and after five days the **PU-1** could be removed as a solid foil. For sensor embedding, the required amount of **Stil-3** or **Stil-4** (**Table 15**) was dissolved in THF (1 mL) and was added to the reaction mixture one minute before the reaction mixture was poured into the Petri dish.

Characterization of **PU-1**:
Appearance: Solid, slightly turbid, colorless
^{1}H-NMR (400 MHz, CDCl$_3$, δ): 7.26 – 6.74 (m, -ArH), 4.17 (m, -COOCH_2-), 3.86 (-ArCH_2), 3.40 (-CH_2O-), 2.51 (-OH), 1.61 (-CH_2CH$_2$O-).
IR (ATIR): ν_{max} (cm^{-1}) = 3327 (w), 2941 (m), 2859 (s), 2800 (w), 1731 (m), 1533 (m), 1369 (m), 1220 (m), 1107 (s), 998 (m).
GPC (THF, 30 °C, RI): M_w = 86600 g/mol, Đ = 1.90.

Characterization of **PU-1** containing **Stil-3** (**Table 15**, entry 5):
Appearance: Solid, slightly turbid, yellow
^{1}H-NMR (400 MHz, CDCl$_3$, δ): 7.28 – 6.75 (m, -ArH), 4.17 (m, -COOCH_2-), 3.86 (-ArCH_2), 3.40 (-CH_2O-), 2.54 (-OH), 1.61 (-CH_2CH$_2$O-).
IR (ATIR): ν_{max} (cm^{-1}) = 3320 (w), 2939 (m), 2854 (s), 2796 (w), 1731 (m), 1533 (m), 1368 (m), 1220 (m), 1102 (s).

Characterization of **PU-1** containing **Stil-4** (**Table 15**, entry 7):
Appearance: Solid, slightly turbid, turquoise
^{1}H-NMR (400 MHz, CDCl$_3$, δ): 7.28 – 6.72 (m, -ArH), 4.18 (m, -COOCH_2-), 3.86 (-ArCH_2), 3.40 (-CH_2O-), 2.52 (-OH), 1.61 (-CH_2CH$_2$O-).
IR (ATIR): ν_{max} (cm^{-1}) = 3320 (w), 2941 (m), 2862 (s), 2799 (w), 1731 (m), 1533 (m), 1371 (m), 1221 (m), 1106 (s), 996 (w).
GPC (THF, 30 °C, RI): M_n = 69000 g/mol, Đ = 1.75.

Table 15 Used sensor amounts and sensor concentrations for embedding **Stil-3** and **Stil-4** in **PU-1**.

Entry	Dye	m (mg)	n (µmol)	c (mg / g resin)	$M_{w, GPC}$ (g/mol) (PDI)
1	**Stil-3**	0.0625	0.14	0.009	83000 (1.90)
2	**Stil-3**	0.125	0.27	0.017	60400 (2.03)
3	**Stil-3**	0.1875	0.41	0.025	53600 (2.00)
4	**Stil-3**	0.25	0.54	0.033	78400 (2.20)
5	**Stil-3**	0.50	1.08	0.067	78300 (1.89)
6	**Stil-4**	0.25	0.45	0.033	76600 (1.80)
7	**Stil-4**	0.50	0.90	0.067	69000 (1.75)

5. Summary

The aim of this work was the development of a sensor system for the inline detection of the thermal degradation of poly(ester imides) (PEIs). PEIs are used as coating materials in electric industry. The possibility to monitor the condition of the protective insulation at any time will improve its safety and sustainability.

Therefore, the pure PEIs **PEI-1PC** and **PEI-2PC** together with the corresponding cross-linked resin **PEI-1** and **PEI-2** using styrene as comonomer were thermally degraded and the degradation products were analyzed to identify suitable target molecules (**Figure 73**).
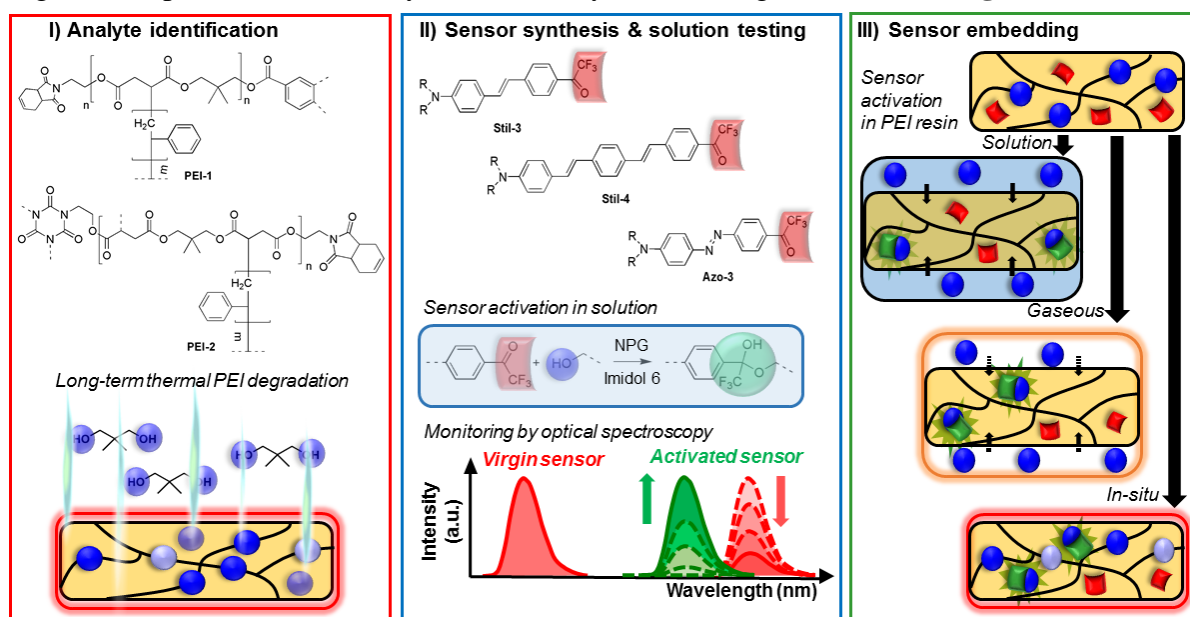
Figure 73 Long-term thermal degradation of **PEI-1** and **PEI-2** and the corresponding pre-condensates yielded alcoholic degradation products, especially NPG as main analytes. Consequently, the alcohol sensitive trifluoroacetyl functionalized optical chemosensors **Stil-3**, **Stil-4** and **Azo-3** were synthesized and their suitability was tested in solution experiments. Subsequently, the suitable sensors **Stil-3** and **Stil-4** were embedded within **PEI-1** and **PEI-2** and their solid state activation was proven under increasingly realistic conditions.

The thermal degradation was carried out under realistic conditions, which required the development of a suitable apparatus. Specimens were stored in glass-tubes which were placed in a sand bath at 180 °C, 200 °C and 220 °C over a period of 5000 h. An applied flow of air flushed the gaseous degradation products into an adsorption column from which the trapped analytes were extracted after 500 h, 1000 h, 3000 h and 5000 h and subsequently were analyzed by ^{1}H-NMR spectroscopy and ESI-TOF-MS.

Overall, **PEI-2** showed a higher thermal stability which was due to the trivalent 1,3,5-tris(2-hydroxyethyl)isocyanurate (THEIC) core structure, which has a higher thermal stability compared to the trimellitic anhydrid (TMA) used for the synthesis of **PEI-1**. The mass loss during thermal aging significantly depended on the degradation temperature. In all cases, higher temperatures accelerated the initial mass loss. After 5000 h of thermal degradation, the mass loss of **PEI-1** was 6.4 % at 220 °C and 6.0 % at 180 °C. For **PEI-2** the mass loss at 220 °C was 7.8 % after 5000 h and 2.7 % at 180 °C. For all investigated PEIs, neopentyl glycol (NPG) was identified as the main degradation product which was constantly released during long-term

thermal experiments. Furthermore, Imidol 6 was identified as second alcoholic target molecule which especially was found in greater amounts within the first 1000 h of thermal degradation. Due to the results from the long-term thermal degradation experiments, three alcohol sensitive sensor molecules **Stil-3**, **Stil-4** and **Azo-3** were synthesized. All sensor molecules were functionalized with a trifluoroacetyl group, serving as nucleophilic receptor and thus allowing a nucleophilic addition of the alcohol which subsequently triggered a shift of the absorption and emission maxima. In solution all three sensor molecules were activated by NPG and the activation was followed by UV-Vis- and fluorescence spectroscopy, with the exception of **Azo-3** which was found to be non-fluorescent. Pre-investigations of the later matrices **PEI-1** and **PEI-2** showed strong absorption at wavelength where the sensor signals were expected and thus fluorescence spectroscopy was assumed to be the more suitable detection method. Therefore, investigations were focused on **Stil-3** and **Stil-4** and they were extensively studied in solution experiments.

The sensitivity towards different nucleophilic analytes with different concentrations was tested and the fastest activation was observed for *n*-butylamine (*n*-BuA) which was due to its higher nucleophilicity compared to alcohols. The rate of sensor activation by alcohols depended on the functionality, the steric demand of the analyte and its concentration. For the following analytes, activation was found to occur at a decreasing rate: 1,4-butanediol (1,4-BuOH), MeOH, NPG, 1-butanol (1-BuOH), Imidol 6 and *tert*-butanol (*t*-BuOH). The fastest sensor reaction was observed for *n*-BuA within seconds and the slowest activation for *t*-BuOH which triggered the maximum conversion after 65 days for **Stil-3** and 49 days for **Stil-4**. Higher analyte concentrations accelerated the sensor activation and led to higher conversion of the corresponding hemiacetal. Overall, **Stil-4** showed faster kinetics compared to **Stil-3** for all investigated analytes.

Afterwards, **Stil-3** and **Stil-4** were embedded within resins and their activation and detection was tested in solid state. First, both sensors were embedded within poly(styrene-*co*-divinylbenzene) **PS/DVB**, serving as non-fluorescent model resin to investigate sensor detection and response without resin interferences. **Stil-3** and **Stil-4** were detectable within **PS/DVB** and their activation by *n*-BuA solution was monitored by fluorescence spectroscopy, showing a decrease of the fluorescence intensity by 27 % after 8 days and by 24 % after 3 days, respectively. Corresponding control experiments did not show significant changes, thus sensor activation within **PS/DVB** was successfully demonstrated, whereas it was slower compared to solution experiments which was due to hindered analyte diffusion.

Subsequently, **Stil-3** and **Stil-4** were embedded within **PEI-1** and were exposed to *n*-BuA to trigger a fast sensor activation which was monitored by fluorescence spectroscopy. A fluorescence intensity decrease by 56 % was observed for both dyes, whereas **Stil-3** reached a maximum conversion after 15 days and **Stil-4** after 4 days. Control experiments of dye containing specimen stored in water showed a decrease of up to 23 %. However, this decrease was attributed to diol formation by water addition and was significantly slower than hemiaminal formation and is assumed to be irrelevant under application similar to conditions in electric motors.

In a next step, sensor activation within **PEI-1** was done by exposure to the gaseous main analyte NPG. **Stil-3** showed a fluorescence decrease by 26 % in the cause of 30 days. When a specimen was stored under the same conditions but in absence of NPG, the control experiments showed only a minor fluorescence decrease by 4 % and thus activation of **Stil-3** in **PEI-1** was proven.

However, for **Stil-4** a strong fluorescence decrease for the actual specimen and the control experiment was observed. This was attributed to the high reactivity of **Stil-4** which probably lowered its suitability at even moderate temperatures due to fast sensor activation in the presence of small quantities of analytes.

Finally, sensor activation was attempted by in-situ analyte generation through thermal PEI degradation. Specimens were stored at 180 °C, the maximum usage temperature of **PEI-1**, and both dyes showed a fast and strong initial fluorescence decrease within 20 days. After 81 days maximum conversion was not reached for **Stil-3** but almost reached for **Stil-4**, thus proving the higher reactivity of **Stil-4**. The progress of sensor activation was in good accordance with the results from the thermal degradation experiments, which also showed a strong initial analyte release.

Similar experiments were conducted for **Stil-3** and **Stil-4** embedded within **PEI-2**. However, while for the activation with *n*-BuA similar activation durations were observed, for the specimens in gaseous NPG activation of **Stil-3** and **Stil-4** was significantly slower compared to **PEI-1**. Again, the results from the thermal activation by in-situ analyte formation were in very good accordance with the results from the degradation pattern found in the initial decomposition experiments. Due to the higher thermal stability sensor activation of both sensor molecules was slower compared to **PEI-1**, because less analytes were generated. **Stil-4** showed the steady decrease of the fluorescence intensity whereas **Stil-3** showed a strong initial decrease and afterwards was constant for 50 days. Thus, the thermal stability for **Stil-3** at 180 °C was proven and all related fluorescence changes were attributed to the activation reaction. Therefore, **Stil-3** and **Stil-4** are suitable sensors to monitor the thermal degradation of **PEI-1** and **PEI-2** by fluorescence spectroscopy, whereas **Stil-3** is more suitable for long-term monitoring.

Sensor embedding within **PEI-3**, which has the similar structure as **PEI-1** but was cross-linked with acrylic comonomers instead of styrene and thus allows less π-π-interactions with the dye molecules, and concentration dependent time-resolved fluorescence spectroscopy were performed to investigate potential dye/matrix interferences. A complex fluorescence pattern of **Stil-3** and **Stil-4** was determined, whereas dye/matrix interactions were stronger for **Stil-4** (**Figure 74**).
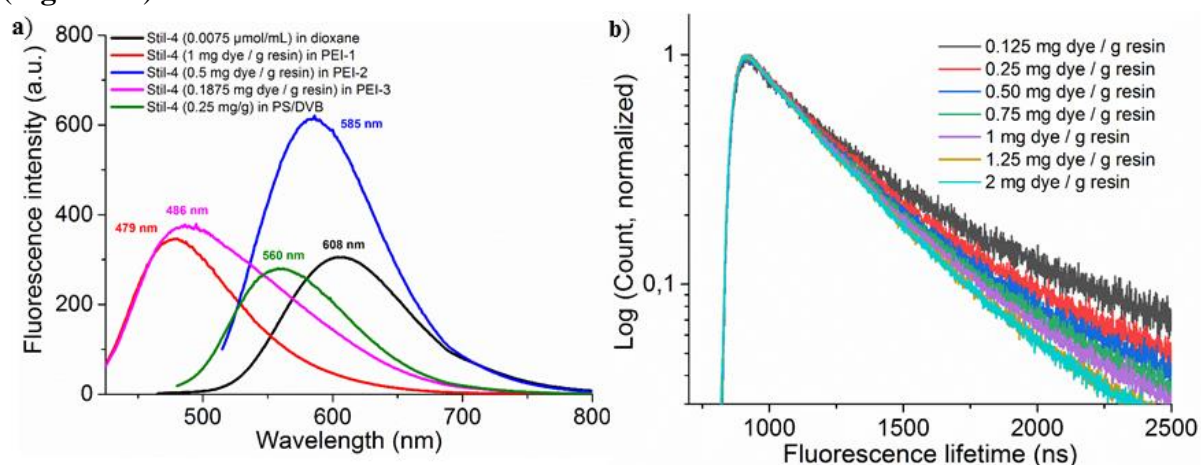
Figure 74 When **Stil-4** was embedded in different resins a strong a) matrix and b) concentration dependency was observed, which was attributed to dye aggregation.

This was explained by the longer conjugated system and poor solubility of **Stil-4** compared to **Stil-3** which consequently allowed stronger dye aggregation.

In addition, beyond the scope of the project, **Stil-3** was embedded within a supramolecular polyurethane (PU) network. **PU-1** was synthesized by a polyaddition of poly(tetrahydrofuran) (PTHF), 1,4-BuOH and 4,4-methylendi(phenylisocyante) (MDI) (**Figure 75a**).
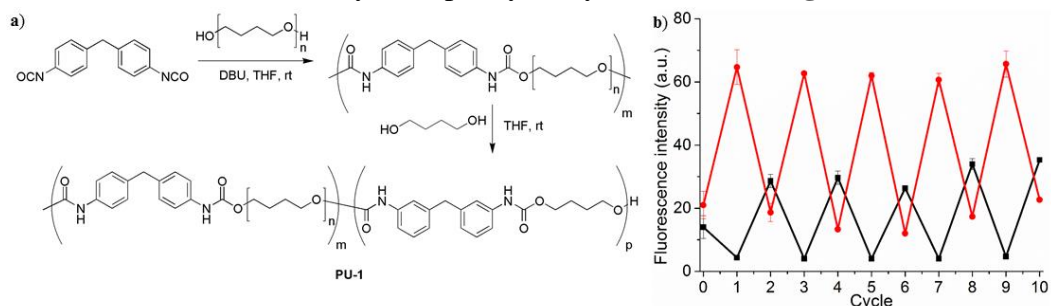
Figure 75 a) **Stil-3** was embedded within the dynamic, supramolecular **PU-1** which allowed a repeated sensor activation and deactivation without decrease in sensor performance.

Due to the dynamic structure of **PU-1**, the specimens could be repeatedly activated and deactivated at different dye concentrations and different concentrations of *n*-BuA without showing sensor exhaustion after 10 cycles consisting of 5 activation processes by 2 days storage in *n*-BuA and 5 deactivation processes by 2 days storage in vacuum (**Figure 75b**). This feature might expand the field of application of **Stil-3** in solid state usage when repeated sensor activation is required.

6. Literature

1. Katz, R., High-Temperature Structural Ceramics. *Science* **1980,** *208*, 841-7.

2. Hirschfeld, D. A.; Li, T. K.; Liu, D. M., Processing of Porous Oxide Ceramics. *Key Eng. Mater.* **1995,** *115*, 65-80.

3. Axinte, E., Glasses as engineering materials: A review. *Mater. Des.* **2011,** *32* (4), 1717-1732.

4. Lu, K., Materials science. The future of metals. *Science* **2010,** *328* (5976), 319-20.

5. Graedel, T. E., On the Future Availability of the Energy Metals. *Annu. Rev. Mater. Res.* **2011,** *41* (1), 323-335.

6. Lahiri, A. K., Classification of Metallic Engineering Materials. In *Applied Metallurgy and Corrosion Control : A Handbook for the Petrochemical Industry*, Springer Singapore: Singapore, **2017**; pp 17-39.

7. Staudinger, H., Über Polymerisation. *Ber. Dtsch. Chem. Ges.* **1920,** *53* (6), 1073-1085.

8. AlMaadeed, M. A. A.; Ponnamma, D.; El-Samak, A. A., Chapter 1 - Polymers to improve the world and lifestyle: physical, mechanical, and chemical needs. In *Polymer Science and Innovative Applications*, AlMaadeed, M. A. A.; Ponnamma, D.; Carignano, M. A., Eds. Elsevier: **2020**; pp 1-19.

9. Wojtecki, R. J.; Nelson, A., Small changes with big effects: Tuning polymer properties with supramolecular interactions. *J. Polym. Sci., Part A: Polym. Chem.* **2016,** *54* (4), 457-472.

10. Hayashi, M., Versatile functionalization of polymeric soft materials by implanting various types of dynamic cross-links. *Polym. J.* **2021,** *53* (7), 779-788.

11. Nicholson, L.; Whitley, K.; Gates, T.; Hinkley, J. *How Molecular Structure Affects Mechanical Properties Of An Advanced Polymer*; 03/02, **2000**.

12. Xu, X.; Fukuda, K.; Karki, A.; Park, S.; Kimura, H.; Jinno, H.; Watanabe, N.; Yamamoto, S.; Shimomura, S.; Kitazawa, D.; Yokota, T.; Umezu, S.; Nguyen, T.-Q.; Someya, T., Thermally stable, highly efficient, ultraflexible organic photovoltaics. *Proc. Natl. Acad. Sci.* **2018,** *115* (18), 4589-4594.

13. Gupta, N. S.; Lee, K.-S.; Labouriau, A., Tuning Thermal and Mechanical Properties of Polydimethylsiloxane with Carbon Fibers. *Polymers* **2021,** *13* (7), 1141.

14. Wang, J.; Zhao, C.; Zhou, L.; Liang, X.; Li, Y.; Sheng, G.; Du, Z.; Tang, J., An Effective Strategy to Design a Large Bandgap Conjugated Polymer by Tuning the Molecular Backbone Curvature. *Macromolecular rapid communications* **2021,** *42* (10), 2000757.

15. Heeger, A. J., Semiconducting and Metallic Polymers: The Fourth Generation of Polymeric Materials. *J. Phys. Chem. B* **2001,** *105* (36), 8475-8491.

16. Dashtizadeh, A.; Abdouss, M.; Mahdavi, H.; Khorassani, M., Acrylic coatings exhibiting improved hardness, solvent resistance and glossiness by using silica nano-composites. *Appl. Surf. Sci.* **2011,** *257* (6), 2118-2125.

17. Shen, M.; Bever, M. B., Gradients in polymeric materials. *J. Mater. Sci.* **1972,** *7* (7), 741-746.

18. Anuar Sharuddin, S. D.; Abnisa, F.; Wan Daud, W. M. A.; Aroua, M. K., A review on pyrolysis of plastic wastes. *Energy Convers. Manage.* **2016,** *115*, 308-326.

19. Blythe, A. R.; Vinson, J., Polymeric materials for devices in optical fibre systems. *Polym. Adv. Technol.* **2000,** *11*, 601-611.

20. Andrady, A. L.; Neal, M. A., Applications and societal benefits of plastics. *Philos. Trans. R. Soc. Lond. B. Biol. Sci.* **2009,** *364* (1526), 1977-1984.

21. Haque, S. M.; Ardila-Rey, J. A.; Umar, Y.; Mas'ud, A. A.; Muhammad-Sukki, F.; Jume, B. H.; Rahman, H.; Bani, N. A., Application and Suitability of Polymeric Materials as Insulators in Electrical Equipment. *Energies* **2021,** *14* (10), 2758.

22. Sazali, N.; Ibrahim, H.; Jamaludin, A. S.; Mohamed, M. A.; Salleh, W. N. W.; Abidin, M. N. Z. In *A short review on polymeric materials concerning degradable polymers*, OIP Conf. Ser. Mater. Sci. Eng., **2020**; p 12047.

23. Zhang, Z. P.; Rong, M. Z.; Zhang, M. Q., Polymer engineering based on reversible covalent chemistry: A promising innovative pathway towards new materials and new functionalities. *Prog. Polym. Sci.* **2018,** *80*, 39-93.

24. Farmer, J.; Choi, J.-S.; Saw, C.; Haslam, J.; Day, D.; Hailey, P.; Lian, T.; Rebak, R.; Perepezko, J.; Payer, J.; Branagan, D.; Beardsley, B.; D'amato, A.; Aprigliano, L., Iron-Based Amorphous Metals: High-Performance Corrosion-Resistant Material Development. *Metall. Mater. Trans. A* **2009,** *40* (6), 1289-1305.

25. Syed, S., Atmospheric corrosion of materials. *Emir. J. Engin. Res.* **2006,** *11*, 1-24.

26. Shaw, B.; Kelly, R., What is Corrosion? *Electrochem. Soc. Interface* **2006,** *15* (1), 24-26.

27. Pineau, A.; Amine Benzerga, A.; Pardoen, T., Failure of metals III: Fracture and fatigue of nanostructured metallic materials. *Acta Mater.* **2016,** *107*, 508-544.

28. Tattersall, H. G.; Tappin, G., The work of fracture and its measurement in metals, ceramics and other materials. *J. Mater. Sci.* **1966,** *1* (3), 296-301.

29. Kumar, K. S.; Van Swygenhoven, H.; Suresh, S., Mechanical behavior of nanocrystalline metals and alloys11The Golden Jubilee Issue—Selected topics in Materials Science and Engineering: Past, Present and Future, edited by S. Suresh. *Acta Mater.* **2003,** *51* (19), 5743-5774.

30. Vernon, W. H. J., A laboratory study of the atmospheric corrosion of metals. Part II.—Iron: the primary oxide film. Part III.—The secondary product or rust (influence of sulphur dioxide, carbon dioxide, and suspended particles on the rusting of iron). *Trans. Faraday Soc.* **1935,** *31* (0), 1668-1700.

31. Rainforth, W. M., The wear behaviour of oxide ceramics-A Review. *J. Mater. Sci.* **2004,** *39* (22), 6705-6721.

32. Kato, K.; Adachi, K., Wear of advanced ceramics. *Wear* **2002,** *253* (11), 1097-1104.

33. Adachi, K.; Kato, K.; Chen, N., Wear map of ceramics. *Wear* **1997,** *203-204*, 291-301.

34. Stivala, S. S.; Reich, L., Structure vs stability in polymer degradation. *Polym. Eng. Sci.* **1980,** *20* (10), 654-661.

35. Celina, M. C., Review of polymer oxidation and its relationship with materials performance and lifetime prediction. *Polym. Degrad. Stab.* **2013,** *98* (12), 2419-2429.

36. Brostow, W.; Hagg Lobland, H. E., Predicting wear from mechanical properties of thermoplastic polymers. *Polym. Eng. Sci.* **2008,** *48* (10), 1982-1985.

37. Mullins, M. J.; Liu, D.; Sue, H. J., Chapter 2 - Mechanical properties of thermosets. In *Thermosets (Second Edition)*, Guo, Q., Ed. Elsevier: **2018**; pp 35-68.

38. Tcharkhtchi, A.; Faivre, S.; Roy, L. E.; Trotignon, J. P.; Verdu, J., Mechanical properties of thermosets. *J. Mater. Sci.* **1996,** *31* (10), 2687-2692.

39. Li, C.; Strachan, A., Molecular scale simulations on thermoset polymers: A review. *J. Polym. Sci., Part B: Polym. Phys.* **2015,** *53* (2), 103-122.

40. Yousefi, A.; Lafleur, P. G.; Gauvin, R., Kinetic studies of thermoset cure reactions: A review. *Polym. Compos.* **1997,** *18* (2), 157-168.

41. Pucci, A., Smart and Modern Thermoplastic Polymer Materials. *Polymers* **2018,** *10* (11), 1211.

42. Genovese, A.; Shanks, R. A., Simulation of the specific interactions between polyamide-6 and a thermoplastic polyurethane. *Comput. Theor. Polym. Sci.* **2001,** *11* (1), 57-62.

43. Mallick, P. K., Chapter 5 - Thermoplastics and thermoplastic–matrix composites for lightweight automotive structures. In *Materials, Design and Manufacturing for Lightweight Vehicles (Second Edition)*, Mallick, P. K., Ed. Woodhead Publishing: **2021**; pp 187-228.

44. Biron, M., 3 - Thermoplastics: Economic Overview. In *Material Selection for Thermoplastic Parts*, Biron, M., Ed. William Andrew Publishing: Oxford, **2016**; pp 77-111.

45. Vaidya, U. K.; Chawla, K. K., Processing of fibre reinforced thermoplastic composites. *Int. Mater. Rev.* **2008,** *53* (4), 185-218.

46. Sastri, V. R., Chapter 3 - Materials Used in Medical Devices. In *Plastics in Medical Devices*, Sastri, V. R., Ed. William Andrew Publishing: Boston, **2010**; pp 21-32.

47. Vaikuntam, S. R.; Bhagavatheswaran, E. S.; Xiang, F.; Wießner, S.; Heinrich, G.; Das, A.; Stöckelhuber, K. W., Friction, Abrasion and Crack Growth Behavior of In-Situ and Ex-Situ Silica Filled Rubber Composites. *Materials* **2020,** *13* (2), 270.

48. Neuhaus, C.; Lion, A.; Johlitz, M.; Heuler, P.; Barkhoff, M.; Duisen, F., Fatigue behaviour of an elastomer under consideration of ageing effects. *Int. J. Fatigue* **2017,** *104*, 72-80.

49. Ouellette, R. J.; Rawn, J. D., 27 - Synthetic Polymers. In *Organic Chemistry (Second Edition)*, Ouellette, R. J.; Rawn, J. D., Eds. Academic Press: **2018**; pp 861-887.

50. Ren, Z.; Mujib, S. B.; Singh, G., High-Temperature Properties and Applications of Si-Based Polymer-Derived Ceramics: A Review. *Materials* **2021,** *14* (3), 614.

51. Hammel, E. C.; Ighodaro, O. L. R.; Okoli, O. I., Processing and properties of advanced porous ceramics: An application based review. *Ceram. Int.* **2014,** *40* (10, Part A), 15351-15370.

52. Du, C.; Jin, S.; Fang, Y.; Li, J.; Hu, S.; Yang, T.; Zhang, Y.; Huang, J.; Sha, G.; Wang, Y.; Shang, Z.; Zhang, X.; Sun, B.; Xin, S.; Shen, T., Ultrastrong nanocrystalline steel with exceptional thermal stability and radiation tolerance. *Nat. Commun.* **2018,** *9* (1), 5389.

53. Gibbs, J. H.; DiMarzio, E. A., Nature of the Glass Transition and the Glassy State. *J. Chem. Phys.* **1958,** *28* (3), 373-383.

54. Leyva-Porras, C.; Cruz-Alcantar, P.; Espinosa-Solís, V.; Martínez-Guerra, E.; Balderrama, C. I. P.; Martínez, I. C.; Saavedra-Leos, M. Z., Application of Differential Scanning Calorimetry (DSC) and Modulated Differential Scanning Calorimetry (MDSC) in Food and Drug Industries. *Polymers* **2019,** *12* (1), 5.

55. Hergenrother, P. M., The Use, Design, Synthesis, and Properties of High Performance/High Temperature Polymers: An Overview. *High Perform. Polym.* **2003,** *15* (1), 3-45.

56. Rånby, B., Photodegradation and photo-oxidation of synthetic polymers. *J. Anal. Appl. Pyrolysis* **1989,** *15*, 237-247.

57. Ray, S.; Cooney, R. P., Chapter 9 - Thermal Degradation of Polymer and Polymer Composites. In *Handbook of Environmental Degradation of Materials (Third Edition)*, Kutz, M., Ed. William Andrew Publishing: **2018**; pp 185-206.

58. Peterson, J. D.; Vyazovkin, S.; Wight, C. A., Kinetics of the Thermal and Thermo-Oxidative Degradation of Polystyrene, Polyethylene and Poly(propylene). *Macromol. Chem. Phys.* **2001,** *202* (6), 775-784.

59. Han, B.; Wu, Y. L.; Feng, W.; Chen, Z.; Yang, M. D., Kinetic Study of PVC Pyrolysis in Air by Thermogravimetric Analysis Using the Friedman Method. *Adv. Mater. Res.* **2012,** *427*, 64-69.

60. Lee, W. A.; Knight, G. J., Ratio of the glass transition temperature to the melting point in polymers. *Br. Polym. J.* **1970,** *2* (1), 73-80.

61. Chrissafis, K., Kinetics of thermal degradation of polymers. *J. Therm. Anal. Calorim.* **2009,** *95* (1), 273-283.

62. Vyazovkin, S.; Sbirrazzuoli, N., Isoconversional Kinetic Analysis of Thermally Stimulated Processes in Polymers. *Macromol. Rapid Commun.* **2006,** *27* (18), 1515-1532.

63. Takeo, O., A New Method of Analyzing Thermogravimetric Data. *Bull. Chem. Soc. Jpn.* **1965,** *38* (11), 1881-1886.

64. Flynn, J. H.; Wall, L. A., General Treatment of the Thermogravimetry of Polymers. *J. Res. Natl. Bur. Stand. A Phys. Chem.* **1966,** *70A* (6), 487-523.

65. Friedman, H. L., Kinetics of thermal degradation of char-forming plastics from thermogravimetry. Application to a phenolic plastic. *J. Polym. Sci., Part C: Polym. Symp.* **1964,** *6* (1), 183-195.

66. Kissinger, H. E., Reaction Kinetics in Differential Thermal Analysis. *Anal. chem.* **1957,** *29* (11), 1702-1706.

67. Akahira, T.; Sunose, T., Method of determining activation deterioration constant of electrical insulating materials. *Res. Report Chiba Inst. Technol.* **1971,** *16*, 22-23.

68. Korshak, V. V.; Vinogradova, S. V., Dependence of Thermal Stability of Polymers on Their Chemical Structure. *Russ. Chem. Rev.* **1968,** *37* (11), 885-906.

69. Martinez, G.; Mijangos, C.; Millán, J., Correlation between tacticity and thermal stability in comparison with other defect structures in PVC. *Eur. Polym. J.* **1985,** *21* (4), 387-391.

70. Aboulkas, A.; El harfi, K.; El Bouadili, A., Thermal degradation behaviors of polyethylene and polypropylene. Part I: Pyrolysis kinetics and mechanisms. *Energy Convers. Manage.* **2010,** *51* (7), 1363-1369.

71. Shafigullin, L. N.; Romanova, N.; Gumerov, I.; Gabrakhmanov, A.; Sarimov, D., Thermal properties of polypropylene and polyethylene blends (PP/LDPE). *IOP Conf. Ser. Mater. Sci. Eng.* **2018,** *412*, 012070.

72. Billingham, N. C., Degradation. In *Encyclopedia of Polymer Science and Technology*, **2002**.

73. Schawe, J. E. K.; Wrana, C., Competition between Structural Relaxation and Crystallization in the Glass Transition Range of Random Copolymers. *Polymers* **2020,** *12* (8), 1778.

74. Amiri Amraee, I., The effect of heat history on thermal degradation of elastomers containing butadiene units. *J. Appl. Polym. Sci.* **2009,** *113* (6), 3896-3900.

75.   McKeen, L. W., 2 - Introduction to the Effect of Heat Aging on Plastics. In *The Effect of Long Term Thermal Exposure on Plastics and Elastomers*, McKeen, L. W., Ed. William Andrew Publishing: Oxford, **2014**; pp 17-42.

76.   He, Y.; Li, H.; Xiao, X.; Zhao, X., Polymer Degradation: Category, Mechanism and Development Prospect. *E3S Web Conf.* **2021,** *290*, 01012.

77.   Manring, L. E.; Sogah, D. Y.; Cohen, G. M., Thermal degradation of poly(methyl methacrylate). 3. Polymer with head-to-head linkages. *Macromolecules* **1989,** *22* (12), 4652-4654.

78.   Chen, K.; Harris, K.; Vyazovkin, S., Tacticity as a Factor Contributing to the Thermal Stability of Polystyrene. *Macromol. Chem. Phys.* **2007,** *208* (23), 2525-2532.

79.   Shaver, M. P.; Cameron, D. J. A., Tacticity Control in the Synthesis of Poly(lactic acid) Polymer Stars with Dipentaerythritol Cores. *Biomacromolecules* **2010,** *11* (12), 3673-3679.

80.   Grigoriadi, K.; Westrik, J. B. H. M.; Vogiatzis, G. G.; van Breemen, L. C. A.; Anderson, P. D.; Hütter, M., Physical Ageing of Polystyrene: Does Tacticity Play a Role? *Macromolecules* **2019,** *52* (15), 5948-5954.

81.   Hatada, K.; Kitayama, T.; Fujimoto, N.; Nishiura, T., Stability and Degradation of Polymethacrylates with Controlled Structure. *J. Macromol. Sci. A* **1993,** *30* (9-10), 645-667.

82.   Cao, K.; Serrano, J. M.; Liu, T.; Stovall, B. J.; Xu, Z.; Arrington, C. B.; Long, T. E.; Odle, R. R.; Liu, G., Impact of metal cations on the thermal, mechanical, and rheological properties of telechelic sulfonated polyetherimides. *Polym. Chem.* **2020,** *11* (2), 393-400.

83.   Zope, I. S.; Dasari, A.; Guan, F.; Yu, Z.-Z., Influence of metal ions on thermo-oxidative stability and combustion response of polyamide 6/clay nanocomposites. *Polymer* **2016,** *92*, 102-113.

84.   Sun, B.-y.; Cui, L.; Jiang, X.-b.; Jiang, B.-y.; Yao, W.; He, A.-h., Influence of Catalyst Residues on Thermo-oxidative Aging and Thermal Stability of Poly(butene-1). *Chin. J. Polym. Sci.* **2014,** *32* (5), 633 - 639.

85.   Kim, K. J.; Doi, Y.; Abe, H., Effects of residual metal compounds and chain-end structure on thermal degradation of poly(3-hydroxybutyric acid). *Polym. Degrad. Stab.* **2006,** *91* (4), 769-777.

86.   Osawa, Z., Role of metals and metal-deactivators in polymer degradation. *Polym. Degrad. Stab.* **1988,** *20* (3), 203-236.

87.   Dan, E.; Guillet, J. E., Photochemistry of Ketone Polymers. X. Chain Scission Reaction in the Solid State. *Macromolecules* **1973,** *6* (2), 230-235.

88.   Guillet, J., Fundamental Processes in the Photodegradation of Polyolefins. In *Stabilization and Degradation of Polymers*, American Chemical Society: **1978**; Vol. 169, pp 1-10.

89.   Corrales, T.; Catalina, F.; Peinado, C.; Allen, N. S.; Fontan, E., Photooxidative and thermal degradation of polyethylenes: interrelationship by chemiluminescence, thermal gravimetric analysis and FTIR data. *J. Photochem. Photobiol., A* **2002,** *147* (3), 213-224.

90.   Mukundan, T.; Kishore, K., Physicochemical behaviour of polyperoxides. *Curr. Sci.* **1991,** *60* (6), 355-362.

91.   Kishore, K.; Ganesh, K., Synthesis, characterization, and thermal degradation studies on group VIA derived weak-link polymers. *Macromolecules* **1993,** *26* (17), 4700-4705.

92.   de la Rie, E. R., Polymer Stabilizers. A Survey with Reference to Possible Applications in the Conservation Field. *Stud. Conserv.* **1988,** *33* (1), 9-22.

93.   Breese, K.; Lamèthe, J.; Dearmitt, C., Improving synthetic hindered phenol antioxidants: learning from vitamin E. *Polym. Degrad. Stab.* **2000,** *70*, 89-96.

94.   Bach, R. D.; Ayala, P. Y.; Schlegel, H. B., A Reassessment of the Bond Dissociation Energies of Peroxides. An ab Initio Study. *J. Am. Chem. Soc.* **1996,** *118* (50), 12758-12765.

95.   Comyn, J., Thermal Properties of Adhesives. In *Handbook of Adhesion Technology*, da Silva, L. F. M.; Öchsner, A.; Adams, R. D., Eds. Springer International Publishing: Cham, **2017**; pp 1-30.

96.   Johnston, P. K.; Doyle, E.; Orzel, R. A., Acrylics: A Literature Review of Thermal Decomposition Products and Toxicity. *J. Med. Toxicol.* **1988,** *7* (2), 139-200.

97.   McNeill, I. C., 15 - Thermal Degradation. In *Comprehensive Polymer Science and Supplements*, Allen, G.; Bevington, J. C., Eds. Pergamon: Amsterdam, **1989**; pp 451-500.

98.   Cameron, G. G.; Kane, D. R., The thermal degradation of poly(methyl acrylate). III. The mechanism of volatile formation. *Makromol. Chem.* **1968,** *113* (1), 75-84.

99.　　Cameron, G. G.; Kane, D. R., The thermal degradation of poly(methyl acrylate). Part II. The mechanism of chain breaking. *Makromol. Chem.* **1967,** *109* (1), 194-203.

100.　　Michal, J.; Mitera, J.; Tardon, S., Toxicity of thermal degradation products of polyethylene and polypropylene. *Fire Mater.* **1976,** *1*, 160-168.

101.　　Holland, B. J.; Hay, J. N., The thermal degradation of PET and analogous polyesters measured by thermal analysis–Fourier transform infrared spectroscopy. *Polymer* **2002,** *43* (6), 1835-1847.

102.　　Montaudo, G.; Puglisi, C.; Samperi, F., Primary thermal degradation mechanisms of PET and PBT. *Polym. Degrad. Stab.* **1993,** *42* (1), 13-28.

103.　　Das, P.; Tiwari, P., Thermal degradation study of waste polyethylene terephthalate (PET) under inert and oxidative environments. *Thermochim. Acta* **2019,** *679*, 178340.

104.　　Pohl, H. A., The Thermal Degradation of Polyesters. *J. Am. Chem. Soc.* **1951,** *73* (12), 5660-5661.

105.　　McKeen, L. W., 5 - Polyesters. In *The Effect of Long Term Thermal Exposure on Plastics and Elastomers*, McKeen, L. W., Ed. William Andrew Publishing: Oxford, **2014**; pp 85-115.

106.　　Ping, Z.; Linbo, W.; Bo-Geng, L., Thermal stability of aromatic polyesters prepared from diphenolic acid and its esters. *Polym. Degrad. Stab.* **2009,** *94* (8), 1261-1266.

107.　　Davis, A.; Golden, J. H., Stability of Polycarbonate. *J. Macromol. Sci. C* **1969,** *3* (1), 49-68.

108.　　Levchik, S.; Weil, E., A review on thermal decomposition and combustion of thermoplastic polyesters. *Polym. Adv. Technol.* **2004,** *15*, 691-700.

109.　　Farong, H.; Xueqiu, W.; Shijin, L., The thermal stability of polyetherimide. *Polym. Degrad. Stab.* **1987,** *18* (3), 247-259.

110.　　Uyar, T.; Tonelli, A. E.; Hacaloğlu, J., Thermal degradation of polycarbonate, poly(vinyl acetate) and their blends. *Polym. Degrad. Stab.* **2006,** *91* (12), 2960-2967.

111.　　Jang, B. N.; Wilkie, C. A., The thermal degradation of bisphenol A polycarbonate in air. *Thermochim. Acta* **2005,** *426* (1), 73-84.

112.　　Yadav, R.; Naebe, M.; Wang, X.; Kandasubramanian, B., Structural and Thermal Stability of Polycarbonate Decorated Fumed Silica Nanocomposite via Thermomechanical Analysis and In-situ Temperature Assisted SAXS. *Sci. Rep.* **2017,** *7* (1), 7706.

113.　　Achhammer, B. G.; Reinhart, F. W.; Kline, G. M., Mechanism of the degradation of polyamides. *J. Appl. Chem.* **1951,** *1* (7), 301-320.

114.　　Herrera, M.; Matuschek, G.; Kettrup, A., Main products and kinetics of the thermal degradation of polyamides. *Chemosphere* **2001,** *42* (5), 601-607.

115.　　Holland, B. J.; Hay, J. N., Thermal degradation of nylon polymers. *Polym. Int.* **2000,** *49* (9), 943-948.

116.　　Duquesne, S.; Le Bras, M.; Bourbigot, S.; Delobel, R.; Camino, G.; Eling, B.; Lindsay, C.; Roels, T., Thermal degradation of polyurethane and polyurethane/expandable graphite coatings. *Polym. Degrad. Stab.* **2001,** *74* (3), 493-499.

117.　　Chambers, J.; Jiricny, J.; Reese, C. B., The thermal decomposition of polyurethanes and polyisocyanurates. *Fire Mater.* **1981,** *5* (4), 133-141.

118.　　Simon, J.; Barla, F.; Kelemen-Haller, A.; Farkas, F.; Kraxner, M., Thermal stability of polyurethanes. *Chromatographia* **1988,** *25* (2), 99-106.

119.　　Huggett, C.; Levin, B. C., Toxicity of the pyrolysis and combustion products of poly(vinyl chlorides): A literature assessment. *Fire Mater.* **1987,** *11* (3), 131-142.

120.　　Yu, J.; Sun, L.; Ma, C.; Qiao, Y.; Yao, H., Thermal degradation of PVC: A review. *Waste Manage.* **2016,** *48*, 300-314.

121.　　Monahan, A. R., Thermal degradation of polyacrylonitrile in the temperature range 280–450 °C. *J. Polym. Sci., Part A: Polym. Chem.* **1966,** *4* (10), 2391-2399.

122.　　Xue, T. J.; McKinney, M. A.; Wilkie, C. A., The thermal degradation of polyacrylonitrile. *Polym. Degrad. Stab.* **1997,** *58* (1), 193-202.

123.　　Özlem, S.; Hacaloglu, J., Thermal degradation of poly(*n*-butyl methacrylate), poly(*n*-butyl acrylate) and poly(*t*-butyl acrylate). *J. Anal. Appl. Pyrolysis* **2013,** *104*, 161-169.

124.　　Marturano, V.; Cerruti, P.; Ambrogi, V., Polymer additives. *Phys. Sci. Rev.* **2017,** *2* (6).

125.   Deanin, R. D., Additives in plastics. *Environ. Health Perspect.* **1975,** *11*, 35-39.

126.   Hahladakis, J. N.; Velis, C. A.; Weber, R.; Iacovidou, E.; Purnell, P., An overview of chemical additives present in plastics: Migration, release, fate and environmental impact during their use, disposal and recycling. *J. Hazard. Mater.* **2018,** *344*, 179-199.

127.   Saron, C.; Felisberti, M., Influence of colorants on the degradation and stabilization of polymers. *Quim. Nova* **2006,** *29*, 124-128.

128.   Calvert, P. D.; Billingham, N. C., Loss of additives from polymers: A theoretical model. *J. Appl. Polym. Sci.* **1979,** *24* (2), 357-370.

129.   Li, B.; Wang, Z.-W.; Lin, Q.-B.; Hu, C.-Y.; Su, Q.-Z.; Wu, Y.-M., Determination of Polymer Additives-Antioxidants, Ultraviolet Stabilizers, Plasticizers and Photoinitiators in Plastic Food Package by Accelerated Solvent Extraction Coupled with High-Performance Liquid Chromatography. *J. Chromatogr. Sci.* **2014,** *53* (6), 1026-1035.

130.   Lau, O.-W.; Wong, S.-K., Contamination in food from packaging material. *J. Chromatogr. A* **2000,** *882* (1), 255-270.

131.   Billingham, N. C., Degradation and Stabilization of Polymers. In *Materials Science and Technology: A Comprehensive Treatment*, **2000**; pp 469-507.

132.   Kirschweng, B.; Vörös, B.; Arroussi, M.; Tátraaljai, D.; Zsuga, M.; Pukánszky, B., Melt stabilization of polyethylene with natural antioxidants: comparison of a natural extract and its main component. *J. Therm. Anal. Calorim.* **2021,** *145* (1), 67-75.

133.   Haider, N.; Karlsson, S., Loss and transformation products of the aromatic antioxidants in MDPE film under long-term exposure to biotic and abiotic conditions. *J. Appl. Polym. Sci.* **2002,** *85* (5), 974-988.

134.   Shabaev, A. S.; Zhansitov, A. A.; Khakyasheva, E. V.; Khashirova, S. Y., Study of Thermo-Oxidative Transformations of Unstabilized and Stabilized Poly(ether ether ketone). *Polym. Sci. Ser. B* **2019,** *61* (5), 582-588.

135.   Archodoulaki, V.; Lüftl, S.; Seidler, S., Thermal degradation behaviour of poly(oxymethylene): 1. Degradation and stabilizer consumption. *Polym. Degrad. Stab.* **2004,** *86*, 75-83.

136.   Kovářová, J.; Rotschová, J.; Brede, O.; Burgers, M., The effect of transformation products of the antioxidant BHT on the initial stages of thermo- and photo-oxidation of LDPE. *Can. J. Chem.* **1995,** *73* (11), 1862-1868.

137.   Coleman, E. A., 21 - Plastics Additives. In *Applied Plastics Engineering Handbook (Second Edition)*, Kutz, M., Ed. William Andrew Publishing: **2017**; pp 489-500.

138.   Li, G.; Guo, X.; Na, W.; Hao, D.; Zhang, M.; Zhang, H.; Xu, J., Performance and synergistic effect of phenolic and thio antioxidants in ABS graft copolymers. *Front. Chem. Sci. Eng.* **2011,** *5* (1), 26-34.

139.   Butola, B. S.; Joshi, M., Photostability of HDPE Filaments Stabilized with UV Absorbers (UVA) and Light Stabilizers (HALS). *J. Eng. Fibers Fabr.* **2013,** *8*.

140.   Pospíšil, J., Chemical and photochemical behaviour of phenolic antioxidants in polymer stabilization: A state of the art report, part II. *Polym. Degrad. Stab.* **1993,** *39* (1), 103-115.

141.   Setnescu, T.; Jipa, S.; Setnescu, R.; Mihalcea, I., Synergistic effects of some phenolic inhibitors used in polyethylene stabilization—II. Oxyluminescence method for studying the synergistic effects of some binary mixtures of phenolic stabilizers. *Polym. Degrad. Stab.* **1996,** *52* (1), 19-23.

142.   Parra, D. F.; do Rosário Matos, J., Some Synergistic Effects of Antioxidants in Natural Rubber. *J. Therm. Anal. Calorim.* **2002,** *67* (2), 287-294.

143.   Bauer, I.; Habicher, W. D.; Korner, S.; Al-Malaika, S., Antioxidant interaction between organic phosphites and hindered amine light stabilizers: effects during photoxidation of polypropylene—II. *Polym. Degrad. Stab.* **1997,** *55* (2), 217-224.

144.   Gensler, R.; Plummer, C. J. G.; Kausch, H. H.; Kramer, E.; Pauquet, J. R.; Zweifel, H., Thermo-oxidative degradation of isotactic polypropylene at high temperatures: phenolic antioxidants versus HAS. *Polym. Degrad. Stab.* **2000,** *67* (2), 195-208.

145.   Allen, N. S.; Edge, M., Perspectives on additives for polymers. 1. Aspects of stabilization. *J. Vinyl. Addit. Technol.* **2021,** *27* (1), 5-27.

146.   Bartsch, N.; Girard, M.; Wilde, A.; Bruhn, T.; Kappenstein, O.; Vieth, B.; Hutzler, C.; Luch, A., Thermal Stability of Polymer Additives: Comparison of Decomposition Models Including Oxidative Pyrolysis. *J. Vinyl. Addit. Technol.* **2019,** *25* (s2), E12-E27.

147. Kirschweng, B.; Tátraaljai, D.; Földes, E.; Pukánszky, B., Natural antioxidants as stabilizers for polymers. *Polym. Degrad. Stab.* **2017,** *145*, 25-40.

148. Hamama, A. A.; Nawar, W. W., Thermal decomposition of some phenolic antioxidants. *J. Agric. Food. Chem.* **1991,** *39* (6), 1063-1069.

149. Coiai, S.; Cicogna, F.; Yang, C.; Tempesti, V.; Carroccio, S. C.; Gorrasi, G.; Mendichi, R.; Dintcheva, N. T.; Passaglia, E., Grafting of Hindered Phenol Groups onto Ethylene/α-Olefin Copolymer by Nitroxide Radical Coupling. *Polymers* **2017,** *9* (12), 670.

150. Manteghi, A.; Ahmadi, S.; Arabi, H., Covalent immobilization of phenolic antioxidant on Ethylene copolymers: An efficient approach toward enhanced long-term stabilization of polypropylene. *Polymer* **2016,** *104*, 31-39.

151. Hlushko, R.; Hlushko, H.; Sukhishvili, S. A., A family of linear phenolic polymers with controlled hydrophobicity, adsorption and antioxidant properties. *Polym. Chem.* **2018,** *9* (4), 506-516.

152. Wypych, G., 15 - Effect of additives on weathering. In *Handbook of Material Weathering (Sixth Edition)*, Wypych, G., Ed. ChemTec Publishing: **2018**; pp 591-624.

153. Habicher, W. D.; Bauer, I.; Pospíšil, J., Organic Phosphites as Polymer Stabilizers. *Macromol. Symp.* **2005,** *225* (1), 147-164.

154. Ghaemy, M.; Fruzandeh, S., Synergistic effects of some phosphites antioxidants used in polypropylene stabilization. **1999**.

155. Tolinski, M., 3 - Antioxidants and Heat Stabilization. In *Additives for Polyolefins (Second Edition)*, Tolinski, M., Ed. William Andrew Publishing: Oxford, **2015**; pp 19-31.

156. Vohlídal, J., Polymer degradation: a short review. *Chem. Teach. Int.* **2021,** *3* (2), 213-220.

157. Nødland, O.; Lohne, A.; Stavland, A.; Hiorth, A., An Investigation of Polymer Mechanical Degradation in Radial Well Geometry. *Transp. Porous Media* **2019,** *128* (1), 1-27.

158. Bhuvaneswari. G, H., 3 - Degradability of Polymers. In *Recycling of Polyurethane Foams*, Thomas, S.; Rane, A. V.; Kanny, K.; V.K, A.; Thomas, M. G., Eds. William Andrew Publishing: **2018**; pp 29-44.

159. Michael, P.; Binder, W. H., A Mechanochemically Triggered "Click" Catalyst. *Angew. Chem. Int. Ed.* **2015,** *54* (47), 13918-13922.

160. Sinha, S. K.; Briscoe, B. J., Surface Mechanical Damage and Wear of Polymers. In *Encyclopedia of Polymer Science and Technology*, **2006**; pp 1-26.

161. Gewert, B.; Plassmann, M. M.; MacLeod, M., Pathways for degradation of plastic polymers floating in the marine environment. *Environ. Sci.; Process. Impacts* **2015,** *17* (9), 1513-1521.

162. MacCallum, J. R., 18 - Photodegradation. In *Comprehensive Polymer Science and Supplements*, Allen, G.; Bevington, J. C., Eds. Pergamon: Amsterdam, **1989**; pp 529-537.

163. Göpferich, A., Mechanisms of polymer degradation and erosion. *Biomaterials* **1996,** *17* (2), 103-114.

164. Moiseev, Y. V.; Markin, V. S.; Zaikov, G. E., Chemical Degradation of Polymers in Corrosive Liquid Media. *Russ. Chem. Rev.* **1976,** *45* (3), 246-266.

165. de Leon, A. C. C.; da Silva, Í. G. M.; Pangilinan, K. D.; Chen, Q.; Caldona, E. B.; Advincula, R. C., High performance polymers for oil and gas applications. *React. Funct. Polym.* **2021,** *162*, 104878.

166. Yang, S.-Y.; Yang, H.-X.; Hu, A.-J., Chapter 4 - Super Engineering Plastics and Forms. In *Advanced Polyimide Materials*, Yang, S.-Y., Ed. Elsevier: **2018**; pp 137-193.

167. Meador, M. A., Recent advances in the development of processable high-temperature polymers. *Annu. Rev. Mater. Sci.* **1998,** *28* (1), 599-630.

168. Lau, K. S. Y., 10 - High-Performance Polyimides and High Temperature Resistant Polymers. In *Handbook of Thermoset Plastics (Third Edition)*, Dodiuk, H.; Goodman, S. H., Eds. William Andrew Publishing: Boston, **2014**; pp 297-424.

169. Hergenrother, P. M.; Jensen, B. J.; Havens, S. J., Poly(arylene ethers). *Polymer* **1988,** *29* (2), 358-369.

170. Herold, F.; Schneller, A., High-Performance Polymers. *Adv. Mater.* **1992,** *4* (3), 143-152.

171. Tant, M. R.; McManus, H. L. N.; Rogers, M. E., High-Temperature Properties and Applications of Polymeric Materials. In *High-Temperature Properties and Applications of Polymeric Materials*, American Chemical Society: **1995**; Vol. 603, pp 1-20.

172.   McKeen, L. W., 6 - Polyimides. In *The Effect of Long Term Thermal Exposure on Plastics and Elastomers*, McKeen, L. W., Ed. William Andrew Publishing: Oxford, **2014**; pp 117-137.

173.   Lisa, G.; Avram, E.; Paduraru, G.; Irimia, M.; Hurduc, N.; Aelenei, N., Thermal behaviour of polystyrene, polysulfone and their substituted derivatives. *Polym. Degrad. Stab.* **2003,** *82* (1), 73-79.

174.   Kumar, R.; Molin, D.; Young, L.; Ke, F. In *New high temperature polymer thin coating for power electronics*, IEEE Applied Power Electronics Conference and Exposition, **2004**; pp 1247-1249.

175.   Hergenrother, P. M., Recent Advances in High Temperature Polymers. *Polym. J.* **1987,** *19* (1), 73-83.

176.   Dhara, M. G.; Banerjee, S., Fluorinated high-performance polymers: Poly(arylene ether)s and aromatic polyimides containing trifluoromethyl groups. *Prog. Polym. Sci.* **2010,** *35* (8), 1022-1077.

177.   Wang, B.; Yao, Y.; Peng, J.; Lin, Y.; Liu, W.; Luo, Y.; Xiang, R.; Li, R.; Wu, D., Preparation of poly(ester imide) ultrafine fibers by gas-jet/electrospinning. *J. Appl. Polym. Sci.* **2009,** *114* (2), 883-891.

178.   Maiti, S.; Das, S., Synthesis and properties of polyesterimides and their isomers. *J. Appl. Polym. Sci.* **1981,** *26* (3), 957-978.

179.   Loncrini, D. F., Aromatic polyesterimides. *J. Polym. Sci., Part A: Polym. Chem.* **1966,** *4* (6), 1531-1541.

180.   Lienert, K.-W., Poly(ester-imide)s for Industrial Use. In *Progress in Polyimide Chemistry II*, Kricheldorf, H. R., Ed. Springer Berlin Heidelberg: Berlin, Heidelberg, **1999**; pp 45-82.

181.   Murray, T. J., Poly(amide-imides): Wire Enamels with Excellent Thermal and Chemical Properties. *Macromol. Mater. Eng.* **2008,** *293* (5), 350-360.

182.   Niu, H.; Liu, W.; Chi, X.; Huang, Y.; Zheng, S.; Min, D.; Li, S.; Xia, Y.; Wang, W. In *Effects of Hygrothermal Ageing on Breakdown Performance of Polyesterimide Nanocomposites*, Condition Monitoring and Diagnosis (CMD), **2018**; pp 1-5.

183.   Fetouhi, L.; Petitgas, B.; Dantras, E.; Martinez-Vega, J., Mechanical, dielectric, and physicochemical properties of impregnating resin based on unsaturated polyesterimides. *Eur. Phys. J. Appl. Phys.* **2017,** *80* (1), 10901.

184.   Maros, C. L.; de Abajo, J., Unstaurated polyester imides. *Angew. Makromol. Chem.* **1976,** *55* (1), 73-83.

185.   Banu, P.; Radhakrishnan, G., Unsaturated poly(ester–imide)s from hydroxy-terminated polybutadiene, dianhydride and diisocyanate. *Eur. Polym. J.* **2004,** *40* (8), 1887-1894.

186.   Korcak, L. L.; Kavanagh, D. F. In *Thermal Accelerated Aging Methods for Magnet Wire: A Review*, International Conference on Diagnostics in Electrical Engineering (Diagnostika), **2018**; pp 1-4.

187.   Ueda, K., Progress of magnet wire technology in Japan. *IEEE Electr. Insul. Mag.* **1989,** *5* (3), 18-26.

188.   Nedjar, M., Investigation in thermal endurance of polyesterimide used in electrical machines. *J. Appl. Polym. Sci.* **2011,** *121* (5), 2886-2892.

189.   Shrivastava, A., 3 - Plastic Properties and Testing. In *Introduction to Plastics Engineering*, Shrivastava, A., Ed. William Andrew Publishing: **2018**; pp 49-110.

190.   Ahmad, Z., Polymeric Dielectric Materials. **2012**; pp 3-26.

191.   Anton, A.; Lienert, K.-W.; Hegemann, G., Wire Enamels – An Application for High Performance Polymers Unknown to Chemists. *Macromol. Mater. Eng.* **2008,** *293* (5), 331-339.

192.   Kavanagh, D. F.; Gyftakis, K. N.; McCulloch, M. D., Thermal Degradation Phenomena of Polymer Film on Magnet Wire for Electromagnetic Coils. *IEEE Trans. Ind. Appl.* **2021,** *57* (1), 458-467.

193.   Guan, Q.; Norder, B.; Dingemans, T. J., Flexible all-aromatic polyesterimide films with high glass transition temperatures. *J. Appl. Polym. Sci.* **2017,** *134* (18), n/a.

194.   Xia, Y.; Zhou, C.; Liang, G.; Gu, A.; Wang, W., Polyester-imide solventless impregnating resin and its nano-silica modified varnishes with excellent corona resistance and thermal stability. *IEEE Trans. Dielectr. Electr. Insul.* **2015,** *22* (1), 372-379.

195.   Li, Y.-S.; Schwarz, G.; Kricheldorf, H. R., New polymers syntheses. 104. synthesis of poly(ester-imide)s from nylon 6, nylon 11, or nylon 12. *J. Polym. Sci., Part A: Polym. Chem.* **2000,** *38* (9), 1630-1638.

196.   Das, S.; Maiti, S.; Maiti, M., Synthesis and Properties of a New Polyesterimide from a Forest Product. *J. Macromol. Sci. A* **1982,** *17* (8), 1177-1192.

197.   Yu, X.; Cheng, Z.; We, W.; Xueping, W.; Shaobo, H.; Chen, W. In *Developing a novel environmental friendly polyester-imide impregnating resin*, IEEE Electrical Insulation Conference (EIC), **2015**; pp 551-554.

198.   Yang, M.; Chen, L.; Zhao, C.-S.; Huang, H.-Z.; Wang, J.-S.; Wang, Y.-Z., A novel phosphorus-containing thermotropic liquid crystalline poly(ester-imide) with high flame retardancy. *Polym. Adv. Technol.* **2009,** *20* (4), 378-383.

199.   Leu, W.-T.; Hsiao, S.-H., Synthesis and properties of novel aromatic poly(ester-imide)s bearing 1,5-bis(benzoyloxy)naphthalene units. *Eur. Polym. J.* **2006,** *42*, 328–335.

200.   Gui, D.; Miao, X.; Zeng, G.; Liu, J., Preparation and thermal stability of amine-terminated polyesterimide modified epoxy resin. *J. Mater. Sci.: Mater. Electron.* **2013,** *24* (11), 4614-4620.

201.   Corneliu, H.; Vlad-Bubulac, T.; Petreus, O.; Lisa, G., Kinetics of thermal degradation in non-isothermal conditions of some phosphorus-containing polyesters and polyesterimides. *Eur. Polym. J.* **2007,** *43*, 980-988.

202.   Fetouhi, L.; Martinez-Vega, J.; Petitgas, B., Electric conductivity, aging and chemical degradation of polyesterimide resins used in the impregnation of rotating machines. *IEEE Trans. Dielectr. Electr. Insul.* **2018,** *25* (1), 294-305.

203.   Araki, C.; Taguchi, T. In *Thermal degradation of polyesterimide magnet wire*, Proceedings of IEEE Conference on Electrical Insulation and Dielectric Phenomena, **1993**; pp 526-531.

204.   Burrell, M. C.; Keane, J. J., Characterization of copper/enamel interfacial reactions during aging. *Surf. Interface Anal.* **1988,** *11* (9), 487-496.

205.   Baumgarten, G.; Hegemann, G. In *Isothermal thermogravimetric analysis as a tool to determine high temperature performance of impregnating resins*, Proceedings:Electrical Electronics Insulation Conference and Electrical Manufacturing & Coil Winding Conference, **1995**; pp 571-575.

206.   Guo, W.; Chuang, T.-H.; Huang, S.-T.; Leu, W.-T.; Hsiao, S.-H., Thermal degradation behaviour of aromatic poly(ester–imide) investigated by pyrolysis–GC/MS. *J. Polym. Res.* **2007,** *14* (5), 401-409.

207.   Gao, Y.; Gu, F.; Zhao, Y., Thermal oxidative aging characterization of SBS modified asphalt. *J. Wuhuan Univ. Technol. Mater. Sci. Ed.* **2013,** *28* (1), 88-91.

208.   Yin, W.; Xie, Z.; Yin, Y.; Yi, J.; Liu, X.; Wu, H.; Wang, S.; Xie, Y.; Yang, Y., Aging behavior and lifetime prediction of PMMA under tensile stress and liquid scintillator conditions. *Adv. Ind. Eng. Polym. Res.* **2019,** *2* (2), 82-87.

209.   Almond, J.; Sugumaar, P.; Wenzel, M. N.; Hill, G.; Wallis, C., Determination of the carbonyl index of polyethylene and polypropylene using specified area under band methodology with ATR-FTIR spectroscopy. *E-Polym.* **2020,** *20* (1), 369-381.

210.   Gill, P. S.; Sauerbrunn, S. R.; Crowe, B. S., High resolution thermogravimetry. *J. Therm. Anal.* **1992,** *38* (3), 255-266.

211.   McNeill, I. C., Thermal volatilization analysis: A new method for the characterization of polymers and the study of polymer degradation. *J. Polym. Sci., Part A: Polym. Chem.* **1966,** *4* (10), 2479-2485.

212.   Böhm, R.; Hufenbach, W., Experimentally based strategy for damage analysis of textile-reinforced composites under static loading. *Compos. Sci. Technol.* **2010,** *70* (9), 1330-1337.

213.   Duchene, P.; Chaki, S.; Ayadi, A.; Krawczak, P., A review of non-destructive techniques used for mechanical damage assessment in polymer composites. *J. Mater. Sci.* **2018,** *53* (11), 7915-7938.

214.   Viets, C.; Kaysser, S.; Schulte, K., Damage mapping of GFRP via electrical resistance measurements using nanocomposite epoxy matrix systems. *Compos. B. Eng.* **2014,** *65*, 80-88.

215.   Trankler, H.; Kanoun, O. In *Recent advances in sensor technology*, Proceedings of the 18th IEEE Instrumentation and Measurement Technology Conference. Rediscovering Measurement in the Age of Informatics, **2001**; pp 309-316.

216.   Andersson, L.; Sellergren, B.; Mosbach, K., Imprinting of amino acid derivatives in macroporous polymers. *Tetrahedron Lett.* **1984,** *25* (45), 5211-5214.

217.   Wulff, G.; Oberkobusch, D.; Minárik, M., Enzyme-analogue built polymers, 18 chiral cavities in polymer layers coated on wide-pore silica. *Reactive Polymers, Ion Exchangers, Sorbents* **1985,** *3* (4), 261-275.

218.   BelBruno, J. J., Molecularly Imprinted Polymers. *Chem. Rev.* **2019,** *119* (1), 94-119.

219.   Cegłowski, M.; Schroeder, G., Chapter Eleven - Molecularly imprinted polymers as adsorbents in mass spectrometry techniques. In *Comprehensive Analytical Chemistry*, Marć, M., Ed. Elsevier: **2019**; Vol. 86, pp 295-336.

220. Cáceres, C.; Bravo, C.; Rivas, B.; Moczko, E.; Sáez, P.; García, Y.; Pereira, E., Molecularly Imprinted Polymers for the Selective Extraction of Bisphenol A and Progesterone from Aqueous Media. *Polymers* **2018,** *10* (6), 679.

221. Subrahmanyam, S.; Piletsky, S. A.; Piletska, E. V.; Chen, B.; Karim, K.; Turner, A. P. F., 'Bite-and-Switch' approach using computationally designed molecularly imprinted polymers for sensing of creatinine. *Biosens. Bioelectron.* **2001,** *16* (9), 631-637.

222. Hashim, S. N. N. S.; Boysen, R. I.; Schwarz, L. J.; Danylec, B.; Hearn, M. T. W., A comparison of covalent and non-covalent imprinting strategies for the synthesis of stigmasterol imprinted polymers. *J. Chromatogr. A* **2014,** *1359*, 35-43.

223. El-Akaad, S.; Mohamed, M. A.; Abdelwahab, N. S.; Abdelaleem, E. A.; De Saeger, S.; Beloglazova, N., Capacitive sensor based on molecularly imprinted polymers for detection of the insecticide imidacloprid in water. *Sci. Rep.* **2020,** *10* (1), 14479.

224. Jenkins, A. L.; Yin, R.; Jensen, J. L., Molecularly imprinted polymer sensors for pesticide and insecticide detection in water. *Analyst* **2001,** *126* (6), 798-802.

225. Alizadeh, T.; Rezaloo, F., A new chemiresistor sensor based on a blend of carbon nanotube, nano-sized molecularly imprinted polymer and poly methyl methacrylate for the selective and sensitive determination of ethanol vapor. *Sens. Actuators, B* **2013,** *176*, 28–37.

226. Yarman, A.; Kurbanoglu, S.; Jetzschmann, K. J.; Ozkan, S. A.; Wollenberger, U.; Scheller, F. W., Electrochemical MIP-Sensors for Drugs. *Current medicinal chemistry* **2018,** *25* (33), 4007-4019.

227. Bunte, G.; Hürttlen, J.; Pontius, H.; Hartlieb, K.; Krause, H., Gas phase detection of explosives such as 2,4,6-trinitrotoluene by molecularly imprinted polymers. *Anal. Chim. Acta* **2007,** *591* (1), 49-56.

228. Kriz, D.; RamstrÖM, O.; Svensson, A.; Mosbach, K., Introducing biomimetic sensors based on molecularly imprinted polymers as recognition elements. *Anal. chem.* **1995,** *67* (13), 2142-2144.

229. Henry, O. Y. F.; Cullen, D. C.; Piletsky, S. A., Optical interrogation of molecularly imprinted polymers and development of MIP sensors: a review. *Anal. Bioanal. Chem.* **2005,** *382* (4), 947-956.

230. McCluskey, A.; Holdsworth, C. I.; Bowyer, M. C., Molecularly imprinted polymers (MIPs): sensing, an explosive new opportunity? *Org. Biomol. Chem.* **2007,** *5* (20), 3233-3244.

231. Ziaullah; Rupasinghe, H. P. V., Chapter 1 - Application of NMR Spectroscopy in Plant Polyphenols Associated with Human Health. In *Applications of NMR Spectroscopy*, ur-Rahman, A.; Choudhary, M. I., Eds. Bentham Science Publishers: **2015**; pp 3-92.

232. Meier, H., The Photochemistry of Stilbenoid Compounds and Their Role in Materials Technology. *Angew. Chem. Int. Ed.* **1992,** *31* (11), 1399-1420.

233. Likhtenshtein, G., Stilbenes Preparation and Analysis. In *Stilbenes*, **2009**; pp 1-41.

234. Hang, C.; Wu, H.-W.; Zhu, L.-L., π-Conjugated cyanostilbene-based optoelectric functional materials. *Chin. Chem. Lett.* **2016,** *27* (8), 1155-1165.

235. Palakollu, V.; Kanvah, S., α-Cyanostilbene based fluorophores: aggregation-induced enhanced emission, solvatochromism and the pH effect. *New J. Chem.* **2014,** *38* (12), 5736-5746.

236. Martinez-Abadia, M.; Gimenez, R.; Ros, M. B., Self-Assembled α-Cyanostilbenes for Advanced Functional Materials. *Adv. Mater.* **2018,** *30* (5), 1704161.

237. Kunzelman, J.; Kinami, M.; Crenshaw, B. R.; Protasiewicz, J. D.; Weder, C., Oligo (*p*-phenylene vinylene)s as a "New" Class of Piezochromic Fluorophores. *Adv. Mater.* **2008,** *20* (1), 119-122.

238. Birks, J. B.; Dyson, D. J.; Munro, I. H.; Flowers, B. H., Excimer fluorescence II. Lifetime studies of pyrene solutions. *Proc. R. Soc. London, Ser. A* **1963,** *275* (1363), 575-588.

239. Hinoue, T.; Shigenoi, Y.; Sugino, M.; Mizobe, Y.; Hisaki, I.; Miyata, M.; Tohnai, N., Regulation of π-Stacked Anthracene Arrangement for Fluorescence Modulation of Organic Solid from Monomer to Excited Oligomer Emission. *Chem. Eur. J.* **2012,** *18* (15), 4634-4643.

240. Sagara, Y.; Lavrenova, A.; Crochet, A.; Simon, Y. C.; Fromm, K. M.; Weder, C., A Thermo- and Mechanoresponsive Cyano-Substituted Oligo(p-phenylene vinylene) Derivative with Five Emissive States. *Chem. Eur. J.* **2016,** *22* (13), 4374-4378.

241. Lavrenova, A.; Balkenende, D. W. R.; Sagara, Y.; Schrettl, S.; Simon, Y. C.; Weder, C., Mechano- and Thermoresponsive Photoluminescent Supramolecular Polymer. *J. Am. Chem. Soc.* **2017,** *139* (12), 4302-4305.

242. Han, T.; Wang, X.; Wang, D.; Tang, B. Z., Functional Polymer Systems with Aggregation-Induced Emission and Stimuli Responses. *Top. Curr. Chem.* **2021,** *379* (1), 7.

243. Bao, S.; Wu, Q.; Qin, W.; Yu, Q.; Wang, J.; Liang, G.; Tang, B. Z., Sensitive and reliable detection of glass transition of polymers by fluorescent probes based on AIE luminogens. *Polym. Chem.* **2015,** *6* (18), 3537-3542.

244. Song, Z.; Lv, X.; Gao, L.; Jiang, L., Dramatic differences in the fluorescence of AIEgen-doped micro- and macrophase separated systems. *J. Mater. Chem. C* **2018,** *6* (1), 171-177.

245. Kim, H. N.; Guo, Z.; Zhu, W.; Yoon, J.; Tian, H., Recent progress on polymer-based fluorescent and colorimetric chemosensors. *Chem. Soc. Rev.* **2011,** *40* (1), 79-93.

246. Heying, R. S.; Nandi, L. G.; Bortoluzzi, A. J.; Machado, V. G., A novel strategy for chromogenic chemosensors highly selective toward cyanide based on its reaction with 4-(2,4-dinitrobenzylideneamino)benzenes or 2,4-dinitrostilbenes. *Spectrochim. Acta, Part A* **2015,** *136*, 1491-1499.

247. Jornet-Martínez, N.; Moliner-Martínez, Y.; Herráez-Hernández, R.; Molins-Legua, C.; Verdú-Andrés, J.; Campíns-Falcó, P., Designing solid optical sensors for in situ passive discrimination of volatile amines based on a new one-step hydrophilic PDMS preparation. *Sensor. Actuat. B-Chem.* **2016,** *223*, 333-342.

248. Mohr, G. J., New chromoreactands for the detection of aldehydes, amines and alcohols. *Sensor. Actuat. B-Chem.* **2003,** *90* (1–3), 31-36.

249. Wang, T.; Zhang, N.; Bai, W.; Bao, Y., Fluorescent chemosensors based on conjugated polymers with *N*-heterocyclic moieties: two decades of progress. *Polym. Chem.* **2020,** *11* (18), 3095-3114.

250. Pecher, J.; Mecking, S., Nanoparticles of Conjugated Polymers. *Chem. Rev.* **2010,** *110* (10), 6260-6279.

251. Moon, J. H.; MacLean, P.; McDaniel, W.; Hancock, L. F., Conjugated polymer nanoparticles for biochemical protein kinase assay. *Chem. Comm.* **2007,** (46), 4910-4912.

252. Pecher, J.; Huber, J.; Winterhalder, M.; Zumbusch, A.; Mecking, S., Tailor-Made Conjugated Polymer Nanoparticles for Multicolor and Multiphoton Cell Imaging. *Biomacromolecules* **2010,** *11* (10), 2776-2780.

253. Baier, M. C.; Huber, J.; Mecking, S., Fluorescent Conjugated Polymer Nanoparticles by Polymerization in Miniemulsion. *J. Am. Chem. Soc.* **2009,** *131* (40), 14267-14273.

254. Micallef, A. S.; Blinco, J. P.; George, G. A.; Reid, D. A.; Rizzardo, E.; Thang, S. H.; Bottle, S. E., The application of a novel profluorescent nitroxide to monitor thermo-oxidative degradation of polypropylene. *Polym. Degrad. Stab.* **2005,** *89* (3), 427-435.

255. Blinco, J. P.; Keddie, D. J.; Wade, T.; Barker, P. J.; George, G. A.; Bottle, S. E., Profluorescent nitroxides: Sensors and stabilizers of radical-mediated oxidative damage. *Polym. Degrad. Stab.* **2008,** *93* (9), 1613-1618.

256. Fairfull-Smith, K. E.; Blinco, J. P.; Keddie, D. J.; George, G. A.; Bottle, S. E., A Novel Profluorescent Dinitroxide for Imaging Polypropylene Degradation. *Macromolecules* **2008,** *41* (5), 1577-1580.

257. Mohr, G. J.; Citterio, D.; Spichiger-Keller, U. E., Development of chromogenic reactands for optical sensing of alcohols. *Sens. Actuators, B* **1998,** *49* (3), 226-234.

258. Mohr, G. J.; Grummt, U.-W., Comparison of Trifluoroacetyl Monostyryl and Distyryl Dyes: effects of Chromophore Elongation on the Spectral Properties and Chemical Reactivity. *J. Fluoresc.* **2006,** *16* (2), 185-190.

259. Mohr, G. J.; Spichiger-Keller, U. E., Synthesis and characterization of novel chromogenic ligands for optical sensing of ethanol. *Proc. SPIE-Int. Soc. Opt. Eng.* **1997,** *3105*, 130-137.

260. Mohr, G. J.; Spichiger-Keller, U. E., Novel fluorescent sensor membranes for alcohols based on *p-N,N*-Dioctylamino-4'-trifluoroacetylstilbene. *Anal. Chim. Acta* **1997,** *351* (1-3), 189-196.

261. Mohr, G. J.; Tirelli, N.; Spichiger-Keller, U. E., Plasticizer-free optode membranes for dissolved amines based on copolymers from alkyl methacrylates and the fluoro reactant ETHT 4014. *Anal. Chem.* **1999,** *71* (8), 1534-1539.

262. Johns, I. B.; McElhill, E. A.; Smith, J. O., Thermal Stability of Some Organic Compounds. *J. Chem. Eng. Data* **1962,** *7* (2), 277-281.

263. Ghasemi, Z.; Fathi, Z., Synthesis of highly fluorescent (E)-Stilbene derivatives containing polysubstituted imidazole scaffold. *Res. Chem. Intermed.* **2017,** *43* (5), 3131-3143.

264. Gegiou, D.; Muszkat, K. A.; Fischer, E., Temperature dependence of photoisomerization. V. Effect of substituents on the photoisomerization of stilbenes and azobenzenes. *J. Am. Chem. Soc.* **1968,** *90* (15), 3907-3918.

265. Mohr, G. J.; Citterio, D.; Demuth, C.; Fehlmann, M.; Jenny, L.; Lohse, C.; Moradian, A.; Nezel, T.; Rothmaier, M.; Spichiger, U. E., Reversible chemical reactions as the basis for optical sensors used to detect amines, alcohols and humidity. *J. Mater. Chem.* **1999,** *9* (9), 2259-2264.

266. Yoshino, J.; Kano, N.; Kawashima, T., Fluorescent azobenzenes and aromatic aldimines featuring an N–B interaction. *Dalton Trans.* **2013,** *42* (45), 15826-15834.

267. Reichardt, C., Solvatochromic Dyes as Solvent Polarity Indicators. *Chem. Rev.* **1994,** *94* (8), 2319-2358.

268. Yan, J.; Wang, X.; Chen, J., Swelling of porous styrene–divinylbenzene copolymers in water. *J. Appl. Polym. Sci.* **2000,** *75* (4), 536-544.

269. Marais, S.; Metayer, M.; Nguyen, T. Q.; Labbe, M.; Saiter, J. M., Diffusion and permeation of water through unsaturated polyester resins—influence of resin curing. *Eur. Polym. J.* **2000,** *36* (3), 453-462.

270. Mohr, G. J.; Klimant, I.; Spichiger-Keller, U. E.; Wolfbeis, O. S., Fluoro reactants and dual luminophor referencing: a technique to optically measure amines. *Anal. Chem.* **2001,** *73* (5), 1053-1056.

271. Hermida-Merino, D.; O'Driscoll, B.; Hart, L. R.; Harris, P. J.; Colquhoun, H. M.; Slark, A. T.; Prisacariu, C.; Hamley, I. W.; Hayes, W., Enhancement of microphase ordering and mechanical properties of supramolecular hydrogen-bonded polyurethane networks. *Polym. Chem.* **2018,** *9* (24), 3406-3414.

272. Tang, X.; Feula, A.; Baker, B. C.; Melia, K.; Hermida Merino, D.; Hamley, I. W.; Buckley, C. P.; Hayes, W.; Siviour, C. R., A dynamic supramolecular polyurethane network whose mechanical properties are kinetically controlled. *Polymer* **2017,** *133*, 143-150.

273. 17 - New Energy-saving and Environmental Protective Building Materials. In *Building Decorative Materials*, Li, Y.; Ren, S., Eds. Woodhead Publishing: **2011**; pp 375-390.

274. Biewend, M.; Michael, P.; Binder, W. H., Detection of stress in polymers: mechanochemical activation of CuAAC click reactions in poly(urethane) networks. *Soft Matter* **2020,** *16* (5), 1137-1141.

275. Nellepalli, P.; Patel, T.; Oh, J. K., Dynamic Covalent Polyurethane Network Materials: Synthesis and Self-Healability. *Macromol. Rapid Commun.* **2021,** *42* (20), 2100391.

276. Deflorian, F.; Rossi, S.; Scrinzi, E., Self-healing supramolecular polyurethane coatings: preliminary study of the corrosion protective properties. *Corros. Eng. Sci.* **2013,** *48* (2), 147-154.

277. Jiao, L.; Xiao, H.; Wang, Q.; Sun, J., Thermal degradation characteristics of rigid polyurethane foam and the volatile products analysis with TG-FTIR-MS. *Polym. Degrad. Stab.* **2013,** *98* (12), 2687-2696.

278. Montaudo, G.; Puglisi, C.; Scamporrino, E.; Vitalini, D., Mechanism of thermal degradation of polyurethanes. Effect of ammonium polyphosphate. *Macromolecules* **1984,** *17* (8), 1605-1614.

279. Mohd-Rus, A. Z.; Kemp, T. J.; Clark, A. J., Degradation studies of polyurethanes based on vegetable oils. Part 2. Thermal degradation and materials properties. *Prog. React. Kinet. Mech.* **2009,** *34* (1), 1-41.

280. Schmitt, F. J.; Campbell, Z. Y.; Bui, M. V.; Hüls, A.; Tomo, T.; Chen, M.; Maksimov, E. G.; Allakhverdiev, S. I.; Friedrich, T., Photosynthesis supported by a chlorophyll f-dependent, entropy-driven uphill energy transfer in Halomicronema hongdechloris cells adapted to far-red light. *Photosynth. Res.* **2019,** *139* (1-3), 185-201.

281. Schmitt, F.-J.; Campbell, Z. Y.; Moldenhauer, M.; Friedrich, T., Light-induced phycobilisome dynamics in Halomicronema hongdechloris. *J. Photochem. Photobiol., A* **2020,** *403*, 112838.

282. Schmitt, F.-J.; Thaa, B.; Junghans, C.; Vitali, M.; Veit, M.; Friedrich, T., eGFP-pHsens as a highly sensitive fluorophore for cellular pH determination by fluorescence lifetime imaging microscopy (FLIM). *Biochem. Biophys. Acta Bioenerg.* **2014,** *1837* (9), 1581-1593.

283. Wilkening, S.; Schmitt, F. J.; Horch, M.; Zebger, I.; Lenz, O.; Friedrich, T., Characterization of Frex as an NADH sensor for in vivo applications in the presence of NAD(+) and at various pH values. *Photosynth. Res.* **2017,** *133* (1-3), 305-315.

284. Scheidt, F.; Schäfer, M.; Sarie, J. C.; Daniliuc, C. G.; Molloy, J. J.; Gilmour, R., Enantioselective, Catalytic Vicinal Difluorination of Alkenes. *Angew. Chem. Int. Ed.* **2018,** *57* (50), 16431-16435.

285. Mohr, G. J.; Lehmann, F.; Grummt, U.-W.; Spichiger-Keller, U. E., Fluorescent ligands for optical sensing of alcohols: Synthesis and characterisation of p-N,N-dialkylamino-trifluoroacetylstilbenes. *Anal. Chim. Acta* **1997,** *344* (3), 215-225.

286. Soga, T.; Jimbo, Y.; Suzuki, K.; Citterio, D., Inkjet-Printed Paper-Based Colorimetric Sensor Array for the Discrimination of Volatile Primary Amines. *Anal. chem.* **2013,** *85* (19), 8973-8978.

7. Appendix

7.1. Thermal degradation of PEIs

Figure A1 a) ^{1}H-NMR spectrum and b) ^{13}C-NMR spectrum of **PEI-1PC** recorded in CDCl$_3$.
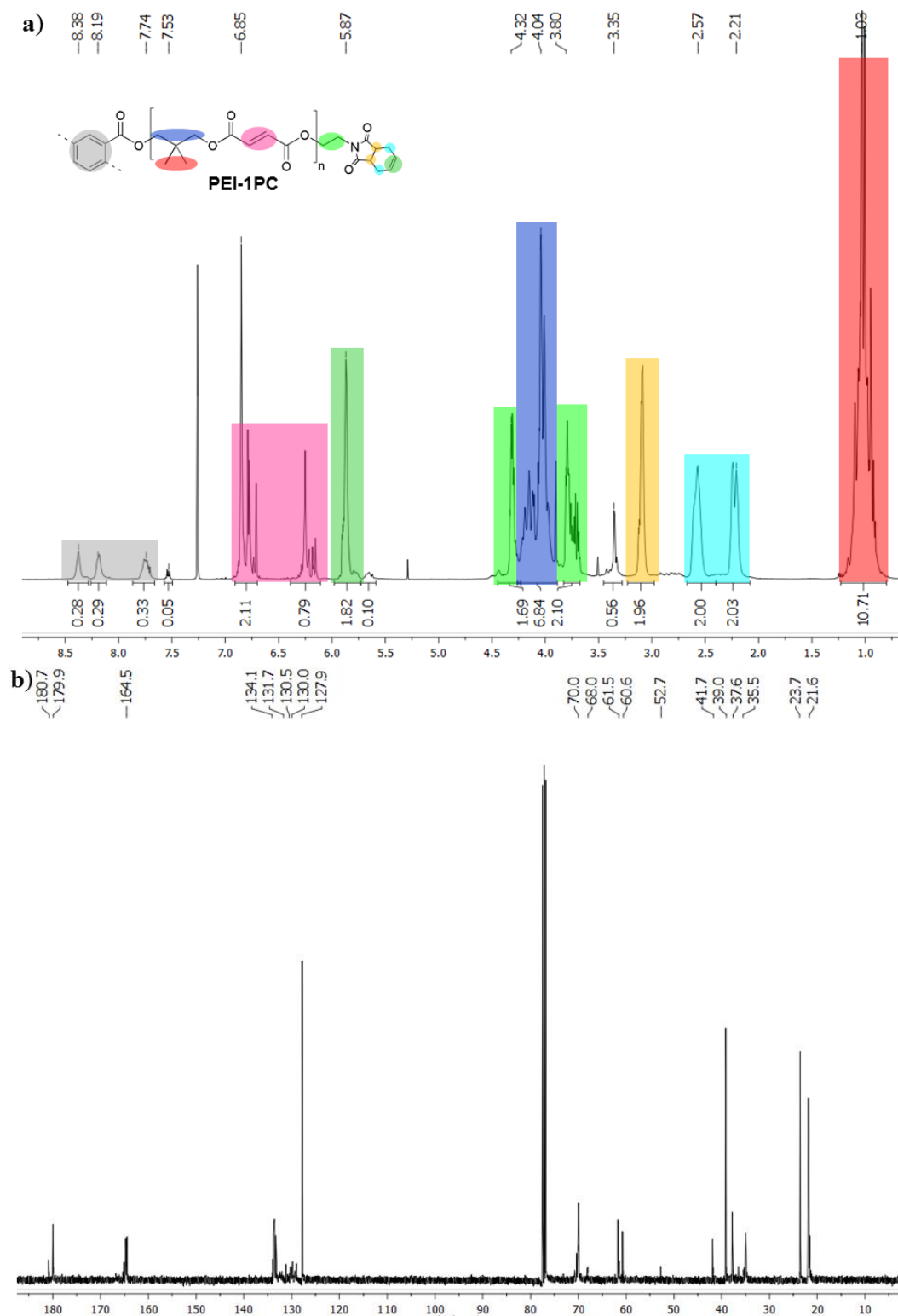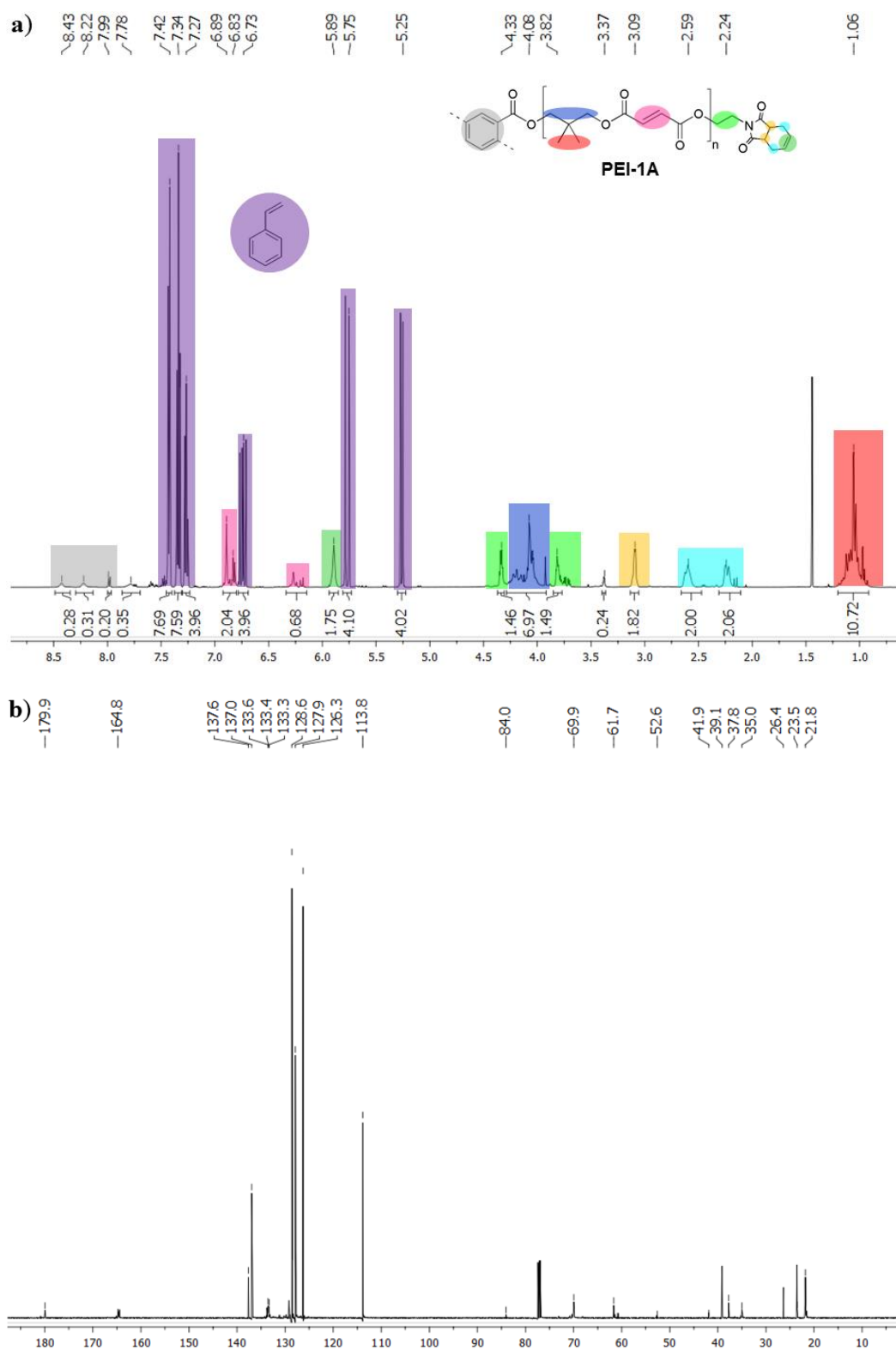
Figure A2 a) ¹H-NMR spectrum and b) ¹³C-NMR spectrum of **PEI-1A** (**PEI-1PC** dissolved in styrene) recorded in CDCl₃.
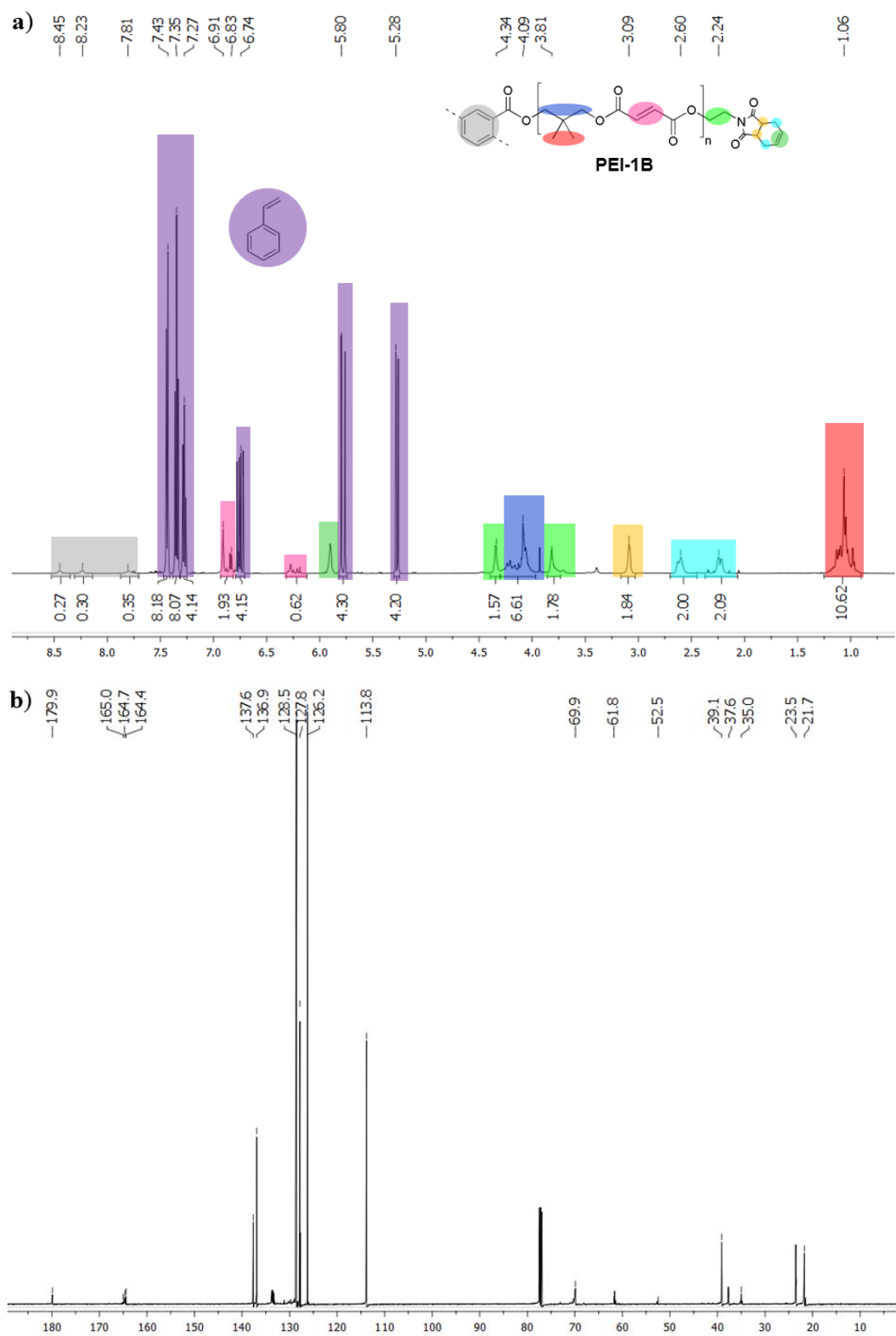
Figure A3 a) ¹H-NMR spectrum and b) ¹³C-NMR spectrum of **PEI-1B** (**PEI-1PC** dissolved in styrene) recorded in CDCl₃.
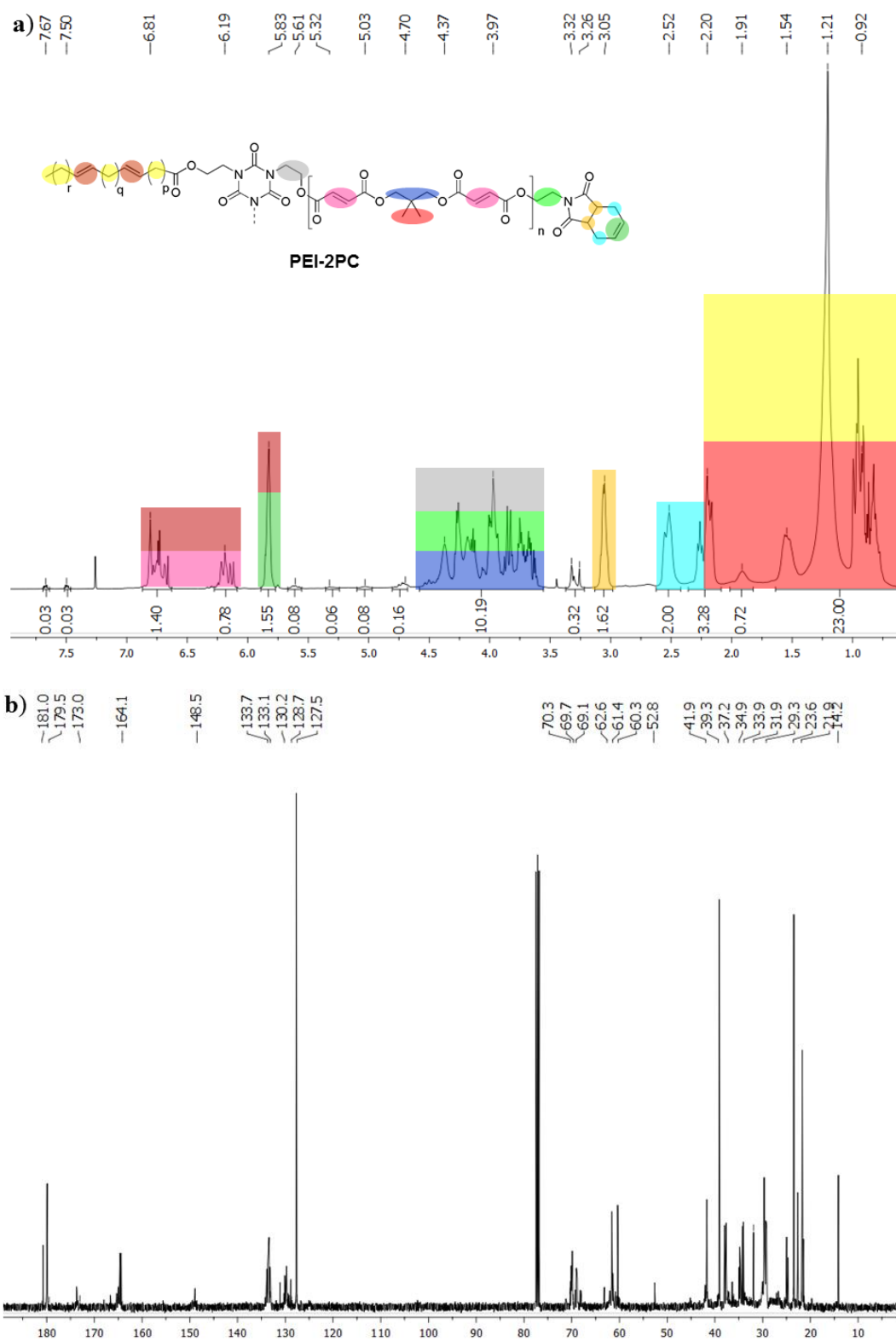
Figure A4 a) ^{1}H-NMR spectrum and b) ^{13}C-NMR spectrum of **PEI-2PC** recorded in CDCl$_3$.
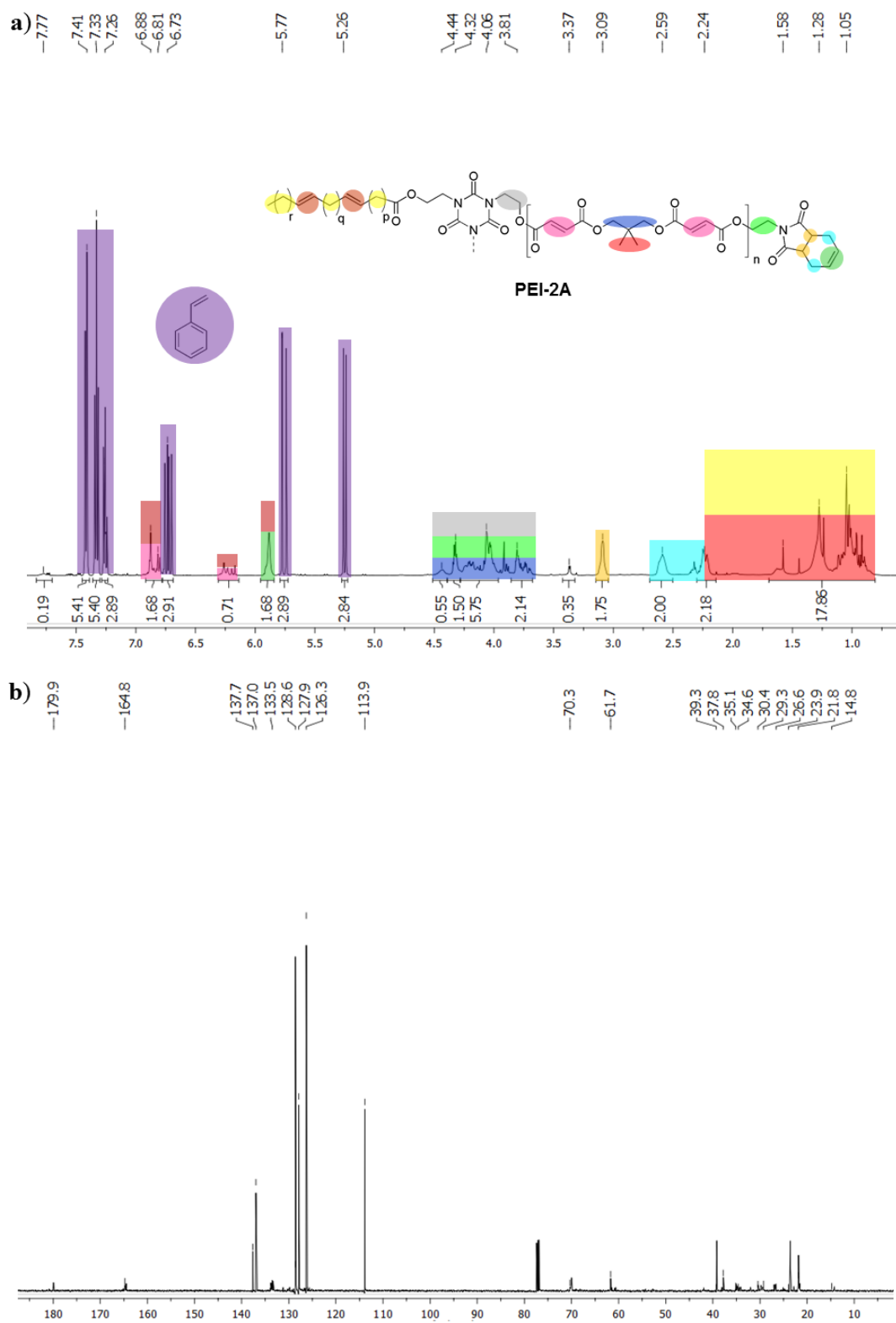
Figure A5 a) ^{1}H-NMR spectrum and b) ^{13}C-NMR spectrum of **PEI-2A** (**PEI-2PC** dissolved in styrene) recorded in CDCl$_3$.

Figure A6 ESI-TOF-MS spectrum of **PEI-1PC**.

Figure A7 ESI-TOF-MS spectrum of **PEI-2PC**.
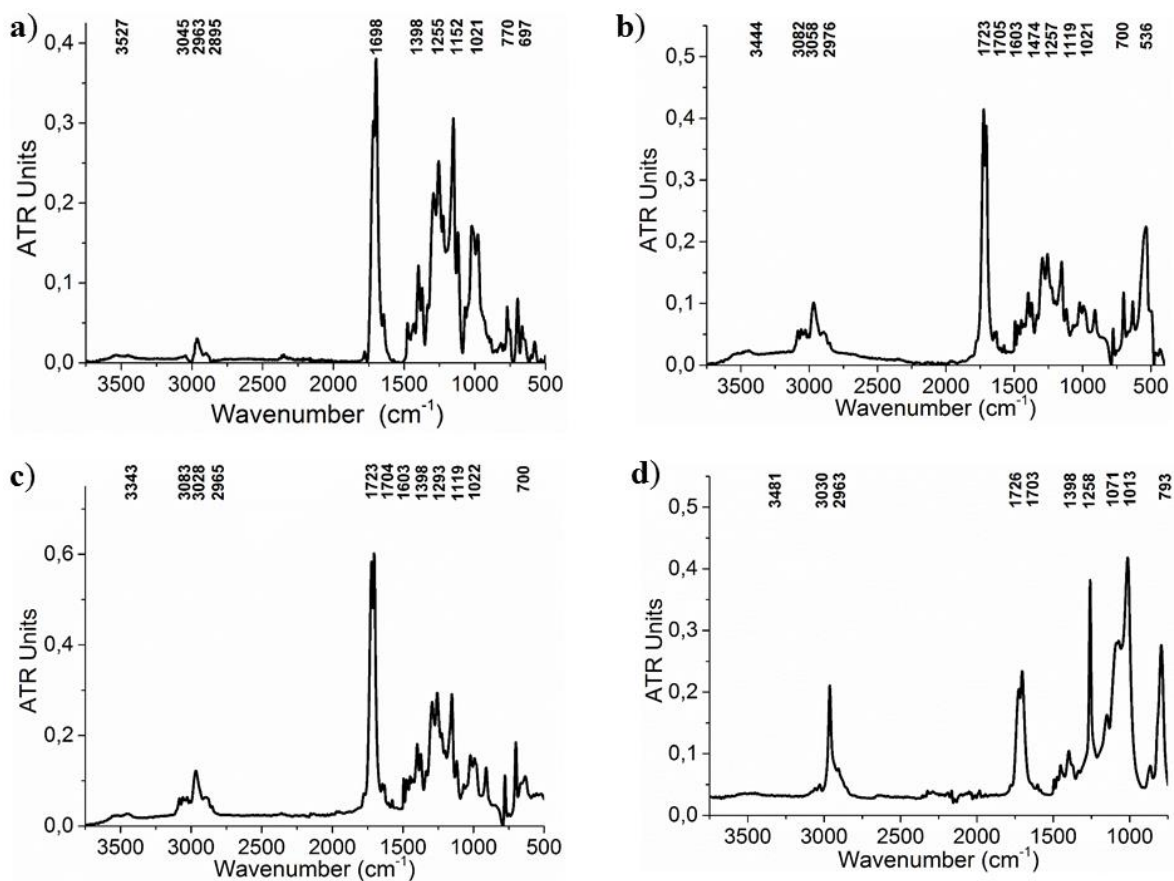
Figure A8 IR spectra of a) **PEI-1PC**, b) **PEI-1A**, c) **PEI-1B** and d) **PEI-1**.
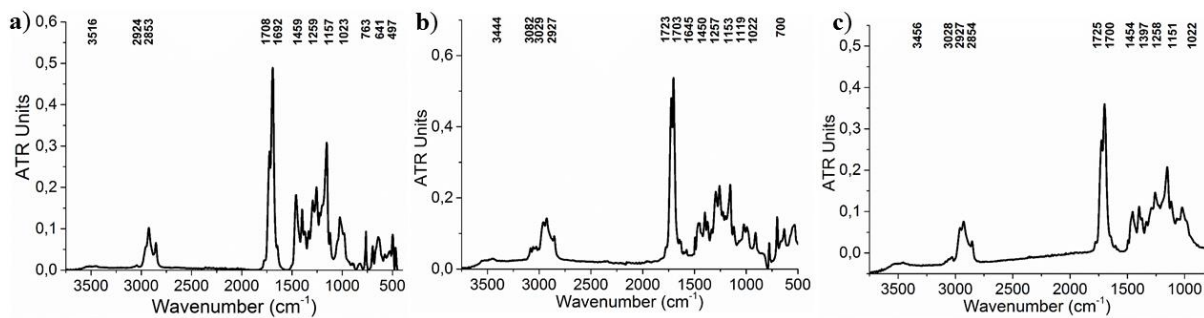
Figure A9 IR spectra of a) **PEI-2PC**, b) **PEI-2A**, and c) **PEI-2**.
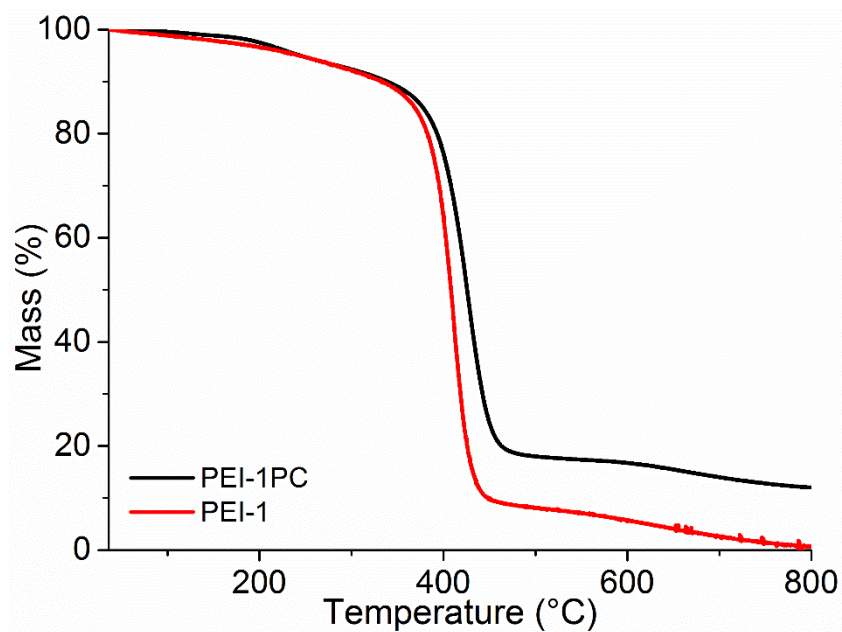
Figure A10 TGA curves of **PEI-1PC** and **PEI-1** under N_2 with a heating rate of 5 K/min.
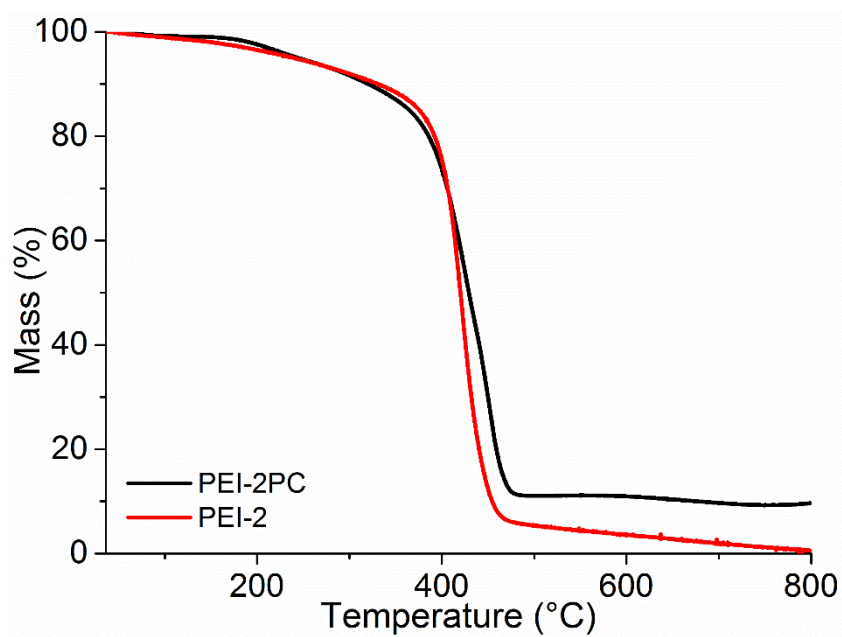
Figure A11 TGA curves of **PEI-2PC** and **PEI-2** under N_2 with a heating rate of 5 K/min.
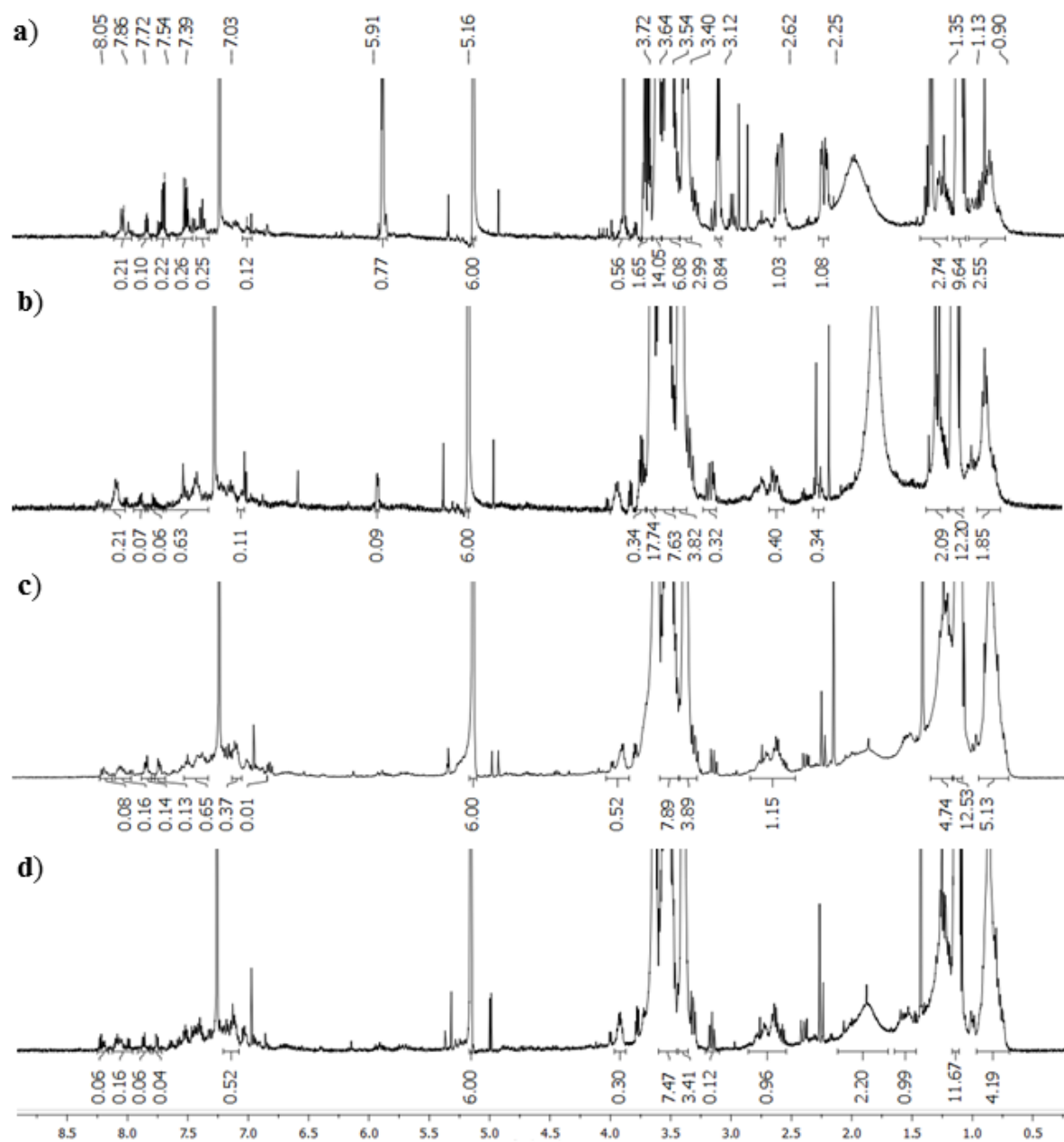
Figure A12 ^{1}H-NMR spectra of the degradation extracts of **PEI-1PC** degraded at 220 °C after a) 500 h, b) 1000 h, c) 3000 h and d) 5000 h recorded in CDCl$_3$.
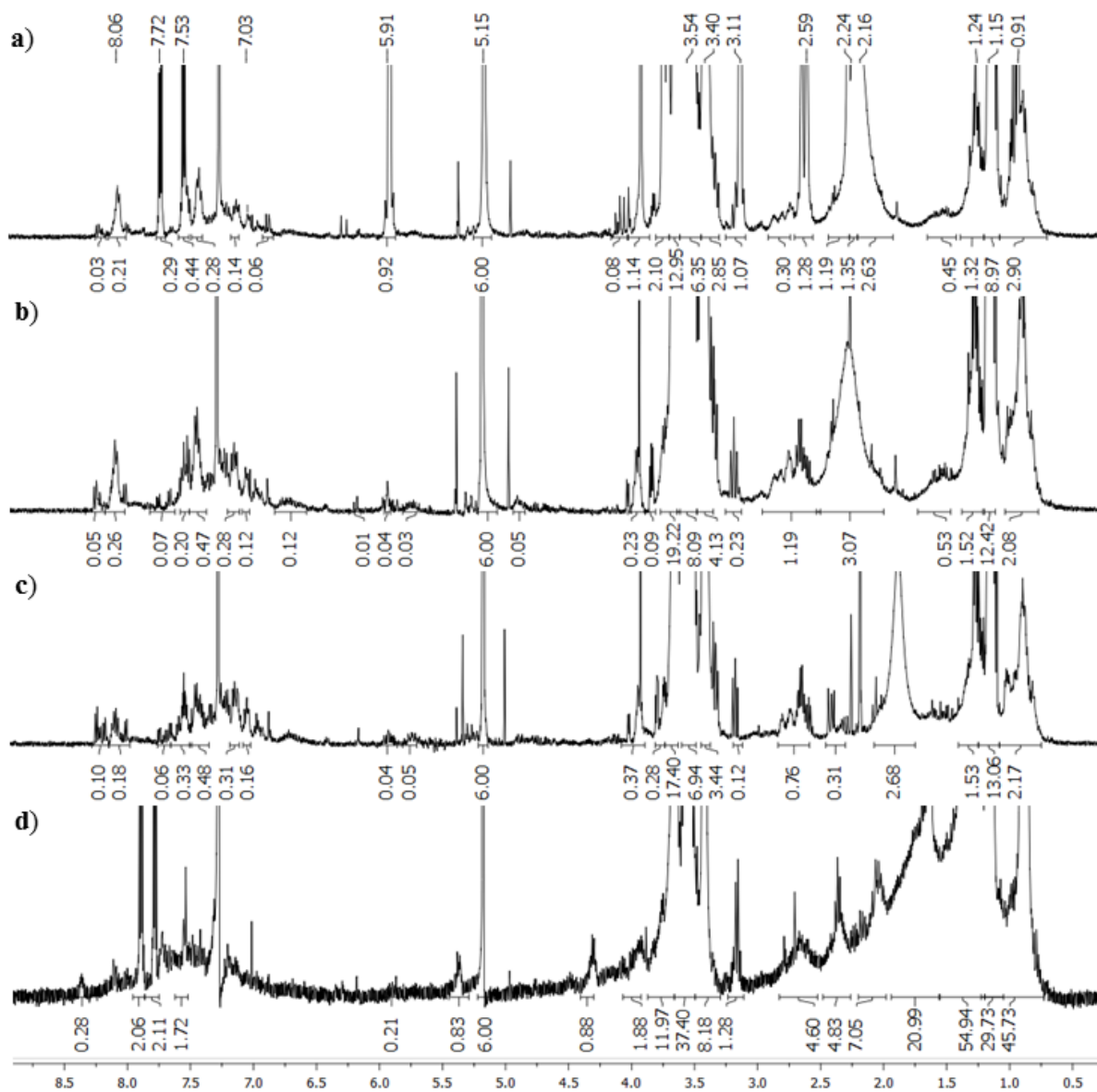
Figure A13 ^{1}H-NMR spectra of the degradation extracts of **PEI-1PC** degraded at 200 °C after a) 500 h, b) 1000 h, c) 3000 h and d) 5000 h recorded in CDCl$_3$.

Figure A14 ^{1}H-NMR spectra of the degradation extracts of **PEI-1PC** degraded at 180 °C after a) 500 h, b) 1000 h, c) 3000 h and d) 5000 h recorded in CDCl$_3$.
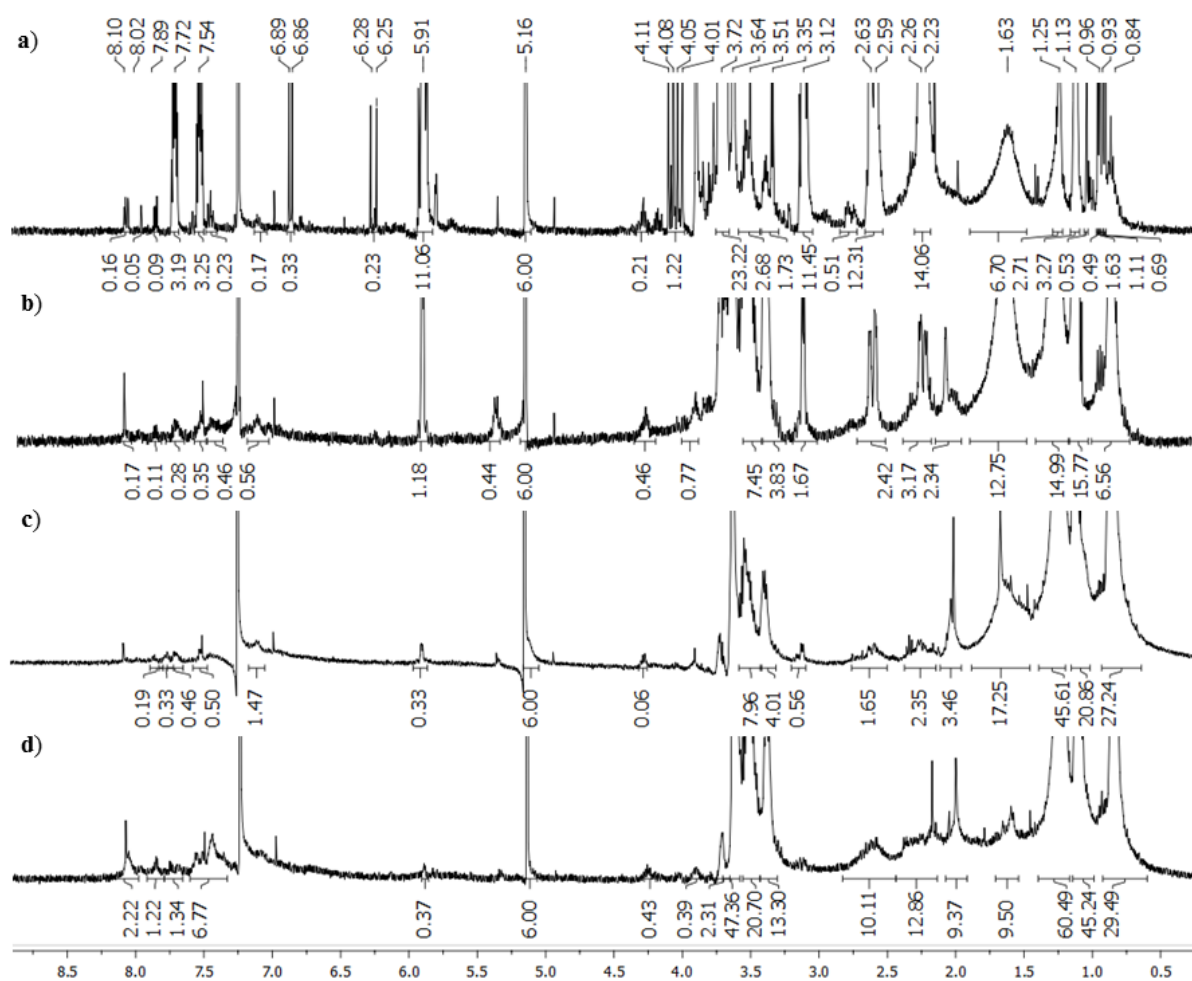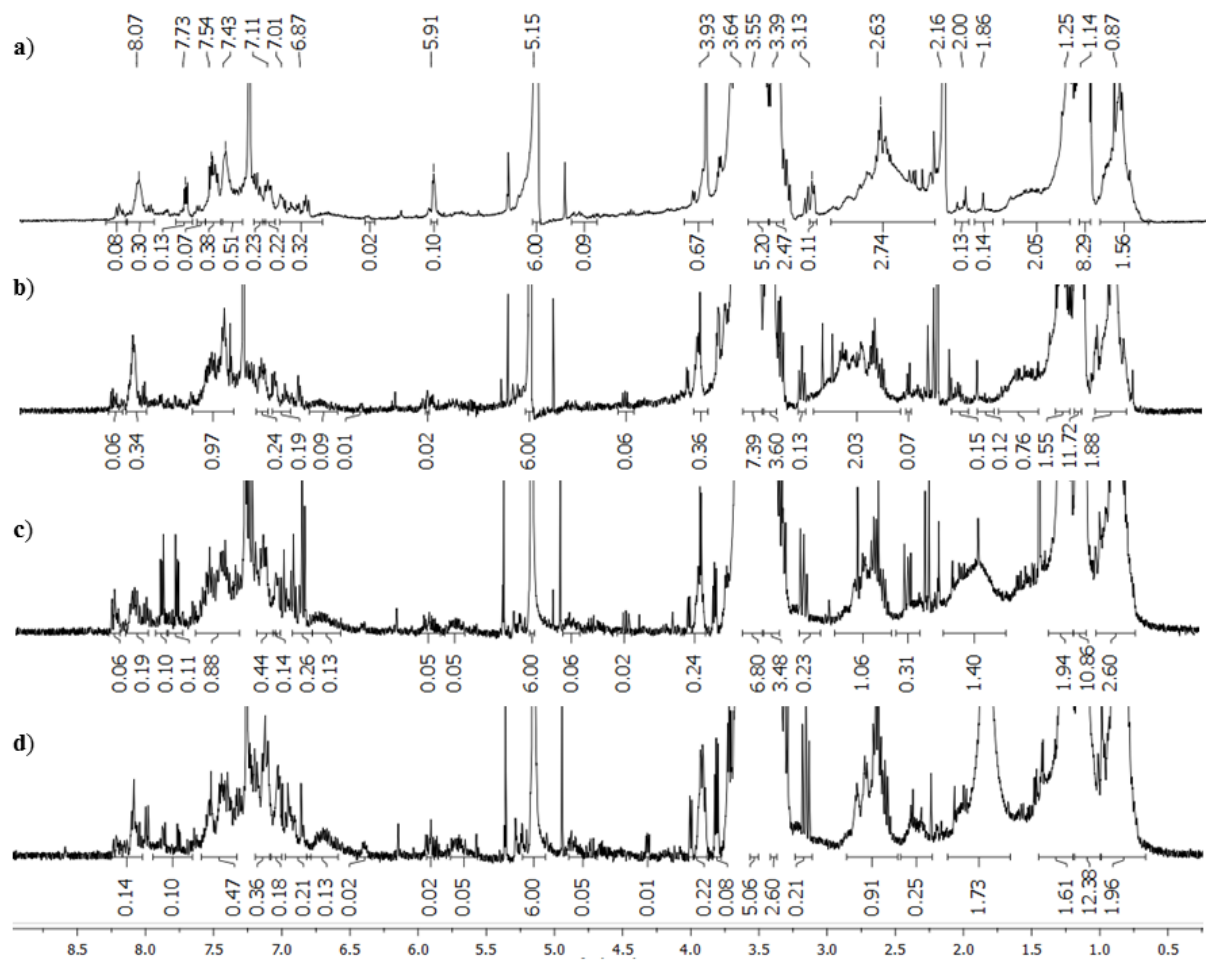
Figure A15 ^{1}H-NMR spectra of the degradation extracts of **PEI-1** degraded at 220 °C after a) 500 h, b) 1000 h, c) 3000 h and d) 5000 h recorded in CDCl$_3$.
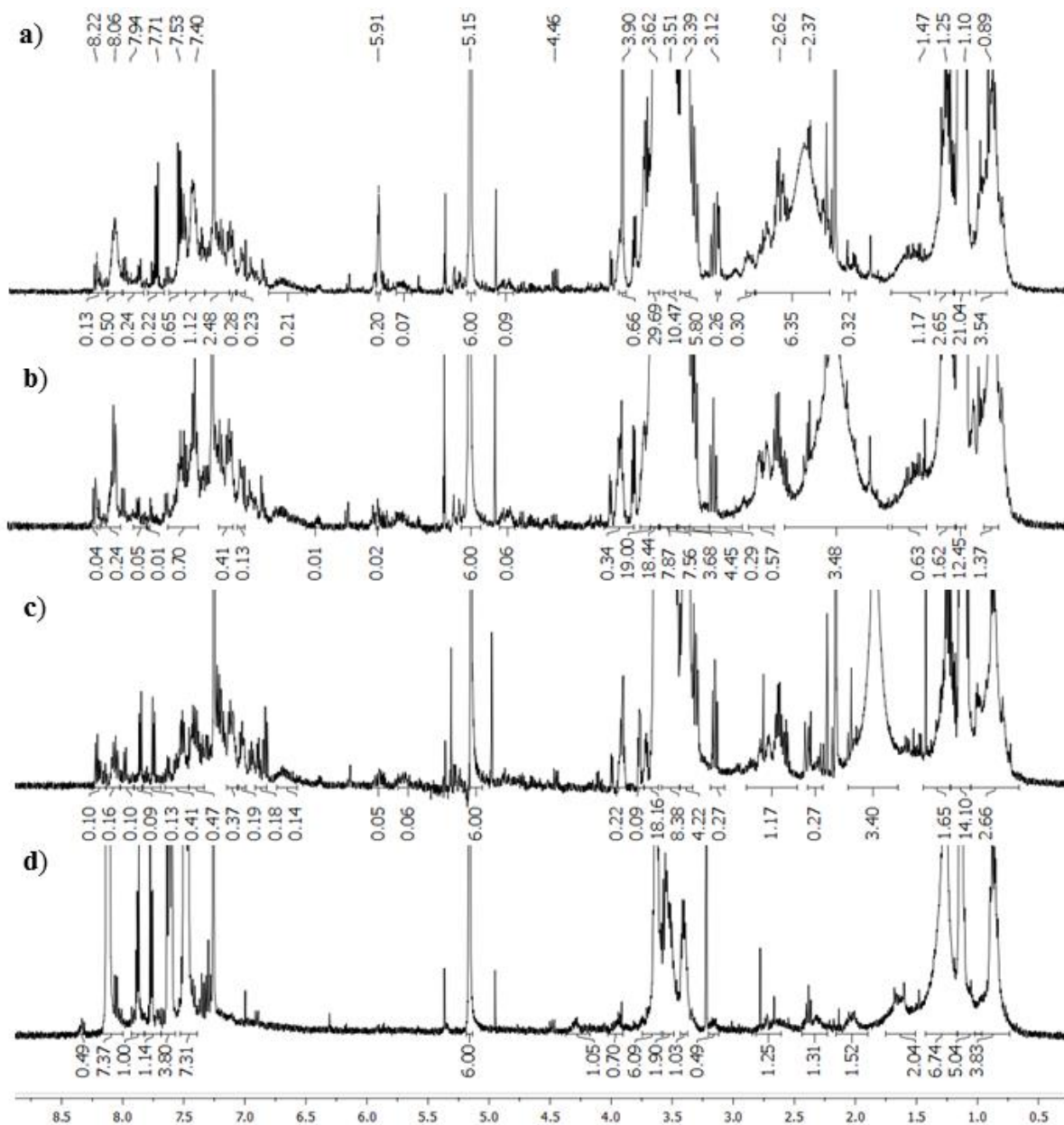
Figure A16 ^{1}H-NMR spectra of the degradation extracts of **PEI-1** degraded at 200 °C after a) 500 h, b) 1000 h, c) 3000 h and d) 5000 h recorded in CDCl₃.
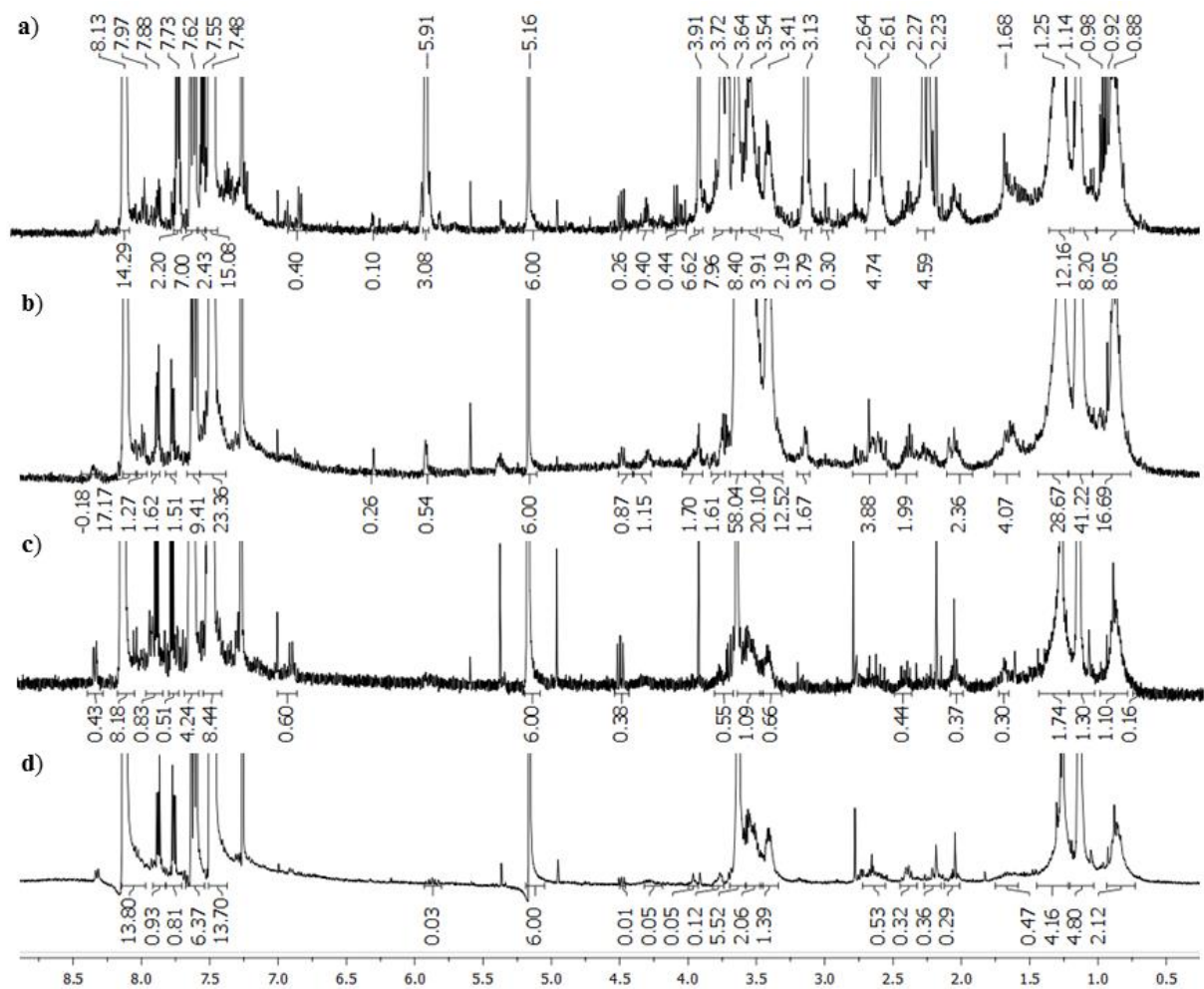
Figure A17 ¹H-NMR spectra of the degradation extracts of **PEI-1** degraded at 180 °C after a) 500 h, b) 1000 h, c) 3000 h and d) 5000 h recorded in CDCl₃.
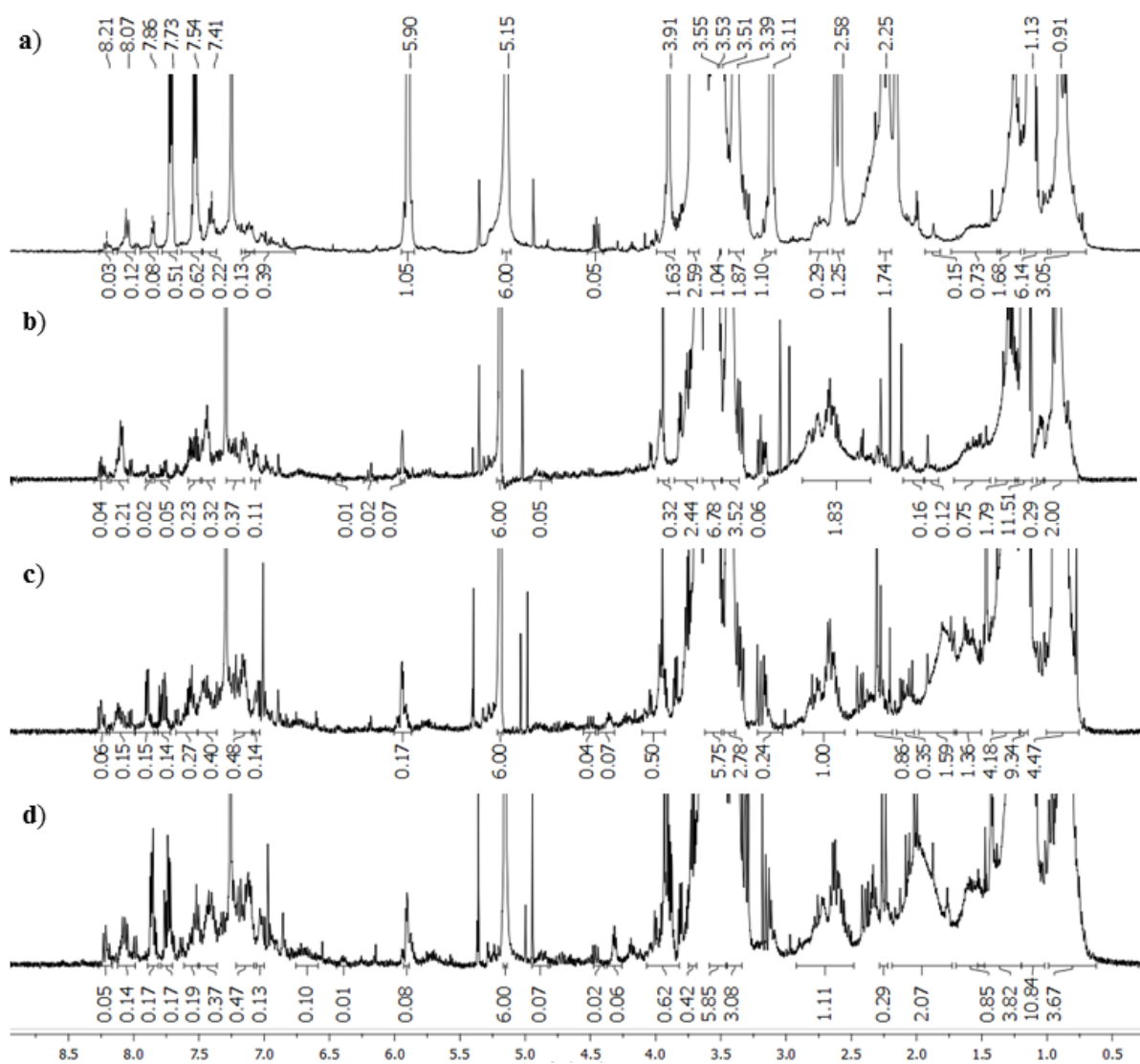
Figure A18 ¹H-NMR spectra of the degradation extracts of **PEI-2PC** degraded at 220 °C after a) 500 h, b) 1000 h, c) 3000 h and d) 5000 h recorded in CDCl₃.
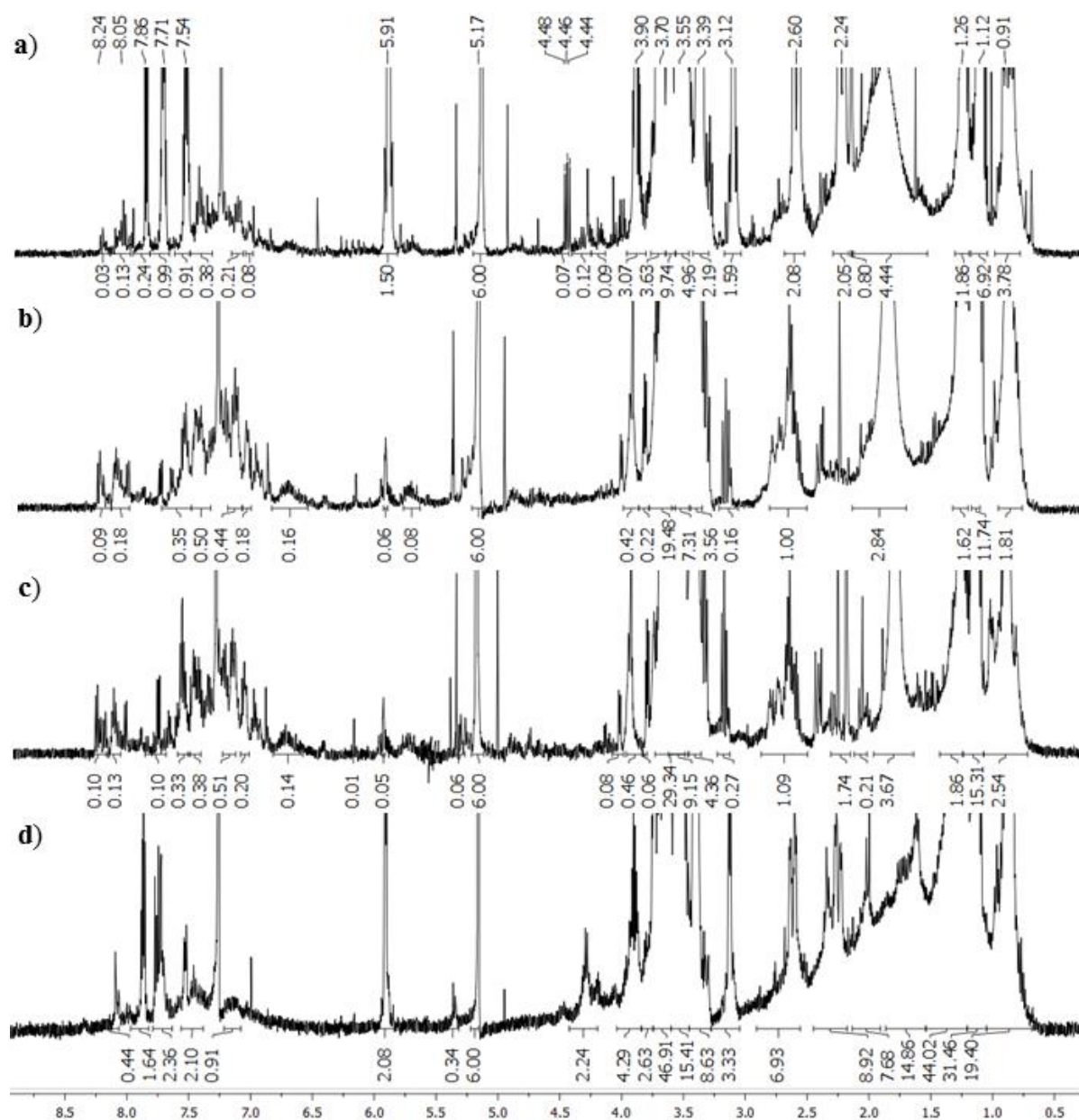
Figure A19 ^{1}H-NMR spectra of the degradation extracts of **PEI-2PC** degraded at 200 °C after a) 500 h, b) 1000 h, c) 3000 h and d) 5000 h recorded in CDCl$_3$.
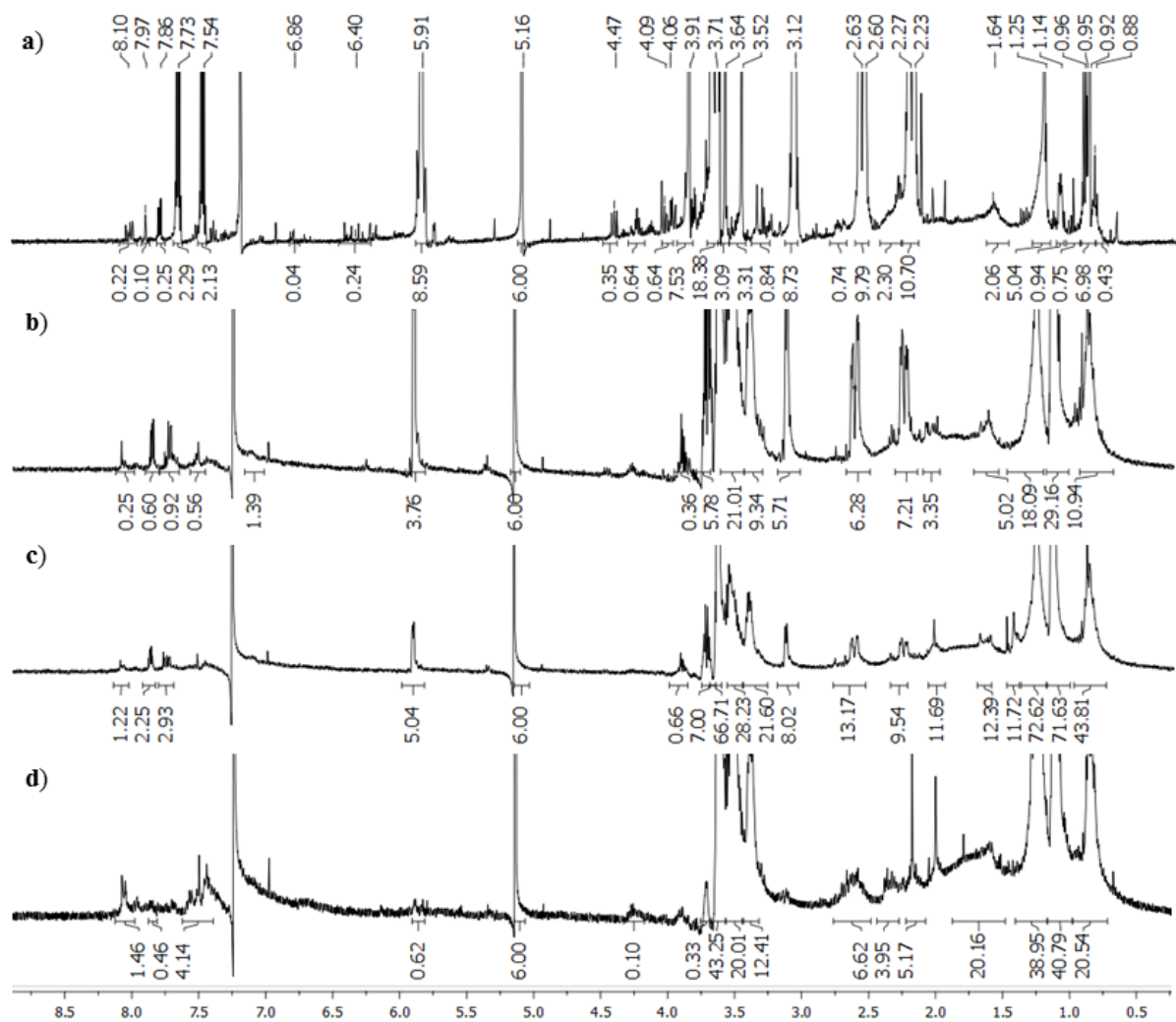
Figure A20 ^{1}H-NMR spectra of the degradation extracts of **PEI-2PC** degraded at 180 °C after a) 500 h, b) 1000 h, c) 3000 h and d) 5000 h recorded in CDCl$_3$.
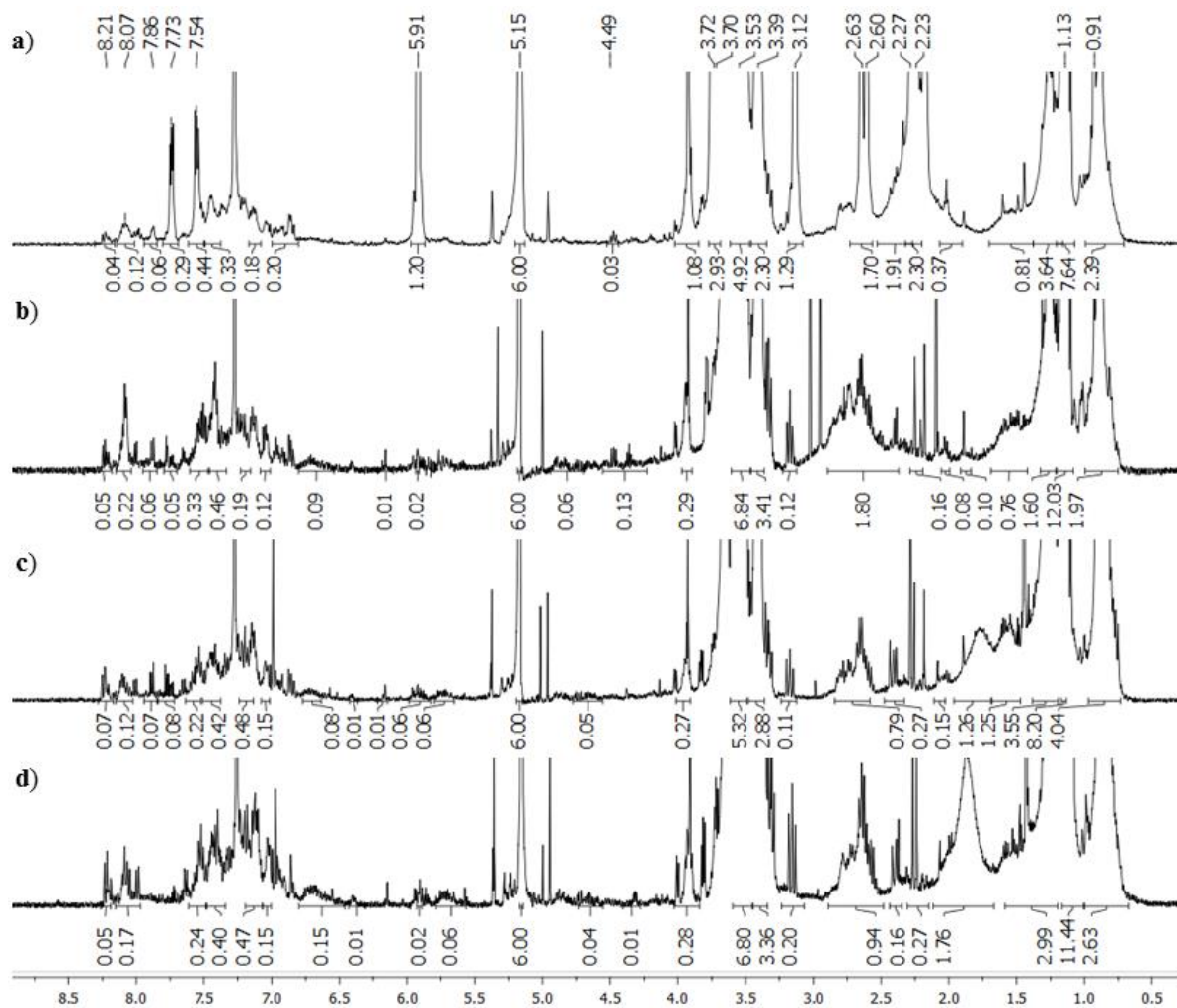
Figure A21 ^{1}H-NMR spectra of the degradation extracts of **PEI-2** degraded at 220 °C after a) 500 h, b) 1000 h, c) 3000 h and d) 5000 h recorded in CDCl$_3$.
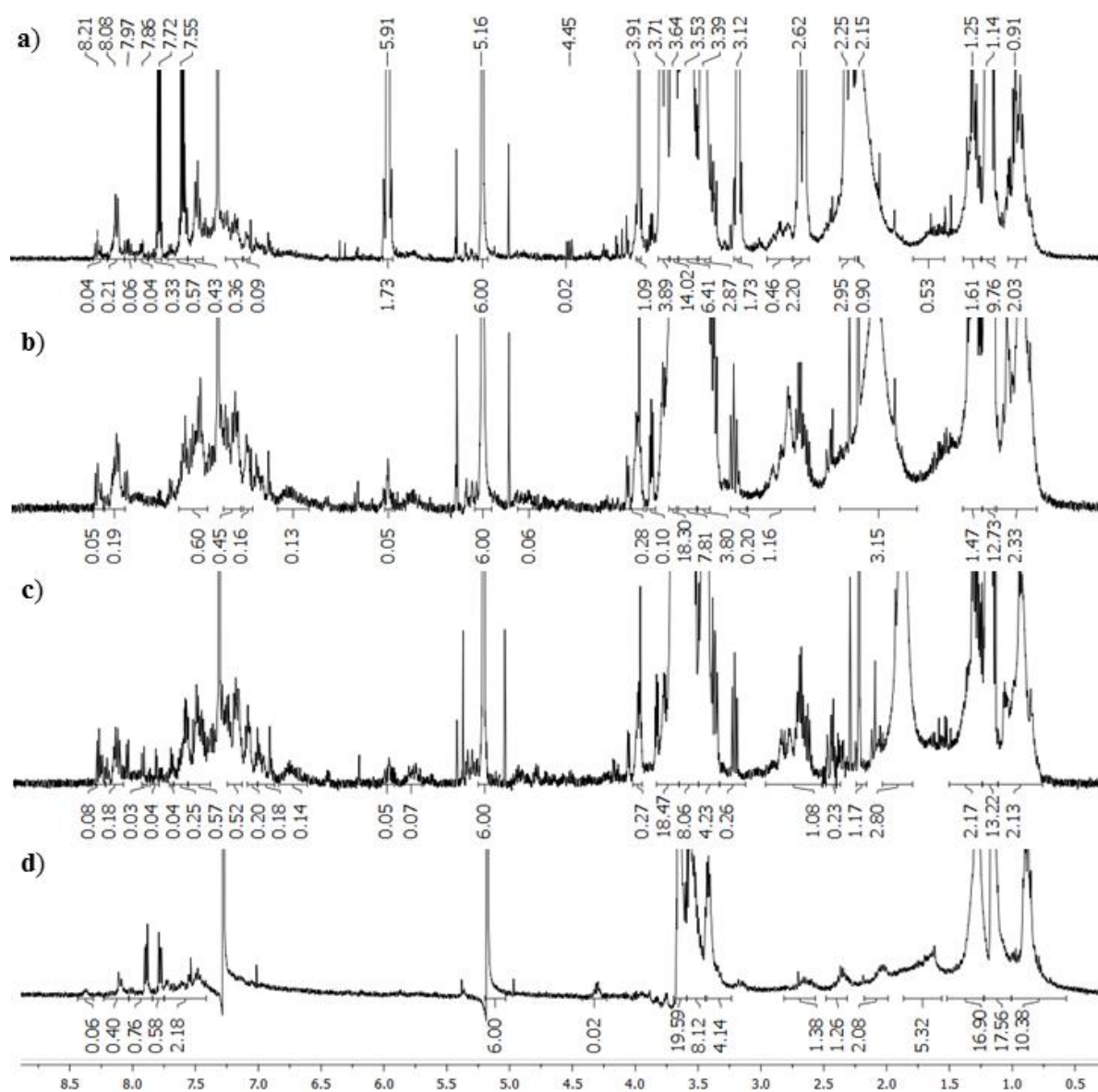
Figure A22 ^{1}H-NMR spectra of the degradation extracts of **PEI-2** degraded at 200 °C after a) 500 h, b) 1000 h, c) 3000 h and d) 5000 h recorded in CDCl$_3$.
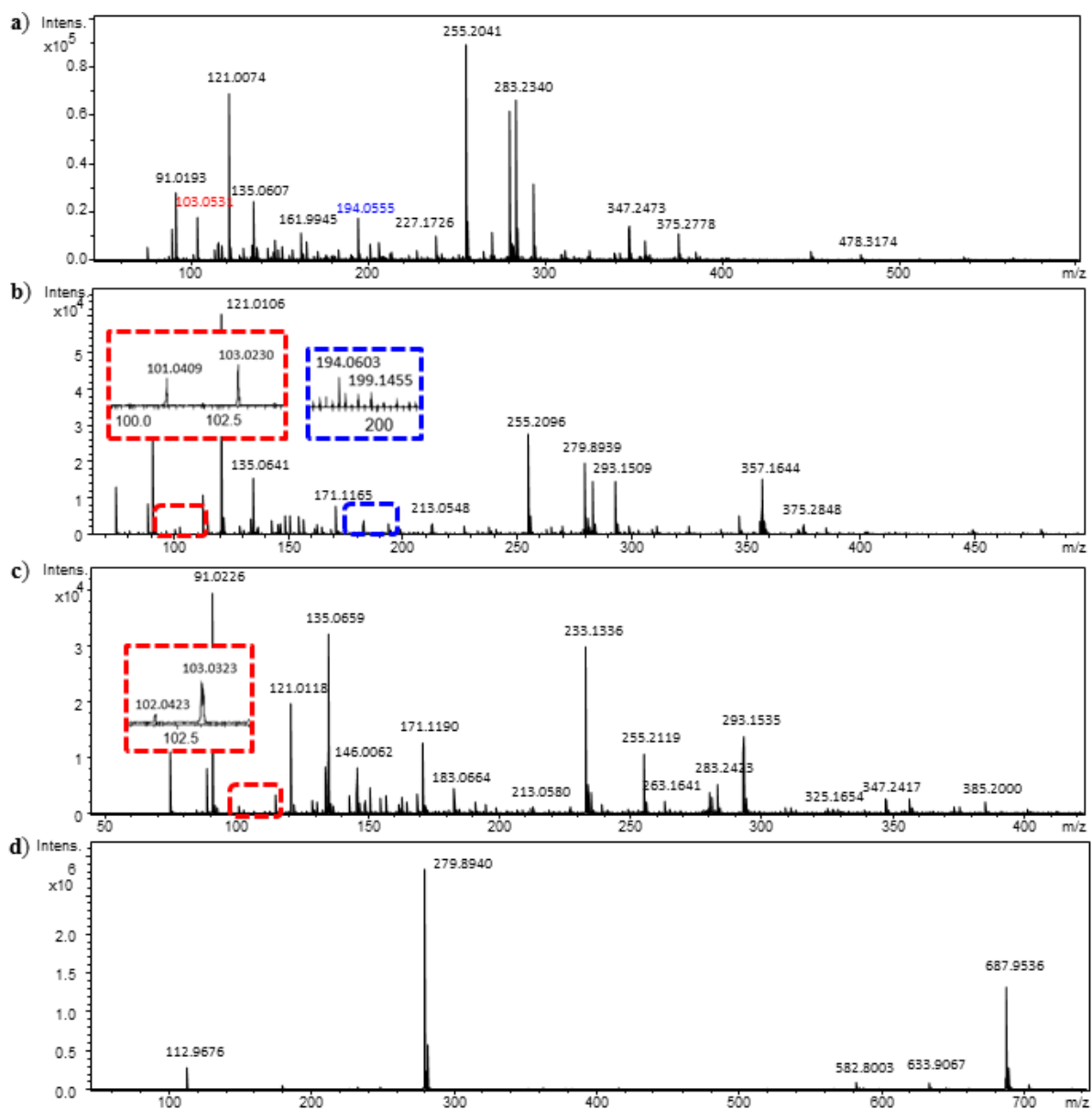
Figure A23 ESI-TOF-MS spectra of the degradation extract of **PEI-1PC** degraded at 220 °C after a) 500 h, b) 1000 h, c) 3000 h and d) 5000 h.
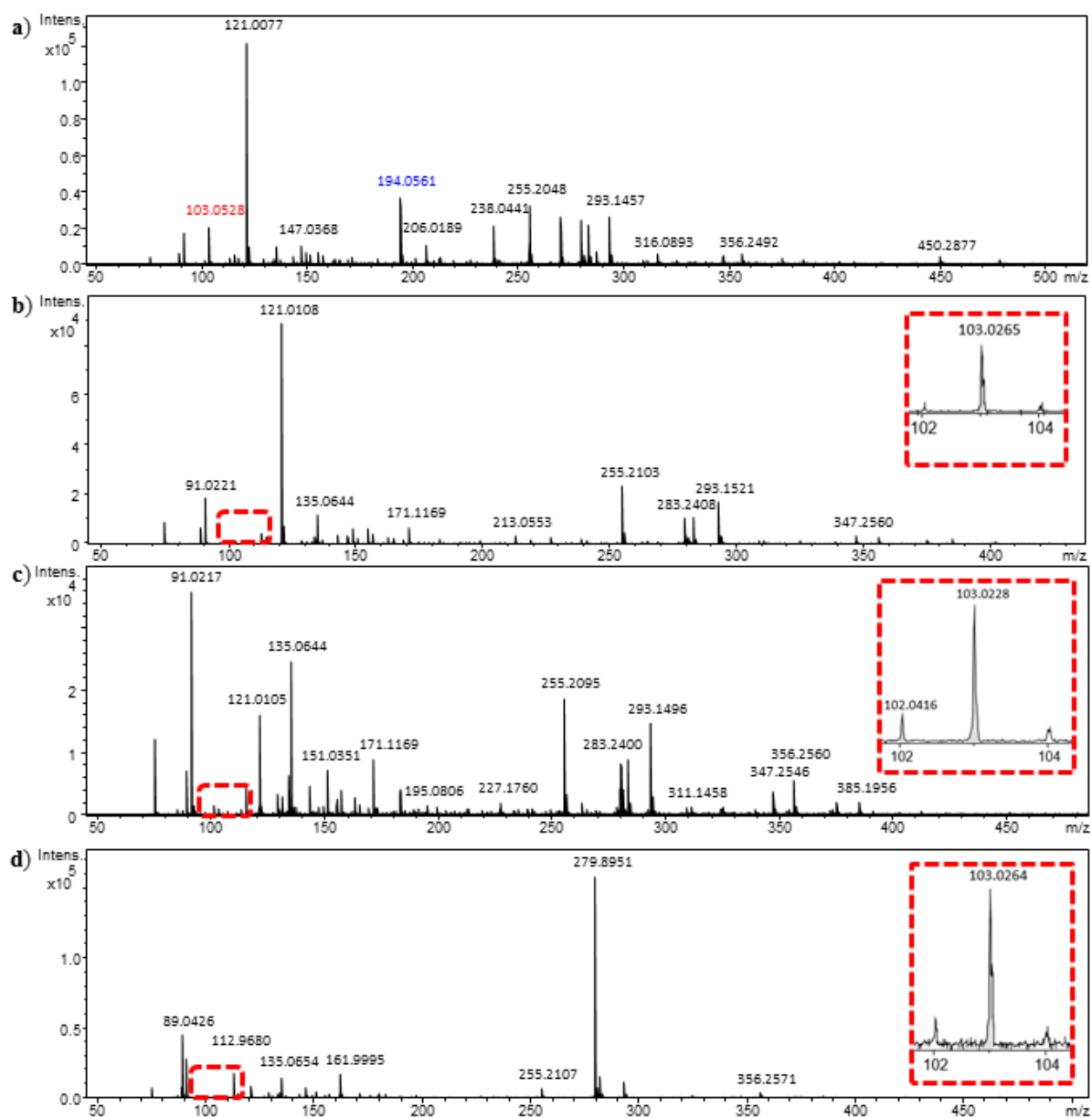
Figure A24 ESI-TOF-MS spectra of the degradation extract of **PEI-1PC** degraded at 200 °C after a) 500 h, b) 1000 h, c) 3000 h and d) 5000 h.
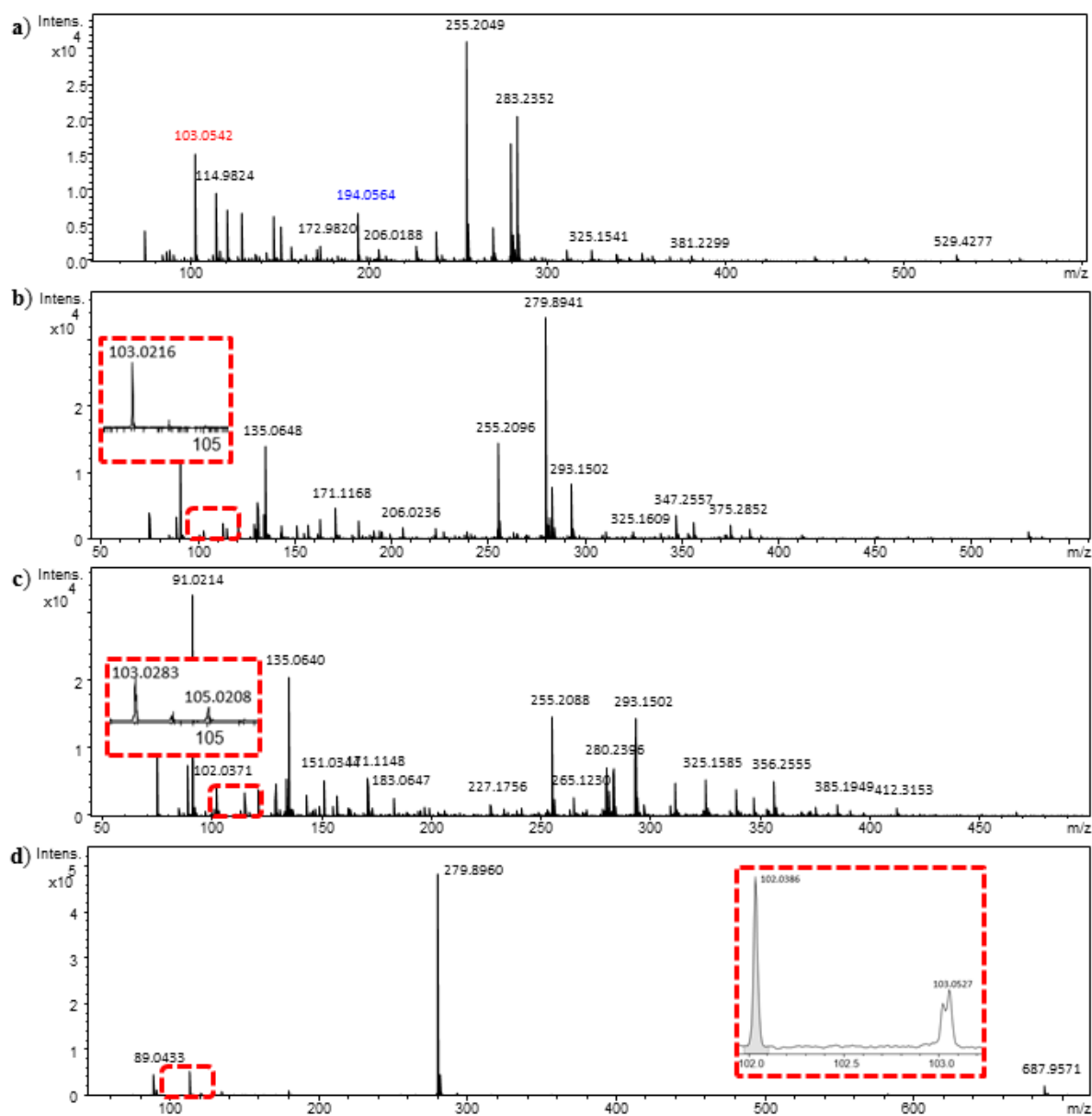
Figure A25 ESI-TOF-MS spectra of the degradation extract of **PEI-1PC** degraded at 180 °C after a) 500 h, b) 1000 h, c) 3000 h and d) 5000 h.
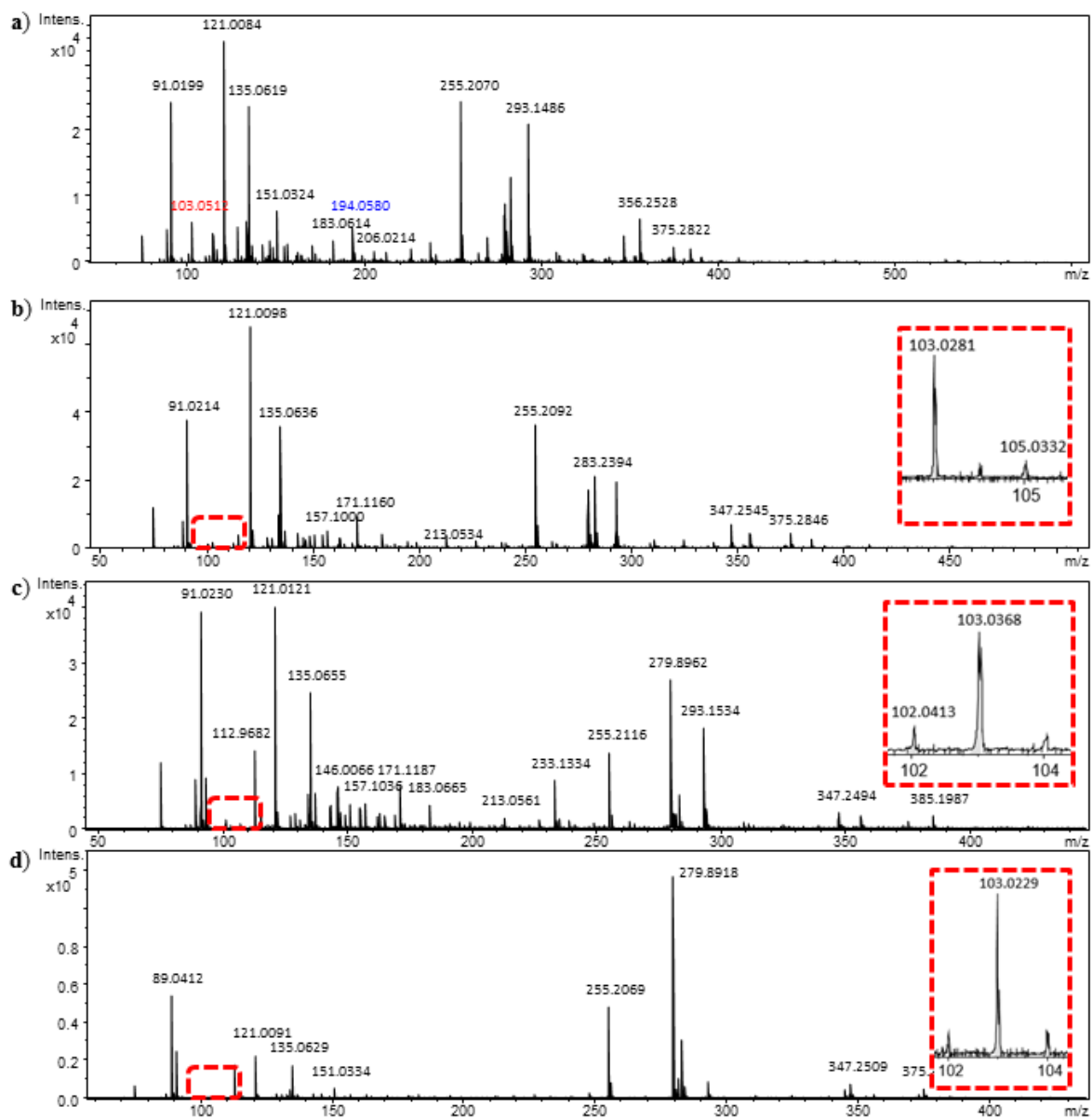
Figure A26 ESI-TOF-MS spectra of the degradation extract of **PEI-1** degraded at 220 °C after a) 500 h, b) 1000 h, c) 3000 h and d) 5000 h.
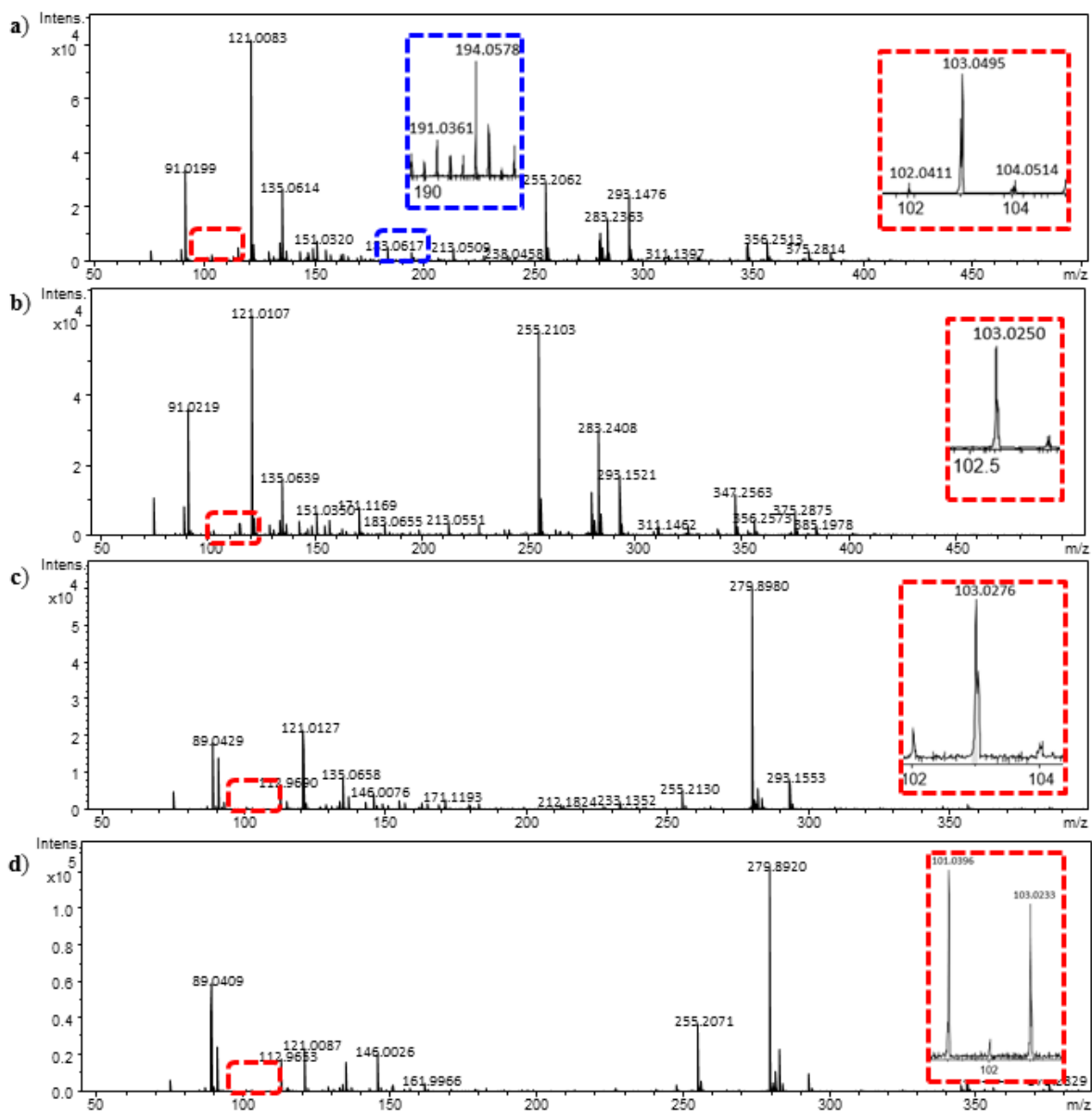
Figure A27 ESI-TOF-MS spectra of the degradation extract of **PEI-1** degraded at 200 °C after a) 500 h, b) 1000 h, c) 3000 h and d) 5000 h.
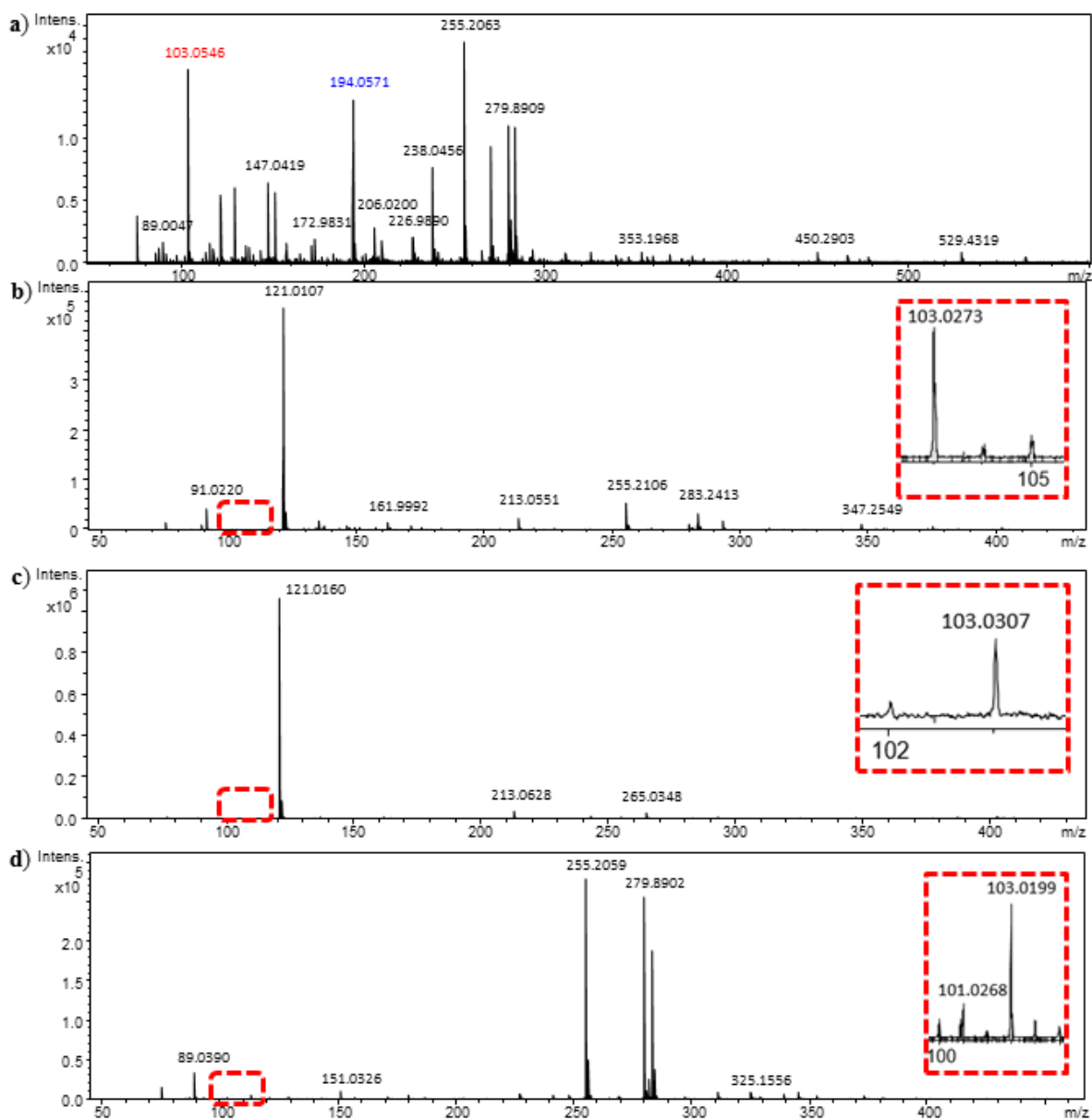
Figure A28 ESI-TOF-MS spectra of the degradation extract of **PEI-1** degraded at 180 °C after a) 500 h, b) 1000 h, c) 3000 h and d) 5000 h.
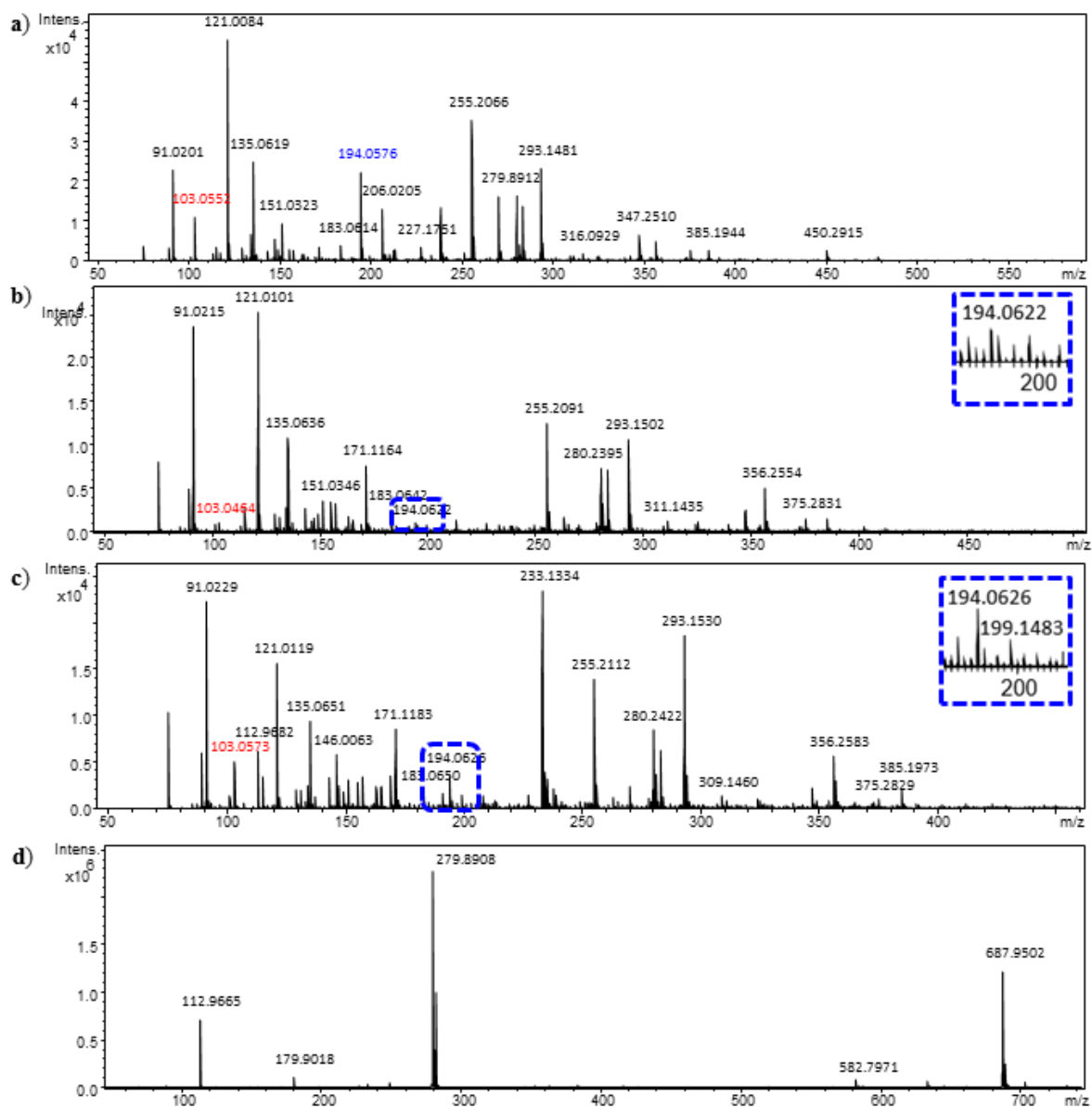
Figure A29 ESI-TOF-MS spectra of the degradation extract of **PEI-2PC** degraded at 220 °C after
a) 500 h, b) 1000 h, c) 3000 h and d) 5000 h.
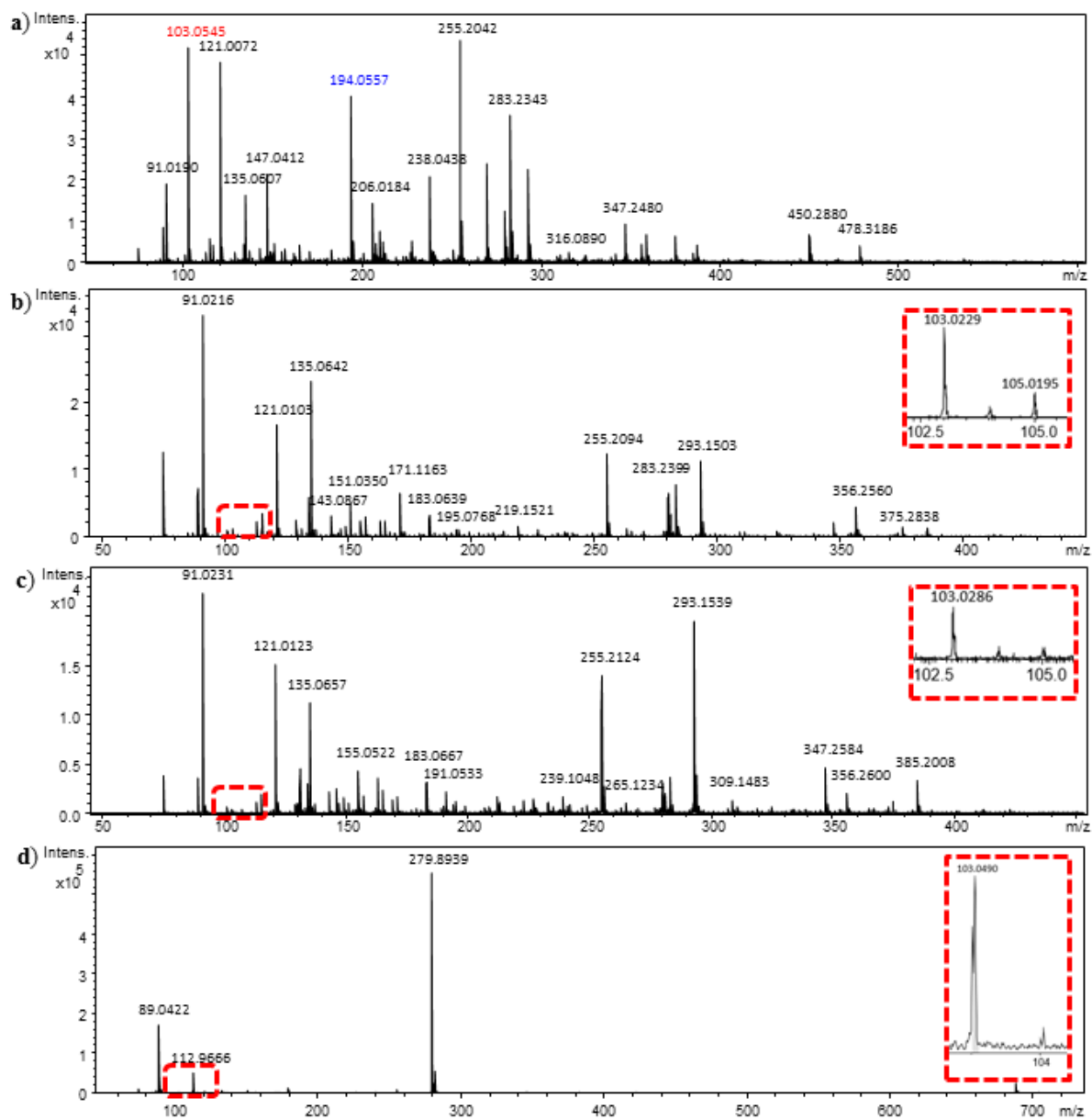
Figure A30 ESI-TOF-MS spectra of the degradation extract of **PEI-2PC** degraded at 200 °C after a) 500 h, b) 1000 h, c) 3000 h and d) 5000 h.
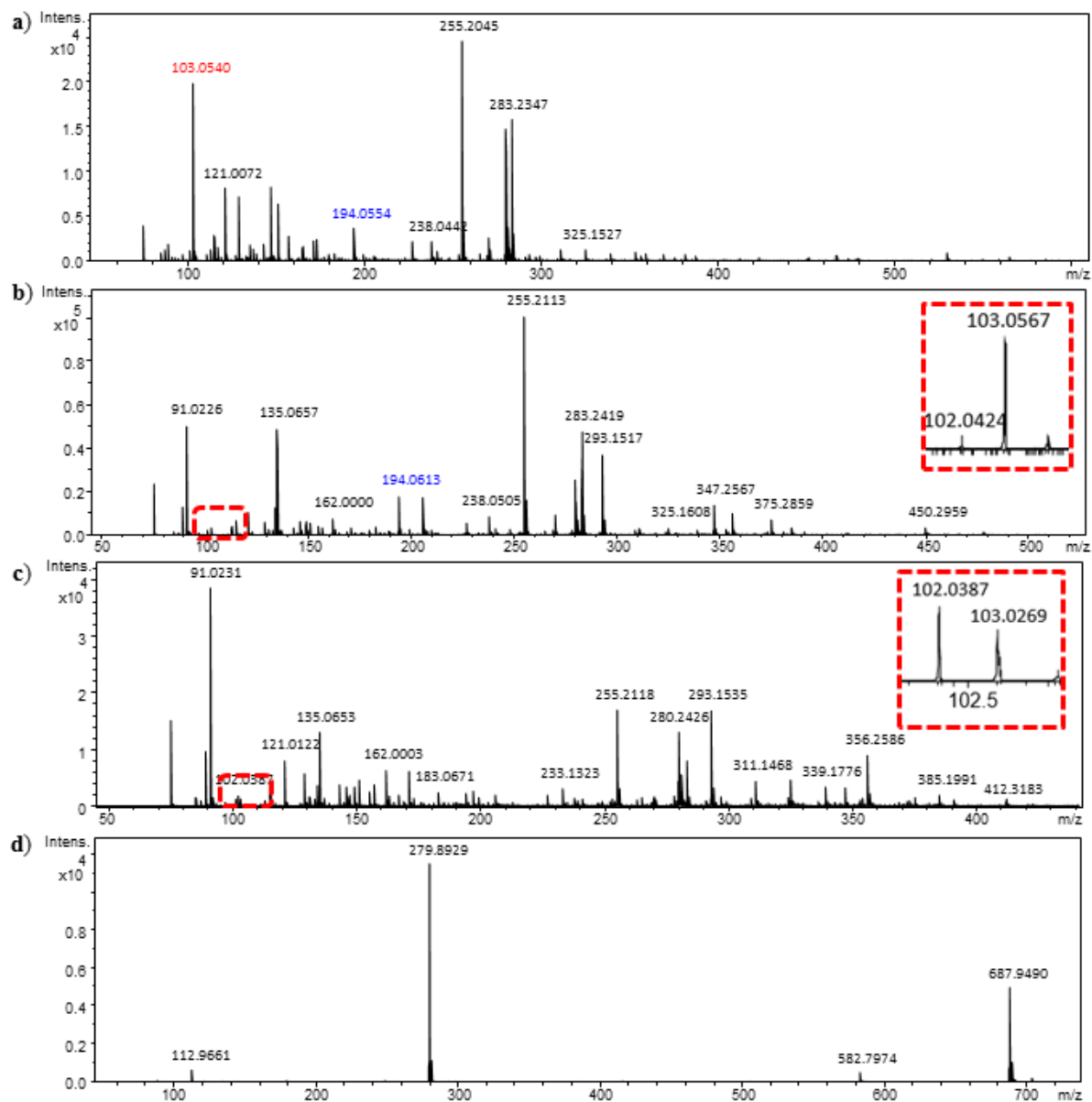
Figure A31 ESI-TOF-MS spectra of the degradation extract of **PEI-2PC** degraded at 180 °C after a) 500 h, b) 1000 h, c) 3000 h and d) 5000 h.
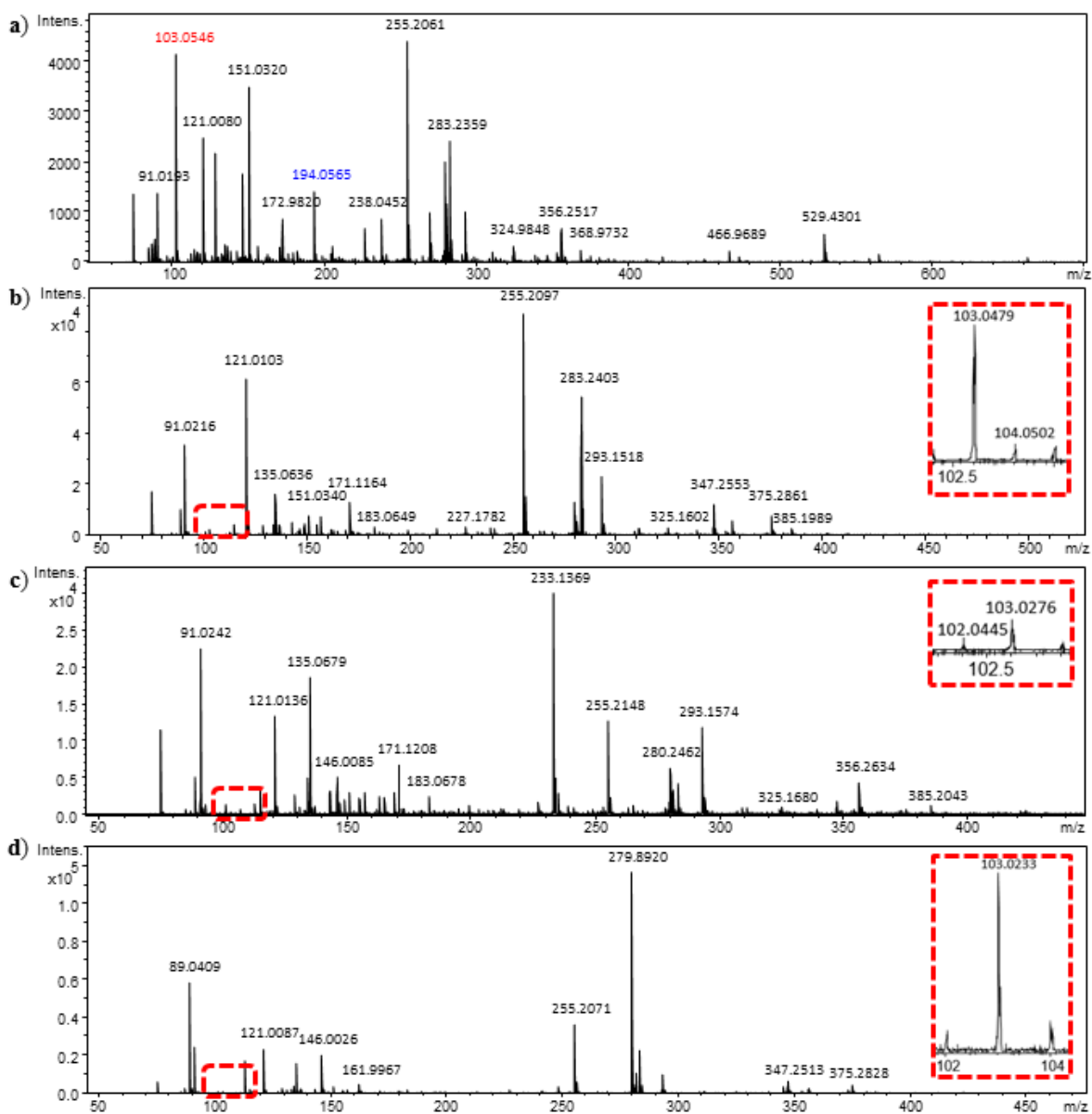
Figure A32 ESI-TOF-MS spectra of the degradation extract of **PEI-2** degraded at 220 °C after a) 500 h, b) 1000 h, c) 3000 h and d) 5000 h.
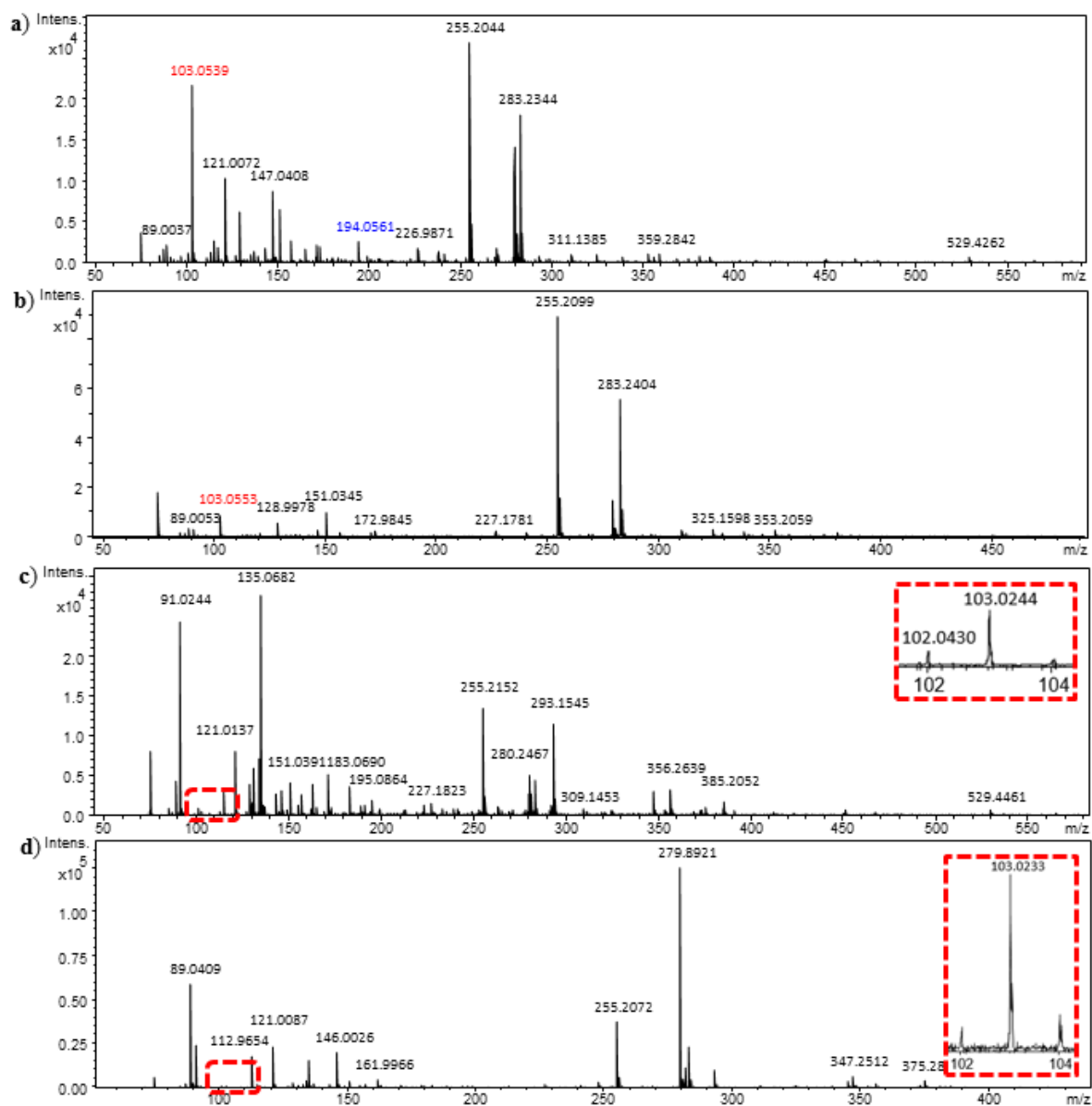
Figure A33 ESI-TOF-MS spectra of the degradation extract of **PEI-2** degraded at 200 °C after a) 500 h, b) 1000 h, c) 3000 h and d) 5000 h.
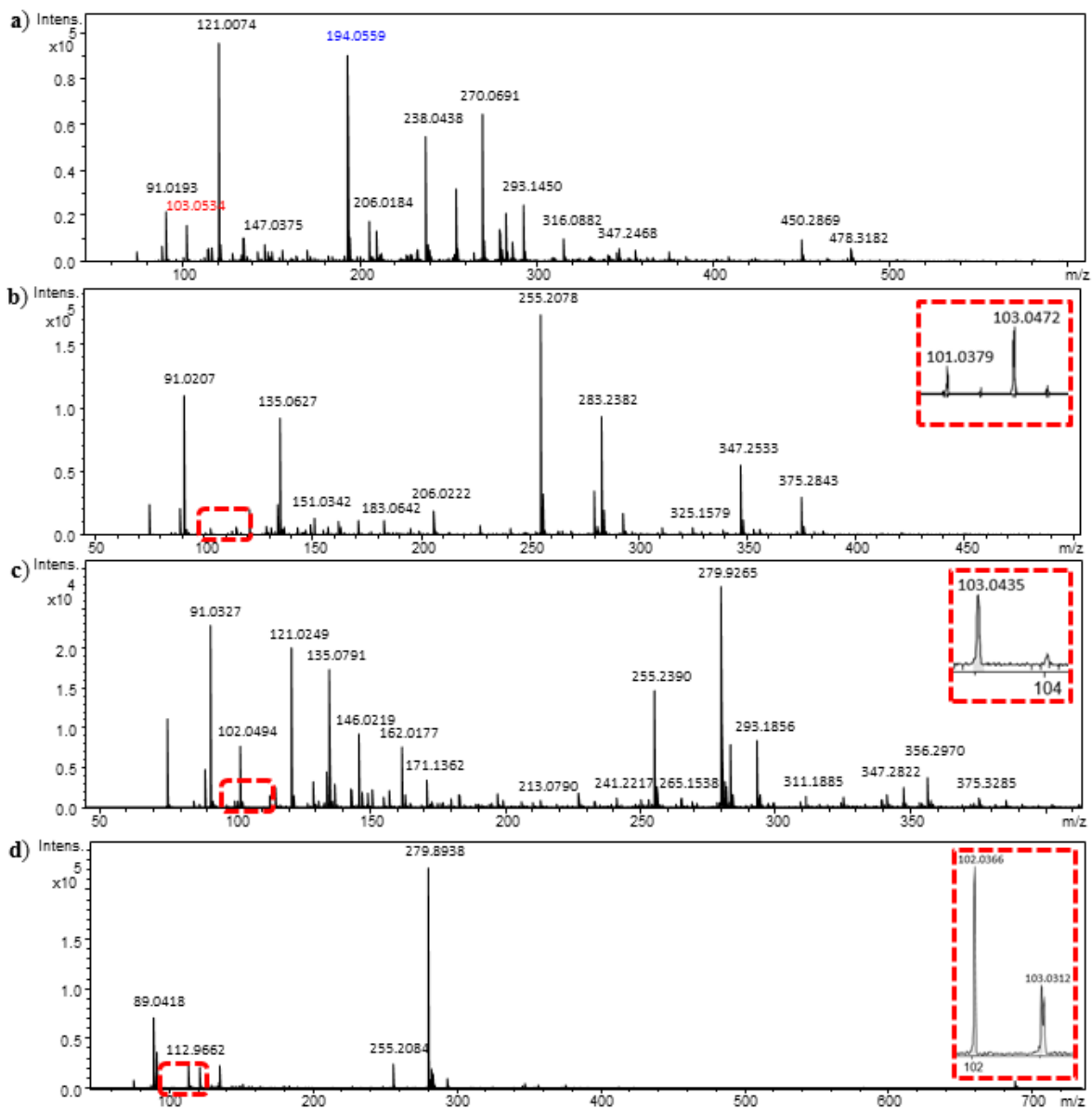
Figure A34 ESI-TOF-MS spectra of the degradation extract of **PEI-2** degraded at 180 °C after a) 500 h, b) 1000 h, c) 3000 h and d) 5000 h.
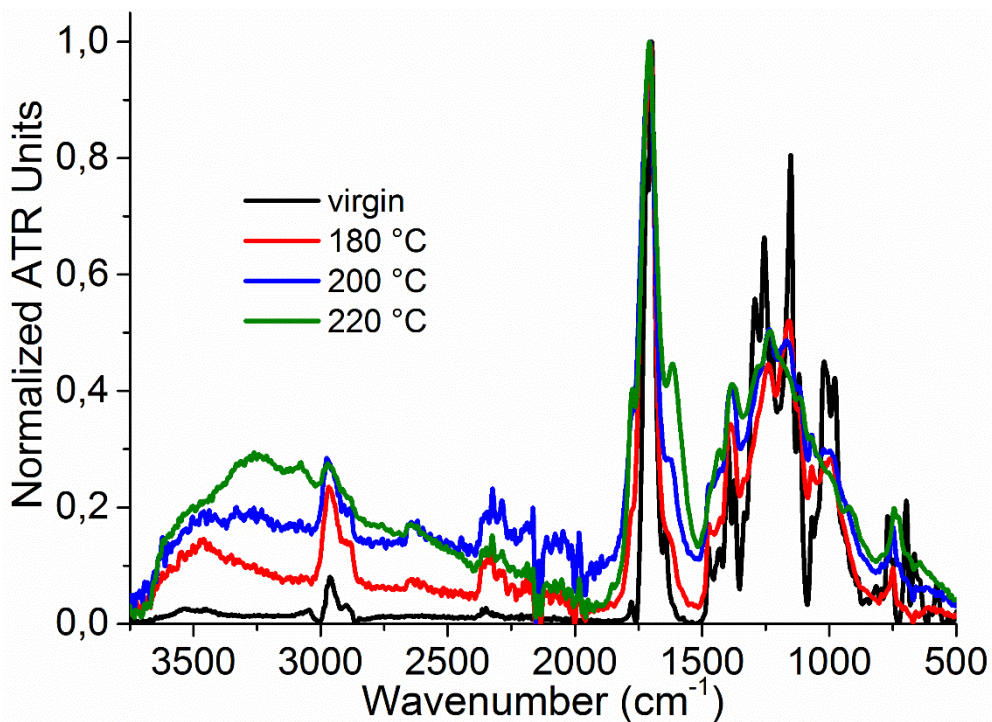
Figure A35 IR spectra of **PEI-1PC** before and after thermal aging after 5000 h at the given temperature.
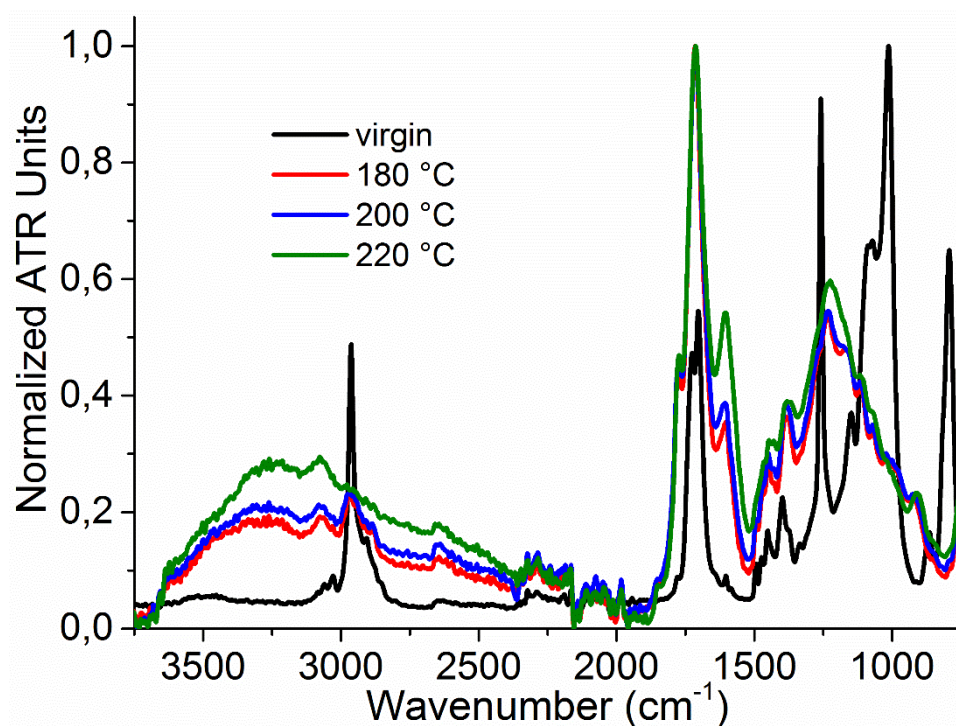
Figure A36 IR spectra of **PEI-1** before and after thermal aging after 5000 h at the given temperature.
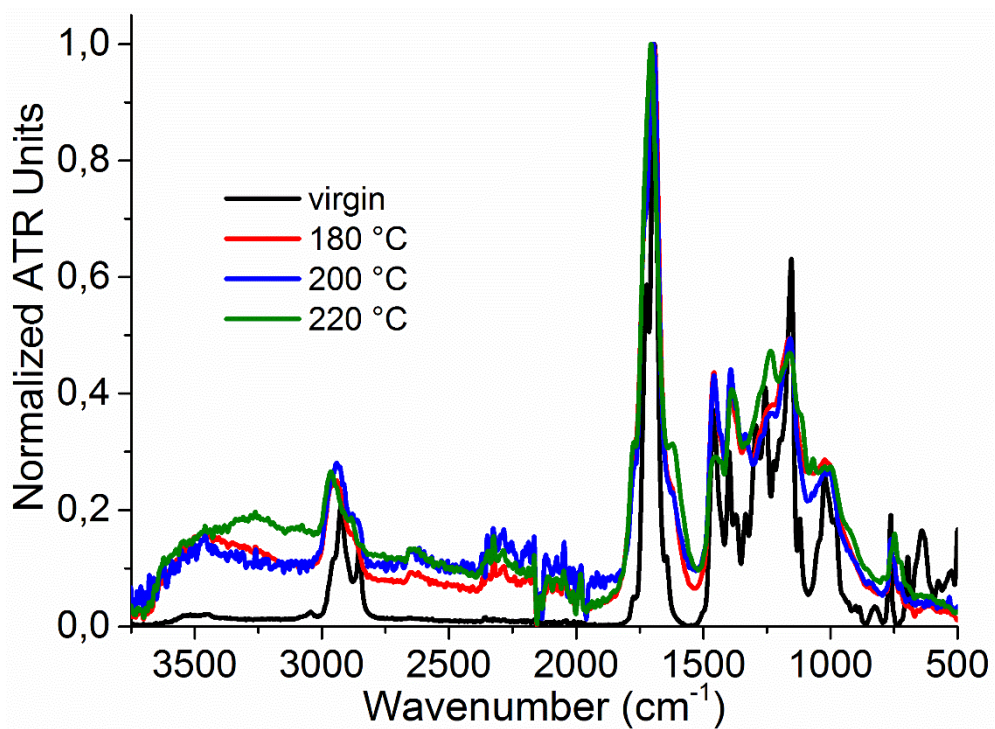
Figure A37 IR spectra of **PEI-2PC** before and after thermal aging after 5000 h at the given temperature.
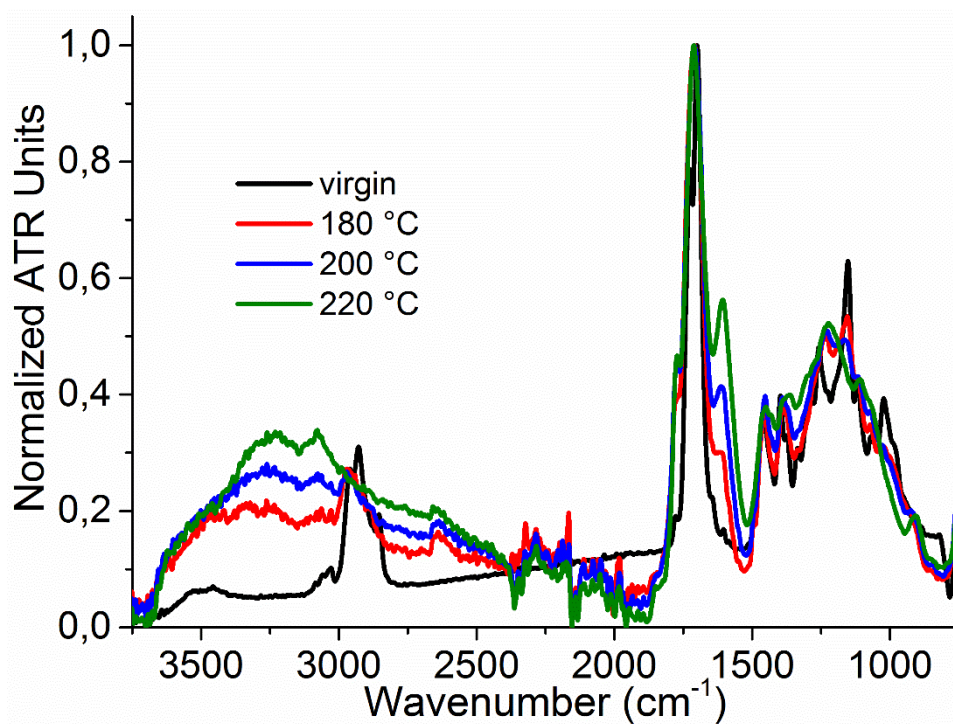
Figure A38 IR spectra of **PEI-2PC** before and after thermal aging after 5000 h at the given temperature.

7.2. Characterization of the sensor molecules (1-5, Stil-3, Stil-4, Azo-3)
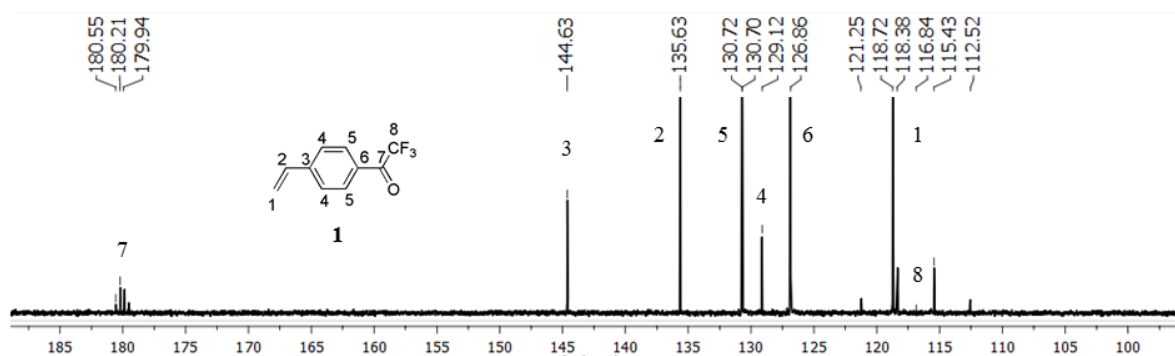
Figure A39 ^{13}C-NMR spectrum of **1** measured in CDCl$_3$.
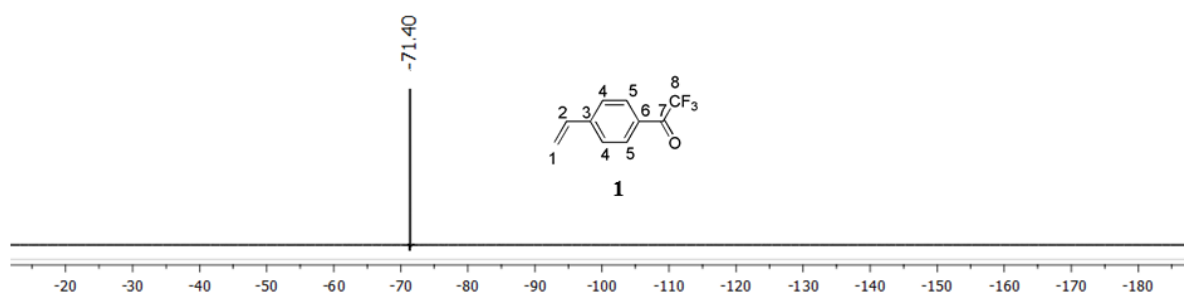
Figure A40 ^{19}F-NMR spectrum of **1** measured in CDCl$_3$.
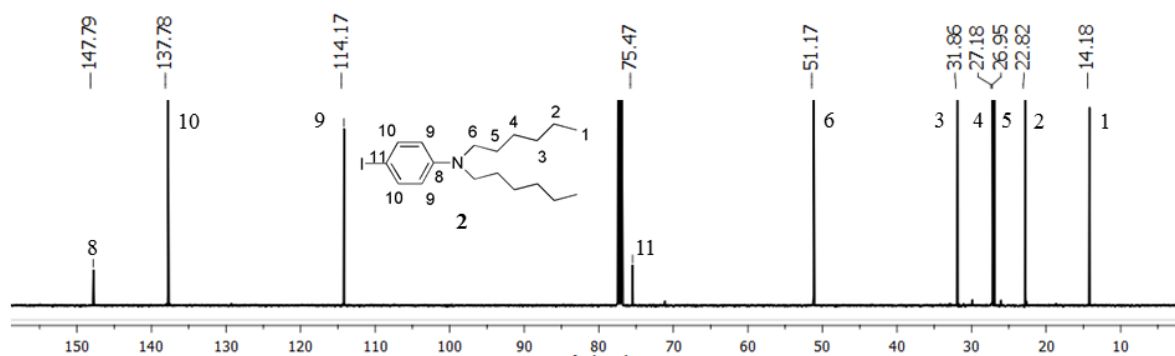
Figure A41 ^{13}C-NMR spectrum of **2** measured in CDCl$_3$.
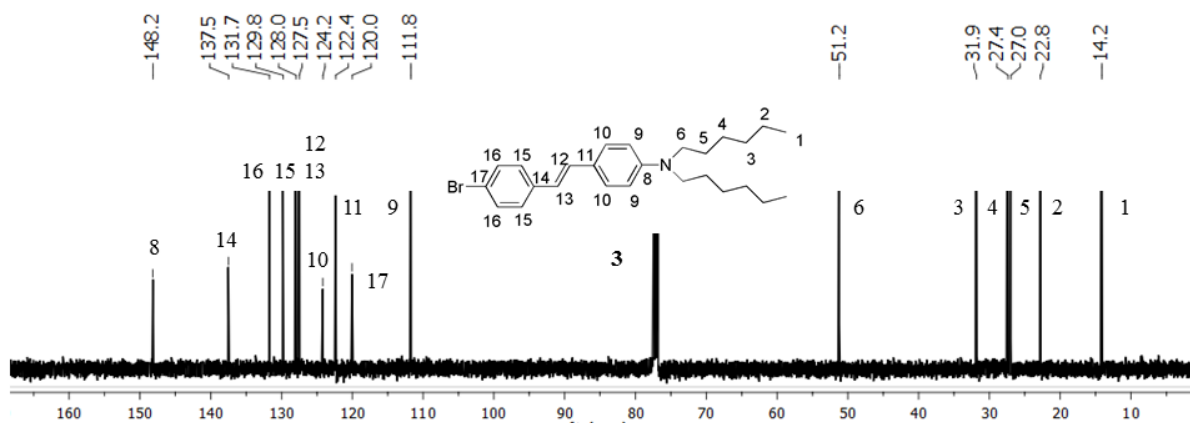
Figure A42 ^{13}C-NMR spectrum of **3** measured in CDCl$_3$.
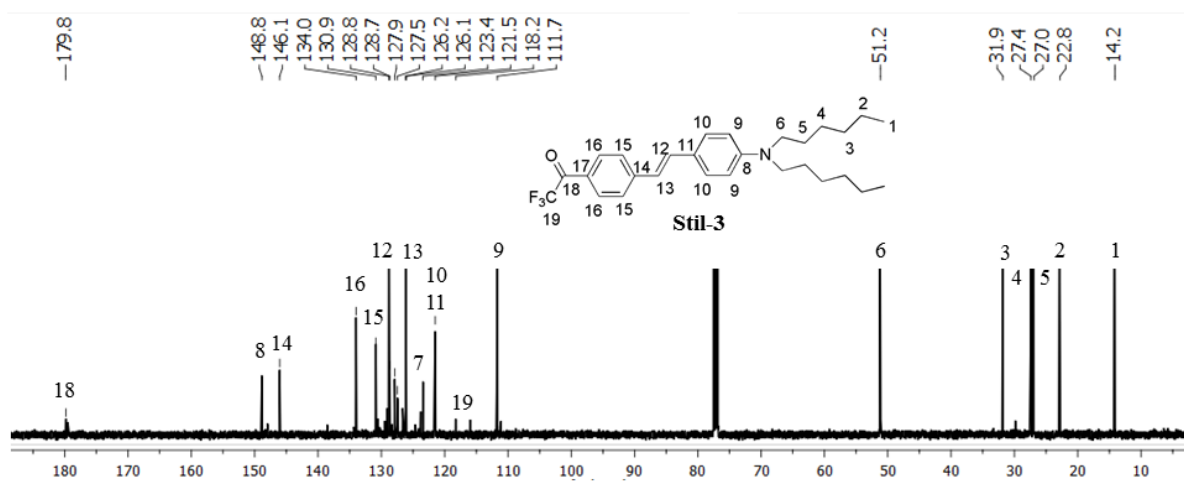
Figure A43 ^{13}C-NMR spectrum of **Stil-3** measured in CDCl$_3$.
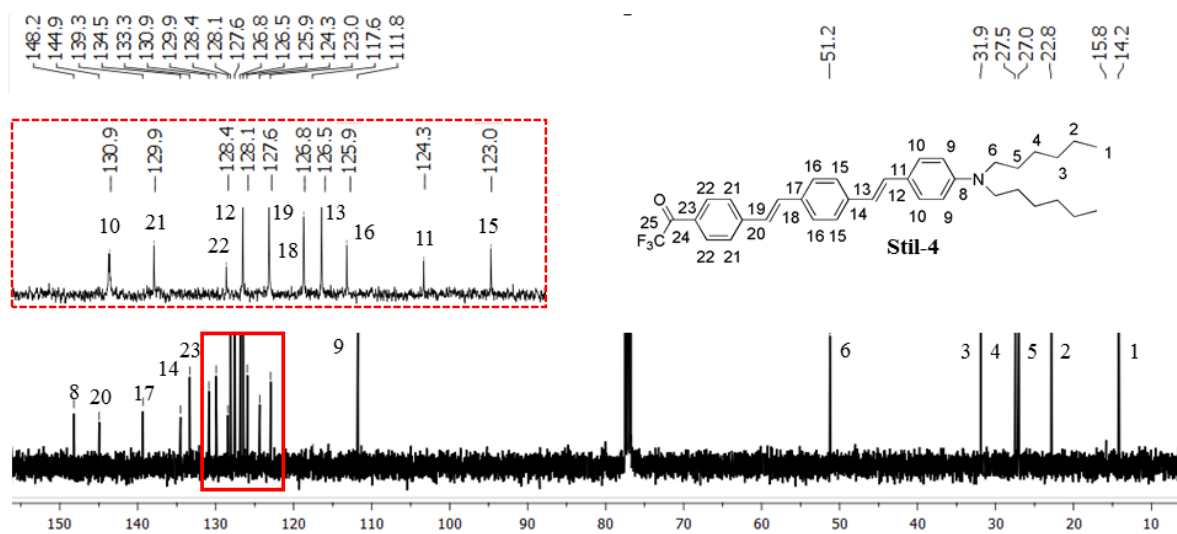
Figure A44 ^{13}C-NMR spectrum of **Stil-4** measured in CDCl$_3$.

143
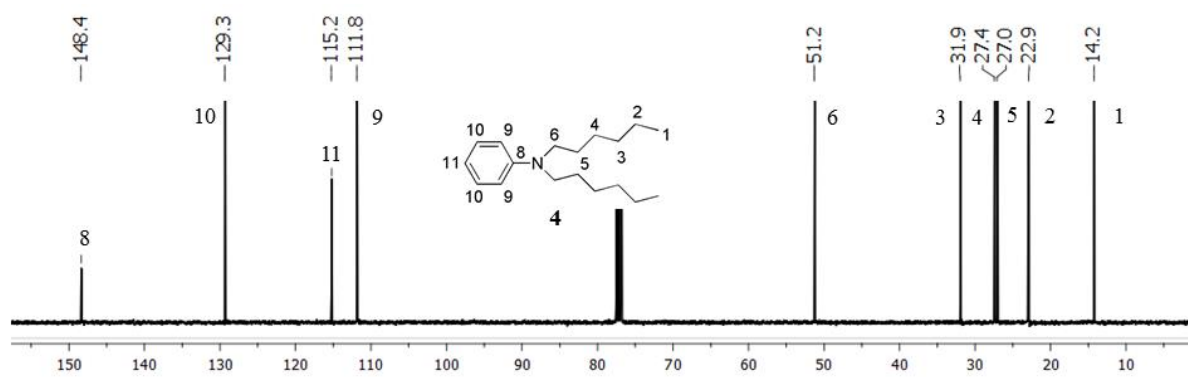
Figure A45 ¹³C-NMR spectrum of **4** measured in CDCl₃.
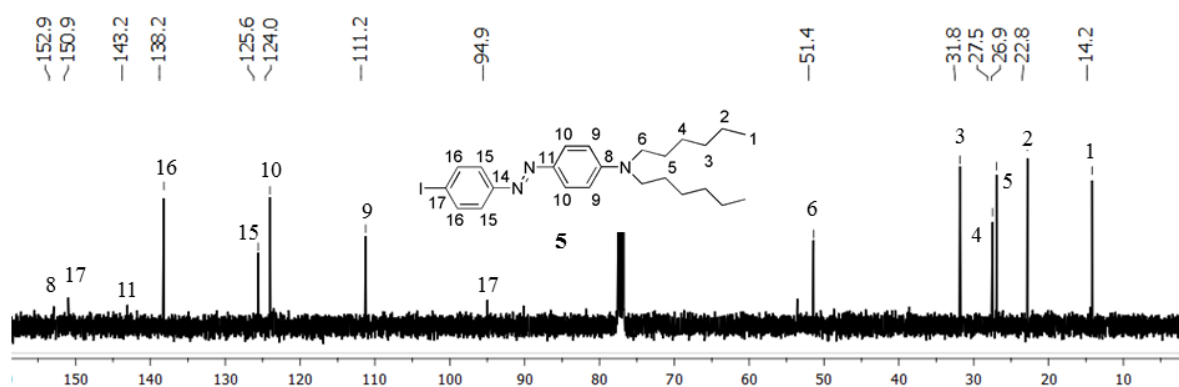
Figure A46 ¹³C-NMR spectrum of **5** measured in CDCl₃.
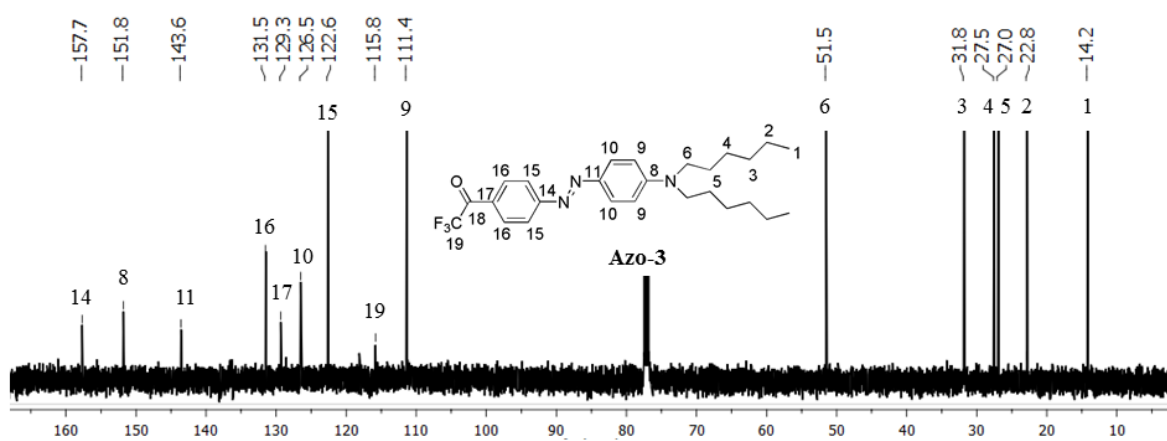
Figure A47 ¹³C-NMR spectrum of **Azo-3** measured in CDCl₃.
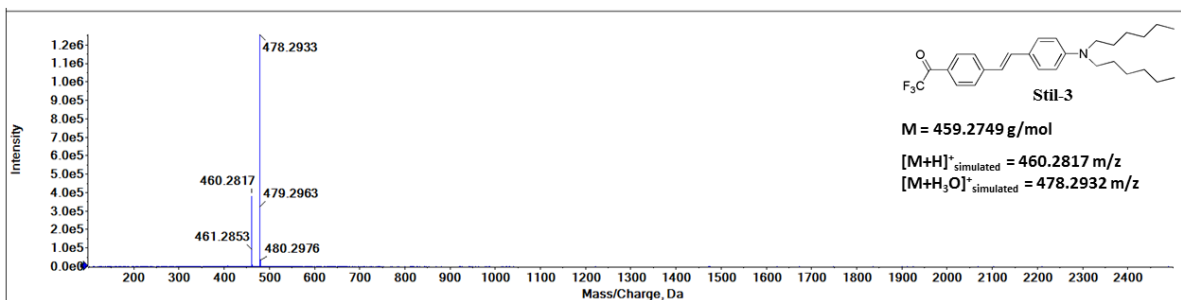
Figure A48 ESI-TOF-MS spectrum of **Stil-3**.
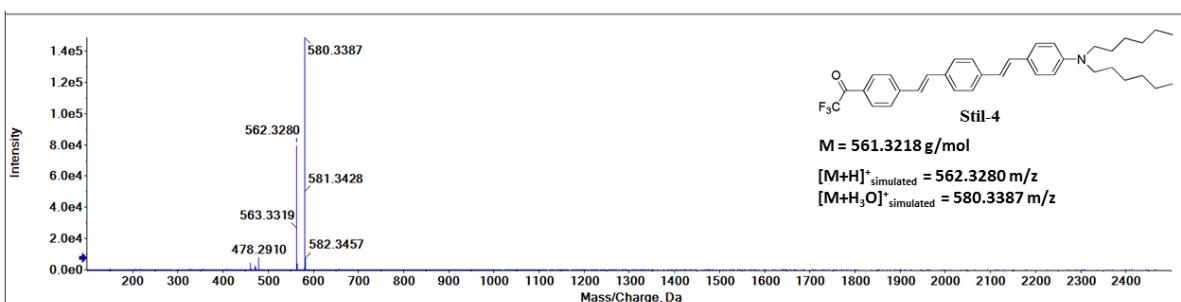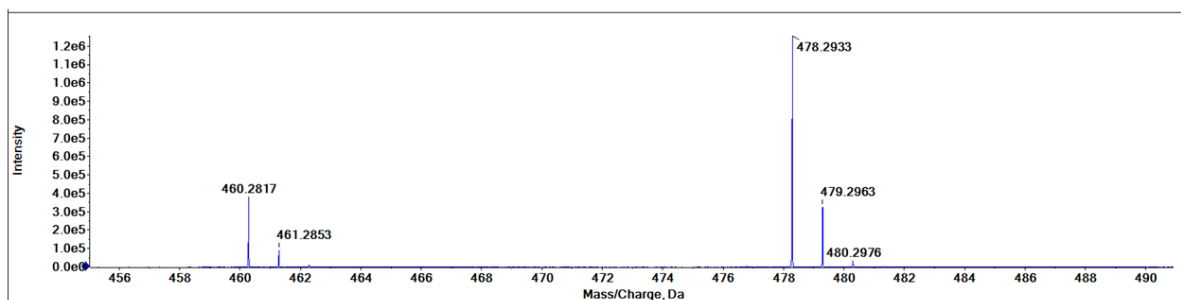
Figure A49 ESI-TOF-MS spectrum of **Stil-4**.
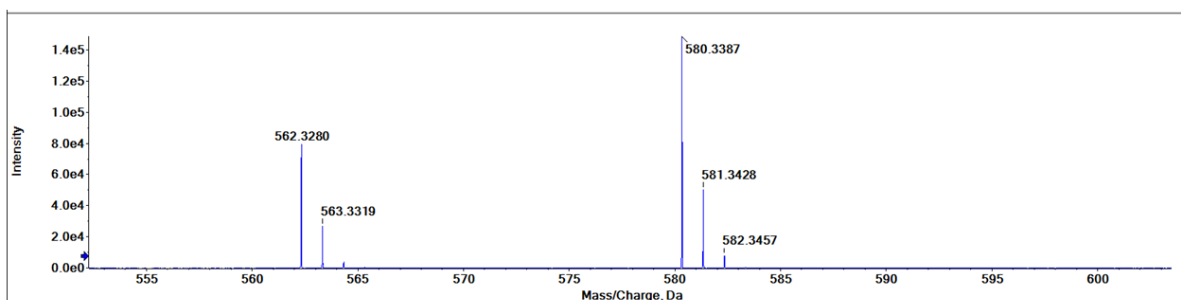
7.3. Solution experiments
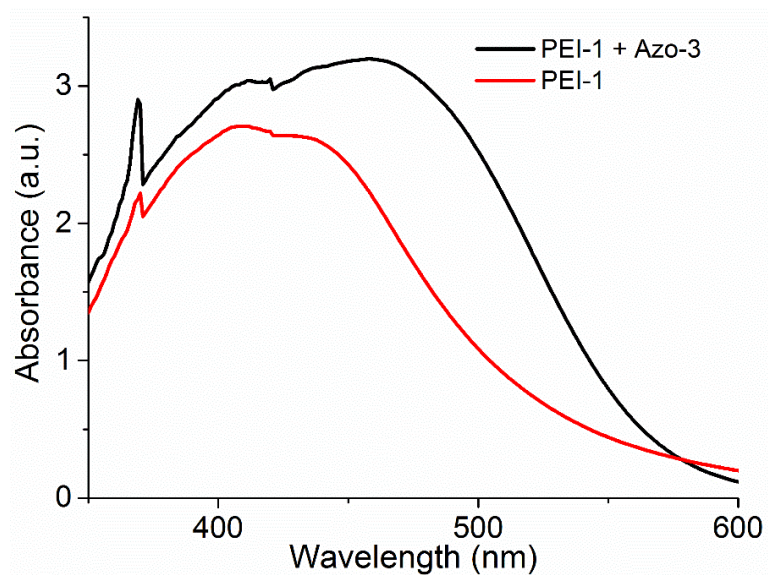
Figure A50 UV/Vis spectra of **PEI-1** without dye and with **Azo-3** ($c = 0.5$ mg/g resin).
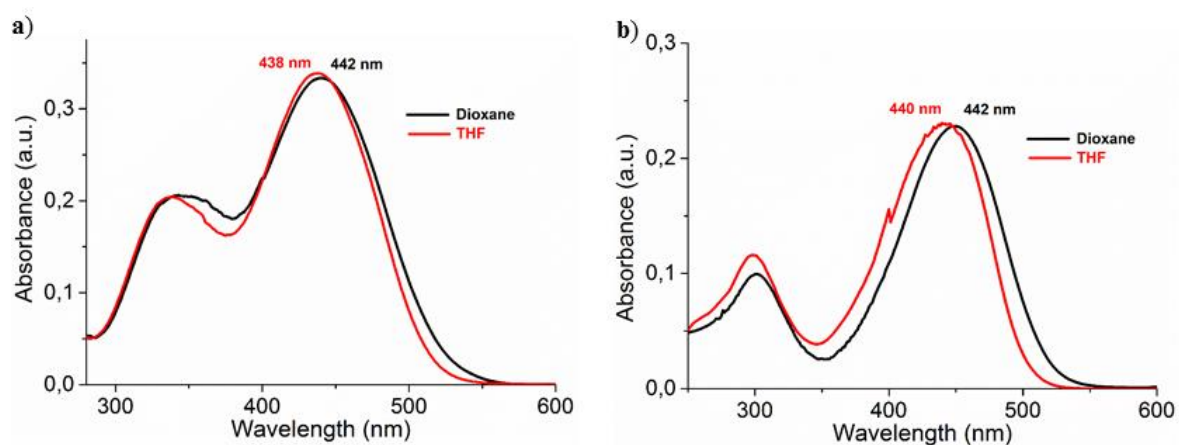
Figure A51 Comparison of UV/Vis spectra of a) **Stil-3** ($c = 0.0075 \, \mu$mol/mL) and b) **Stil-4** ($c = 0.005 \, \mu$mol/mL) measured in 1,4-dioxane and THF.
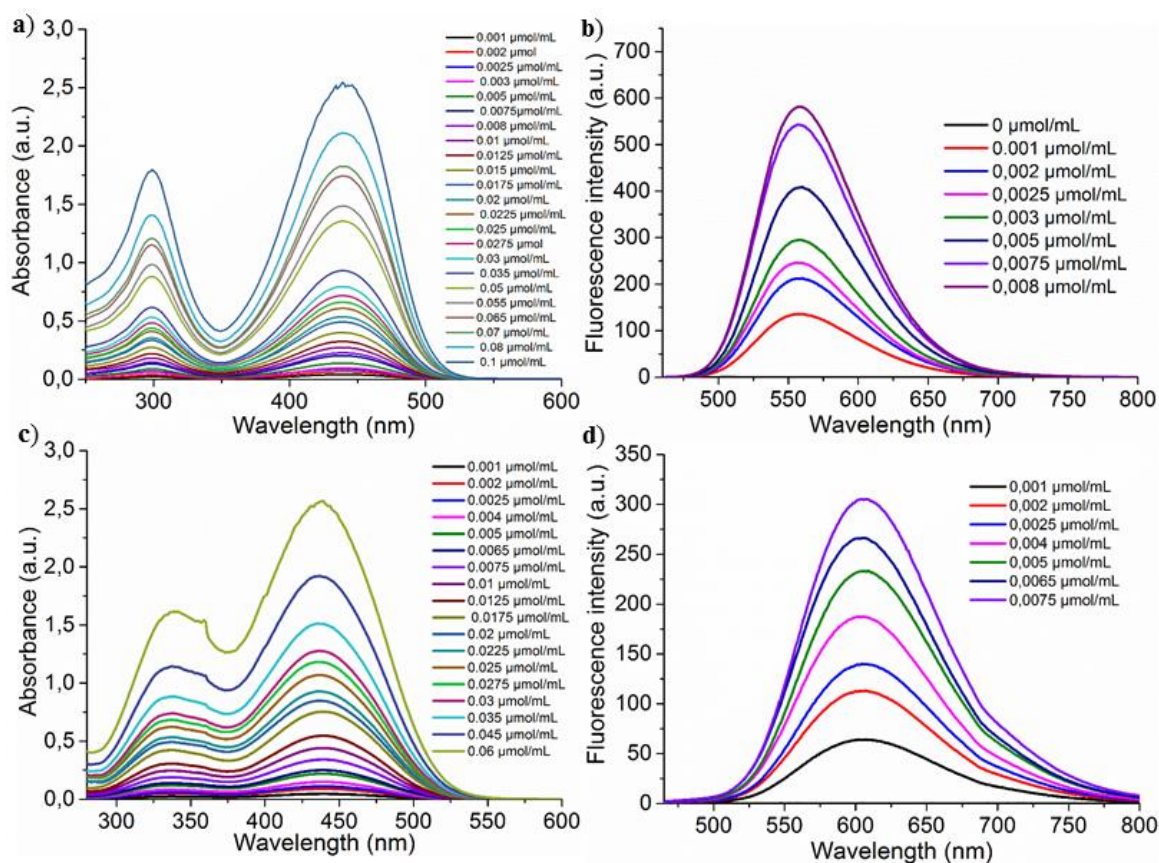
Figure A52 a) UV/Vis and b) fluorescence spectra of **Stil-3** and c) UV/Vis and d) fluorescence spectra of **Stil-4** for the concentrations series recorded in dioxane.
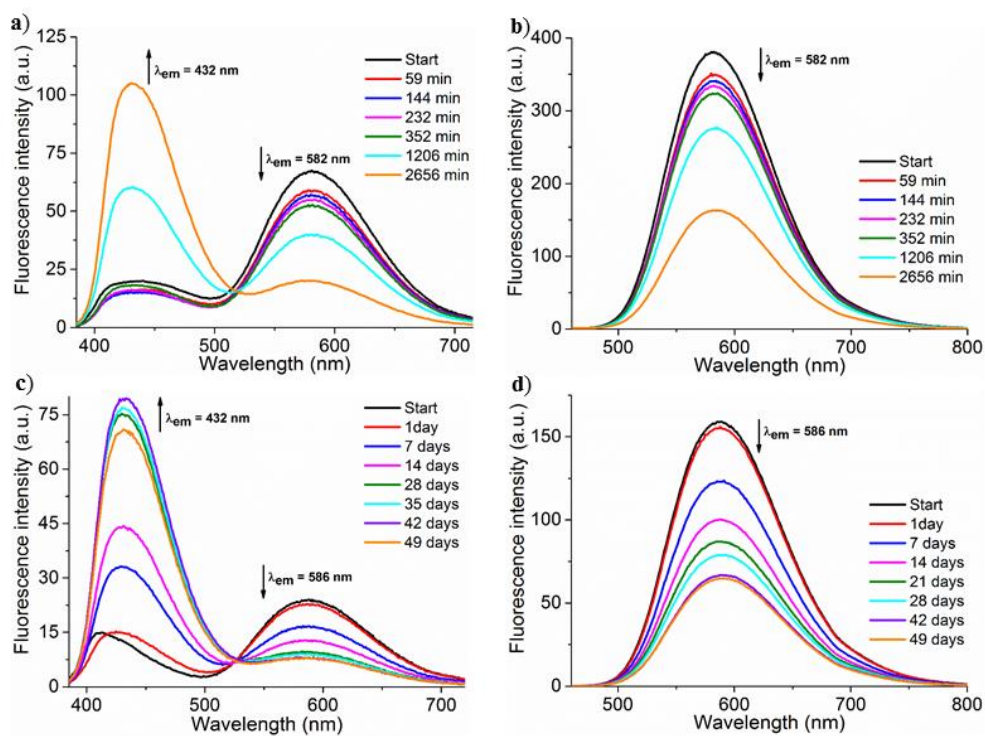
Figure A53 Emission spectra of **Stil-3** in dioxane ($c = 0.0075\,\mu$mol/mL) activated by MeOH ($c = 1$ mmol/mL) and excited at a) $\lambda_{ex} = 366$ nm and b) $\lambda_{ex} = 442$ nm and activated by NPG ($c = 1$ mmol/mL) and excited at c) $\lambda_{ex} = 366$ nm and d) $\lambda_{ex} = 442$ nm.
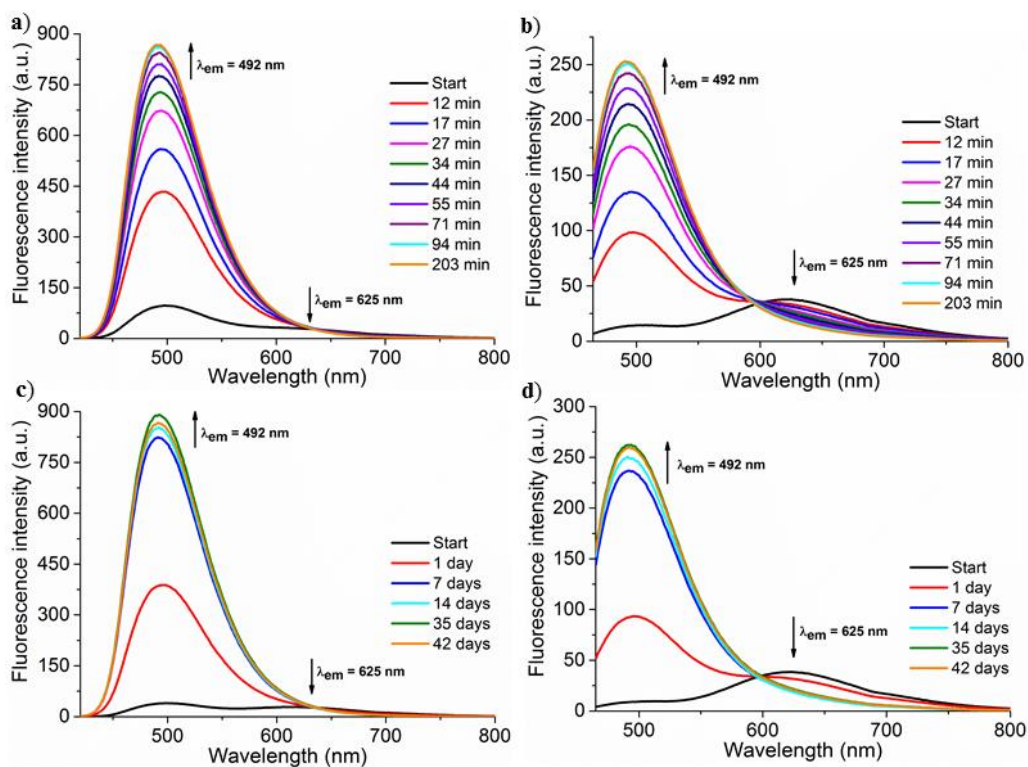
Figure A54 Emission spectra of **Stil-4** in dioxane (c = 0.0075 µmol/mL) activated by MeOH (c = 1 mmol/mL) and excited at a) λ_{ex} = 406 nm and b) λ_{ex} = 448 nm and activated by NPG (c = 1 mmol/mL) and excited at c) λ_{ex} = 406 nm and d) λ_{ex} = 448 nm.

7.4. Solid state experiments
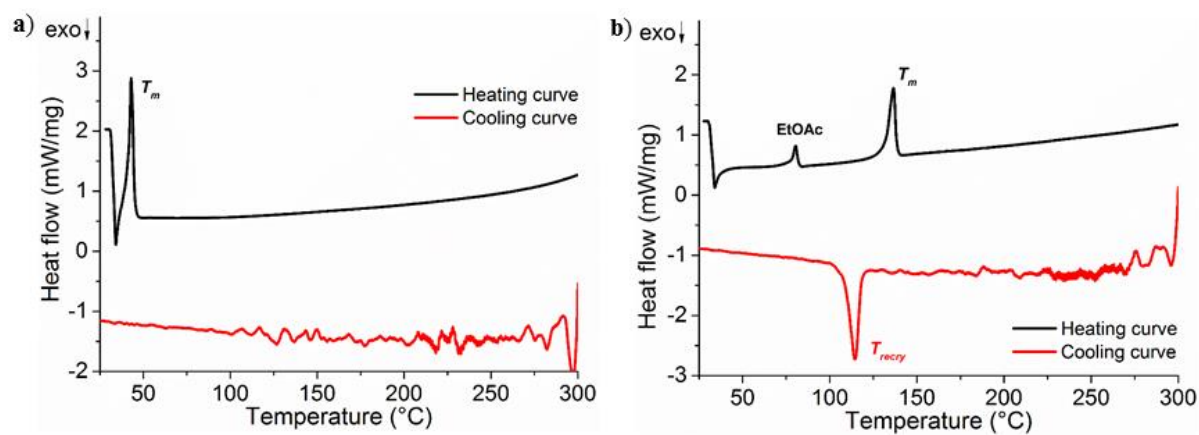
Figure A55 DSC heating and cooling curves of a) **Stil-3** and b) **Stil-4**.
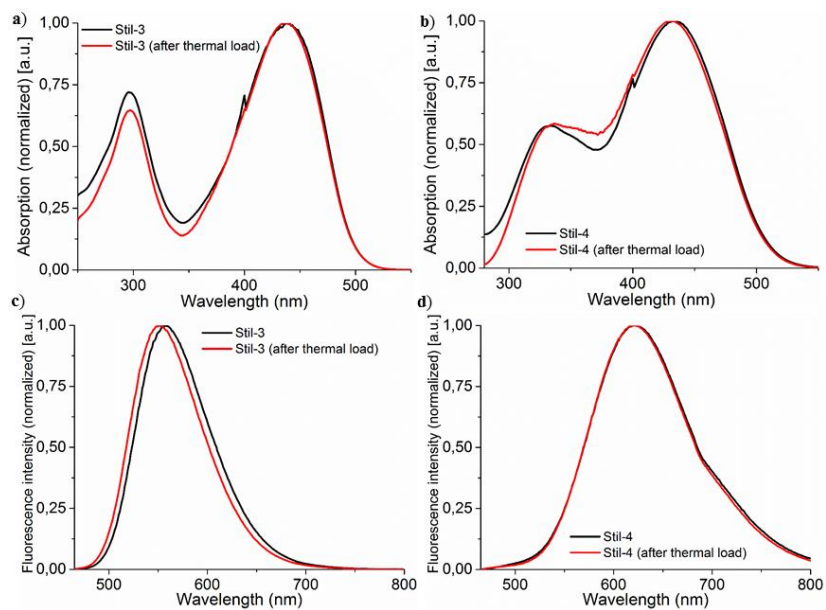
Figure A56 UV/Vis spectra of a) **Stil-3** and b) **Stil-4** together with the fluorescence spectra of c) **Stil-3** and d) **Stil-4** before and after thermal load (3 hours at 80 °C, followed by 1 hour at 140 °C).
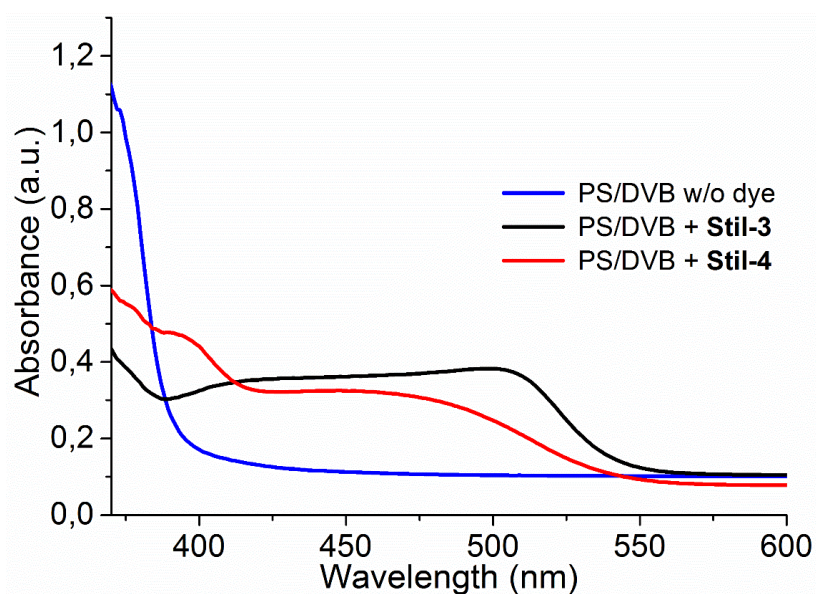
Figure A57 UV/Vis spectra of **PS/DVB** without dye and with **Stil-3** ($c = 0.5$ mg/g resin) and **Stil-4** ($c = 0.5$ mg/g resin).
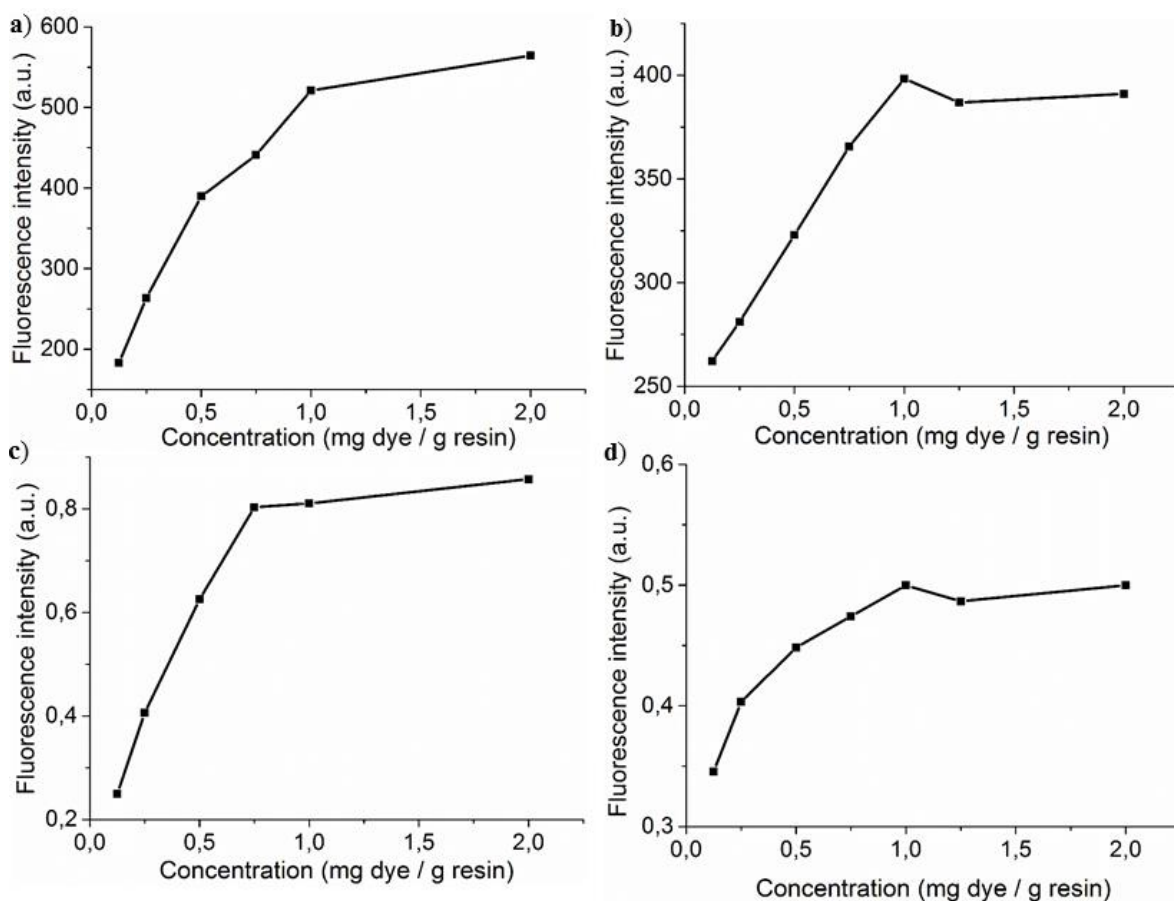
Figure A58 Concentrations series of a) + b) **Stil-3** and c) + d) **Stil-4** within **PEI-1** measured with the Agilent Spectrophotometer (*left*) and the spectro2guide (*right*).
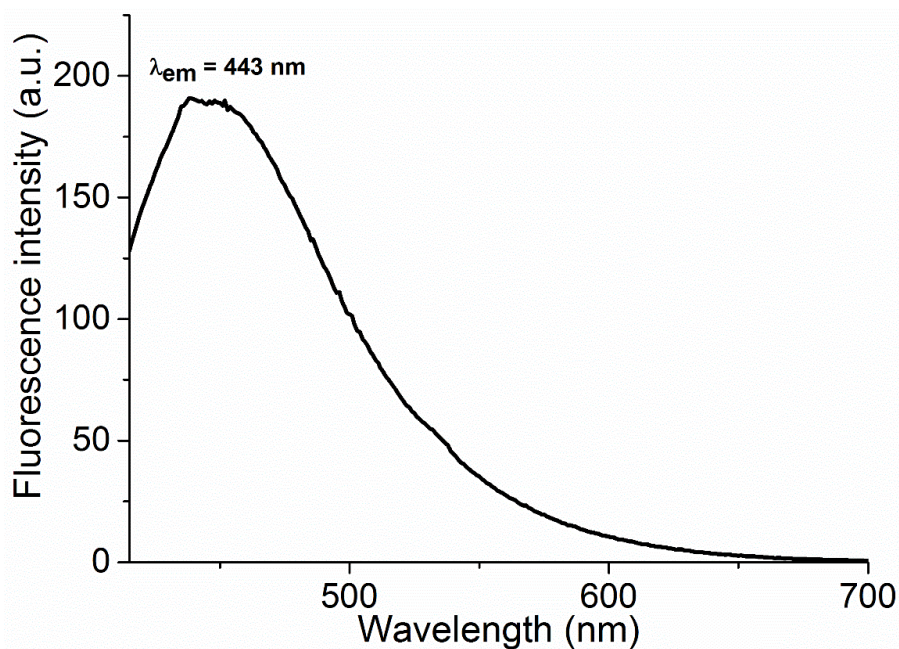
Figure A59 Emission spectrum of **PEI-1** without dye excited at $\lambda_{ex} = 390$ nm.
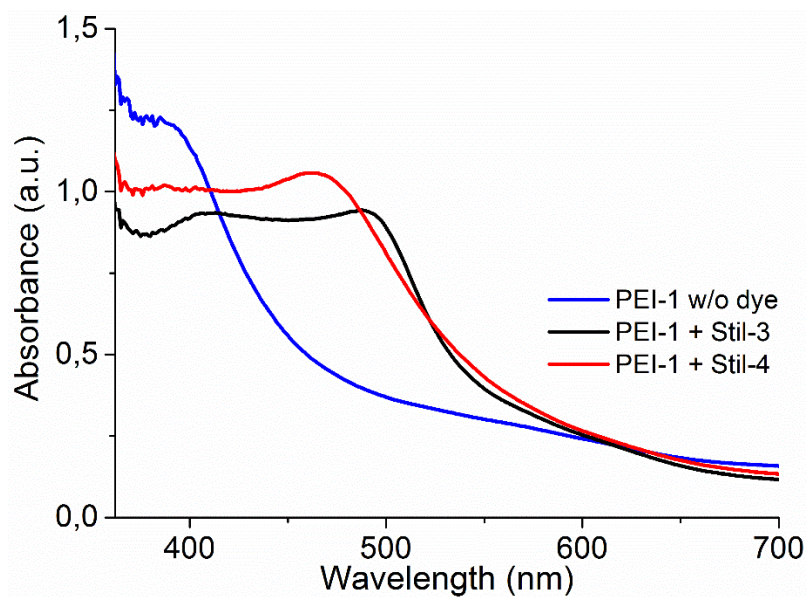
Figure A60 UV/Vis spectra of **PEI-1** without dye and with **Stil-3** ($c = 1$ mg/g resin) and **Stil-4** ($c = 1$ mg/g resin).
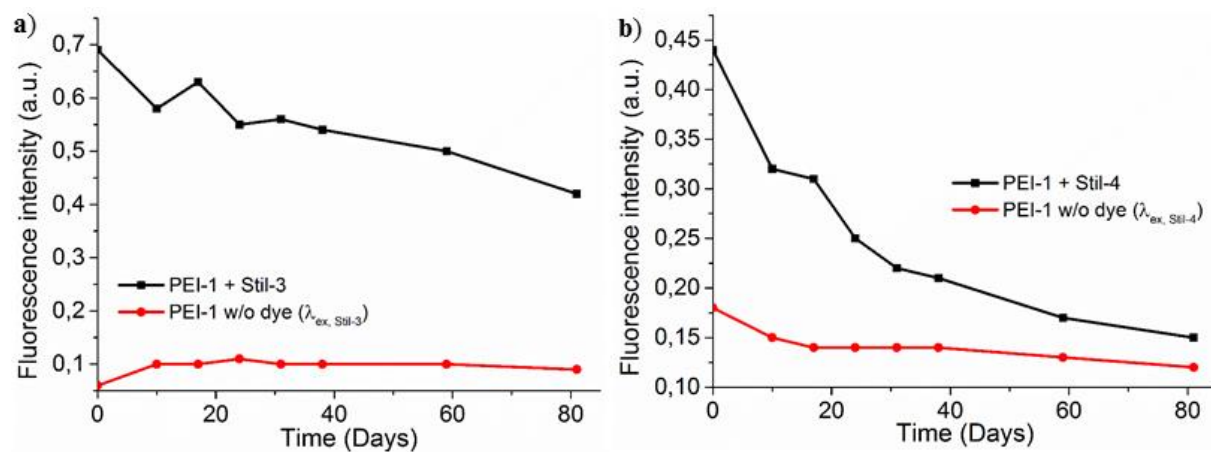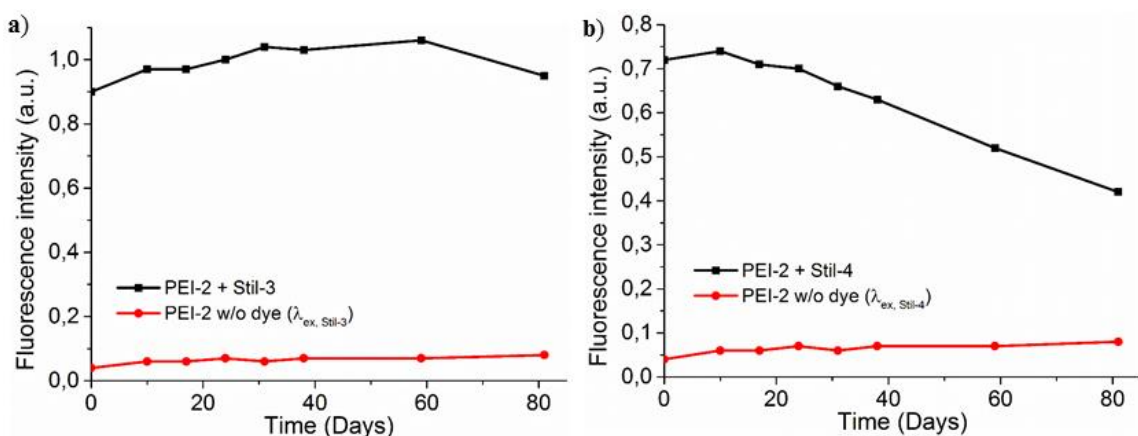

Figure A61 Plot of the fluorescence intensities *vs.* time together with the corresponding control experiment for a) **Stil-3** ($c = 1$ mg/g resin, $\lambda_{ex} = 460$ nm) b) **Stil-4** ($c = 1$ mg/g resin, $\lambda_{ex} = 410$ nm) embedded within **PEI-1** and thermally aged at 180 °C measured with the spectro2guide.
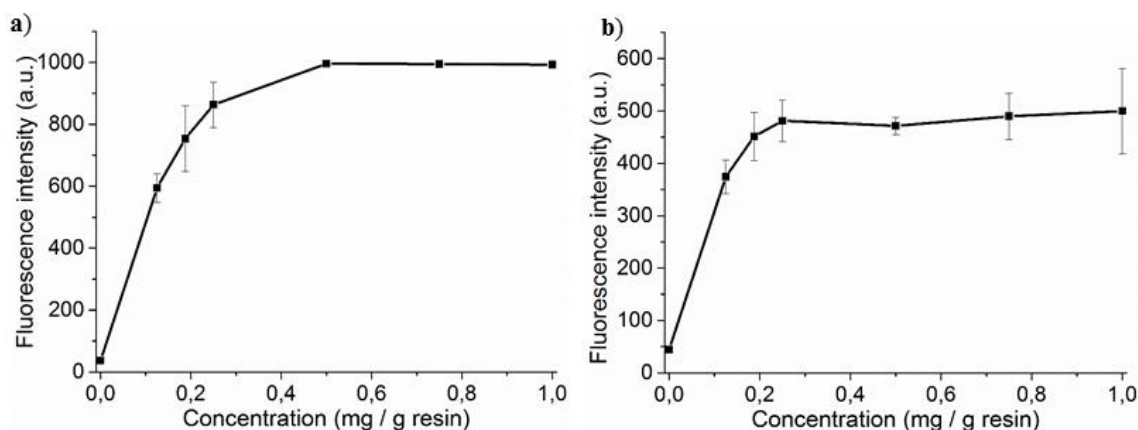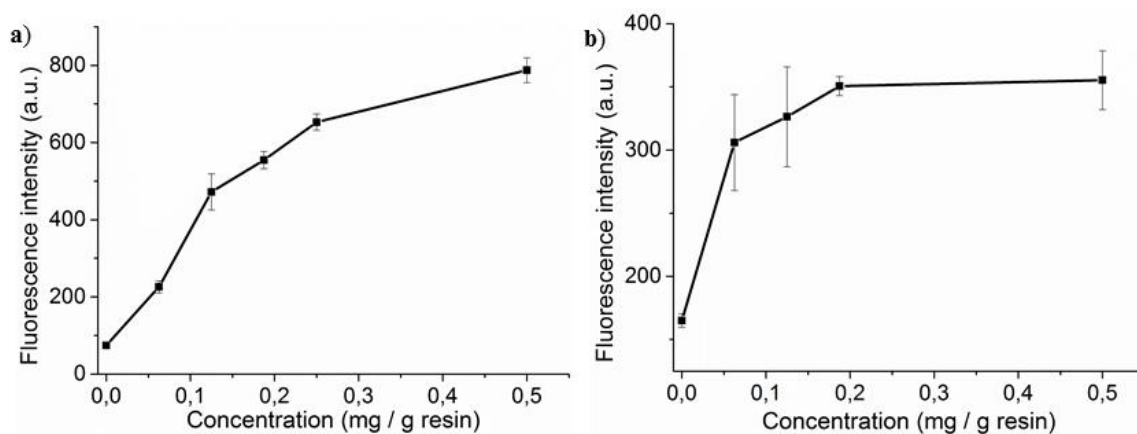
**Figure A62** Concentration series of a) **Stil-3** and b) **Stil-4** within **PEI-2**.
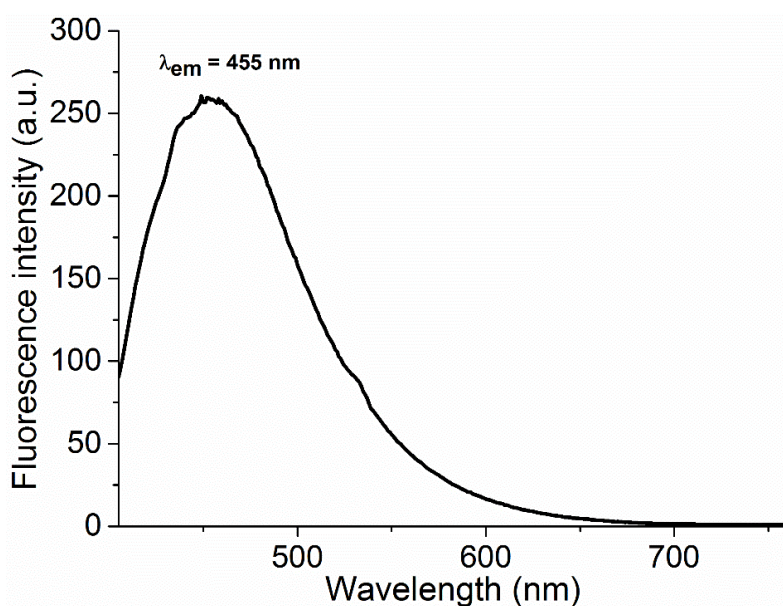
Figure A63 Emission spectrum of **PEI-2** without dye excited at λ_{ex} = 390 nm.

Figure A64 Plot of the fluorescence intensities *vs*. time together with the corresponding control experiment for a) **Stil-3** (c = 1 mg/g resin, λ_{ex} = 500 nm) b) **Stil-4** (c = 1 mg/g resin, λ_{ex} = 500 nm) embedded within **PEI-2** and thermally aged at 180 °C measured with the spectro2guide.

Figure A65 Concentrations series of a) **Stil-3** and b) **Stil-4** within **PEI-3**.
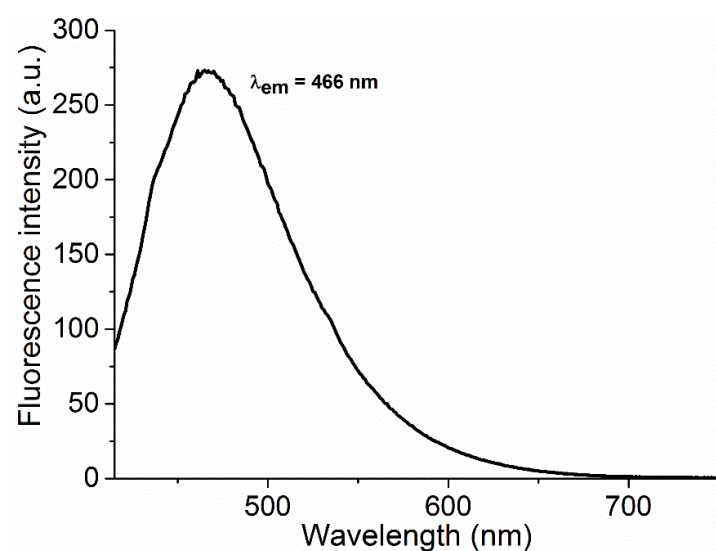
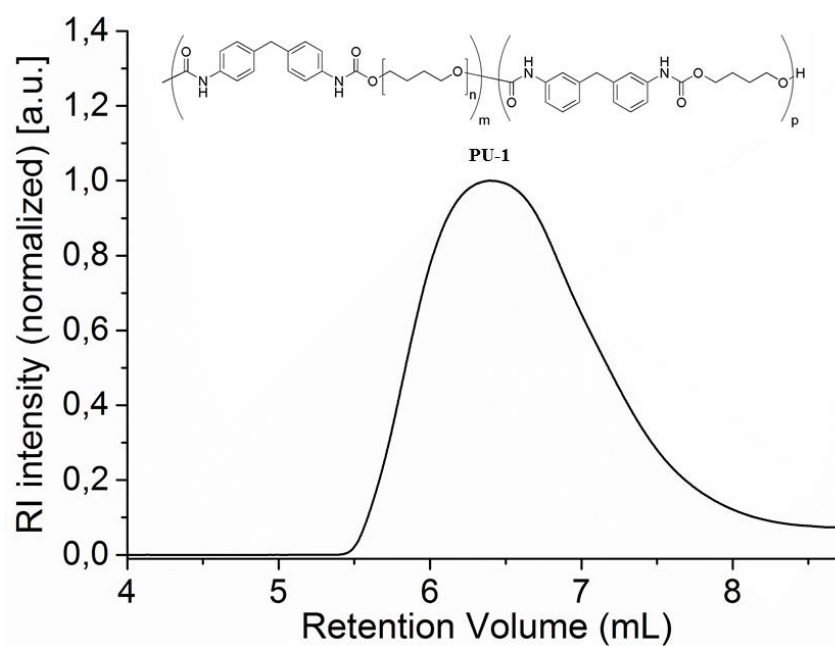**Figure A66** Emission spectrum of **PEI-3** without dye excited at λ_{ex} = 392 nm.
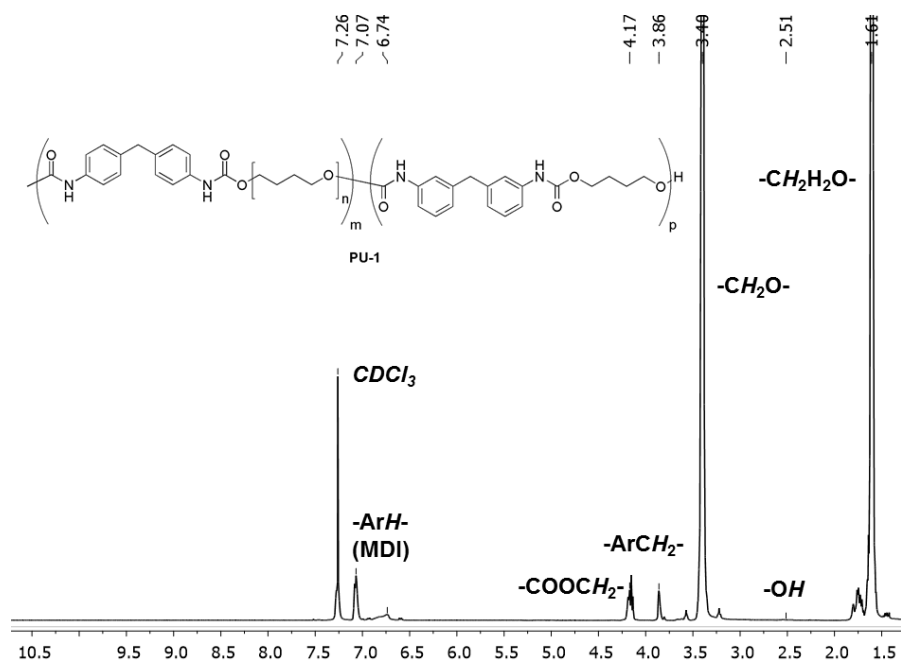

Figure A67 GPC trace of **PU-1**.

Figure A68 ¹H-NMR spectrum of **PU-1** measured in CDCl₃.
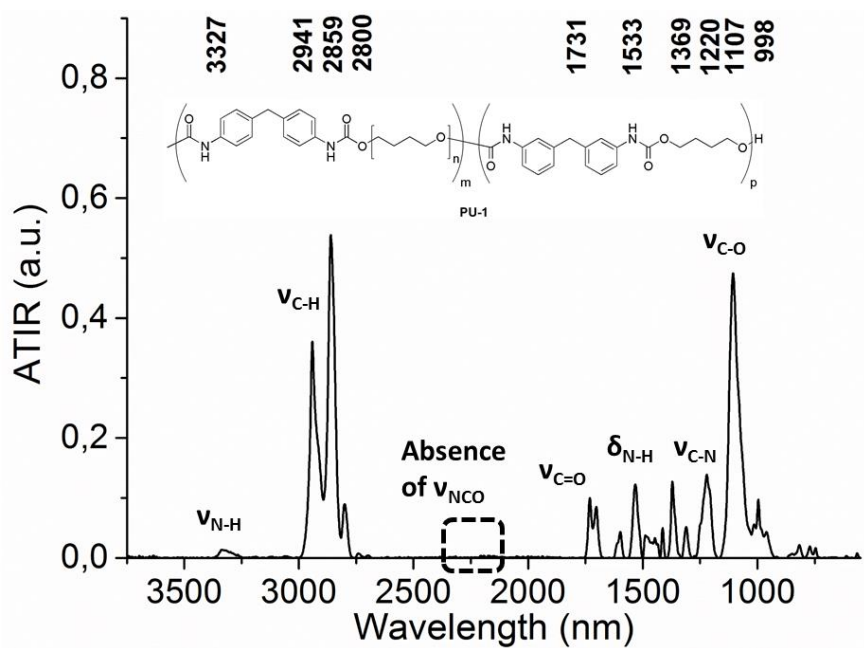

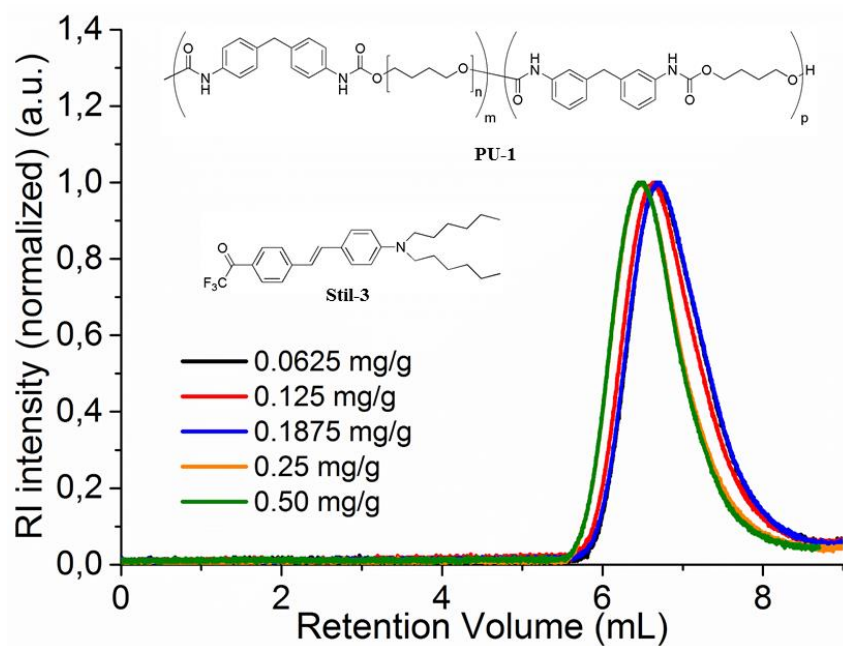**Figure A69** IR spectrum of **PU-1**.

Figure A70 GPC traces of **PU-1** containing different concentrations of **Stil-3** (mg dye/g resin) (R = -C_6H_{13}).
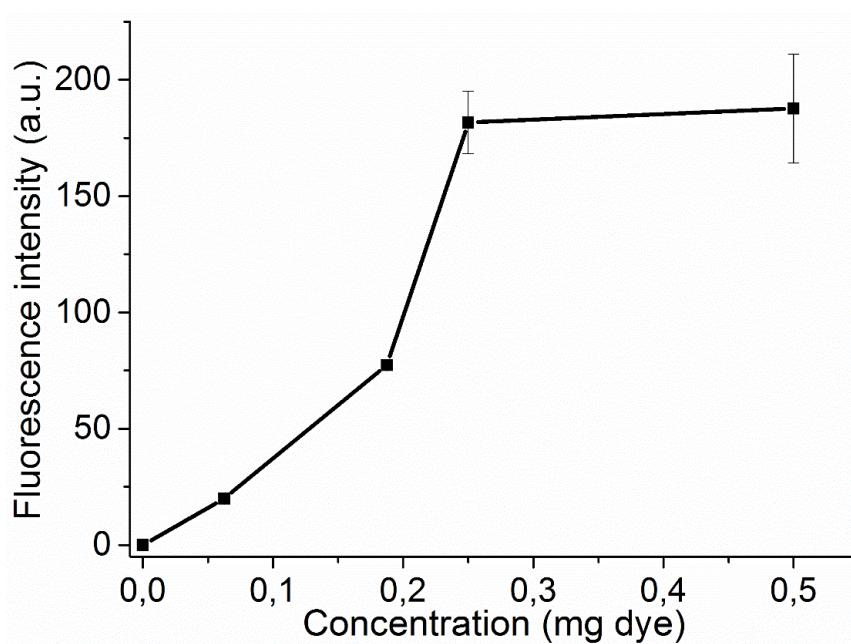

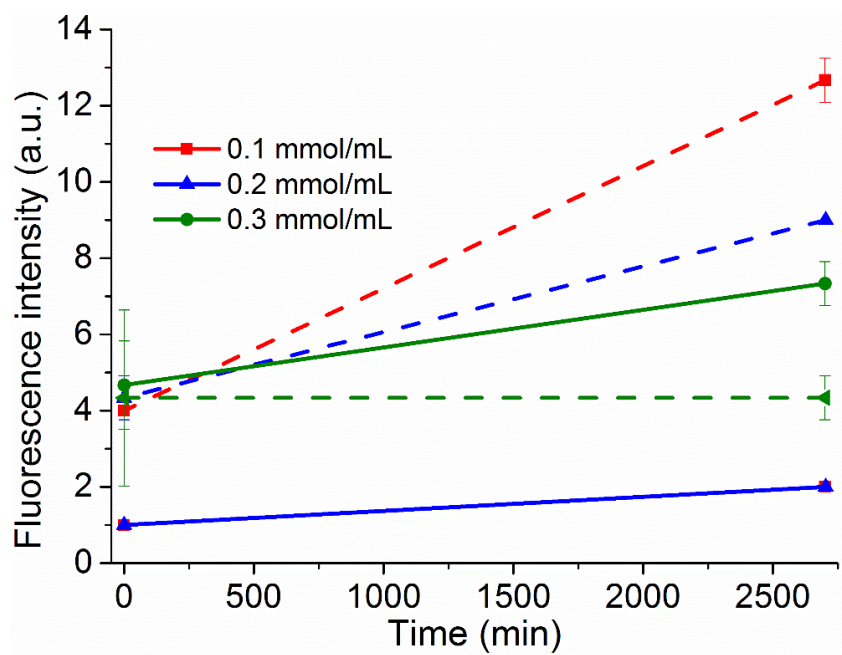**Figure A71** Concentration series of **Stil-3** within **PU-1**.

Figure A72 Fluorescence control experiments of **PU-1** exposed to different concentrations of an aqueous *n*-BuA solution excited at $\lambda_{ex1} = 465$ nm ($\lambda_{em} = 575$ nm, solid) and $\lambda_{ex2} = 350$ nm ($\lambda_{em} = 425$ nm, dashed)

8. Curriculum Vitae

Persönliche Angaben

Alexander Funtan

Geburtsdatum: 07.08.1989

Geburtsort: Kassel

Familienstand: Verheiratet

Berufliche Erfahrung

01/2018 – 02/2022   **Wissenschaftlicher Mitarbeiter (Doktorand)**

                      Martin-Luther-Universität Halle-Wittenberg, Makromolekulare Chemie

06/2012 – 09/2012   **Mitarbeiter Qualifizierung und Validierung**

                      B. Braun Melsungen AG, Berlin

Bildungsweg

10/2015 – 12/2017   Masterstudium Chemie, Martin-Luther-Universität Halle-Wittenberg

                      Masterarbeit in der Makromolekularen Chemie

10/2012 – 10/2015   Bachelorstudium Chemie, Martin-Luther-Universität Halle-Wittenberg

                      Bachelorarbeit in der Makromolekularen Chemie

09/2009 – 06/2012   Ausbildung zum Pharmakanten

                      B. Braun Melsungen AG, Berlin

08/2006 – 06/2009   Jacob-Grimm-Schule (Oberstufengymnasium), Kassel

08/2000 – 07/2006   Heinrich-Schütz-Schule (Gymnasialzweig), Kassel

Publikationsliste

Funtan, A.; Michael, P.; Rost, S.; Omeis, J., Lienert, K.; Binder, W. H., Self-Diagnostic Polymers – Inline Detection of Thermal Degradation of Unsaturated Poly(ester imide)s, *Advanced Materials* **2021**, 2100068.

Funtan, A.; Binder, W. H., Thermischen Abbau erkennen, *Nachrichten aus der Chemie* **2022**, *70*, 40.

Funtan, A.; Binder, W. H., Towards in-line detection of thermal polymer degradation, *Research Outreach* **2021**, *125*, 190.

Parts of this thesis have been protected by the patent 10577PFA WO filed from ALTANA AG.

Halle (Saale), den 15.11.2022 _____

Alexander Funtan

9. Eigenständigkeitserklärung

Hiermit versichere ich an Eides statt, dass ich die vorliegende Arbeit selbstständig und ausschließlich unter Benutzung der in der Arbeit angegebenen Quellen und Hilfsmittel angefertigt habe. Alle, aus anderen Quellen, direkt oder dem Sinn nach entnommenen Inhalte wurden als solche kenntlich gemacht.

Außerdem erkläre ich, dass die vorliegende Dissertation an keiner anderen wissenschaftlichen Einrichtung zur Erlangung eines akademischen Grades eingereicht wurde.

Halle (Saale), den 15.11.2022   _____

                                                                          Alexander Funtan